MULTIPHASE FLOW HANDBOOK

SECOND EDITION

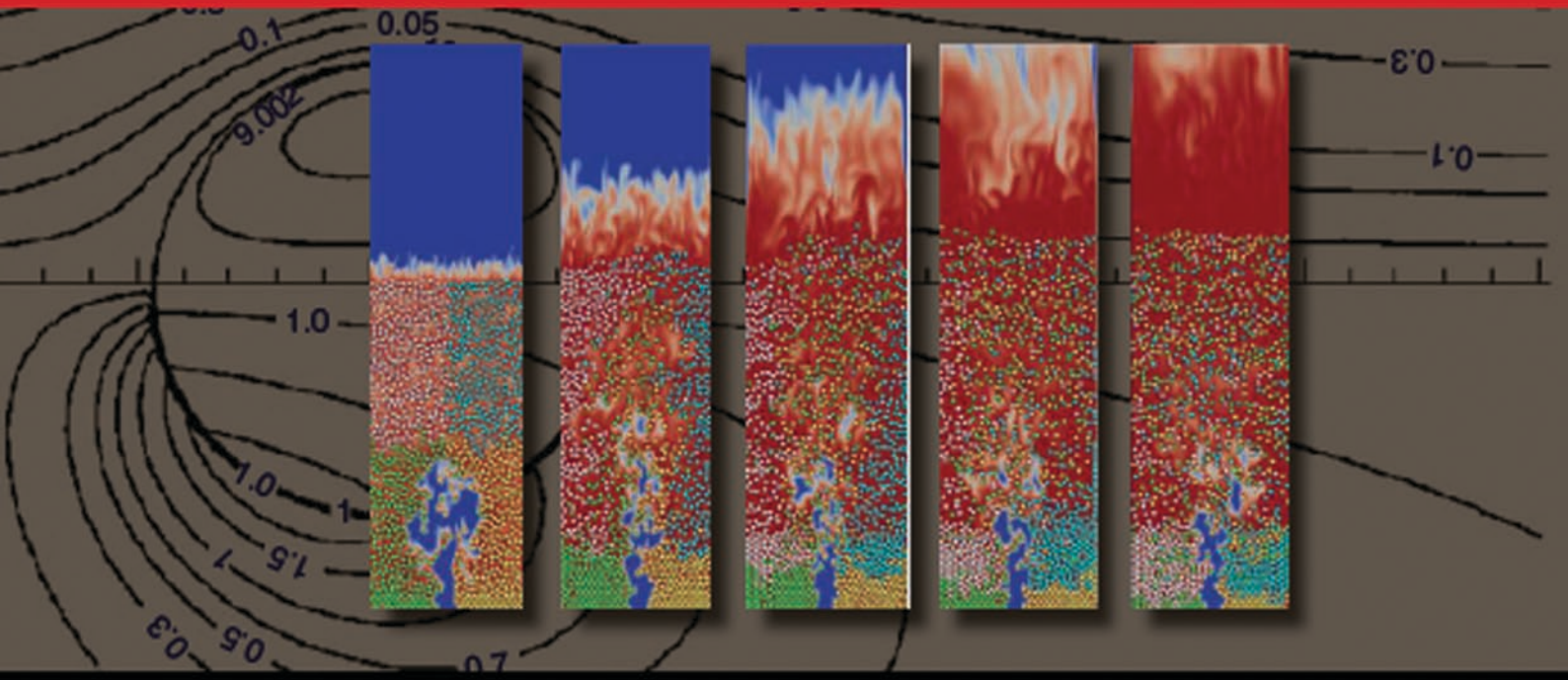

EDITED BY

Efstathios E. Michaelides

Clayton T. Crowe

John D. Schwarzkopf

CRC Press

Taylor & Francis Group

MULTIPHASE FLOW HANDBOOK

SECOND EDITION

MECHANICAL and AEROSPACE ENGINEERING

Frank Kreith
Series Editor

RECENTLY PUBLISHED TITLES

Air Distribution in Buildings, *Essam E. Khalil*

Alternative Fuels for Transportation, *Edited by Arumugam S. Ramadhas*

Computer Techniques in Vibration, *Edited by Clarence W. de Silva*

Design and Control of Automotive Propulsion Systems,
Zongxuan Sun and Guoming (George) Zhu

Distributed Generation: The Power Paradigm for the New Millennium,
Edited by Anne-Marie Borbely and Jan F. Kreider

Elastic Waves in Composite Media and Structures: With Applications to Ultrasonic Nondestructive Evaluation, *Subhendu K. Datta and Arvind H. Shah*

Elastoplasticity Theory, *Vlado A. Lubarda*

Energy Audit of Building Systems: An Engineering Approach, *Moncef Krarti*

Energy Conversion, Second Edition, *Edited by D. Yogi Goswami and Frank Kreith*

Energy Efficiency and Renewable Energy Handbook, Second Edition,
Edited by D. Yogi Goswami and Frank Kreith

Energy Efficiency in the Urban Environment, *Heba Allah Essam E. Khalil and Essam E. Khalil*

Energy Management and Conservation Handbook, Second Edition,
Edited by Frank Kreith and D. Yogi Goswami

Essentials of Mechanical Stress Analysis, *Amir Javidinejad*

The Finite Element Method Using MATLAB®, Second Edition, *Young W. Kwon and Hyochoong Bang*

Fluid Power Circuits and Controls: Fundamentals and Applications, *John S. Cundiff*

Fuel Cells: Principles, Design, and Analysis, *Shripad Revankar and Pradip Majumdar*

Fundamentals of Environmental Discharge Modeling, *Lorin R. Davis*

Handbook of Hydrogen Energy, *Edited by S.A. Sherif, D. Yogi Goswami, Elias K. Stefanakos, and Aldo Steinfeld*

Heat Transfer in Single and Multiphase Systems, *Greg F. Naterer*

Heating and Cooling of Buildings: Design for Efficiency, Revised Second Edition,
Jan F. Kreider, Peter S. Curtiss, and Ari Rabl

Intelligent Transportation Systems: Smart and Green Infrastructure Design, Second Edition, *Sumit Ghosh and Tony S. Lee*

Introduction to Biofuels, *David M. Mousdale*

Introduction to Precision Machine Design and Error Assessment, *Edited by Samir Mekid*

Introductory Finite Element Method, *Chandrakant S. Desai and Tribikram Kundu*

Large Energy Storage Systems Handbook, *Edited by Frank S. Barnes and Jonah G. Levine*

Machine Elements: Life and Design, *Boris M. Klebanov, David M. Barlam, and Frederic E. Nystrom*

Mathematical and Physical Modeling of Materials Processing Operations, *Olusegun Johnson Ilegbusi, Manabu Iguchi, and Walter E. Wahnsiedler*

Mechanics of Composite Materials, *Autar K. Kaw*

Mechanics of Fatigue, *Vladimir V. Bolotin*

Mechanism Design: Enumeration of Kinematic Structures According to Function, *Lung-Wen Tsai*

Mechatronic Systems: Devices, Design, Control, Operation and Monitoring, *Edited by Clarence W. de Silva*

The MEMS Handbook, Second Edition (3 volumes), *Edited by Mohamed Gad-el-Hak*

- MEMS: Introduction and Fundamentals
- MEMS: Applications
- MEMS: Design and Fabrication

Multiphase Flow Handbook, *Edited by Clayton T. Crowe*

Nanotechnology: Understanding Small Systems, Third Edition, *Ben Rogers, Jesse Adams, Sumita Pennathur*

Nuclear Engineering Handbook, *Edited by Kenneth D. Kok*

Optomechatronics: Fusion of Optical and Mechatronic Engineering, *Hyungsuck Cho*

Practical Inverse Analysis in Engineering, *David M. Trujillo and Henry R. Busby*

Pressure Vessels: Design and Practice, *Somnath Chattopadhyay*

Principles of Solid Mechanics, *Rowland Richards, Jr.*

Principles of Sustainable Energy Systems, Second Edition, *Edited by Frank Kreith with Susan Krumdieck, Co-Editor*

Thermodynamics for Engineers, *Kau-Fui Vincent Wong*

Vibration and Shock Handbook, *Edited by Clarence W. de Silva*

Vibration Damping, Control, and Design, *Edited by Clarence W. de Silva*

Viscoelastic Solids, *Roderic S. Lakes*

Weatherization and Energy Efficiency Improvement for Existing Homes: An Engineering Approach, *Moncef Krarti*

Taylor & Francis
Taylor & Francis Group
http://taylorandfrancis.com

MULTIPHASE FLOW HANDBOOK

SECOND EDITION

EDITED BY

Efstathios E. Michaelides
Clayton T. Crowe
John D. Schwarzkopf

CRC Press
Taylor & Francis Group
Boca Raton London New York

CRC Press is an imprint of the
Taylor & Francis Group, an **informa** business

CRC Press
Taylor & Francis Group
6000 Broken Sound Parkway NW, Suite 300
Boca Raton, FL 33487-2742

© 2017 by Taylor & Francis Group, LLC
CRC Press is an imprint of Taylor & Francis Group, an Informa business

No claim to original U.S. Government works

Printed on acid-free paper
Version Date: 20160404

International Standard Book Number-13: 978-1-4987-0100-6 (Hardback)

This book contains information obtained from authentic and highly regarded sources. Reasonable efforts have been made to publish reliable data and information, but the author and publisher cannot assume responsibility for the validity of all materials or the consequences of their use. The authors and publishers have attempted to trace the copyright holders of all material reproduced in this publication and apologize to copyright holders if permission to publish in this form has not been obtained. If any copyright material has not been acknowledged please write and let us know so we may rectify in any future reprint.

Except as permitted under U.S. Copyright Law, no part of this book may be reprinted, reproduced, transmitted, or utilized in any form by any electronic, mechanical, or other means, now known or hereafter invented, including photocopying, microfilming, and recording, or in any information storage or retrieval system, without written permission from the publishers.

For permission to photocopy or use material electronically from this work, please access www.copyright.com (http://www.copyright.com/) or contact the Copyright Clearance Center, Inc. (CCC), 222 Rosewood Drive, Danvers, MA 01923, 978-750-8400. CCC is a not-for-profit organization that provides licenses and registration for a variety of users. For organizations that have been granted a photocopy license by the CCC, a separate system of payment has been arranged.

Trademark Notice: Product or corporate names may be trademarks or registered trademarks, and are used only for identification and explanation without intent to infringe.

Library of Congress Cataloging-in-Publication Data

Names: Michaelides, Efstathios, editor. | Crowe, C. T. (Clayton T.), editor. | Schwarzkopf, John D., editor.
Title: Multiphase flow handbook / editors, Efstathios E. Michaelides, Clayton T. Crowe, and John D. Schwarzkopf.
Description: Second edition. | Boca Raton : Taylor & Francis, CRC Press, 2015. | Series: Mechanical and aerospace engineering | Includes
bibliographical references and index.
Identifiers: LCCN 2015048725 | ISBN 9781498701006 (alk. paper)
Subjects: LCSH: Multiphase flow--Handbooks, manuals, etc.
Classification: LCC TA357.5.M84 M85 2015 | DDC 620.1/064--dc23
LC record available at http://lccn.loc.gov/2015048725

Visit the Taylor & Francis Web site at
http://www.taylorandfrancis.com

and the CRC Press Web site at
http://www.crcpress.com

To all the assiduous researchers and students of Multiphase Flow, who contributed to the rapid and significant scientific progress of this field in the last fifty years.

Taylor & Francis
Taylor & Francis Group
http://taylorandfrancis.com

Contents

Taylor & Francis
Taylor & Francis Group
http://taylorandfrancis.com

Preface

Multiphase flow is the flow of heterogeneous mixtures of two or more phases, such as gas–liquid, solid–liquid, or gas–solid. Multiphase flow is encountered in numerous industrial and scientific applications, such as boiling and condensation processes, aerosol flows in the environment, gas and petroleum flows, gas–solid and slurry flows in pipelines, particle and fiber flows in airways, fluidized bed reactors, and nanofluids.

The first edition of the *Multiphase Flow Handbook* was published ten years ago with the late professor C.T. Crowe as the editor. The handbook provided a plethora of scientific and practical information to scientists, engineers, researchers, and students and has been useful to many. A great deal of research and development in multiphase flow occurred since the first edition of the handbook, and a lot of additional information is now available, especially in the area of computational modeling. The purpose of this second edition is to provide the reader with the fundamental principles of multiphase flow and useful current information for research, engineering design, and the classroom.

The structure of the second edition is different from that of the first: Several new chapters have been added, primarily on the applications. The material is divided into three sections: (1) fundamentals, (2) descriptions of specific types of multiphase flow and processes, and (3) significant applications. Chapters 1 and 2 pertain to fundamental concepts and numerical methods that are used in all types and applications of multiphase flow. Chapters 3 through 13 describe general types of multiphase flow, such as gas–solid, compressible multiphase flow, flow in porous media, bubble formation and cavitation, etc. Chapters 14 and 15 cover the processes of aggregation and industrial separation of particles, bubbles, and drops. Chapters 16 through 21 examine significant applications of multiphase flow from fluidized bed reactors to nanofluids to multiphase flow with non-Newtonian fluids.

I am grateful to the many distinguished contributors who lent their expertise and spent significant time and effort writing the chapters of this handbook within the time constraints of a publication. Jonathan Plant of Taylor & Francis Group/CRC Press was always there to provide managerial support and advice. Jessica Vakilli put together three of the sections from edited material supplied by the contributors. She and Kyra Lindholm completed all the administrative work such a big undertaking requires. Dr. John Schwarzkopf assisted in the early stages of the project. I am also indebted to Mr. Aranganathan Arunkumar of the production team of this publication, who spent many hours putting together the chapters and sections of this handbook. Last, but not least, I am thankful to my family, Laura, Emmanuel, Dimitri, and Eleni, for their continuous support and encouragement for such ambitious projects.

Efstathios E. Michaelides
Fort Worth, Texas

Taylor & Francis
Taylor & Francis Group
http://taylorandfrancis.com

Editors

Efstathios E. Michaelides holds the Tex Moncrief Chair of Engineering at Texas Christian University (TCU), Fort Worth, Texas. Prior to this, he was chair in the Department of Mechanical Engineering at the University of Texas in San Antonio, where he also held the Robert F. McDermott Chair in engineering and was the founder and director of the NSF-supported Center on Simulation, Visualization and Real Time Computing (SiViRT). He was also the founding chair of the Department of Mechanical and Energy Engineering at the University of North Texas (2006–2007); the Leo S. Weil professor of mechanical engineering at Tulane University (1998–2007); director of the South-Central Center of the National Institute for Global Environmental Change (2002–2007); associate dean for graduate studies and research in the School of Engineering at Tulane University (1992–2003); head of the Mechanical Engineering Department at Tulane University (1990–1992). Between 1980 and 1989, he was on the faculty of the University of Delaware, where he also served as the acting chair of the Mechanical Engineering Department (1985–1987).

Professor Michaelides was awarded an honorary MA from Oxford University (1983); the Casberg and Schillizzi scholarships at St. Johns College, Oxford; the student chapter ASME/Phi, Beta, Tau excellence in teaching award (1991 and 2001); the Lee H. Johnson award for teaching excellence (1995); a senior Fulbright fellowship (1997); the ASME Freeman Scholar award (2002); the Outstanding Researcher award at Tulane (2003); and the ASME Fluids Engineering award (2014).

Professor Michaelides was a member of the executive committee of the Fluids Engineering Division of the ASME (2002–2008) and served as the chair of the Division in 2005–2006. Prior to this, he served as the chair (1996–1998) of the Multiphase Flow Technical Committee. He also served as the president of the ASEE Gulf-South Region (1992–1993 and 2015–2016); he chaired the *Fourth International Conference on Multiphase Flows* (New Orleans, Louisiana, May 27 to June 1, 2001) and was the vice-chair of the *Fifth International Conference on Multiphase Flows* (Yokohama, Japan, May 2004). He has published more than 140 journal papers and has contributed more than 250 papers in national and international conferences. He has also published four books: *Particles, Bubbles and Drops—Their Motion and Heat Transfer* (World Scientific, 2006); *Alternative Energy Sources* (Springer, 2012); *Heat and Mass Transfer in Particulate Suspensions* (Springer, 2013); and *Nanofluidics—Thermodynamic and Transport Properties* (Springer, 2014). Professor Michaelides earned a bachelor's degree (honors) from Oxford University and master's and doctorate degrees from Brown University.

Clayton T. Crowe was a professor of mechanical and materials engineering at Washington State University in Pullman, Pullman, Washington. He is recognized as a leading scholar and author in fluid mechanics, and, in particular, the area of multiphase flows. Among his achievements was the development of the particle-source-in-cell (PSI-Cell) method for the numerical simulation of multiphase flow that has been used extensively in industry and in commercial simulation software. He was the author of numerous technical articles and of *Engineering Fluid Mechanics*, a widely used college textbook now in its eleventh edition. His other publications include *Multiphase Flows with Droplets and Particles, Second Edition* (CRC Press, 2012), and *Multiphase Flow Handbook, First Edition* (CRC Press, 2005). He received many honors for his work, including ASME fellow, the ASME Fluids Engineering Award, and the Senior International Prize for Multiphase Flows. Dr. Crowe passed away in 2012.

John D. Schwarzkopf is a staff scientist within the Theoretical Design Division at Los Alamos National Laboratory, Los Alamos, New Mexico. He has more than 10 years of experience in the application of multiphase flows and computational code development. His work contributed to two patents and several technical articles on the topic of multiphase and multicomponent flow applied to electronics cooling, atomization, and turbulence modeling. He is a coauthor of the book *Multiphase Flows with Droplets and Particles, Second Edition* (CRC Press, 2012).

Contributors

Omid Abouali
Shiraz University
Shiraz, Iran

Goodarz Ahmadi
Clarkson University
Potsdam, New York

Cyrus K. Aidun
G.W. Woodruff School of Mechanical Engineering
Parker H. Petit Institute for Bioengineering and Bioscience
Renewable Bioproducts Institute
Georgia Institute of Technology
Atlanta, Georgia

S. Balachandar
Department of Mechanical and Aerospace Engineering
University of Florida
Gainesville, Florida

Swanand M. Bhagwat
School of Mechanical and Aerospace Engineering
Oklahoma State University
Stillwater, Oklahoma

William T. Buttler
Physics Division
Los Alamos National Laboratory
Los Alamos, New Mexico

Steven L. Ceccio
University of Michigan
Ann Arbor, Michigan

Tailian Chen
Department of Mechanical Engineering
Gonzaga University
Spokane, Washington

Yi Cheng
Department of Chemical Engineering
Tsinghua University
Haidian, Beijing, People's Republic of China

Raj P. Chhabra
Department of Chemical Engineering
Indian Institute of Technology at Kanpur
Kanpur, India

Jacob N. Chung
Department of Mechanical and Aerospace Engineering
University of Florida
Gainesville, Florida

Shrikant Dhodapkar
The Dow Chemical Company
Freeport, Texas

Jean-François Dietiker
West Virginia University Research Corporation
Morgantown, West Virginia

Yulong Ding
School of Chemical Engineering
University of Birmingham
Birmingham, England

Yannis Drossinos
Joint Research Centre
European Commission
Ispra, Italy

John K. Eaton
Department of Mechanical Engineering
Stanford University
Palo Alto, California

John R. Fanchi
Department of Engineering
Texas Christian University
Fort Worth, Texas

Pascal Fede
Université de Toulouse
Toulouse, France

Zhi-Gang Feng
Department of Mechanical Engineering
University of Texas at San Antonio
San Antonio, Texas

Udo Fritsching
Department of Particles and Process Engineering
University of Bremen
Bremen, Germany

Kunihiro Fukui
Department of Chemical Engineering
Hiroshima University
Higashi-Hiroshima, Japan

Kamiel S. Gabriel
University of Ontario Institute of Technology
Oshawa, Ontario, Canada

Afshin J. Ghajar
School of Mechanical and Aerospace Engineering
Oklahoma State University
Stillwater, Oklahoma

John R. Grace
University of British Columbia
Vancouver, British Columbia, Canada

Yoshimichi Hagiwara
Department of Mechanical and System Engineering
Kyoto Institute of Technology
Kyoto, Japan

Christos Housiadas
Institute of Nuclear & Radiological Sciences & Technology, Energy & Safety
"Demokritos" National Centre for Scientific Research
Athens, Greece

Shenggen Hu
Commonwealth Scientific and Industrial Research Organisation
Pullenvale, Queensland, Australia

Satoshi Ii
Department of Mechanical Science and Bioengineering
Osaka University
Osaka, Japan

Farhad A. Jaberi
Department of Mechanical Engineering
Michigan State University
East Lansing, Michigan

Karl Jacob
Solids Processing Laboratory
The Dow Chemical Company
Midland, Michigan

Chikao Kanaoka
Department of Civil Engineering
Kanazawa University
Kanazawa, Japan

Satish G. Kandlikar
Department of Mechanical Engineering
Rochester Institute of Technology
Rochester, New York

Santiago Lain
Department of Mechanical Engineering
Universidad Autónoma de Occidente
Cali, Colombia

Bo Leckner
Department of Energy and Environment
Chalmers University of Technology
Göteborg, Sweden

Keng-Lin Lee
Department of Mechanical Engineering
National Taiwan University
Taipei, Taiwan, Republic of China

Xing-gang Li
Process and Chemical Engineering Division
IWT Foundation Institute of Materials Science
Bremen, Germany

Ellen K. Longmire
Department of Aerospace Engineering and Mechanics
University of Minnesota
Minneapolis, Minnesota

Eric Loth
University of Virginia
Charlottesville, Virginia

Fredrik Lundell
KTH Royal Institute of Technology
Stockholm, Sweden

Hisao Makino
Energy Engineering Research Laboratory
Central Research Institute of Electric Power Industry
Yokosuka, Japan

Farzad Mashayek
Department of Mechanical and Industrial Engineering
University of Illinois at Chicago
Chicago, Illinois

Yoichiro Matsumoto
Department of Mechanical Engineering
The University of Tokyo
Tokyo, Japan

and

RIKEN
Wako, Japan

Efstathios E. Michaelides
Department of Engineering
Texas Christian University
Fort Worth, Texas

Jordan Musser
National Energy Technology Laboratory
U.S. Department of Energy
Morgantown, West Virginia

Naoki Noda
Energy Engineering Research Laboratory
Central Research Institute of Electric Power Industry
Yokosuka, Japan

Dennis E. Oztekin
Georgia Institute of Technology
Atlanta, Georgia

Michael W. Reeks
Newcastle University
Newcastle, England

Ilia V. Roisman
Institute of Fluid Mechanics and Aerodynamics
Technische Universität Darmstadt
Darmstadt, Germany

Tomas Rosén
KTH Royal Institute of Technology
Stockholm, Sweden

John D. Schwarzkopf
Theoretical Design Division
Los Alamos National Laboratory
Los Alamos, New Mexico

John P. Seidle
MHA Petroleum Consultants
Denver, Colorado

Olivier Simonin
Institut National Polytechnique de Toulouse
Toulouse, France

Martin Sommerfeld
Center for Engineering Science
Martin-Luther University Halle-Wittenberg
Halle (Saale), Germany

Kazuyasu Sugiyama
Department of Mechanical Science and Bioengineering
Osaka University
Osaka, Japan

Madhava Syamlal
National Energy Technology Laboratory
U.S. Department of Energy
Morgantown, West Virginia

Shu Takagi
Department of Mechanical Engineering
The University of Tokyo
Tokyo, Japan

Cameron Tropea
Institute of Fluid Mechanics and Aerodynamics
Technische Universität Darmstadt
Darmstadt, Germany

Gretar Tryggvason
Department of Aerospace and Mechanical Engineering
University of Notre Dame
Notre Dame, Indiana

Yutaka Tsuji
Osaka University
Osaka, Japan

Fu-Ling Yang
Department of Mechanical Engineering
National Taiwan University
Taipei, Taiwan, Republic of China

Hideto Yoshida
Department of Chemical Engineering
Hiroshima University
Higashi-Hiroshima, Japan

Jesse Zhu
Particle Technology Research Centre
University of Western Ontario
London, Ontario, Canada

Yuanzheng Zhu
Georgia Institute of Technology
Atlanta, Georgia

Taylor & Francis
Taylor & Francis Group
http://taylorandfrancis.com

Nomenclature

Latin Symbols

a	Acceleration
A	Area
A_{eff}	Hamaker constant
B	Blowing factor
Bo	Bond number
Boi	Boiling number
c	Specific heat capacity
c_A, c_B,…	Mass concentration of species A, B,…
c_l	Speed of sound in liquid
C	Coefficient (dimensionless)
Ca	Capillary number
Co	Convection number
C_A	Added mass coefficient
C_D	Drag coefficient
C_H	History term coefficient
d	Diameter of small-scale features (particles, droplets, bubbles, etc.)
d_{32}	Sauter mean diameter (SMD)
D	Diameter of large-scale features (pipes, bends, etc.)
$\mathfrak{D}_{(\ )}$	Diffusion coefficient
e	Internal energy
E	Young's modulus
$E(\kappa)$	Energy intensity (for spectra)
Eo	Eötvös number
Eu	Euler number
f	Friction factor
$\mathfrak{F}$	Frequency
$F(D)$	Cumulative distribution
F_i	Force vector
Fo	Fourier number
Fr	Froude number
g	Gravitational acceleration
g_I	(i = 1, 2, 3,…) Gibbs free energy (molar)
G	Mass flux
Gr	Grashoff number
h	Enthalpy
h_c	Convective heat transfer coefficient
h_{fg}	Latent heat of evaporation
h_m	Convective mass transfer coefficient

H	Head
He	Hedstrom number
I	Intensity
Ja	Jakob number
J_A, J_B,…	Mole fluxes of species A, B,…
k	Thermal conductivity
k_B	Boltzmann constant
k_s	Pipe roughness
k_w	Wave number
K	Turbulent kinetic energy
K_{nu}	Knudsen number
Ki	Kirpichev number
Ku	Kutateladze number
l	Length scale
L	Characteristic length
m	Mass
M	Mass flux
$\mathfrak{M}$	Molecular weight
M_a	Mach number
n	Power-law factor, number or number density
n_A, n_B,…	Mole concentration of species A, B,…
n_i	Unit normal vector
N	Total number
N_{av}	Avogadro number
Nu	Nusselt number
Oh	Ohnesorge number
P	Pressure
p	Perimeter
P_{ij}	Collision frequency
Pe	Peclet number
q_e	Electric charge
$\dot{Q}$	Heat rate
q''	Heat flux
r, θ, φ	Spherical coordinates
r, θ, z	Cylindrical coordinates
$\mathfrak{R}_u$	Universal gas constant
Ra	Rayleigh number
Re	Reynolds number
R_{ij}	Turbulence Reynolds stress tensor
$R(\tau)$	Velocity correlation function
S	Surface
S_w	Swirl parameter
Sh	Sherwood number
Sha	Shannon number
St	Stokes number
St_h	Strouhal number
S_{ij}	Stress tensor
S_{mass}	Mass source term
S_{mom}	Momentum source term
t	Time
T	Temperature
$T(\kappa)$	Spectral energy transfer rate
U, u	Continuous phase velocity
u_i, v_i, w_i	Velocity vectors
v	Dispersed phase velocity

v_T	Terminal velocity
V	Volume
$\dot{V}$	Volumetric flow rate
We	Weber number
x, y, z	Cartesian coordinates
X	Lockhart–Martinelli parameter
Y	Mass fraction
Y_{mol}	Mole fraction
Z	Loading
z	Length scale

Greek Symbols

a	Particle radius
α_f	Thermal diffusivity of fluid
α_s	Absorptivity
β	Slip parameter
β_P	Expansion coefficient at constant pressure
β_T	Expansion coefficient at constant temperature
γ	Specific gravity
Γ	Torque
δ	Distance or spacing
δ_{ij}	Kronecker delta
ε	Turbulence energy dissipation rate
ε_0	Electric permeability of vacuum
ε_p	Porosity
ϵ	Emissivity
ζ	Dimensionless parameter
η	Kolmogorov length scale, amplitude
θ	Angle
Θ	Granular temperature, dimensionless temperature, wall scattering function
κ	Wave number, ratio of specific heats
κ_p	Permeability
κ_T	Expansion coefficient
λ_m	Molecular mean free path
λ	Factor of ratio
μ	Chemical potential, dynamic viscosity
ν	Kinematic viscosity
ρ	Density
Π	Coupling parameter
σ	Surface tension, standard deviation, Stefan–Boltzmann constant
$\sigma_n, \sigma_1, \sigma_2, \sigma_3$	Normal or principal stresses
τ	Response time, time scale
τ_s	Shear stress
φ	Velocity ratio
ϕ	Porosity
Φ	Two-phase flow multiplier, potential
ϕ_c	Volume fraction of continuous phase, void fraction
ϕ_d	Volume fraction of dispersed phase
χ	Gas mass quality
ψ	Stream function
ψ_s	Surface potential
Ψ	Shape factor
ω	Frequency
ω_i	Chemical source for species “i”
ω_n	Natural frequency
Ω	Angular velocity

Subscripts

,	Derivative
an	Annular
avg	Average
agg	Agglomeration
b	Bubble
B	Bulk
c	Continuous phase
ch	Characteristic
cr	Critical
co	Core
coag	Coagulation
coll	Collision
conv	Convective
d	Dispersed or dense phase
D	Drag
e	Eddy or equilibrium
eff	Effective
eq	Equivalent
f, *F*	Fluid
fg	Latent heat/enthalpy
fr	Friction
gas, *G*	Gas
gs	Superficial gas
GM	Geometric mean
h	Homogeneous
HM	Harmonic mean
i	Indices (1, 2, 3)
in	In or inlet
int	Interface
in	In or inlet
iso	Isolated
j	Indices (1, 2, 3)
k	Indices (1, 2, 3) or particle number
l	Lift
liq, *L*	Liquid
lo	Liquid only
ls	Superficial liquid
m	Mixture or pertains to mass
max	Maximum
min	Minimum
mom	Momentum
mol	Molecular
M	Mean
MD	Median
n	Number
nw	Nonwetting
nuc	Nucleation
NB	Nucleate boiling
o	Oil
opt	Optimum
out	Out or outlet
ONB	Onset of nucleate boiling
p	Particle
PB	Partial boiling region

r	Relative or reduced
rad	Radiation
rot	Rotational
s	Solid
sat	Saturation
sen	Sensor
sl	Slip
sol	Solution
ss	Steady state
str	Stratified
sub	Subcooled
sur	Surface
SM	Surface mean
th	Thermal
tot	Total
tp	Two-phase
tr	Transition
vap	Vapor phase
VM	Volumetric mean
W	Wall
w	Wetting phase or water
∞	Ambient, far away, free stream, undisturbed
0	Initial or incident

Superscripts

*	Dimensionless
0	Undisturbed field, incident or pure component at infinite dilution
′	Temporal fluctuation or spatial deviation
″	Favre fluctuation
·	Rate
g	Gas
I	Image variable
inc	Incident vector
m	Mixture
s	Sensor
S	Solid
sca	Scattered vector

Abbreviations

BL	Boundary layer
CFD	Computational fluid dynamics
CHF	Critical heat flux
DNS	Direct numerical simulations
MD	Molecular dynamics

Taylor & Francis
Taylor & Francis Group
http://taylorandfrancis.com

1

Fundamentals of Multiphase Flow

Efstathios E. Michaelides and Zhi-Gang Feng

1.1 General Features of Multiphase Flows

Solid, liquid, and vapor are the three natural phases of materials. Gases and ideal gases are parts of the vapor phase where specific constitutive equations, for example, the ideal gas equation, apply. A multiphase system contains materials of two or more phases. Multiphase flow is the flow of a mixture of phases such as gases (bubbles) in a liquid or liquid (droplets) in gases. Liquids of different densities and solids of different crystalline systems are often considered as separate phases. Thus, the flow of oil droplets in water is considered multiphase flow.

1.1.1 Dispersed Phase and Separated Flows

In dispersed phase flows, one phase consists of discrete, noncontinuous elements and the second phase consists of a continuous fluid matrix. Examples of dispersed multiphase flows are the flow of bubbles in a liquid and the flow of particles or droplets in a gaseous matrix. In a separated flow, the two phases are separated by a single surface of contact. For example, the annular flow in a pipe, which includes a liquid layer on the pipe wall and a vapor core, is a separated flow.

1.1.2 Gas–Liquid Flows

The motion of bubbles in liquids and the motion of droplets in gas streams are examples of gas–liquid flows. Bubble columns are commonly used in several process industries including chemical reactions and fluid purification processes. The atomization of a liquid to generate small droplets for combustion is important in power generation and automotive systems. Droplet formation and impaction are important in spray forming for materials processing. Steam–water flows in pipes and heat exchangers are very common in power systems with vapor cycles, such as fossil fuel plants and nuclear reactors. Gas–liquid flows in pipes can assume several geometric configurations ranging from bubbly flow to churn and annular flow.

1.1.3 Gas–Particle Flows

The particles in this case are either solid particles or liquid droplets. This type of multiphase flow includes the pneumatic transport of solids, fluidized beds for solids combustion, and the burning of fuel droplets.

The operation of pollution control devices, such as cyclone separators and electrostatic precipitators, is based on the principles of gas–solid flows. The combustion process of coal in fossil fuel power systems depends on the dispersion and burning of coal particles. The micron-size particles in a solid propellant rocket exhaust affect the performance of the rocket. Another type of a gas–solid flow is the motion of particles down a chute or an inclined plane. These are known as granular flows where particle–particle and particle–wall interactions determine the transport of the solid phase. In the extreme case, where the particulate phase is motionless, the flow becomes flow through a porous medium as, for example, in a pebble-bed heat exchanger or a stationary bed reactor.

1.1.4 Liquid–Solid Flows

Liquid–solid flows are flows where solid particles are carried by the liquid. Oftentimes, such flows are referred to as slurry flows. Slurries cover a wide spectrum of applications ranging from the transport of minerals (including coal) to the flow of toothpaste. Several environmental flows and processes, such as the removal of sediment from water and waterways, involve slurry transport. Typically, the solid particles are discrete and for this reason, slurry flows are classified as dispersed flows. When the solids are stationary, the flow of liquid through the solid is another example of flow in a porous medium.

1.1.5 Three-Phase Flows

Three-phase flows are also encountered in a few engineering systems. For example, gaseous bubbles rising in slurry are three phases flowing together. Three-phase flows are met in specialized systems and have a high degree of complexity. For this reason, not much research work has been reported in the literature on these flows.

1.1.6 Scope of This Handbook

Before the 1980s, the design of multiphase systems was based primarily on empirical observations and correlations of experimental data. Since the early 1980s, the design of more advanced instruments and the application of more scientific measurement techniques have led to the measurement and quantification of fundamental parameters that improved our understanding of multiphase systems and processes. In parallel, the tremendous improvement of computational capacity and numerical techniques has enabled the development of numerical models that are now reliably used to complement engineering design. The improvements of the experimental instruments and the numerical models for multiphase flows are rapidly growing areas of technology, which have far-reaching benefits in upgrading the operation and efficiency of current engineering systems and processes and in supporting the development of new and innovative technologies.

This handbook is designed to provide a background for engineers and scientists and to serve as a source of information on current technology. This chapter introduces fundamental definitions of dispersed multiphase flows, including size distributions and fundamental interactions of particles, bubbles, and drops with fluids. This chapter also addresses the current state of the art and examines commonly used instruments and processes for measuring multiphase flows. Chapter 2 deals with the numerical modeling of multiphase flows. It includes numerical modeling methods such as direct simulation, Lagrangian modeling, two-fluid modeling, and PDF modeling, as well as specific numerical techniques, such as the discrete element, the immersed boundary, and the lattice Boltzmann techniques. Chapters 3 and 4 cover the fundamentals of multiphase flow in ducts and apply to engineering systems for the transport of gas–liquid mixtures, pneumatic transport, and slurry transport. Chapter 5 addresses a more recently researched area, the area of compressible multiphase flow, and includes the interactions of particles, bubbles, and drops in compressible fluids. Chapter 6 addresses the subject of chemical reactions and combustion with drops and particles. The subject of Chapter 7 is multiphase flow and heat transfer under microgravity and zero-gravity conditions. Chapters 8 and 9 address the boiling and condensation processes in multiphase systems and include the local and global heat transfer processes in industrial boiling and condensation equipment. Chapter 10 addresses powder and granular flows, where the forces between the solid particles or between the solid particles and the boundaries are by far greater than the hydrodynamic forces between the particles and the interstitial fluid. The subject of multiphase flow in porous media, such as the flow of oil and gas in rock formations and cracks, is surveyed in Chapter 11. The complex interactions between the dispersed phase (bubbles, particles, and drops) and

the turbulence of the continuous fluid phase are the subject of Chapter 12. Chapter 13 addresses the dynamics of deformable bubbles and the process of bubble cavitation, which is of paramount importance in the shipping industry. Chapter 14 addresses the fundamentals of the collision process, which may result in the aggregation of particles and the formation or breakup of clusters. Chapter 15 addresses the separation processes and equipment, including the removal of dust and droplets from gaseous streams. Chapter 16 covers the flow of particles in biological systems, such as the blood stream and the respiratory tract. Chapter 17 is devoted to the industrial systems known as fluidized bed reactors that are increasingly used for chemical and combustion processes. Chapter 18 is devoted to the new application of multiphase fluids, which are known as nanofluids. Nanofluids exhibit very high heat and mass transfer characteristics. The formation and dynamics of spray systems is addressed in Chapter 19. The flow and processes of aerosols, with particular emphasis on aerosol deposition, are covered in Chapter 20. Finally, Chapter 21 addresses the fundamentals of flow and heat transfer characteristics of a dispersed phase in a non-Newtonian fluid.

1.2 Fundamental Definitions

This section introduces parameters that are fundamental to multiphase flows. For brevity and convenience, the terms *discrete phase* and *dispersed phase* will be used for the particles, drops, or bubbles, while the terms *carrier fluid* and *continuous phase* will be used for the fluid that carries the dispersed phase.

1.2.1 Volume Fraction and Densities

The continuum hypothesis enables one to define material properties at any point (x, y, z) despite the fact that matter is discontinuous at the molecular level. According to the continuum hypothesis, all properties, variables, and derivatives of the variables are defined within a limit volume, V_{lim}, that is big enough and contains a sufficient number of molecules so that all the variables and their derivatives have stationary values. An extension of the continuum hypothesis may be used with dispersed multiphase systems to define their properties (Michaelides, 2014). The extension defines the property of an inhomogeneous mixture at a point (x, y, z) by considering a volume, V, around the point (x, y, z). This volume must be greater than a limit volume, V_0, which is defined so that the calculated or measured values of the properties of the dispersed phase are stationary and independent of the motion of the dispersed phase elements (Michaelides, 2014).

Under this extension of the continuum hypothesis, the volume fraction of the dispersed phase is defined as

$$\alpha_d(x,y,z) = \frac{V_d}{V} \quad \text{with } V > V_0, \tag{1.1}$$

where V_d is the volume of the dispersed phase within the volume V. The volume V_0 is the limit volume that ensures a stationary average of the volume fraction despite the motion of the elements of the dispersed phase (particles, bubbles, or drops).

Similarly, the volume fraction of the continuous phase is

$$\alpha_c(x,y,z) = \frac{V_c}{V} \quad \text{with } V > V_0, \tag{1.2}$$

where V_c is the volume of the continuous phase in the volume under consideration.

In gas–liquid flows, the volume fraction is sometimes referred to as the "void fraction." From the volume conservation principle, the total volume is occupied either by the dispersed or by the continuous phase. This implies that, at any point of the continuum, the sum of the two volume fractions equals 1:

$$\alpha_c(x,y,z) + \alpha_d(x,y,z) \equiv 1. \tag{1.3}$$

The *density* or *apparent density* of the dispersed phase is equal to the mass of the dispersed phase per unit volume of the mixture. Similarly, the apparent density of the continuous phase is equal to the mass of the

continuous phase per unit volume of the mixture. If the dispersed material is composed of a single chemical substance with material density ρ_d and the material density of the continuous phase is ρ_c, the apparent densities of the two phases are

$$\bar{\rho}_d = \rho_d \alpha_d \quad \text{and} \quad \bar{\rho}_c = \rho_c \alpha_c. \tag{1.4}$$

Finally, the *mixture density*, which is defined as the total mass of the mixture divided by the total volume, is equal to the sum of the two apparent densities:

$$\rho_m = \bar{\rho}_c + \bar{\rho}_d. \tag{1.5}$$

1.2.2 Phase Velocities and Superficial Velocities

The *phase velocity* of a phase—u_c and u_d for the continuous and dispersed phases, respectively—is the actual velocity of each phase of a multiphase flow mixture and may be defined and measured at any point of the mixture. The *superficial velocity* of a phase is oftentimes used for calculations in channel flows and is defined as the mass flow rate of the phase divided by the total channel area and the material density of the phase:

$$U_d = \frac{\dot{m}_d}{A\rho_d} \quad \text{and} \quad U_c = \frac{\dot{m}_c}{A\rho_c} \tag{1.6}$$

It is apparent that the superficial velocity is the velocity of the phase if that phase were flowing alone and occupied the entire channel area. The phase velocities and the superficial velocities are related through the following volume fractions:

$$u_d = \frac{U_d}{\alpha_d} \quad \text{and} \quad u_c = \frac{U_c}{\alpha_c} \tag{1.7}$$

1.2.3 Quality, Concentration, and Loading

The quality, which is primarily used in vapor–liquid flows, is the ratio of the mass of the gas to the mass of the mixture. If the gas is the dispersed phase, the quality is defined as follows:

$$x = \frac{m_d}{m_c + m_d} = \frac{\bar{\rho}_d}{\bar{\rho}_m}. \tag{1.8}$$

The *mass concentration* or simply *concentration* of the dispersed phase is used in fluid–solid mixtures. This is a local variable defined at every point and is equal to the ratio of the apparent densities:

$$C = \frac{\bar{\rho}_d}{\bar{\rho}_c}. \tag{1.9}$$

The volume fraction, α_d, is used by some authors as an alternative definition of the concentration. A third variable, the loading, is often used in fluid–solid flows. The loading is the ratio of the two mass flow rates and is defined as follows:

$$Z = \frac{\dot{m}_d}{\dot{m}_c}. \tag{1.10}$$

1.2.4 Response Times

The response times of particles, bubbles, and drops are pertinent to their interactions with fluids and the interfacial transfer of momentum, energy, and mass. Oftentimes, the response times are called characteristic times. The momentum response time, τ_v, is of the order of magnitude of the time required for a sphere

to respond to a change in velocity. A measure of the momentum response time for a sphere may be derived from the equation of motion of a sphere in a fluid, which, in the absence of the transient terms, may be written as

$$\frac{\pi d^3}{6}\rho_d\frac{dv}{dt}=\frac{1}{2}C_D\frac{\pi d^2}{4}\rho_c(u-v)|u-v|, \tag{1.11}$$

where v is the particle velocity in the direction of the carrier fluid velocity u. The drag coefficient C_D is a function of the Reynolds number of the sphere, which is defined in terms of the relative velocity

$$Re_r=\frac{\rho_c d|u-v|}{\mu_c}, \tag{1.12}$$

where μ_c is the viscosity of the continuous phase. Rearranging the terms of Equation 1.11, one obtains

$$\frac{dv}{dt}=\left(\frac{C_D Re_s}{24}\right)\left(\frac{18\mu_c}{\rho_d d^2}\right)(u-v). \tag{1.13}$$

At the limit of vanishingly small Re_r, the so-called Stokes flow, the factor in the first parenthesis, $C_D Re_s/24$, is equal to 1. The factor in the second parenthesis has the dimension of (time)$^{-1}$. The inverse of this variable defines the momentum response time

$$\tau_V=\frac{d^2\rho_d}{18\mu_c}. \tag{1.14}$$

With this definition of the response time, the equation of motion is simplified to

$$\frac{dv}{dt}=\frac{1}{\tau_V}(u-v). \tag{1.15}$$

When the (uniform) fluid velocity undergoes a step from 0 to U, the solution to the last equation is

$$v=U\left[1-\exp\left(-\frac{t}{\tau_V}\right)\right]. \tag{1.16}$$

Therefore, the momentum response time is the time required for a particle released from rest to reach 63% or $(1-1/e)$ of the free-stream velocity under Stokes flow conditions.

The thermal response time, τ_T, is defined in a similar way, using a simplified form of the energy equation of a solid sphere at the limit of vanishingly small Peclet numbers:

$$\frac{dT_d}{dt}=\frac{Nu}{2}\left(\frac{12k_c}{\rho_d c_d d^2}\right)(T_c-T_d). \tag{1.17}$$

Since at vanishingly small Peclet numbers $Nu = 2$, the last equation defines the thermal response time

$$\tau_T=\frac{\rho_d c_d d^2}{12k_c}, \tag{1.18}$$

where c_d is the specific heat (at constant pressure) of the dispersed phase. When the fluid temperature undergoes a temperature step, τ_T is the time required for a particle's temperature to reach 63% or $(1-1/e)$ of this temperature step.

A third response time may be defined for the mass transfer process from a sphere. Since the mass transfer process is analogous to the heat transfer, the characteristic time for the mass transfer is

$$\tau_M = \frac{d^2}{12D_c}, \tag{1.19}$$

where D_c is the diffusion coefficient of the dispersed phase species inside the continuous phase. The three response times are related as follows:

$$\frac{\tau_V}{\tau_T} = \frac{2}{3}\frac{c_c}{c_d}\frac{1}{Pr}, \quad \frac{\tau_V}{\tau_M} = \frac{12D_c\rho_d}{18\mu_c} = \frac{2\rho_d}{3\rho_c}Sc, \quad \frac{\tau_T}{\tau_M} = \frac{Pr}{Sc}\frac{\rho_d}{\rho_c}\frac{c_d}{c_c}. \tag{1.20}$$

The Prandtl and Schmidt numbers pertain to the properties of the continuous phase. The order of magnitude considerations of the two dimensionless numbers proves that the mass transfer process is by far the slowest of the three transfer processes (Michaelides, 2014).

1.2.5 Dimensionless Numbers

The carrier fluid also has characteristic times and length scales that depend on the process under consideration and the domain geometry. The ratios of the particle to fluid characteristic times and length scales define several dimensionless numbers. These numbers are classified here according to the pertinent effects (Michaelides, 2013a,b, 2014):

1. *Viscosity effects*: Three Reynolds numbers for the particles are defined with respect to the rectilinear velocity, the rotational velocity, and the local fluid shear. In addition, a separate Reynolds number is defined for the carrier fluid. The first three dimensionless groups are based on the particle diameter. The last is defined with respect to the characteristic length scale of the fluid, L, and pertains to the entire suspension. The four Reynolds numbers are defined as follows:

$$Re_r = \frac{d\rho_c|\vec{u}-\vec{v}|}{\mu_c}, \quad Re_\gamma = \frac{d^2\rho_c\gamma}{\mu_c}, \quad Re_{rot} = \frac{d^2\rho_c|\vec{\Omega}|}{\mu_c}, \quad Re_c = \frac{L\rho_c|\vec{u}|}{\mu_c}. \tag{1.21}$$

2. *Heat and mass transfer effects:* Four Peclet numbers that correspond to the four Reynolds numbers ($Pe = Re * Pr$), the Nusselt number, the Biot number, and the Sherwood number of the particles and the suspension are defined as follows:

$$\begin{aligned} &Pe_r = \frac{d\rho_c c_c|\vec{u}-\vec{v}|}{k_c}, \quad Pe_\gamma = \frac{d^2\gamma\rho_c c_c}{k_c}, \quad Pe_M = \frac{d|\vec{u}-\vec{v}|}{D_c}, \\ &Pe_c = \frac{L\rho_c c_c|\vec{u}|}{k_c}, \quad Nu = \frac{2\alpha h_c}{k_c}, \quad Bi = \frac{dh_c}{k_c}, \quad Sh = \frac{dh_M}{D_c}. \end{aligned} \tag{1.22}$$

3. *Surface tension effects*: These are characterized by the Bond number, the capillary number, the Eötvos number, the Morton number, and the Weber number:

$$\begin{aligned} &Bo = \frac{gd^2|\rho_d-\rho_c|}{\sigma}, \quad Ca = \frac{\mu_c|\vec{u}-\vec{v}|}{\sigma} = \frac{We}{Re_r}, \quad Eo = \frac{d^2g\rho_c}{\sigma}, \\ &Mo = \frac{g\mu_c^4}{\rho_c\sigma^3}, \quad We = \frac{d\rho_c|\vec{u}-\vec{v}|^2}{\sigma} = Re_rCa. \end{aligned} \tag{1.23}$$

4. *Dimensionless property numbers*: The Prandtl number, the Lewis number, and the Schmidt number, which are pertinent to the transport properties of the fluid, are defined as follows:

$$Pr = \frac{c_c \mu_c}{k_c}, \quad Le = \frac{k_c}{\rho_c D_c c_c}, \quad Sc = \frac{\mu_c}{\rho_c D_c}. \tag{1.24}$$

5. *Other effects*: Molecular or rarefaction effects are quantified by the Knudsen number, phase-change effects by the Stefan number, and oscillatory and transient effects by the Strouhal number:

$$Kn = \frac{L_{mol}}{d}, \quad Ste = \frac{c_c \Delta T}{h_{fg}}, \quad Sl = \frac{df}{|\vec{u} - \vec{v}|}. \tag{1.25}$$

Of particular significance in the literature of dispersed multiphase flow is the Stokes number, *St*. The Stokes number characterizes the inertia of the particle and is defined as the ratio of the momentum timescale of the sphere to the characteristic timescale of the carrier fluid:

$$St = \frac{\tau_V}{\tau_c}. \tag{1.26}$$

The characteristic time of the fluid, τ_c, related to a spherical particle is defined as the diameter of the particle divided by the pertinent fluid velocity or by the rms of the velocity fluctuations in the case of turbulence. When $St \ll 1$, the particle has ample time to respond to changes in the flow velocity and follows closely the fluid velocity changes. When $St \gg 1$, the particle has no time to respond to the fluid velocity and does not follow the carrier fluid changes or fluctuations. The Stokes number is frequently used in turbulent flows to determine the response of particles, drops, and bubbles to the turbulent velocity fluctuations.

1.3 Size of Particles, Drops, and Bubbles

While drops and bubbles are largely spherical or ellipsoidal, most particles have irregular shapes that may not be described by one or two easily measurable dimensions. Despite this, it is often advantageous to include in calculations the characteristic length or *size* of the elements of the dispersed phase. The *size* of a spherical particle is equal to its diameter. The *size* of a nonspherical particle is subject to interpretation and must be well defined. Following the practice of spherical particles—for which most of the analytical and experimental work has been performed in the past—fan *equivalent diameter* may be defined for nonspherical particles, drops, and bubbles. The practical usefulness of the equivalent diameter is that one may correlate the transport coefficients of irregularly shaped particles, for example, drag coefficients and heat/mass transfer coefficients, with the known transport coefficients for spheres. Several equivalent diameters have been proposed in the past for nonspherical particles including the diameter of a sphere that would have the same volume, *V*; the diameter of a sphere that would have the same area, *A*; and the diameter of a sphere that would have the same perimeter, *P*, projected in the direction of the motion of the nonspherical particle. These three equivalent diameters are defined as follows:

$$d_V = \sqrt[3]{\frac{6V}{\pi}}, \quad d_A = \sqrt{\frac{4A}{\pi}}, \quad \text{and} \quad d_P = \frac{P}{\pi}. \tag{1.27}$$

For a sphere, the three equivalent diameters are the same and equal to the actual diameter, *d*. A fourth equivalent diameter, which is frequently used with irregular particles and aggregates, is the diameter of the minimum sphere, in which the irregular particle will fit in. Typically, this is the longest dimension of the particle, d_L. While d_P depends on the direction of the particle movement and its magnitude may vary in an arbitrary way, for all the other measures of the *size* of a particle, the inequality $d_V \leq d_A \leq d_L$ holds, with the equal sign applying to spheres only. Figure 1.1 shows schematically the last three diameters or *sizes* for a particle that appears as an elongated parallelepiped. It may be seen in this figure that the three equivalent

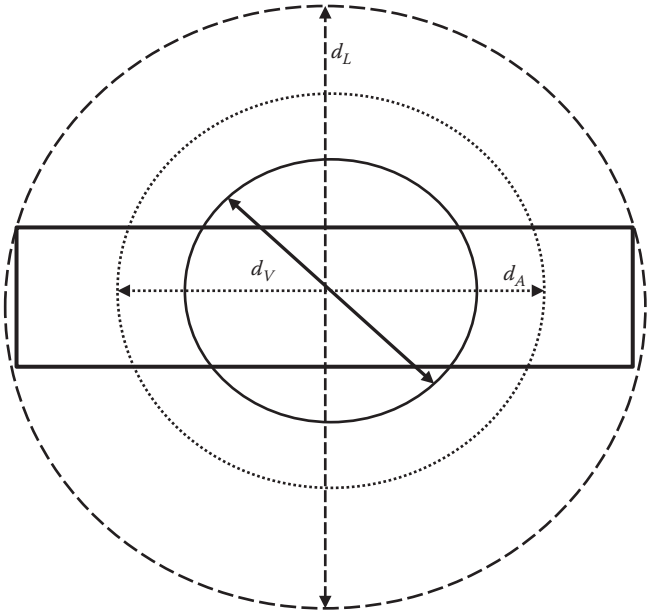

Figure 1.1

A schematic diagram of the three equivalent diameters, d_V, d_A, and d_L, for a particle with the shape of a parallelepiped.

diameters, which are also depicted, vary significantly in magnitude. Because of the significant variability, a precise definition or measurement of the *size* of particles, bubbles, and drops must include how this *size* has been defined or measured (Michaelides, 2014).

Another definition of an equivalent diameter that is extensively used with sediments and sedimentary suspensions of particles is the "sieve diameter." This is obtained from a sieve mesh analysis and is defined as the maximum standard sieve mesh size (or minimum sieve aperture) through which the particles may pass through (Leeder, 1982). Since the standard sieves do not extend to the micrometer and nanometer sizes, this method is not applicable to micro- and nanosize particles.

Regarding shapes, the *Corey shape factor* has been defined as the ratio of the shortest principal axis of the particle to the square root of the product of the longest two principal axes. The Corey factor, although widely used in the past with ellipsoidal particles, is not related to volume or area calculations, which are important in the calculations of the transport coefficients. In addition, it is difficult to apply this factor to irregular particles, where the principal axes are not well defined.

1.3.1 Fractal Dimensions of Particles and Aggregates

Fractal geometry is a recent tool that is often used to analyze the structure of irregular patterns of lines, surfaces, and volumes. The fractal shapes are composed of self-similar parts when viewed or measured by different length scales. For example, if we take photographs of a fractal object at different scales, as the scale changes, we will observe that the shapes in the photographs remain the same. When viewed and measured at the different length scales, the length and area of the fractal shape are different and, actually, increase when the scale of measurement decreases. The classical example of a fractal shape is the coastline of a country (Mandelbrot, 1967): one may measure the length of the coastline using a map, using aerial photographs, using a 1 m ruler on the ground, or using a smaller ruler, whose length is one grain of sand. The length of the coastline increases as the unit of measurement becomes smaller, and more details are revealed and counted. Figure 1.2 illustrates an example of this concept using the so-called Koch curve. The Koch curve is a complex, self-similar curve that evolves from a single straight segment according to the following rule: at each stage of evolution, every straight segment of the curve is substituted by four other straight segments of length 1/3 the length of the old segment. Two of the new segments span the ends of the old segment. The other two segments, which occupy one-third of the old segment's length, form the sides of an equilateral triangle and make up the inner part of the new segment. The process of evolution of the curve may produce an infinite number of stages, three of

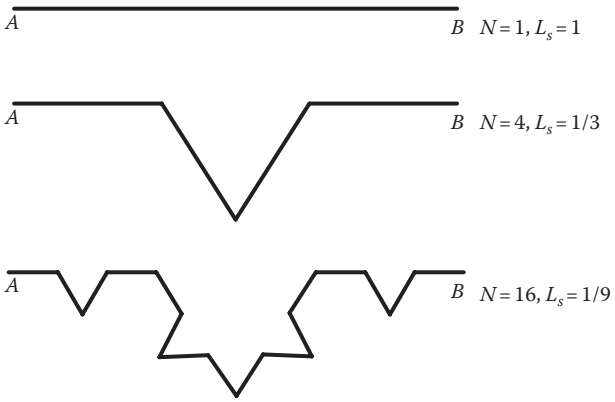

Figure 1.2

The length of a complex, fractal curve increases as the unit of measurement decreases.

which are shown in Figure 1.2. The end points of all the stages, A and B, are at the same distance apart in all the stages of the pattern evolution.

Without loss of generality, we may stipulate that the segment AB is of unit length. The measure of the length in the first stage of the curve is $N = 1$. In the second stage, the length scale is $L_s = 1/3$ and the number of segments $N = 4$. In the third stage, the length scale is $L_s = 1/9$ and the number of segments $N = 16$. In terms of the original units, the total length of the curve is 4/3 units in the second stage, 16/9 in the third stage, and so on. For self-similar objects, such as this curve, there is a fundamental dimension, the *fractal dimension*, L_f, which does not change with the scale of measurement. The fundamental dimension is related to the fundamental equation of self-similar patterns:

$$N = \left(L_s\right)^{-L_f}, \tag{1.28}$$

where N is the number of straight line segments of the scale length, L_s, that spans the entire length of the curve. From the definition of the fractal shapes, N is a strong function of the scale length. The value of L_f for a straight line is 1 and for a sphere 3. All other shapes have fractal dimensions between the two limits.

It must be noted that fractal dimensions describe a shape or a surface in very general terms. They do not define shapes and patterns and they do not contain enough information to construct them. In the case of the Koch curve, which has $L_s = 1.2619$, there are several other complex patterns that have the same fractal dimension but are dramatically different in shape and complexity.

Single particles have irregular but not self-similar shapes. The fractal dimension, L_f, of single particles is meaningless in most cases. Aggregates of primary particles, and especially very large aggregates of spheres, have been observed to have complex shapes, surfaces, and perimeters, which are oftentimes approximated as self-similar surfaces and lengths. In these cases, a fractal dimension of the aggregates, L_f, may be defined using the limit of Equation 1.28 as the length scale, L_s, vanishes (Vicsek, 1999):

$$L_f = -\lim \frac{\ln\left(N\right)}{\ln\left(L_s\right)} \quad \text{as } L_s \to 0. \tag{1.29}$$

For particle aggregates, L_f is typically calculated by taking microscopic images of the aggregates at different scales and using Equation 1.29 with the measuring length scale, L_s, taking several different values. Oftentimes, optical image software performs this task (Lee and Kramer, 2004, Wang and Chau, 2009). A simpler, albeit not as accurate method, is to measure the fractal dimension from light scattering (Bushell et al., 2002).

It must be noted that in the determination process of the fractal dimension of aggregates, the scale L_s cannot attain values that are smaller than the dimension of the largest primary particle of the aggregate. Therefore, the determination of the fractal dimension of particle aggregates is only an approximation to Equation 1.29. Also that for any measurement of L_f to be meaningful, the variation of the measurement length scale, L_s, must span at least two orders of magnitude. This implies that the method may only be used with big aggregates that contain a very large number of primary particles (at least 500).

The fractal dimension of the aggregates is often used to give an estimate of the porosity, ε_p, of the aggregate (Li and Logan, 2001):

$$\varepsilon_p = 1 - \left(\frac{d_a}{d}\right)^{3-L_f}, \tag{1.30}$$

where
d is the diameter of the primary particles
d_a is the *diameter* of the aggregate

The latter is typically assumed to be equal to the longest dimension of the aggregate, that is, $d_a = d_L$.

Several authors have used the fractal dimension to describe the structure and morphology of particles or aggregates of particles. Two conditions must be explicitly satisfied when one uses the fractal dimension in a quantitative manner:

1. The original object must have a self-similar shape to make the fractal dimension, L_f, meaningful.
2. The 2D microscopic images or the light scattering method must be adequate for the determination of the fractal dimension, L_f, of particles that are inherently three dimensional.

Because the second condition is not always satisfied, it has been observed that measurements of L_f by 2D photographic images may be laden with high measurement errors. The measurement error becomes significantly high if the *measured* fractal dimension is close to or greater than 2 (Vicsek, 1999).

1.3.2 Size Distributions

The sizes of particles, drops, and bubbles are important parameters that govern the flow of a dispersed multiphase mixture. In most cases, there is not a single size of these elements of dispersed flows but several sizes, which constitute the size distribution. Because of this, it is important to have a basic knowledge of the statistical parameters of the size distributions. A general characterization of particle size distribution is *monodisperse* and *polydisperse*. In a monodisperse mixture, the particles' sizes are close to a single size and typically, the standard deviation of the sizes is less than 10% of the mean size. In a polydisperse mixture, there is a wide range of particle sizes. Particle, drop, and bubble size distributions can also be classified as discrete or continuous. The continuous size distribution derives from the discrete distribution as the sampling interval approaches zero.

1.3.2.1 Discrete Size Distribution

For the size measurements of particles, one chooses a measuring technique, such as photography or sieve measurements, and also chooses size intervals, Δd, which are not necessarily of equal magnitude. The size intervals are large enough to contain a significant fraction of particles, yet small enough to yield sufficient detail. The representative size of the particles in each interval may be defined as the diameter corresponding to the midpoint of the interval. For the size measurements, the number of particles in each interval is counted, recorded, and divided by the total number of particles in the sample. The results are plotted in the form of a histogram (bar chart) as shown in Figure 1.3. Such histograms are identified as the *discrete number frequency distribution* for the particle size. For large samples of particles, the distribution is also referred to as the "probability density function" or "pdf." The ordinate of the histogram is the number frequency of the particles, $\tilde{f}_n$, within a size interval. The sum of the number frequency over all the size categories is equal to 1.

The number-average particle diameter of this distribution is defined as

$$\bar{d}_n = \sum_{i=1}^{N} d_i \tilde{f}_n(d_i), \tag{1.31}$$

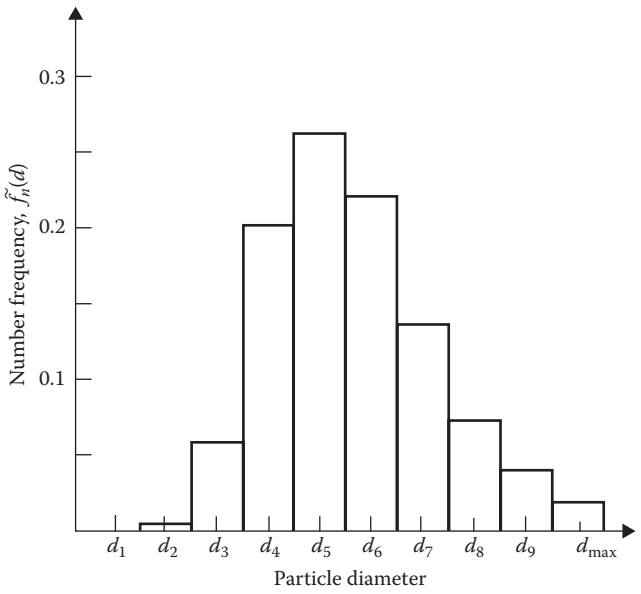

Figure 1.3

Histogram of the number frequency distribution of a sample of particles. The sum of the nine values of the frequency distribution is equal to 1.

where N is the total number of intervals. The number variance is

$$\sigma_n^2 = \frac{N}{N-1}\sum_{i=1}^{N}\left(d_i - \bar{d}_n\right)^2 \tilde{f}_n(d_i) = \frac{N}{N-1}\sum_{i=1}^{N} d_i^2 \tilde{f}_n(d_i) - \bar{d}_n^2 . \tag{1.32}$$

The standard deviation, σ_n, is the square root of the variance of the sizes. Oftentimes, the ratio of the standard deviation to the average diameter is used as a measure of the spread of the distribution. A narrow distribution is characterized by the relationship $\sigma_n/d_n < 0.1$, and the mixture is characterized as monodisperse.

Two other approaches are used to describe the size distribution using the particle mass and volume *in lieu* of the particle number as the dependent variable. Thus, for the mass distribution, the mass of each particle is measured or inferred from measurements, and the fraction of mass associated with each size interval is used to construct the distribution. This is known as the discrete mass frequency distribution, $\tilde{f}_m$. Using this distribution, one may calculate the mass-averaged particle diameter and mass-averaged variance as follows:

$$\bar{d}_m = \sum_{i=1}^{N} d_i \tilde{f}_m(d_i), \tag{1.33}$$

and

$$\sigma_m^2 = \frac{N}{N-1}\sum_{i=1}^{N}\left(d_i - \bar{d}_m\right)^2 \tilde{f}_m(d_i) = \frac{N}{N-1}\sum_{i=1}^{N} d_i^2 \tilde{f}_m(d_i) - \bar{d}_m^2 \tag{1.34}$$

The volume-averaged particle diameter and volume-averaged variance are calculated in a similar manner. If the material density of the particles is constant, the volume- and mass-averaged distributions are identical. It must be noted that in order to achieve a reasonably smooth frequency distribution function, a very large number of particles must be counted. Several modern optical experimental techniques make this task feasible with relatively low effort.

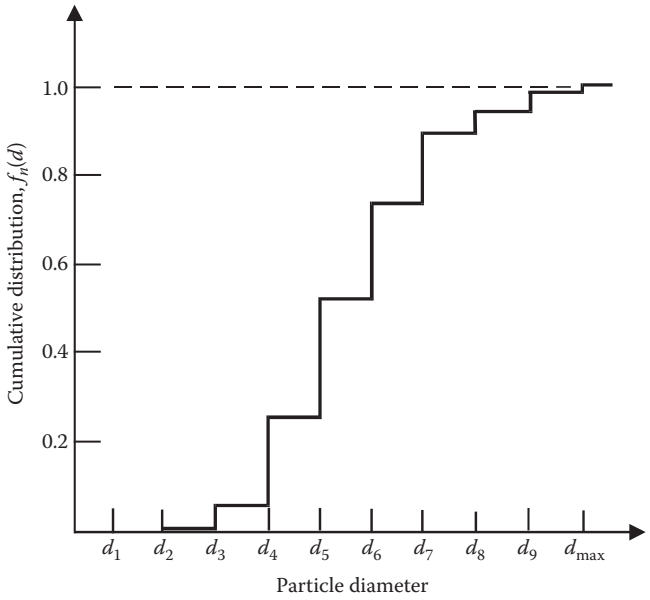

Figure 1.4

The cumulative number distribution that corresponds to the number frequency distribution of Figure 1.3.

Another commonly used method to quantify particle size is using the *cumulative* distribution, which is the sum of the components of the frequency distribution. The cumulative number distribution associated with size d_k is

$$\tilde{F}_n(d_k) = \sum_{i=1}^{k} \tilde{f}_n(d_i). \tag{1.35}$$

The numerical value of $\tilde{F}_n$ is the fraction of particles with sizes less than d_k. It is apparent that the cumulative number distribution is equal to 0 at the very fine sizes and close to 1 at the higher end of the sizes of the particles. The cumulative number distribution that corresponds to the number frequency distribution of Figure 1.3 is shown in Figure 1.4. Both cumulative number and cumulative mass distributions may be determined from the data of the corresponding frequency distribution.

1.3.2.2 Continuous Size Distributions

If the size intervals in a discrete distribution are made progressively smaller, in the limit as Δd approaches very small values, one obtains the continuous number frequency function

$$f_n(d) = \lim_{\Delta d \to 0} \left(\frac{\tilde{f}_n(d)}{\Delta d} \right). \tag{1.36}$$

The number fraction of particles with diameters between d and $d + d(d)$ is given by the differential $f_n(d)\, d(d)$. The function of the continuous frequency distribution is a continuous function of the diameter as shown in Figure 1.5. In a similar manner, one obtains the mass frequency function based on the mass distribution $\tilde{f}_m$. If the continuous distribution is normalized, as in Figure 1.5, then the area under the continuous frequency distribution curve is equal to 1.

The continuous cumulative distribution is obtained from the integral of the continuous frequency distribution as follows:

$$F_n(d) = \int_0^d f_n(\xi) d\xi. \tag{1.37}$$

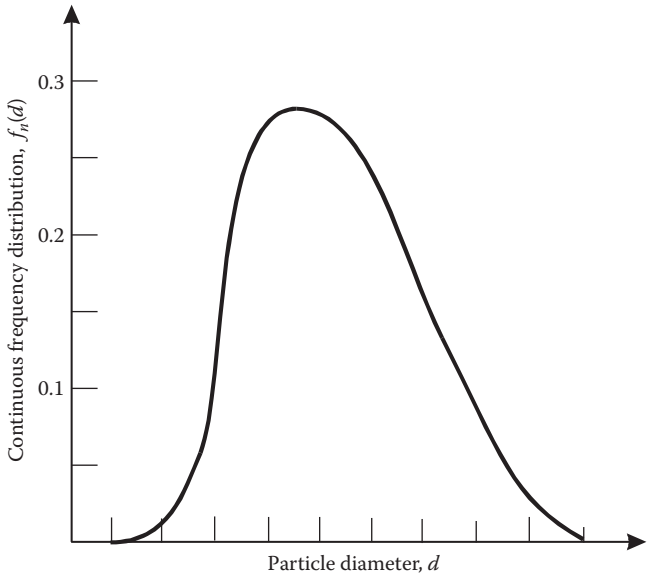

Figure 1.5

Continuous number frequency distribution of a sample of particles.

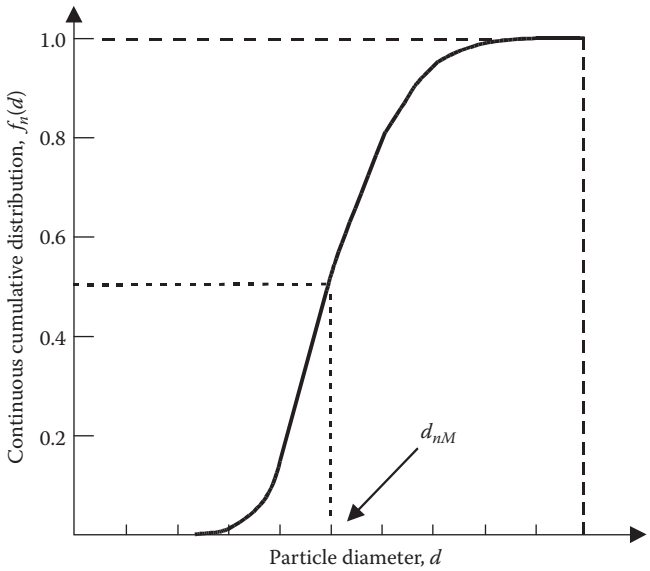

Figure 1.6

The cumulative distribution function that corresponds to the continuous distribution function of Figure 1.5.

The cumulative distribution function associated with the continuous distribution function of Figure 1.5 is an S-shaped curve, which is shown in Figure 1.6. The cumulative distribution of a uniform (constant) continuous distribution is a straight line. All cumulative distribution functions approach the value 1, as the particle size approaches the maximum size.

It must be noted that measurements of size data for particles generate discrete distributions. Continuous distributions may be obtained for convenience by fitting empirical functions to the discrete size data.

1.3.3 Statistical Parameters of the Size Distributions

Several parameters are used with discrete and continuous size distributions. We present here the most commonly used parameters in dispersed multiphase flow. Typically, these parameters have different values for the number, mass, and volume distributions.

1.3.3.1 Mode

The mode is the size that corresponds to the maximum of a continuous frequency function. A distribution that has two local maxima is referred to as a bimodal distribution and it has two modes. Similarly, trimodal and multimodal distributions may be defined, but they are seldom met in dispersed multiphase flows. The corresponding mode for a discrete size distribution is the size that corresponds to the highest value in the frequency histogram. For example, d_5 is the mode of the discrete distribution depicted in Figure 1.3.

1.3.3.2 Mean

For a discrete distribution, the mean is equal to the average and is given by Equations 1.31 and 1.33. The mean of a continuous distribution is obtained from the integral of the size, d, multiplied by the pertinent frequency distribution. For the continuous number distribution function, the corresponding mean is

$$\mu_n = \int_0^{d_{\max}} d\tilde{f}_n d(d). \tag{1.38}$$

A similar expression applies to the continuous mass distribution mean, μ_m. Sometimes, this mean is called the arithmetic mean diameter d_{AM}. Other mean diameters that are used in dispersed multiphase flows are the surface mean diameter

$$d_{SM} = \left[\int_0^{d_{\max}} d^2 \tilde{f}_n d(d)\right]^{1/2} \tag{1.39}$$

and the volume mean diameter

$$d_{VM} = \left[\int_0^{d_{\max}} d^3 \tilde{f}_n d(d)\right]^{1/3}. \tag{1.40}$$

1.3.3.3 Sauter Mean Diameter

The Sauter mean diameter (SMD) is encountered frequently in the spray and atomization literature and is defined as follows:

$$d_{32} = \frac{\int_0^{d_{\max}} d^3 f_n(d) d(d)}{\int_0^{d_{\max}} d^2 f_n(d) d(d)}. \tag{1.41}$$

The SMD is a measure of the volume-to-surface area ratio for particles, bubbles, and drops.

1.3.3.4 Variance

The variance of the continuous distribution with mean μ is calculated from the expression

$$\sigma^2 = \int_0^{d_{\max}} (d-\mu)^2 f(d) d(d) = \int_0^{d_{\max}} d^2 f(d) d(d) - \mu^2. \tag{1.42}$$

As with the mean, a variance may be defined to the number, the mass, or the volume distributions of particle sizes. As with the discrete distributions, the variance is a measure of the spread of the distribution and the square root of the variance is the standard deviation. A continuous distribution may be classified as monodisperse if $\sigma/\mu < 0.1$.

1.3.3.5 Median

The median diameter, d_M, corresponds to the diameter for which the cumulative distribution has the value 0.5. The number median diameter, d_{nM}, is shown in the cumulative distribution of Figure 1.6. A corresponding value for the mass median diameter, d_{mM}, may be determined from the cumulative mass distribution function.

1.3.4 Size Distributions

While there is a multitude of distributions in the literature of statistics, this section presents the statistical distributions that are most often used in the literature of dispersed multiphase flow.

1.3.4.1 Log-Normal Distribution

The number frequency function of the log-normal distribution is (Marshall, 1954)

$$f_n(d) = \frac{1}{\sqrt{2\pi} d\sigma_G} \exp\left[-\frac{1}{2}\left(\frac{\ln(d) - \ln(d_{nM})}{\sigma_G} \right)^2 \right], \tag{1.43}$$

where

d_{nM} is the median diameter of the number distribution
σ_G is the geometric standard deviation

The corresponding expression for the mass frequency distribution is

$$f_m(d) = \frac{1}{\sqrt{2\pi} d\sigma_G} \exp\left[-\frac{1}{2}\left(\frac{\ln(d) - \ln(d_{mM})}{\sigma_G} \right)^2 \right], \tag{1.44}$$

where d_{mM} is the mass median diameter. The geometric standard deviation is determined by plotting the cumulative distribution on logarithmic coordinates. The plot is a straight line with a positive slope, and the value for σ_G may be determined from the relationship

$$\sigma_G = \ln \frac{d_{84}}{d_M}, \tag{1.45}$$

where

d_{84} is the diameter corresponding to the 84th percentile on the logarithmic plot
d_M is the median diameter, which is the diameter corresponding to the 50th percentile

The same value for σ_G is used for the mass and number distributions. For the calculation of the several statistical parameters in this distribution, a useful mathematical relationship is

$$d_M^k \exp\left(\frac{k^2 \sigma_G^2}{2} \right) = \frac{1}{\sqrt{2\pi}\sigma_G} \int_0^\infty \left[d^k \exp\left[-\frac{1}{2}\left(\frac{\ln(d) - \ln(d_{mM})}{\sigma_G} \right)^2 \right] \right] \frac{d(d)}{d}, \tag{1.46}$$

or

$$d_M^k \exp\left(\frac{k^2 \sigma_G^2}{2} \right) = \int_0^\infty d^k f(d) d(d). \tag{1.47}$$

These relationships may be readily used to calculate the various statistical parameters of the distribution.

1.3.4.2 Upper-Limit Log-Normal Distribution

A derivative of the log-normal distribution is the upper-limit log-normal distribution (Mugele and Evans, 1951), which is frequently used to model droplet data from spray nozzles. The distribution makes use of a maximum particle size as the upper limit of the distribution and its number frequency function is defined as

$$f_n(d) = \frac{1}{\sqrt{2\pi}d\sigma_G}\exp\left[-\frac{1}{2}\left(\frac{\ln(\alpha d) - \ln\left(d_{\max} - d_{nM}\right)}{\sigma_G}\right)^2\right], \tag{1.48}$$

where

$d_{\max}$ is the maximum diameter in the distribution
a is a constant equal to

$$\alpha = \frac{d_{\max}}{d_M} - 1. \tag{1.49}$$

As with the log-normal distribution, the standard deviation may be calculated from the slope of the logarithmic plot of the data.

1.3.4.3 Square-Root Normal Distribution

The number frequency function for the square-root normal distribution is given by the expression (Tate and Marshall, 1953)

$$f_n(d) = \frac{1}{2\sqrt{2\pi\sigma}d}\exp\left[-\left(\frac{\left(\sqrt{d} - \sqrt{\bar{d}}\right)}{2\sigma}\right)^2\right], \tag{1.50}$$

where σ is the variance of the square-root normal distribution. This distribution appears to fit well empirical data from vane-type atomizers and does not have the end "tails" of a normal distribution. When using this distribution, one must be cognizant that several relationships that were derived for the other types of normal distributions are not applicable to the square-root normal distribution.

1.3.4.4 Rosin–Rammler Distribution

The Rosin–Rammler distribution (Mugele and Evans, 1951) is frequently used to model droplet size distributions in sprays. It is expressed in terms of the cumulative mass distribution

$$F_m(d) = 1 - \exp\left[-\left(\frac{d}{\delta}\right)^n\right]. \tag{1.51}$$

where δ and n are two empirical constants, which are determined by plotting the cumulative distribution on logarithmic coordinates. By taking twice the logarithm of Equation 1.51, one obtains

$$\ln\left[-\ln\left(1 - F_m(d)\right)\right] = n\left(\ln(d) - \ln(\delta)\right). \tag{1.52}$$

Therefore, n is the slope of this line and δ can be obtained from the expression

$$\delta = \frac{d_{mM}}{0.693^{1/n}}. \tag{1.53}$$

The mass frequency function of this distribution may be obtained by taking the derivative of the cumulative distribution of Equation 1.51:

$$f_m(d) = \frac{dF_m(d)}{d(d)} = \frac{n}{\delta}\left(\frac{d}{\delta}\right)^{n-1} \exp\left(\left[-\left(\frac{d}{\delta}\right)^n\right]\right). \tag{1.54}$$

When using the Rosin–Rammler distribution, the gamma function,

$$\Gamma(x) = \int_0^\infty \lambda^{x-1} \exp(-\lambda) d\lambda, \tag{1.55}$$

is a useful tool to calculate the moments of the distribution because

$$\int_0^\infty n d^\alpha \left(\frac{d}{\delta}\right)^{n-1} \exp\left[-\left(\frac{d}{\delta}\right)^n\right] d\left(\frac{d}{\delta}\right) = \delta^\alpha \Gamma\left(\frac{\alpha}{n}+1\right), \tag{1.56}$$

which leads to the relationship for the statistical parameters of this distribution

$$\int_0^\infty d^\alpha f_m(d) d(d) = \delta^\alpha \Gamma\left(\frac{\alpha}{n}+1\right). \tag{1.57}$$

1.3.4.5 Nukiyama–Tanasawa Distribution

The Nukiyama–Tanasawa distribution is a more general distribution from which the Rosin–Rammler distribution is a special case. The frequency function of this distribution is

$$f_n(d) = Bd^2 \exp\left(-Cd^q\right), \tag{1.58}$$

where B, C, and q are empirical parameters. For spray distributions, q typically varies from 1/6 to 2 with the higher values corresponding to narrower distributions.

1.3.4.6 Log-Hyperbolic Distribution

Some empirical studies on sprays showed that neither the log-normal nor the Rosin–Rammler distribution fits the data sufficiently well. Two droplet size distributions fitted with a Rosin–Rammler distribution may have the same parameters, but the actual distribution may be quite different. This happens because one of the shortcomings of both the log-normal and Rosin–Rammler distributions is the representation of the tails of the distribution—the values of the frequency function for very large and very small values of the sizes. A better fit for the tails of the distributions is the log-hyperbolic distribution proposed by Barndorff-Nielsen (1977). The form of the number frequency function for this distribution is

$$f_n(d) = A \exp\left[-\alpha\sqrt{\delta^2 - \left(\ln(d)-\mu\right)^2} + \beta\left(d-\mu\right)\right], \tag{1.59}$$

where α, β, δ, and μ are empirical parameters. It is apparent that the random variable of this distribution is the logarithm of the particle diameter. The coefficient A is a normalization factor related to the other parameters by the expression

$$A = \frac{\sqrt{\left(\alpha^2-\beta^2\right)}}{2\alpha\delta K_1\left(\delta\sqrt{\left(\alpha^2-\beta^2\right)}\right)}, \tag{1.60}$$

where K_1 is the third-order Bessel function of the third kind. The logarithm of the frequency function yields the equation of a hyperbola:

$$\ln(f_n) = \ln(A) - \alpha\sqrt{\delta^2 - (\ln(d) - \mu)^2} + \beta(d - \mu). \tag{1.61}$$

For $[\ln(d) - \mu]/\delta < 0$, the slope of the asymptote is $\alpha + \beta$, while for $[\ln(d) - \mu]/\delta > 0$, the slope of the asymptote is $-\alpha + \beta$. Thus, when the logarithm of the frequency data is plotted versus $\ln(d)$, the slopes of the two asymptotes may be measured to determine the parameters α and β. It may be proven that the parameter μ is the mode of the distribution. The value of this parameter may be determined from data fitting. A practical problem of the log-hyperbolic distribution for particle or drop size distributions is that if the tails are not long enough to generate accurate values of the slopes, there is a great deal of inaccuracy in the determination of the parameters α and β. A three-parameter log-hyperbolic distribution may be used in such cases to alleviate this problem.

1.4 Interactions of Fluids with Particles, Drops, and Bubbles

1.4.1 Introduction

Because the sphere is the simplest, 3D shape, mass, momentum, and heat transport problems pertaining to spheres have been the subjects of the first analytical methods as well as of the intellectual curiosity of scientists. These problems belong to the class of the most fundamental problems in fluid dynamics, heat transfer, and mass transfer and have attracted the attention of many mathematicians, physicists, and engineers. They are also subjects that have numerous practical applications including combustion and propulsion, chemical reactions and catalysis, mixing and separation, boiling and condensation, environmental sedimentation and resuspension, and biological flows. The transport of momentum, heat, and mass is of primary interest in all of these processes, which are often expressed in terms of *transport coefficients* or in terms of dimensionless parameters that are pertinent to these coefficients. For example, the instantaneous loss or gain of mass of a sphere during any process may be expressed in terms of the mass transfer coefficient, h_M, or its dimensionless representation, the Sherwood number, Sh, and the material properties of the sphere and the carrier fluid:

$$\dot{m}_s = \frac{dm_s}{dt} = -\pi h_M d^2 \rho_c (Y_s - Y_\infty) = -\pi (Sh) d D_c \rho_f (Y_s - Y_\infty), \tag{1.62}$$

where D_c is the diffusivity of the material of the sphere inside the carrier fluid. Similarly, the instantaneous temperature change of the sphere, in the case of convective heating (when radiation is negligible), may be expressed in terms of the heat transfer coefficient, h, or its dimensionless representation, the Nusselt number:

$$m_s c_{ps} \frac{dT_s}{dt} = \dot{Q} = -\pi h d^2 (T_s - T_\infty) = -\pi d Nu k_c d (T_s - T_\infty). \tag{1.63}$$

Finally, the equation of motion of a sphere may be expressed by Newton's second law in terms of all the instantaneous forces that act on the sphere. These forces are the hydrodynamic force on the sphere, F_H (which is composed of two parts, the drag and lift, F_D, and, F_L), and the body or volume force, F_B. The latter is normally the gravity/buoyancy force, and the former may be written in terms of two dimensionless factors: the drag coefficient, C_D, and the lift coefficient, C_L:

$$\begin{aligned} m_s \frac{dv_i}{dt} = F_{Di} + F_{Li} + F_{Bi} + F_{AMi} + F_{Hi} &= \frac{1}{8}\pi d^2 \rho_c C_D (u_i - v_i)\left|u_m - v_m\right| \\ &+ \frac{1}{8}\pi d^2 \rho_c C_L \left|u_m - v_m\right| \frac{e_{ijk}(u_k - v_k)\Omega_j}{\sqrt{\Omega_i \Omega_i}} + \frac{1}{6}\pi(\rho_s - \rho_c) d^3 g_i + F_{AM} + F_H, \end{aligned} \tag{1.64}$$

where e_{ijk} is the permutation symbol. The added mass force, F_{AM}, and the history term, F_H, emanate from the transient response of the particle and the surrounding fluid. Functional forms for the two terms are given in

Section 1.4.3.6. For the performance of any calculations on the motion of the sphere, one would need accurate information for the *transport coefficients*: drag coefficient, lift coefficient, heat transfer coefficient, and mass transfer coefficient. The numerical values of these coefficients emanate from analytical or numerical results and from experimental data.

This section intends to be a succinct presentation of analytical, experimental, and numerical results that pertain to the transport processes involving a carrier fluid and bubbles, drops, or particles and are useful for the performance of engineering calculations. In particular, mass transfer, momentum transfer, and heat transfer from a particle, bubble, or drop with the carrier fluid will be examined. For a historical background and a more extensive description of the development of these subjects, one may consult the review article by Michaelides (2003). Of the other recent studies, the main results on the momentum transfer from a sphere to a fluid as well as the energy and mass transfer at wide ranges of Reynolds and Peclet numbers may be found in several treatises and monographs, such as those by Leal (1992), Kim and Karila (1991), Crowe et al. (1998), Sirignano (1999), Michaelides (2006), and Michaelides (2014).

1.4.2 Mass Transfer

1.4.2.1 Thermodynamic Relations of Evaporation, Sublimation, and Condensation

In this section, we seek to determine the thermodynamic equilibrium relations between the carrier fluid and a sphere that undergoes phase change. For this reason, the thermodynamic properties are assumed to be equilibrium properties and this implies no (or very weak) heat and mass transfer within the system. Consider a sphere of radius a, inside a carrier gas of density ρ_f, in a spherical system of coordinates that follow the center of the sphere. The carrier gas and the sphere have different chemical composition, and their species will be denoted by c and l, respectively. Mass is allowed to cross the boundary of the sphere due to one of the processes of sublimation, evaporation, or condensation. Because of this, the gaseous phase is composed of both the species l and c, while the sphere, which may be either solid or liquid, is composed solely of the species l. Figure 1.7 is a schematic diagram of such a process. The directions and numerical signs of the pressure and temperature gradients in this figure are such that they correspond to the case of condensation. The total pressure in the gaseous mixture is constant and equal to p_T. The total pressure comprises two parts: the partial pressure, or vapor pressure, of the species l, p_l, and the partial pressure of the carrier gaseous species c, p_c. In all the transport processes that are pertinent to mass transfer, both the partial pressures are functions of the radial direction, r:

$$p_T = p_c(r) + p_l(r). \tag{1.65}$$

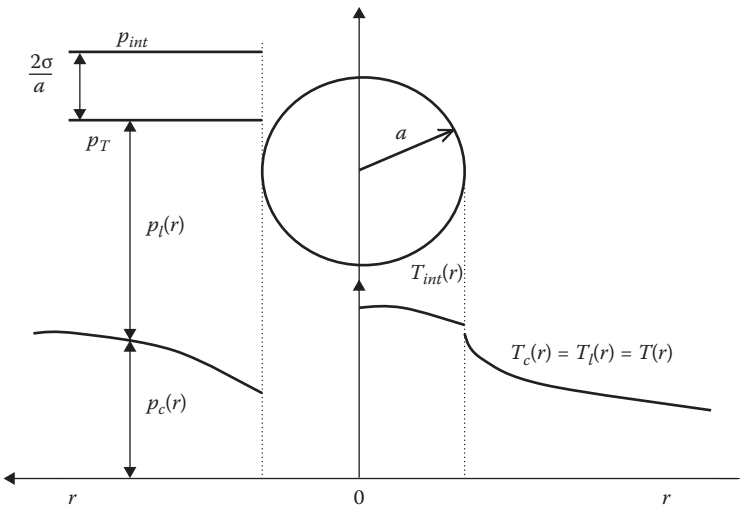

Figure 1.7

Pressure and temperature fields developed in the vicinity of a drop carried by the fluid of different compositions.

If the carrier phase is composed of a number of species, $c1$, $c2$, $c3$, … as, for example, in the case of air, then the total pressure is the sum of all the partial pressures of these species:

$$p_T = \sum_i p_{ci}(r) + p_l(r). \tag{1.66}$$

When the sphere is a liquid drop, the pressure in the interior of the drop would be higher than p_T by the amount contributed by the surface tension:

$$p_{int} = p_T + \frac{2\sigma}{a}. \tag{1.67}$$

In most practical applications, the radius of the sphere, a, is large enough to satisfy the condition $p_T \gg 2\sigma/a$. Hence, the internal pressure, p_{int}, is approximately equal to the total pressure in the gas phase, p_T. Thermodynamic equilibrium implies that the temperatures of the species l and c at the surface anywhere in the gaseous mixture are equal, that is, $T_c(r) = T_l(r) = T(r)$, where $r > a$. The temperature inside the sphere may be nonuniform and hence a function of the radial distance. This temperature will be denoted as $T_{int}(r)$, where $r < a$.

At the surface of the sphere, there is a phase transition, for example, liquid–vapor or solid–vapor, that normally occurs within a very short layer of molecular dimensions. The phase of the matter in this film layer is not well defined. Hence, the material and thermodynamic properties within this molecular layer are not well defined too. For this reason, they are depicted by the dashed lines in Figure 1.7. It is known that the specific properties of matter exhibit a jump discontinuity within this layer, for example, from liquid-specific enthalpy to vapor-specific enthalpy. The intensive properties of matter, temperature, and pressure exhibit a discontinuity of lower magnitude. The discontinuity of the intensive properties is not noticeable unless the Knudsen number of the flow is higher than 0.01 (see Section 1.4.3.5. for more details) where the molecular effects play an important role in the behavior of the sphere.

With the exception of very fast combustion processes, in most of the practical applications involving drops and particles that undergo mass, momentum, and heat transfer with a carrier fluid, the thermodynamic relaxation time is much shorter than all the response times of the sphere. For this reason, thermodynamic equilibrium is normally established fast at the interface and does not affect significantly the transport processes. When the interface may be considered sufficiently flat for the surface tension to have negligible impact, the partial pressure of the vapor and the temperature of the vapor at the interface are related via the Clausius–Clapeyron equation

$$\frac{dp_l}{dT}\Big|_a = \frac{h_{fg}}{T(a)\left[\dfrac{1}{\rho_v(a)} - \dfrac{1}{\rho_s(a)}\right]}, \tag{1.68}$$

where the symbols in parentheses denote arguments of functions and the derivative must be evaluated at the conditions of the interface $r = a$. Thus, $T(a)$ is the temperature at the interface, $\rho_v(a)$ is the density of the species l in its vapor phase at the interfacial pressure and temperature, and $\rho_s(a)$ is the density of the material in the sphere, evaluated also at the interfacial pressure and temperature. Therefore, the temperature and vapor pressure at the interface of the sphere are related by the so-called saturation relation, $p_l = p_{sat}(T)$. The function $p_{sat}(T)$ for any of the commonly used materials may be obtained in tabular form from thermodynamics texts or in tables of properties. It must be emphasized that this thermodynamic relationship between the prevailing pressure and temperature applies only at the surface of the sphere $r = a$. In general, $p_l(r)$ and $T_l(r)$ are two independent functions that are only related at $r = a$.

As in the case of the pressure (Equation 1.67), the surface tension may have an influence on the saturation relation. In this case, the value for the partial pressure of the vapor at the interface must be corrected as follows:

$$p_l(a) = p_{sat}(T(a))\exp\left[\frac{2\sigma(T(a))}{a\rho_s(a)R_vT(a)}\right]. \tag{1.69}$$

where the parentheses denote arguments of functions and R_v is the specific gas constant for the material species of the vapor, l, that is, $R_v = R/\mathcal{M}_l$ and $R = 8.314$ kJ/kg > K. The term in the square brackets is sometimes called the "Kelvin number," Ke, and in most practical applications its value is very low ($Ke \ll 1$). Hence, in most practical applications, $p_l(a) \approx p_{sat}(T(a))$. A glance at Equation 1.69 proves that the Kelvin number and hence the effects of surface tension become significant when $a \to 0$, a condition that is met at the last stages of combustion, evaporation, or sublimation of a sphere.

Within the gaseous phase that comprises the vapor of the sphere and the carrier fluid, the mole fraction of the vapor and the mole fraction of the components of the carrier fluid at any distance $r > a$ are defined in terms of their partial pressures as follows:

$$X_v(r) = \frac{p_l(r)}{p_T} \quad \text{and} \quad X_{ci}(r) = \frac{p_{ci}(r)}{p_T}. \tag{1.70}$$

Obviously, at any point, the condition applies that the sum of all the mole fractions in the gaseous mixture is equal to one. At the surface of the sphere, the pressure $p_l(a)$ is equal to the saturation pressure at the prevailing temperature, $T(a)$. Hence, the mole fraction of the vapor at the interface is determined from the knowledge of the total pressure and the temperature of the sphere.

The mole fraction of any species, denoted by the letter X_j, and the mass fraction of this species, Y_j, are related via the molecular weights, M_i, of the species that are present in the gaseous mixture:

$$Y_j = \frac{X_j M_j}{\sum_i X_i M_i} \quad \text{and} \quad X_j = \frac{Y_j/M_j}{\sum_i Y_j/M_j}, \tag{1.71}$$

where the sum in the denominator is over all the species that are present in the gaseous phase, namely, the carrier gas and the vapor. As in the case of the mole fractions, at any point outside the sphere, the sum of all the mass fractions is equal to one.

In the cases of sublimation and evaporation, the variation of the intensive vapor properties $T_v(r)$ and $p_v(r)$ is in the opposite direction from the one shown in Figure 1.7. In such processes, any mass flow rate from the sphere to the gas results in a radial velocity w from the surface of the sphere to the gas, which is described by the following mass conservation equation:

$$d^2 \frac{d\rho_f}{dt} + \frac{d(\rho_f d^2 w)}{dr} = 0. \tag{1.72}$$

where d, when it is not part of a differential operator such as d/dt or d/dr, is the diameter of the sphere and r is the radial coordinate. In a quasi-steady case, where the density of the carrier fluid may be considered to be constant, the aforementioned equation may be integrated on the surface of the sphere to yield the mass flow rate from the sphere to the fluid:

$$\frac{dm}{dt} = -\pi d^2 \rho_f w\big|_s. \tag{1.73}$$

The velocity w is evaluated with respect to the surface of the sphere at the gas side. Since the radial velocity w is an outward velocity with respect to a control volume that encloses the sphere, the negative sign signifies that mass is transferred from the sphere to the fluid when w is positive.

Evaporation, condensation, sublimation, and chemical reactions are the basic processes for the mass transfer to or from a sphere. Processes without chemical reactions will be examined in this section, while processes with chemical reactions, such as combustion, will be mentioned briefly in the next section and will be examined in more detail in Chapter 6. It must be recalled that when mass transfer occurs without chemical reactions, the driving force for the process is the difference of the concentration of the species the sphere is composed of (evaluated at the surface of the sphere) and the concentration of the same species in the carrier fluid (evaluated far from the sphere). For example, in the case of an evaporating water droplet in air, the driving force is the difference of the specific humidity at the surface of the sphere and

the specific humidity of the carrier fluid, far from the sphere. The former is a function of the temperature and pressure at the surface of the sphere, while the latter is a property of the carrier fluid. If the carrier fluid becomes completely saturated with water vapor, there is no such difference, and hence, no evaporation takes place.

The mass flux at the surface of an evaporating or condensing droplet in a binary mixture is given by Fick's law:

$$\rho_f w = -\rho_f D_c \frac{\partial Y_s}{\partial r}\Big|_s, \tag{1.74}$$

where D_c is the diffusion coefficient of the species the drop is composed of in the carrier fluid.

At the surface, we also require the following condition:

$$D_c \frac{\partial Y_s}{\partial r} = h_M (Y_s - Y_c), \tag{1.75}$$

where h_M is the convective mass transfer coefficient, which is analogous to the convective heat transfer coefficient. For a droplet of diameter $d = 2a$, the gradient of the mass fraction of any species at the droplet surface is proportional to the difference between the mass fraction at the surface and in the free stream and inversely proportional to the droplet diameter. Therefore,

$$\frac{\partial Y_s}{\partial r}\Big|_s \sim \frac{Y_s - Y_\infty}{d}, \tag{1.76}$$

where Y_∞ is the mass faction of the species in the free stream far from the droplet. A combination of the last two equations yields

$$\frac{dm}{dt} \sim \pi \rho_f D d (Y_\infty - Y_s). \tag{1.77}$$

The parameter that makes this expression an equation is the Sherwood number, *Sh*, which is often determined by experiment. Thus, the following expression may be derived for the rate of mass transfer from a sphere:

$$\frac{dm}{dt} = Sh \pi \rho_f D_c d (Y_\infty - Y_s). \tag{1.78}$$

Without mass advection caused by forced or free convection processes, the pure molecular diffusion dominates the mass transfer process, and hence, $Sh = 2$. The effect of fluid advection and relative velocity between the droplet and the carrier fluid is frequently represented by the so-called "Ranz–Marshall relation" (Ranz and Marshall, 1952):

$$Sh = 2 + 0.6 Re_r^{1/2} Sc^{1/3}, \tag{1.79}$$

where

Re_r is the Reynolds number based on the relative velocity
Sc is the Schmidt number

Since the mass transfer process from a sphere is closely related to the heat transfer process via the well-known heat/mass transfer analogy, one may also use alternative expressions for the Sherwood number, which are given as expressions for the Nusselt number in Section 1.4.4. In particular, one may use the *Sh*–*Nu* analogy and obtain expressions for the Sherwood number based on the numerical correlations of Section 1.4.4.2 for the heat and mass transfer from viscous spheres at finite Reynolds numbers.

1.4.2.2 Chemical Reactions

When chemical reactions take place, the mass transfer from the sphere is related to the reaction rate of the fuel, ξ. This is expressed in units of the reaction per unit time, which are sometimes referred to as DeDonder/second. If we assume that the spherical symmetry of the drop is retained during the processes of mass transfer and chemical reaction, the mass conservation equation for the fuel, the oxidant, and an inert component, such as nitrogen, which may be present in the reaction, may be written as follows:

1. For the fuel, whose mass fraction is denoted by the subscript *F*:

$$\frac{\partial}{\partial t}(\rho d^2 Y_F) + \frac{\partial}{\partial r}(\rho u d^2 Y_F) - \frac{\partial}{\partial r}\left(\rho d^2 D_F \frac{\partial Y_F}{\partial r}\right) = \rho d^2 \xi. \tag{1.80}$$

   The last term in this equation is a measure of the mass of the fuel that is consumed by the reaction.
2. For an oxidant, whose mass fraction is denoted by the subscript *O*:

$$\frac{\partial}{\partial t}(\rho d^2 Y_O) + \frac{\partial}{\partial r}(\rho u d^2 Y_O) - \frac{\partial}{\partial r}\left(\rho d^2 D_O \frac{\partial Y_O}{\partial r}\right) = \rho d^2 F_{OF} \xi, \tag{1.81}$$

   where FOF is the stoichiometric ratio of oxidant to the fuel that is consumed by the reaction.
3. For an inert component, such as nitrogen, the total mass is conserved and the right-hand side of the corresponding equation is equal to zero:

$$\frac{\partial}{\partial t}(\rho d^2 Y_N) + \frac{\partial}{\partial r}(\rho u d^2 Y_N) - \frac{\partial}{\partial r}\left(\rho d^2 D_N \frac{\partial Y_N}{\partial r}\right) = 0. \tag{1.82}$$

4. The mass conservation equation for any product, denoted by the subscript *P*, which appears as a result of the reaction, is

$$\frac{\partial}{\partial t}(\rho d^2 Y_P) + \frac{\partial}{\partial r}(\rho u d^2 Y_P) - \frac{\partial}{\partial r}\left(\rho d^2 D_P \frac{\partial Y_P}{\partial r}\right) = -\rho d^2 (F_{OF} + 1)\xi. \tag{1.83}$$

From the definition of the mass fractions for all the components of the reaction, one may also derive the following identity, which is useful as a closure equation:

$$Y_F + Y_O + Y_N + Y_P = 1. \tag{1.84}$$

The mass balance for any species at the surface of an evaporating or reacting droplet may be imposed on all the species that are present in the droplet and the gas. Because of the loss of liquid mass, there is a radial convection at the surface that is often called "Stefan convection." The rate of mass convection on the side of the gas is equal to the rate of mass convection on the liquid side:

$$\dot{M} Y_{is} - \rho \pi d^2 D_c \frac{\partial Y_i}{\partial r}\Big|_s = \dot{M} \delta_{iF} \quad i = O, F, N, P, \tag{1.85}$$

where
the left-hand side represents the advection and diffusion at the gas side
$\dot{M}$ is the rate of mass vaporization or reaction of the droplet
the subscript i extends over the species of fuel, oxidant, inert, and products
δ_{iF} is the Kronecker delta

More details on the combustion processes and methods for calculating the mass transfer from a burning drop are presented in Chapter 6. Since the subject of mass transfer from a sphere is closely connected to the processes of evaporation and sublimation and since the corresponding mass transfer or *blowing effect*

influences significantly the momentum transfer and the hydrodynamic forces exerted on the droplet, the relevant correlations and useful information on engineering computations will be presented in Sections 1.4.3.4 and 1.4.4.4.

1.4.3 Momentum Transfer

The functional form and expressions for the steady and transient hydrodynamic force exerted by a fluid on a sphere will be presented in this section. The hydrodynamic force is a surface force. The body forces (gravity, magnetic, electric, etc.) that may act on the sphere will not be included in the analysis for brevity. These forces are added to the hydrodynamic force and all the other forces acting on the sphere to generate the Lagrangian equation of motion.

We consider the rectilinear flow of a viscous fluid around a sphere of radius $a(d = 2a)$. The fluid velocity field is nonuniform and given by the function $u_i(x_i, t)$ outside the volume occupied by the sphere. If the sphere is solid that does not rotate,* its velocity is only a function of the time, $v_i(t)$. If the sphere is composed of a viscous fluid (as in bubbles and drops), its velocity is $v_i(x_i, t)$, which signifies that there is fluid motion inside the fluid sphere. In both cases, the governing equations for the process of mass and momentum exchange are the continuity, or mass conservation, equation

$$\frac{\partial \rho_f}{\partial t} + \rho_f \vec{\nabla} \cdot \vec{u} = 0, \tag{1.86}$$

and the momentum conservation equation

$$-\vec{\nabla} p + \mu_f \nabla^2 \vec{u} = \rho_f \left(\frac{\partial \vec{u}}{\partial t} + \vec{U} \cdot \vec{\nabla} \vec{u} \right), \tag{1.87}$$

where U is the fluid velocity at the surface of the sphere. The last equation may be rendered dimensionless by using the diameter, $2a$, as the characteristic dimension of the problem and the characteristic time $\tau_s = 4\alpha^2 \rho_f / \mu_f$. This yields the following dimensionless expression:

$$-\vec{\nabla}^\star p^\star + \nabla^{\star 2} \vec{u}^\star = \frac{\partial \vec{u}^\star}{\partial t^\star} + Re\left(\vec{U}^\star \cdot \vec{\nabla}^\star \vec{u}^\star \right). \tag{1.88}$$

Depending on the details of the process, the characteristic velocity for the definition of $u^\star$ is either the characteristic velocity of the fluid itself or the relative velocity of the sphere with respect to the fluid. This defines two Reynolds numbers for the flow, Re and Re_r:

$$Re = \frac{2a\rho_f |\vec{u}|}{\mu_f} \quad \text{and} \quad Re_r = \frac{2a\rho_f |\vec{u} - \vec{v}|}{\mu_f} \tag{1.89}$$

When applied to particulate flows, Equations 1.87 and 1.88 are sometimes referred to as the "Oseen equations." They contain the velocity at the surface of the sphere and the nonlinear advection term of the fluid flow, which is the last term in the two equations (Oseen, 1913). When $Re \ll 1$, the nonlinear advection term may be neglected in comparison to the viscous term. Then the momentum equation becomes linear and reads as follows:

$$\rho_f \frac{\partial \vec{u}}{\partial t} = -\vec{\nabla} p + \mu_f \nabla^2 \vec{u} \tag{1.90}$$

or in dimensionless form

$$-\vec{\nabla}^\star p^\star + \nabla^{\star 2} \vec{u}^\star = \frac{\partial \vec{u}^\star}{\partial t^\star}. \tag{1.91}$$

* If the solid sphere rotates, its interior points move according to the solid body rotation principles.

This flow is often called "Stokes flow" or "creeping flow" (Stokes, 1851) and the last two equations *Stokes equations*. Creeping or Stokes flow basically implies that the relative Reynolds number of the flow, Re_r, is very small, the viscous effects dominate the hydrodynamic force on the sphere, and the inertia effects, which are represented by the nonlinear term of the governing equation, may be neglected. Micron-size and nanoparticles satisfy this condition as well as larger particles in fluids of high viscosity and low relative velocity.

1.4.3.1 Stokes or Creeping Flow

The steady-state solution of Equation 1.90 yields the *Stokes drag* for the hydrodynamic force ($F_D = 6\pi a v \mu_f$). The full, transient solution of the equation is the so-called Boussinesq–Basset expression (Maxey and Riley, 1983, Boussinesq, 1885, Basset, 1888a, Michaelides, 2003), which is elucidated in Section 1.4.3.6. Although the Stokes drag is obtained for $Re_r \ll 1$, the expression for it is accurate up to $Re_r = 0.5$ (see Table 1.1). Because many industrial applications with small particles and drops in viscous fluids occur at $Re_r < 1$, this type of flow is of immense interest to engineers and scientists.

Consider the motion of a viscous fluid sphere inside the fluid of different viscosities at $Re_r \ll 1$. The fluid velocity is uniform and equal to U, far from the sphere and the no-slip condition applied on the surface of the sphere. The center of coordinates is coincident with the center of the sphere, and the flow domain is much larger than the diameter of the sphere. This is referred to sometimes as an "infinite domain." The viscous sphere problem in a fluid was solved independently by Hadamard (1911) and Rybczynski (1911) who obtained the following analytical expressions for the stream functions inside and outside the sphere:

$$\psi_i = \frac{Ur^2(a^2 - r^2)\sin^2\theta}{4(\lambda+1)a^2} \tag{1.92}$$

and

$$\psi_o = \frac{Ur^2\sin^2\theta}{2}\left[1 - \frac{(3\lambda+2)a}{2(\lambda+1)r} + \frac{\lambda a^3}{2(\lambda+1)r^3}\right], \tag{1.93}$$

where λ is the ratio of the dynamic viscosities, μ_s/μ_c. The case of a solid sphere is given at the limit $\lambda \to \infty$, and the case of an inviscid sphere (a bubble) is given at the limit $\lambda \to 0$. It is apparent that even at this very low relative velocity, the presence of the sphere in a flow field creates a disturbance in the velocity field of the fluid, which is determined in the radial and transverse directions from the following last two equations:

$$u_r = U\cos\theta\left[1 - \frac{(3\lambda+2)a}{2(\lambda+1)r} + \frac{\lambda a^3}{2(\lambda+1)r^3}\right] \tag{1.94}$$

and

$$u_\theta = -U\sin\theta\left[1 - \frac{(3\lambda+2)a}{4(\lambda+1)r} - \frac{\lambda a^3}{4(\lambda+1)r^3}\right]. \tag{1.95}$$

Table 1.1 Drag Coefficients of Spherical Particles Calculated by Four Different Expressions

Re_r	Stokes	Equation 1.103	Equation 1.104	Equation 1.105
0.05	480.0	484.5	484.3	489.2
0.1	240.0	244.5	244.1	247.4
0.2	120.0	124.5	123.9	126.0
0.5	48.0	52.5	51.6	52.5
0.8	30.0	34.5	33.5	33.9
1.0	24.0	28.5	27.6	27.6
1.2	20.0	24.5	23.7	23.4
1.5	16.0	20.5	19.9	19.2
1.8	13.3	17.8	17.6	16.3
2.0	12.0	16.5	16.5	14.9

It is evident that the velocity field described by these equations yields $u_r = 0$ on the surface of the sphere and $u = U$ far away from the sphere. These velocity solutions can be used to determine the pressure field and the fluid stress tensor.

Integration of the normal and shear stresses on the surface of the fluid sphere yields the total hydrodynamic force exerted by the fluid on the viscous sphere as follows:

$$F_D = 2\pi a U \mu_c \frac{3\lambda + 2}{\lambda + 1}. \tag{1.96}$$

The corresponding drag coefficient for the viscous sphere in Stokes flow becomes

$$C_D = \frac{2F_D}{\pi \rho U^2 a^2} = \frac{8(3\lambda + 2)}{Re_r(\lambda + 1)}. \tag{1.97}$$

The last expression yields the so-called Stokes drag for a solid sphere $C_D = 24/Re_r$ and for an inviscid bubble $C_D = 16/Re_r$. The corresponding expressions for the drag force are $F_D = 6\pi a U \mu_c$ for the solid sphere and $F_D = 4\pi a U \mu_c$ for the inviscid bubble. The latter is sometimes referred to as the "form drag," while the difference of the two expressions, which is equal to $2\pi a U \mu_c$, is referred to as the "friction drag." The form drag or pressure drag is due to pressure distribution over the surface of the sphere, while the friction drag results from the viscous stress at the surface of the sphere. While several authors make this distinction between the two parts of the drag force, it must be noted that the drag force is a single entity that arises from the interactions between the fluid and the sphere and not two different forces.

Spheres settling or rising under gravity at Stokes flow conditions are subjected to the gravity and buoyancy force and the hydrodynamic/drag force. At steady flow, the two opposing forces are equal in magnitude and the spheres move at constant velocity. Depending on the actual application, this velocity is known as the "terminal, rising, or settling velocity" of the sphere. An expression for the terminal velocity of a viscous sphere in Stokesian flow is

$$V_t = \frac{2}{3} \frac{g a^2 (\rho_c - \rho_s)}{\mu_c} \frac{\lambda + 1}{3\lambda + 2}. \tag{1.98}$$

In some industrial applications, bubbles and drops do not follow the predictions of the Hadamard–Rybczynski analysis, because of the presence of impurities that act as surfactants in the fluid. The surfactants, in general, dampen the internal velocity field, thus increasing the effective viscosity of the internal fluid. In this case, the viscous sphere behaves as a solid sphere. When the bubble or drop is in motion, the surfactants are swept to the aft, leaving the forward surface relatively uncontaminated. This establishes a concentration gradient on the surface of the sphere, which results in a surface tension gradient and, subsequently, in a tangential stress that opposes the motion of the surface. The net result of this phenomenon is an increase in the total drag force, which is manifested in the retardation of the terminal velocity of the viscous sphere (Levitch, 1962). In practical cases of bubble and droplet flows, one must consider the drag given by Equation 1.96 as the lower limit of the hydrodynamic force, which is reached under conditions of exceptional carrier fluid purity. Similarly, the terminal velocity given by Equation 1.98 is the upper limit of the velocity that can be attained by a bubble or drop under Stokes flow (or creeping flow) conditions.

The work by Bond and Newton (1928) and similar more recent studies suggest that as long as the flow may be characterized as Stokes flow and $Re_r \ll 1$, the viscous spheres behave as solid spheres in the range $Eo < 4$. This Eötvos number is based on the density difference between the two fluids:

$$Eo = \frac{(\rho_c - \rho_s) g d^2}{\sigma}. \tag{1.99}$$

In the range $Eo > 4$, the spheres follow more closely the Hadamard–Rybczynski analysis and Equations 1.97 through 1.99. It must be noted that in the Stokes flow regime ($Re_r \ll 1$), all viscous spheres (bubbles and drops) remain spherical, regardless of the value of the Eötvos number (for more details see Section 1.4.3.8).

1.4.3.2 Reynolds Number Effects

1.4.3.2.1 Solid Spheres At finite Re_r, the fore-aft symmetry of the flow around the sphere, which is implied by the Stokes flow conditions, breaks down and the equations of the last section do not apply. Experimental observations have proven that, even at low Re_r, a wake is formed behind the sphere. This is a steady wake that becomes stronger as the Reynolds number increases and the inertia of the flow around the sphere overcomes the viscosity effects on the surface of the sphere. Experimental observations (Taneda, 1956, Achenbach, 1974, Seeley et al., 1975), as well as numerical computations, give sufficient evidence that the following flow descriptions or *regimes*, related to the presence and behavior of the wake, are observed around a sphere:

1. *Attached flow*: In the range $0 < Re_r < 20$, the flow is attached to the sphere and there is no visible recirculation behind it. There is a *velocity defect* region behind the sphere, which is the characteristic of a weak wake. The fore-aft asymmetry of the flow becomes progressively more pronounced as Re_r increases.
2. *Steady wake*: The onset of wake separation occurs at approximately $Re_r = 20$ and a very weak recirculating wake becomes visible. The wake is very small in volume and is attached to the aft of the sphere. As the Re_r increases, the wake becomes wider and longer and its point of attachment on the sphere moves forward. The wake is steady up to approximately $Re_r = 150$. With the steady wake, the separation angle is a monotonically decreasing function of Re_r, while the wake length and volume increase with Re_r. An approximate correlation for the length of the wake in this flow regime is

$$L_W = 2a\left[0.0203\left(Re_r - 20\right) + 0.00012\left(Re_r - 20\right)^2\right]. \tag{1.100}$$

3. *Unsteady wake regime in laminar flow*: The onset of the wake instability occurs in the range $130 < Re_r < 150$, where a weak, long-period, laminar oscillation appears at the tip of the wake and its amplitude increases with Re_r. Pockets of vorticity begin to shed from the tip of the sphere and influence the flow field downstream. The unsteady wake regime has been observed in experiments in the range $(130–150) < Re_r < 270$.
4. *High subcritical range*: This regime covers the range $270 < Re_r < 3 * 10^5$. As Re_r increases, vortices are shed regularly from alternate sides of the sphere. At the lower end of this regime, the Strouhal number, *Sl*, of the vortices is a monotonic function of Re_r and ranges from 0.1 at $Re_r = 400$ to approximately 2 at $Re_r = 6000$. The following relationship between the *Sl* and Re_r shows the best fit with the data in the range $400 < Re_r < 4000$:

$$Sl = 1.89 * 10^{-5} Re_r^{1.43}. \tag{1.101}$$

   In the range $4000 < Re_r < 6000$, there is too much scatter in the experimental data, with *Sl* appearing to level at the value 0.21. In the range $Re_r > 6000$, separation occurs at a point that rotates around the sphere with frequency equal to the shedding frequency. The result of the wake separation above $Re_r = 6000$ is the drastic reduction of *Sl* to 0.125. In the range $6000 < Re_r < 3 * 10^4$, *Sl* rises from 0.125 to 0.18, while in the range $3 * 10^4 < Re_r < 2 * 10^5$ *Sl* only rises to 0.19 (Achenbach, 1974). All the studies indicate that in this flow regime, the wake is periodic but not turbulent. The observations by Seeley et al. (1975) have shown that at values of Re_r above 1300 small jets and eddies appeared, signifying 3D rotation of the flow. The observations confirm that, in the subcritical range, the separation point moves forward and the angle where separation occurs is

$$\theta_S = 83 + 660 Re_r^{-0.5}. \tag{1.102}$$

5. *Supercritical flow*: The onset of the transition to a turbulent wake occurs at $Re_r = 2 * 10^5$, and the transition is completed at $Re_r = 3.7 * 10^5$. In this range, changes in the flow pattern occur that are referred to as "critical transition." At $Re_r > 3.7 * 10^5$, the separation begins to move downstream and fluctuations in the position of the separation point become evident. The free shear layer becomes turbulent and attaches to the surface of the sphere. The most evident result of the transition is a

sharp drop of the drag coefficient from approximately 0.44 to approximately 0.07. It must be noted that the transition to a turbulent boundary layer is sensitive to the intensity of the free-stream turbulence and it may be accelerated by "tripping" the flow with a thin wire, a devise that has often been used in experimental studies of turbulent boundary layers (Maxworthy, 1969). The effects of the free turbulence on the flow field and other transient effects are presented in Sections 1.4.3.3 and 1.4.3.6, respectively.

The first accurate determination of the hydrodynamic force on a sphere at finite Reynolds numbers is attributed to Oseen (1913). He used a simple perturbation method to calculate a first-order correction for the steady drag coefficient. His expression

$$C_D = \frac{24}{Re_r}\left(1+\frac{3}{16}Re_r\right) \tag{1.103}$$

is valid for finite but small values of Re_r. Maxworthy (1975) verified experimentally that the Oseen correction is accurate up to $Re_r = 0.45$. This range covers many practical applications in the chemical industry, where particles are very small and the fluids have high viscosity.

At finite values of Re_r, the nonlinear advection term in the governing momentum equation (1.87) or (1.88) is retained in the solution of the equations. This implies that the vorticity and vorticity gradients around the sphere are transported by the advection of the fluid as well as by the molecular diffusion processes. An analysis of the governing equations reveals that the diffusion part of the process is dominant in an inner region surrounding the sphere with radius aRe_r^{-1}, while the advection process is dominant at distances far from this region. At the overlap of the two regions, $r \sim aRe_r^{-1}$, the two processes, advection and diffusion, are of the same order of magnitude, and their effects must be calculated simultaneously. In this case, the characteristic time of the advection process is a/U, while that of the diffusion process is equal to a^2/ν_f. Because the characteristic times are of different orders of magnitude, an analytic solution for the problems of the transport of momentum and energy at finite Reynolds and Peclet numbers may be solved asymptotically, usually by a singular perturbation method.

Proudman and Pearson (1956) used an asymptotic method to calculate the velocity field around a solid sphere and around a cylinder at steady flow. This approximation enabled them to extend the Oseen result and to calculate the steady drag coefficient to $O(Re_r^2 \ln Re_r)$. Their expression for the drag coefficient is

$$C_D = \frac{24}{Re_r}\left[1+\frac{3}{16}Re_r+\frac{9}{160}Re_r^2\ln\left(\frac{Re_r}{2}\right)+O\left(Re_r^2\right)\right]. \tag{1.104}$$

Expressions such as this may be used with accuracy in applications of finite but small Re_r in the range from 0 to 1.5. At higher values of Re_r it is advisable to use one of the empirical or semiempirical expressions for the steady drag coefficient that abound in the literature. One of them is the Schiller and Nauman (1933) correlation, which is relatively simple and accurate:

$$C_D = \frac{24\left(1+0.15Re_r^{0.687}\right)}{Re_r}. \tag{1.105}$$

This expression is recommended in the range $1 < Re_r < 800$. The similar and simpler expression

$$C_D = \frac{24}{Re_r}\left(1+\frac{1}{6}Re_r^{2/3}\right) \tag{1.106}$$

is easier to integrate analytically and is also recommended in the same range $1 < Re_r < 800$.

Of interest to several engineering applications is the range $Re_r < 2$, and Table 1.1 gives the numerical values of the drag coefficients calculated by the Stokes equation, the Oseen equation (Equation 1.103), the Proudman and Pearson equation (1.104), and the Schiller and Nauman correlation (Equation 1.105).

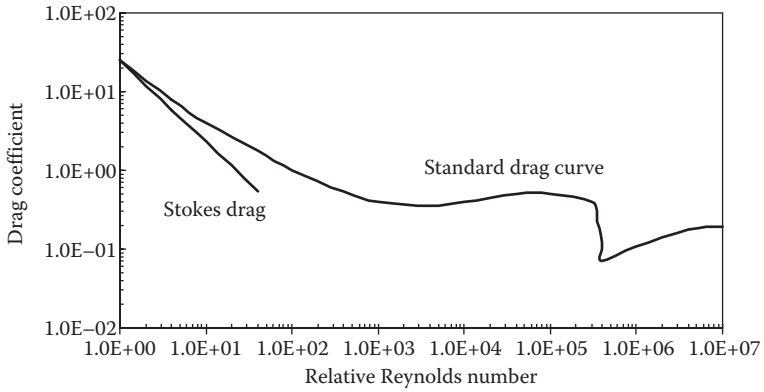

Figure 1.8

The standard drag coefficient curve for a solid sphere in steady flow.

It is observed in Table 1.1 that the Stokes drag agrees within 10% with the values of the other expressions up to $Re_r = 0.5$ and that the other three expressions agree within 10% up to $Re_r = 2$ despite the fact that the analytical equations were derived under the condition $Re_r < 1$.

The empirical equations give rise to the *standard, steady drag coefficient curve*, which is depicted in Figure 1.8 and extends to $Re_r = 10^7$. It is apparent in this figure that the steady drag coefficient of a sphere becomes constant and approximately equal to 0.44 in the range $10^3 < Re_r < 3 * 10^5$. In this range, the friction part of the drag force is insignificant and all the contribution comes from the form drag.

A key determinant of the magnitude of the drag coefficient is the type of the boundary layer that is formed outside the sphere and the separation point of the flow field behind the sphere. At $Re_r = 3 * 10^5$, this boundary layer becomes turbulent and the separation point of the flow moves downstream. The result is a sharp reduction of the form drag and hence a drastic reduction of the drag coefficient from 0.42 to 0.07, which is typical of laminar-to-turbulent transitions. At these high values of Re_r, the flow becomes inherently unsteady because vortices are shed regularly behind the sphere. In this case, as well as in all transient flows, the standard hydrodynamic drag on a sphere may be used (instead of the transient expressions that are presented in Section 1.4.3.6) only if the timescale of the sphere ($\tau_s = 4\alpha^2\rho_f/\mu_f$) is much smaller than the timescale of the transients in the carrier fluid, $\tau_s \ll \tau_f$. This condition implies that $St \ll 1$.

1.4.3.2.2 Viscous Spheres At higher Re_r, internal circulation creates a flow field inside the viscous spheres. This modifies the external flow field and hence the drag coefficient. Figure 1.9 (from Feng and Michaelides, 2001a) shows the streamlines (a) and vorticity (b) of these flow fields for $\lambda = 7$ and $Re_r = 10$, 100, and 500. At first, it is evident from the streamlines that there is a fore-aft asymmetry, which is also seen in the case of rigid spheres. Even though at $Re_r = 10$ the recirculation region behind the sphere has not been formed, there is an obvious velocity defect region. At $Re_r = 100$, there is a well-defined recirculation region, and at $Re_r = 500$, this region expands considerably and extends to a distance more than one diameter downstream. Second, at $Re_r = 500$, there are sharp gradients of vorticity in the outer field of the sphere, which indicate the formation of a boundary layer. This boundary layer is characteristic of flows with $Re_r > 400$, and its thickness is of the order of $Re_r^{-1/2}$. Third, there are two counterrotating vortices inside the sphere (sometimes referred to as "Hill's vortices") whose strength increases with Re_r. An internal recirculation region at the aft end of the sphere may also be formed at higher values of Re_r or at lower values of λ. The formation of the internal flow in viscous spheres modifies the whole velocity field and results in the lower drag on the spheres.

LeClair and Hamielec (1972), Rivkind et al. (1976), and Oliver and Chung (1987) used analytical and numerical studies to derive expressions for the drag coefficients of viscous spheres (bubbles and drops) at relatively low Re_r. Feng and Michaelides (2001a) used a two-layer concept for the computational grid and were able to perform more accurate computations that extend to higher values of Re_r, where the boundary layer is well formed on the outside of the viscous sphere. They used their computational results to derive simple engineering correlations for the drag coefficients in terms of the viscosity ratio up to $Re_r = 1000$. Figure 1.10 depicts these results for several values of the viscosity ratio, λ. The standard drag coefficient

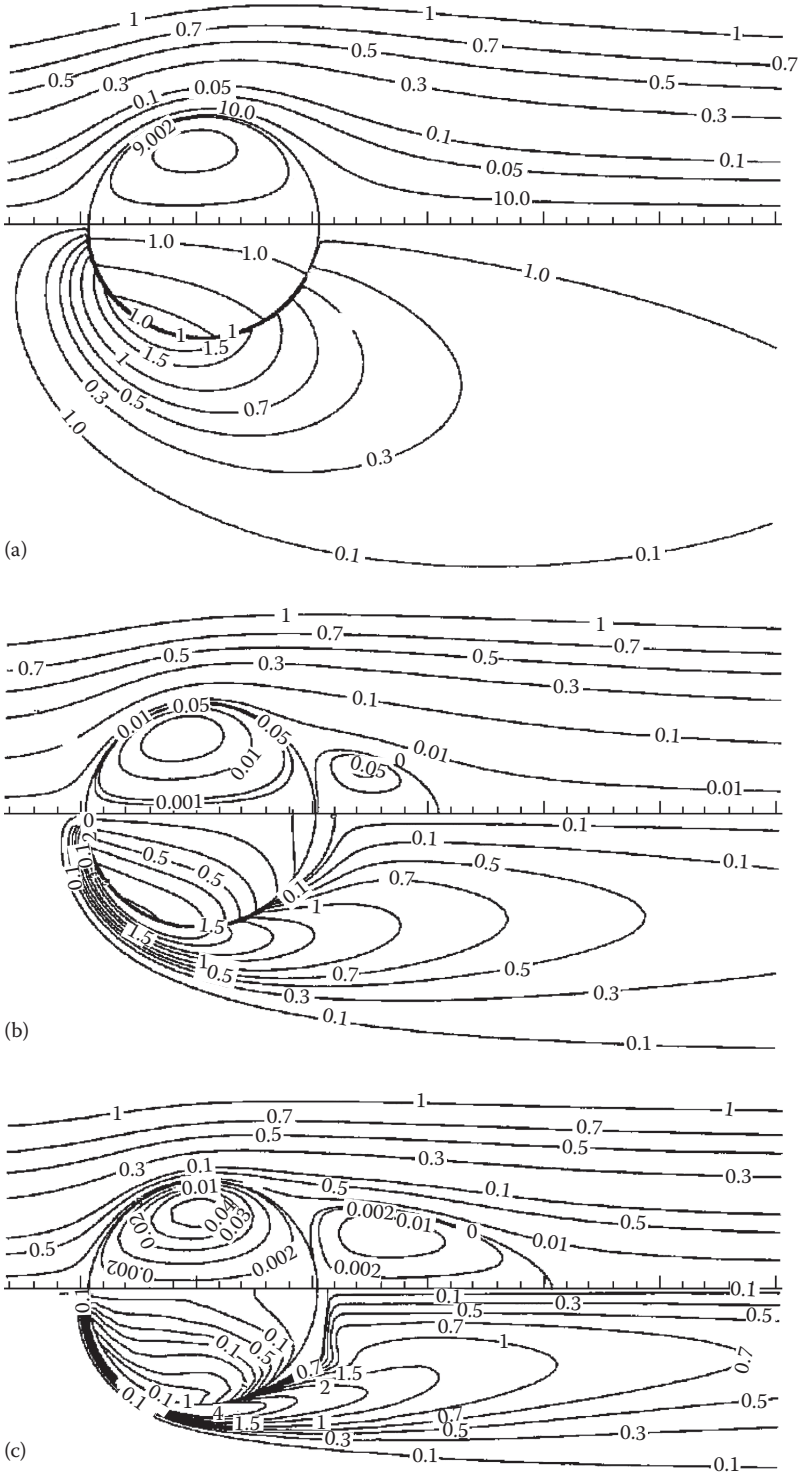

Figure 1.9

Streamlines and vorticity around a viscous sphere with viscosity ratio 7 at *Re* = 10 (a), 100 (b), and 500 (c).

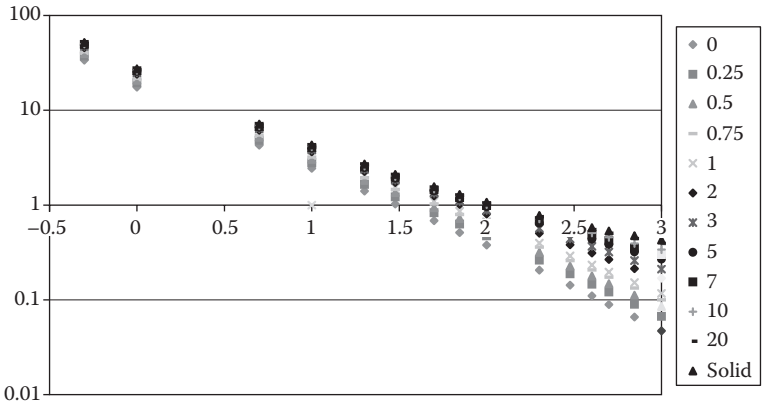

Figure 1.10

Drag coefficients for viscous spheres at different values of λ.

curve for solid spheres in this figure corresponds to the limit $\lambda \to \infty$. When expressed in terms of Re_r, the correlations derived by Feng and Michaelides (2001a) may be written as follows:

$$C_D\left(Re_r,\lambda\right)=\frac{2-\lambda}{2}C_D\left(Re_r,0\right)+\frac{4\lambda}{6+\lambda}C_D\left(Re_r,2\right) \quad \text{for } 0\le\lambda\le 2 \quad \text{and} \quad 5<Re_r\le 1000 \tag{1.107}$$

and

$$C_D\left(Re_r,\lambda\right)=\frac{4}{\lambda+2}C_D\left(Re_r,2\right)+\frac{\lambda-2}{\lambda+2}C_D\left(Re_r,\infty\right) \quad \text{for } 2\le\lambda\le\infty \quad \text{and} \quad 5<Re_r\le 1000 \tag{1.108}$$

The functions $C_D(Re_r, 0)$, $C_D(Re_r, 2)$, and $C_D(Re_r, \infty)$ are the drag coefficient for inviscid bubbles, for viscous drops with $\lambda = 2$, and for solid spheres, respectively. The following functions are recommended to be used with the two aforementioned correlations:

$$C_D\left(Re_r,0\right)=\frac{48}{Re_r}\left(1+\frac{2.21}{\sqrt{Re_r}}-\frac{2.14}{Re_r}\right), \tag{1.109}$$

$$C_D\left(Re_r,2\right)=17.0Re_r^{-2/3}, \tag{1.110}$$

and

$$C_D\left(Re_r,\infty\right)=\frac{24}{Re_r}\left(1+\frac{1}{6}Re_r^{2/3}\right). \tag{1.111}$$

In the lower range of Re_r, which is not covered by these equations, the following expression is recommended:

$$C_D=\frac{8}{Re_r}\frac{3\lambda+2}{\lambda+1}\left(1+0.05\frac{3\lambda+2}{\lambda+1}Re_r\right)-0.01\frac{3\lambda+2}{\lambda+1}Re_r\ln\left(Re_r\right) \quad 0\le Re_r\le 5. \tag{1.112}$$

The last expression has been derived from the results of the numerical computations in a way that it reduces asymptotically to the Hadamard–Rybczynski solution at $Re_r = 0$ and to the Oliver and Chung expression for very small Re_r.

The density ratio ρ_f/ρ_s does not influence significantly the drag coefficient of viscous spheres. Feng and Michaelides (2001a) observed that the variation of the density ratio by two orders of magnitude had an effect of less than 2% on the values of the drag coefficients. The maximum fractional difference of the correlations from the pertinent computational results is 4.6%, and the standard deviation of all the fractional differences is 2.1%. It must be noted that at the high range of Re_r the wake behind the spheres is unsteady and a transient expression for the total drag force should be used, if one is known. In such cases, the aforementioned expressions may be used for the steady part of the total hydrodynamic force.

It is well known that viscous spheres at higher Re_r become elongated. The drag coefficient of elongated viscous spheres is a function of the variables that appear in the aforementioned correlations as well as of the amount of deformation, which is characterized by the elongation or eccentricity. Correction functions must be used with these correlations, such as the ones presented in Sections 1.4.3.7 and 1.4.3.8. Experimental results by Winnikow and Chao (1966) and others on the free fall or rise of drops in liquids show that a liquid drop will remain spherical when the dimensionless Bond number, *Bo*, is less than or equal to 0.2, that is, when

$$Bo = \frac{We}{Fr} = \frac{gd^2\left|\rho_s - \rho_f\right|}{\sigma} \le 0.2. \tag{1.113}$$

Accordingly, water droplets in air will maintain their spherical shape at values of Re_r up to 470. In the case of substances with high surface tension (liquid metals), the corresponding Re_r is much larger (up to $Re_r = 1150$ for mercury droplets in air).

1.4.3.2.3 Effect of Interfacial Velocity Slip All the aforementioned results and expressions for the drag force and the drag coefficient pertain to applications where the no-slip boundary condition applies at the interface of the carrier fluid and the bubble, particle, or drop. It has been observed that when the size of the elements of the dispersed phase is very small, of the order of 1000 nm and lower, there is velocity slip at the interface that modifies significantly the drag coefficient. This modification of the drag is of immense interest in flows of nanoparticles and nanodroplets. Several authors, starting with Basset (1888b), derived expressions for the drag modification due to interfacial slip. Basset (1888b) stipulated that the shear stress on the sphere is proportional to the tangential slip: $\tau = \beta\Delta u_t$. The coefficient β is often referred to as the "slip parameter" and the dimensionless ratio $\mu_c/a\beta$ as the "slip ratio." Feng et al. (2012) derived a comprehensive correction to the steady drag force with slip, which applies to viscous as well as inviscid spheres:

$$\frac{F_D}{6\pi\alpha\mu_c U} = \frac{1}{3}\frac{2\beta\alpha + 3\lambda\beta\alpha + 6\lambda\mu_c}{\beta\alpha + \lambda\beta\alpha + 3\lambda\mu_c} + \frac{1}{24}\left(\frac{2\beta\alpha + 3\lambda\beta\alpha + 6\lambda\mu_c}{\beta\alpha + \lambda\beta\alpha + 3\lambda\mu_c}\right)^2 \frac{Re_r}{2} + \frac{1}{120}\left(\frac{2\beta\alpha + 3\lambda\beta\alpha + 6\lambda\mu_c}{\beta\alpha + \lambda\beta\alpha + 3\lambda\mu_c}\right)^3 \frac{Re_r^2}{4}\ln\left(\frac{Re_r}{2}\right) + O\left(Re_r^2\right). \tag{1.114}$$

For a solid sphere, $\lambda \to \infty$, the last equation yields

$$\frac{F_D}{6\pi\alpha\mu_c U} = \frac{\beta\alpha + 2\mu_c}{\beta\alpha + 3\mu_c} + \frac{3}{8}\left(\frac{\beta\alpha + 2\mu_c}{\beta\alpha + 3\mu_c}\right)^2 \frac{Re_r}{2} + \frac{9}{40}\left(\frac{\beta\alpha + 2\mu_c}{\beta\alpha + 3\mu_c}\right)^3 \frac{Re_r^2}{4}\ln\left(\frac{Re_r}{2}\right) + O\left(Re_r^2\right). \tag{1.115}$$

By using dimensionless slip ratio $S = \mu_c/a\beta$, this equation can be expressed as the drag coefficient of the solid sphere:

$$C_D = \left(\frac{1+2S}{1+3S}\right)\frac{24}{Re_r}\left(1 + \frac{3}{16}\left(\frac{1+2S}{1+3S}\right)Re_r + \frac{9}{160}\left(\frac{1+2S}{1+3S}\right)^2 Re_r^2 \ln\left(\frac{Re_r}{2}\right) + O\left(Re_r^2\right)\right). \tag{1.116}$$

The last equation reduces to the expression (Equation 1.104) derived by Proudman and Pierson (1956) when there is no slip at the interface ($S \to 0$).

Under rarefied conditions, interfacial slip may occur at higher values of the Re_r. Feng et al. (2012) performed extensive numerical simulations at higher Re_r and derived a correlation for the drag coefficient with slip flow, for S between 0 and ∞, at Reynolds number up to 150:

$$C_D = \frac{1+2S}{1+3S}\frac{24}{Re_r}\left(1+0.1509\sqrt{\frac{1+2S}{1+3S}}Re_r^{0.678} - 0.0254\frac{S}{1+3S}Re_r^{1.104}\right). \tag{1.117}$$

1.4.3.3 Effects of Flow Turbulence

Turbulence in the carrier fluid (free-stream turbulence) implies an unsteady flow field and unsteady motion of particles, bubbles, and drops. For this reason, the effects of the free-stream turbulence are transient flow effects. Numerous experiments on the drag for solid spheres proved that the free-stream turbulence modifies the drag coefficient of particles, sometimes significantly. Typical results of such experiments are reproduced in Figure 1.11 from Clift et al. (1978). It is observed in this figure that when the relative Reynolds number is in the range $10 < Re_r < 500$, the drag coefficient of solid spheres in a turbulent flow is almost always higher than the values of the standard curve. The influence of the free-stream turbulence on the boundary layer around the sphere and the wake behind the sphere is manifested by the sharp changes observed at approximately $Re_r = 50$ and the leveling of the drag coefficient curves at values that are 2–4 times higher than the corresponding values of the standard drag curve. In the range $500 < Re_r < 20{,}000$, the drag coefficient of a sphere is first reduced dramatically in a short range of Reynolds numbers, often reaching a value 50% lower than the value of the standard curve (Clamen and Gauvin, 1969). Then, C_D increases gradually and may reach a maximum, which is two to five times higher than the values predicted by the standard curve. Thereafter, C_D decreases to the values of the standard curve. The sudden dip of the drag coefficients is often attributed to the formation of a turbulent boundary on the surface of the particle. Apparently, the transition, which in the standard drag curve occurs at $Re_r = 3 * 10^5$, is accelerated and occurs earlier when the free stream is turbulent. Clift and Gauvin (1970) introduced the critical Reynolds number for the gaseous boundary layer. This is the relative Reynolds number at which the turbulent transition happens and is given by the following expressions:

$$\begin{aligned} Re_{cr} &= 10^{5.477-15.8I_r} \quad \text{for } I_r \le 0.15 \\ Re_{cr} &= 10^{3.371-1.75I_r} \quad \text{for } I_r > 0.15 \end{aligned}, \tag{1.118}$$

where I_r is the turbulence intensity based on the relative velocity of the sphere. As with all the correlations that involve exponential expressions, the results of the two aforementioned equations must be strictly used within the range of the experimental conditions (Re_r and I_r) for which they were derived.

It must be noted that the experimental uncertainty associated with the results of Figure 1.11 and Equation 1.118 is significant and that there is a considerable discrepancy with the data emanating from the different experimental studies. Part of this uncertainty is inherent in the measurements of unsteady turbulent flows.

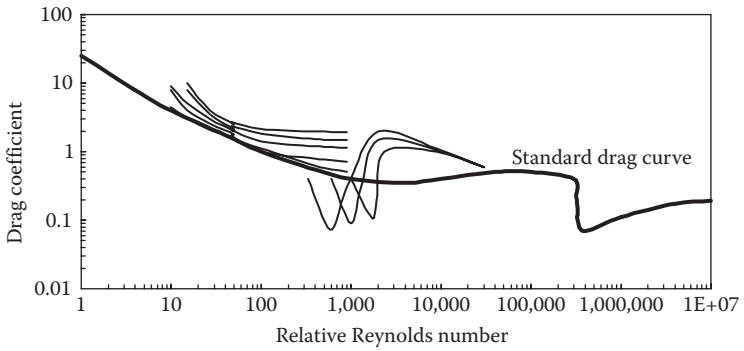

Figure 1.11

The effect of the free-stream turbulence on the standard drag coefficient for a solid sphere.

Another part of the uncertainty stems from the fact that the response of particles in a turbulent flow has been implicitly treated as steady and not as transient process, while it is evident that the response of particles to the turbulent eddies depends strongly on the frequency of the eddies and that the particle movement is transient.

The presence of particles, bubbles, and drops in turbulent flows also has an effect on the intensity and characteristics of the carrier fluid turbulence. This was observed in many relatively recent experimental studies and is called "modulation" or "modification" of the turbulence, regardless of any transition in the boundary layer of the particles. A great deal of work was devoted in the last 30 years on this subject, which is treated extensively in Chapter 12.

1.4.3.4 Blowing Effects

The mass transfer from the surface of a sublimating particle or an evaporating droplet causes an outward radial flow and hence a drastic change in the gaseous boundary layer around the sphere. This flow modification reduces the drag coefficient from the steady value as it is given by the standard curve. The exchange of mass from the particle or droplet to the surrounding fluid causes two significant effects:

1. The change in the viscosity of the surrounding fluid, because of temperature and composition changes
2. A regression of the surface of the droplet, which is associated with the flow of the vapor from the surface to the carrier fluid (Stefan convection)

Yuen and Chen (1976) conducted experiments on the drag force of evaporating drops and on the effect of the change of the transport properties of the carrier fluid as a result of the transfer of mass from the surface of the droplet. They concluded that their results are well represented when a reference viscosity for the carrier fluid is used, the *film viscosity*, which is defined as follows:

$$\mu_m = \mu_s + \frac{1}{3}(\mu_\infty - \mu_s), \tag{1.119}$$

where

μ_∞ is the viscosity of the fluid far from the sphere
μ_s is the gas viscosity on the surface of the sphere

This equation is sometimes referred to as the 1/3 *rule* for the film properties. The experimental data and analysis on the density and viscosity averages by Lerner et al. (1980) confirmed this relationship. The data also suggested that the standard drag curve with the aforementioned correction for the viscosity may be applied to slightly ellipsoidal drops if the equivalent diameter of the ellipsoid, d_V, is used and the two axes of the ellipsoid are within 10% of each other.

Eisenklam et al. (1967) and later Renksizbulut and Yuen (1983) examined the effects of the radial flow and Stefan convection process away from the surface of an evaporating droplet. They recommend that the following correction for the effect of the Stefan convection on the drag coefficient be used in calculations:

$$C_D = \frac{C_{D,0}}{1 + B_M}, \tag{1.120}$$

where $C_{D,0}$ is the value of the drag coefficient in the absence of mass transfer, which is calculated from the correlations presented in Section 1.4.3.2.

The coefficient B_M is the *blowing coefficient* and is based on the mass transfer from the surface of the sphere.

It is defined in terms of the mass fractions of the vapor on the surface and far away from the sphere:

$$B_M = \frac{Y_s - Y_\infty}{1 - Y_s}. \tag{1.121}$$

Chiang et al. (1992) conducted a numerical study of evaporating droplets with variable transport properties and derived a correlation for their drag coefficients, which is valid in the range $30 < Re_r < 200$:

$$C_D = \frac{24.432}{\left(1+B_H\right)^{0.27}\left(Re_m/2\right)^{0.721}}. \tag{1.122}$$

The relative Reynolds number in this case, Re_m, is defined in terms of the gas-film viscosity (Equation 1.119) and the free-stream gas density, $\rho_{f\infty}$. In the last equation, B_H is another blowing coefficient, which is based on the thermodynamic enthalpy of the evaporating fluid:

$$B_H = \frac{h_\infty - h_s}{h_{fg}^{eff}}. \tag{1.123}$$

The effective latent heat of vaporization, in the denominator of the last expression, is the sum of the latent heat of the vapor at the drop surface and the sensible heat conducted to the interior of the drop.

When the radial velocity of blowing, V_n, is known or may be calculated from mass flow rate data, Clift and Lever (1985) used a numerical analysis and derived the following relationship for the drag coefficient:

$$C_D = \frac{24}{Re_r}\frac{1+0.545Re_r+0.1Re_r^{0.5}\left(1-0.03Re_r\right)}{1+ARe_n^B}, \tag{1.124}$$

where Re_n is the blowing Reynolds number based on the radial (normal to the surface) velocity, $Re_n = \rho d V_n/\mu$, and the functions A and B are correlated to Re_r:

$$A = 0.09 + 0.077\exp\left(-0.4Re_r\right) \quad \text{and} \quad B = 0.4 + 0.77\exp\left(-0.04Re_r\right). \tag{1.125}$$

The last two expressions are valid in the ranges $10 < Re_r < 200$ and $1 < Re_n < 20$. At lower values of the Reynolds numbers, $Re_r < 10$ and $Re_n < 1$, the following modification in the function $A(Re_r)$ has been recommended:

$$A = 0.06 + 0.077\exp(-0.4Re_r). \tag{1.126}$$

These correlations and the pertinent studies suggest that the drag coefficient of burning and evaporating droplets departs only slightly from the corresponding values without mass transfer. The blowing effects may be perceived as corrections to the standard drag curve for spheres, caused by the different composition of the gaseous boundary layer and by mass convection from the sphere.

1.4.3.5 Compressibility and Rarefaction Effects

When the carrier gas is rarefied, for example, under conditions that are prevalent in the upper atmosphere, the length of the molecular free path, L_m, is comparable or even greater than the size of the particles or drops. Therefore, the medium surrounding the particle/drop may not be considered to be a continuum, and hence, the hydrodynamic force is not the same as in the case of continuum flows. The Knudsen number,

$$Kn = \frac{L_m}{d}, \tag{1.127}$$

is a dimensionless measure of the relative magnitude of the two length scales. Continuum flows imply that $Kn \ll 1$. Since the molecular free path of a gas is proportional to the ratio of the viscosity divided by the

product of the speed of sound and the gas density ($L_m \sim \mu/c\rho$), it follows that Kn is proportional to the ratio of the Mach number and the Reynolds number ($Kn \sim M/Re$). Schaaf and Chambre (1958) identified four flow regimes to characterize rarefaction flows, and Crowe et al. (1969) showed that, in the case of rocket nozzles, a burning particle or droplet is subjected to all four flow regimes:

1. The *free molecule flow*, where there are no interactions among the molecules and individual molecules collide with the particles exchanging momentum ($Kn > 10$ and $M > 3Re_r$). In this regime, the drag coefficient of a sphere is equal to 2, regardless of the value of the Reynolds number.
2. The *transitional flow*, where the size of the particles is comparable to the size of the mean free path. Since molecules interact by collisions, the collisions between the particles and the molecules create a distinct flow field around the particles. The effect of this flow field and the collisions is manifested on the force exerted by the gas on the particles ($0.25 < Kn < 10$, $0.1\, Re_r^{1/2} < M < 3Re_r$).
3. In the *slip flow* regime, there is a distinct flow field around the particles. The temperature and velocity at the surface of the particle are different from the temperature and velocity on the side of the gas close to the surface ($0.001 < Kn < 0.25$ and $0.01\, Re_r^{1/2} < M < 0.1\, Re_r^{1/2}$). This gives rise to a velocity difference (slip) between the gas and particle velocities at the particle surface. When $Kn < 0.01$, the flow field around the particles may be obtained from the solution of the Navier–Stokes equations with the stipulation of a suitable closure equation for the slip. Equations 1.114 and 1.115 were obtained using the stipulation for the slip velocity $\tau = \beta \Delta u_t$.
4. The *continuum flow* is characterized by the absence of velocity slip on the surface of the particles ($Kn < 0.01$, $M < 0.1\, Re_r^{1/2}$). The no-slip boundary condition applies to the surface of the particles, and the flow field is obtained by the analytical or numerical solution of the Navier–Stokes equations.

It is intuitive that an evaporating droplet or a sublimating particle will pass sequentially through all these flow regimes, starting in continuum flow and ending in the free molecular flow regime. However, under ambient conditions, when $Kn > 0.001$, there is very small mass remaining in the particle or droplet. Under these conditions and typical rates of evaporation, sublimation, and burning, the process passes rapidly through the first three regimes. When treating these processes by a numerical scheme, one has to be cognizant of this fact and to use the timescales and time steps that are appropriate to the processes.

At high Reynolds numbers, the effects of the Mach number on the drag coefficient become significant when $M > 0.6$. This is sometimes called the critical Mach number, and the flow around the particle is characterized by the formation of a shock wave, which increases significantly the form drag of the particle. Hence, the drag coefficient, which does not vary with the Mach number in the range $0 < M < 0.6$, increases rapidly beyond $M = 0.6$; reaches a maximum, which depends on the value of Re but is always greater than 2; and, thereafter, decreases gradually and approaches asymptotically the theoretically predicted value of 2 for free molecular flows (Schaaf and Chambre, 1958). At low Reynolds numbers, an increased Mach number signifies that the flow is rarefied. In this case, there is a shock wave associated with the presence of the particle and the drag coefficient decreases monotonically with M.

In general, the effect of the Knudsen number and the Mach number on the drag coefficient is given by correction factors $f(M)$ and $f(Kn)$. The classic experiment by Millikan (1923) yields the following correction factor for drops in rarefied flows, which is valid in the Stokesian flow regime:

$$f\left(Kn\right) = \frac{24C_D}{Re_r} = \left[1 + Kn\left[1.209 + 0.406\exp\left(-\frac{0.447}{Kn}\right)\right]\right]^{-1}. \tag{1.128}$$

The coefficients in the last equation appear with the corrections made for the more accurate knowledge of the molecular free path for air by Kim et al. (2005). The latter suggests that the three coefficients in the square bracket be 1.165, 0.483, and 0.449, respectively. An assessment of several studies on the subject reveals that these coefficients are approximately 1.15, 0.5, and 0.5 (Michaelides, 2014).

An equation for the drag coefficient, proposed by Crowe et al. (1973) and later simplified by Hermsen (1979), has been applied successfully to burning particles in solid propellant rocket nozzles:

$$C_D = 2 + \left(C_{D,0} - 2\right)\exp\left[-\frac{3.07\sqrt{k}\,g\left(Re_r\right)M}{Re_r}\right] + \frac{h\left(M\right)}{M\sqrt{k}}\exp\left(-\frac{Re_r}{2M}\right), \tag{1.129}$$

where

k is the ratio of the specific heats of the gas

$g(Re)$ and $h(M)$ are the empirical functions

$$g\left(Re\right) = \frac{1 + Re_r\left(12.278 + 0.548Re_r\right)}{1 + 11.278Re_r} \quad \text{and} \quad h\left(M\right) = \frac{5.6}{1+M} + 1.7\sqrt{\frac{T_p}{T_c}}. \tag{1.130}$$

In the last expressions

T_c is the mean temperature of the carrier gas far from the particle

T_p is the temperature of the particle

Alternatively, Carlson and Hoglund (1964) derived the following empirical relationship for the function $f(M)$, which is used in some computations pertaining to particles in shock waves and other compressible flow fields:

$$f\left(M\right) = \frac{1 + \exp\left(-\dfrac{0.427}{M^{4.63}} - \dfrac{3}{Re_r^{0.88}}\right)}{1 + \dfrac{M}{Re_r}\left[3.82 + 1.28\exp\left(-1.25\dfrac{Re_r}{M}\right)\right]}. \tag{1.131}$$

It must be noted that the last three equations are correlations of experimental data and must be used within the range of the independent variables for which the original data have been derived.

1.4.3.6 Transient Flow Effects

Most of the practical applications of dispersed multiphase flows involve time-dependent flows. When the characteristic time of the flow transients is of the same order of magnitude as the response time of bubbles, drops, or particles, a transient equation should be used for the exchange of momentum between the carrier fluid and the dispersed phase. Exact analytical expressions for transient flows have been derived for creeping flow (Stokes flow) conditions ($Re \ll 1$), and asymptotic expressions have been derived for finite but small Reynolds numbers ($Re_r < 1$). Semiempirical expressions, which emanate from a combination of experimental data and analyses, have also been developed and frequently used at high Re_r.

1.4.3.6.1 Creeping Flow ($Re \ll 1$) The so-called Boussinesq–Basset equation,

$$F_i(t) = -6\pi\alpha\mu_c(v_i - u_i) - \frac{1}{2}m_c\frac{d}{dt}(v_i - u_i) - 6\alpha^2\sqrt{\pi\mu_c\rho_c}\int_0^t \frac{d/d\tau(v_i - u_i)}{\sqrt{t-\tau}}d\tau, \tag{1.132}$$

which was independently derived by Boussinesq (1885) and Basset (1888a), is the first equation for the transient hydrodynamic force acting on a solid sphere. The expression applies to creeping flow conditions ($Re \ll 1$), where the inertia terms in the momentum equation of the fluid may be neglected in

comparison to the viscous effects. Maxey and Riley (1983) performed a more detailed analysis for a rigid sphere in an arbitrary nonuniform flow field, whose velocity is given by the functional relationship $u_i(x_i, t)$. The latter is not an arbitrary function, since it must be a solution of the Navier–Stokes equations. Maxey and Riley (1983) obtained the following expression for the equation of motion of a sphere:

$$m_s\frac{dv_i}{dt} = -\frac{1}{2}m_c\frac{d}{dt}\left(v_i - u_i - \frac{a^2}{10}u_{i,jj}\right) - 6\pi a\mu_c\left(v_i - u_i - \frac{a^2}{6}u_{i,jj}\right)$$
$$-\frac{6\pi a^2\mu_c}{\sqrt{\pi\nu_f}}\int_0^t \frac{d/d\tau\left(v_i - u_i - \frac{a^2}{6}u_{i,jj}\right)}{\sqrt{t-\tau}}d\tau + (m_s - m_c)g_i + m_c\frac{Du_i}{Dt}. \tag{1.133}$$

In the last equation

m_s is the mass of the sphere

m_c is the mass of the carrier fluid that occupies the same volume as that of the sphere

The repeated index with comma ($,jj$) denotes the Laplacian operator and the derivative D/Dt is the total Lagrangian derivative following the center of the sphere

All the spatial derivatives are evaluated at the center of the sphere. The left-hand side in this equation represents the acceleration of the sphere. Of the terms on the right-hand side, the first is the steady drag, the second is the added mass (or virtual mass) of the fluid, and third term is the history term. The remaining terms on the right-hand side are the net gravitational or body force and the Lagrangian acceleration term of the fluid. The Laplacian terms in all the parentheses account for the nonuniformity of the fluid velocity field. They are second-order corrections for the curvature of the flow field and are called sometimes the "Faxen terms." These derivatives become zero when the fluid velocity field is uniform. The Faxen terms scale as a^2/L^2, where L is the macroscopic characteristic length of the fluid velocity field, and in most applications of dispersed multiphase flows, where $a/L \ll 1$, they are small enough to be neglected.

It must be noted that the derivation of the last equation is based on the following assumptions:

- Spherical shape
- Infinite fluid domain initially undisturbed
- No rotation
- Rigid sphere ($\mu_f/\mu_s \ll 1$)
- Zero initial relative velocity
- Negligible inertia effects ($Re_r \ll 1$)

If the initial relative velocity is different than zero, the following expression/correction replaces the history term (Michaelides, 2003, 2006):

$$\frac{6\pi a^2\mu_c}{\sqrt{\pi\nu_c}}\int_0^t \frac{d/d\tau\left[v_i - u_i - \frac{a^2}{6}u_{i,jj}\right]}{\sqrt{t-\tau}}d\tau + \frac{6\pi a^2\mu_c[v_i(0) - u_i(0)]}{\sqrt{\pi\nu_c t}}, \tag{1.134}$$

where the quantity $v_i(0) - u_i(0)$ represents the initial relative velocity at time $t = 0$.

Integrodifferential equations, such as (1.133), do not have an explicit analytical solution for the dependent variable (v_i). Since they are implicit in their dependent variable, they must be solved numerically by an iteration method and this requires a great deal of computational resources in both memory and CPU time with repetitive calculations, such as the Lagrangian computations of a large group of particle trajectories. Michaelides (1992) and later Vojir and Michaelides (1994) devised an analytical method to convert such first-order implicit integrodifferential equations to second-order integrodifferential equations, which are explicit in the dependent variables v_i (or T_s in the case of temperature).

For viscous spheres (drops and bubbles) in a carrier fluid, there are two timescales for the motion of the fluid inside the sphere and the motion of the external fluid. For this reason, an analytical expression for the equation of motion, similar to Equation 1.133, is impossible to be derived in the time domain. Galindo and Gerbeth (1993) derived an expression for the hydrodynamic force on a viscous sphere under creeping flow conditions in the Laplace domain, which is as follows:

$$\overline{F_i} = -6\pi a \mu_c \left[\overline{v_i} - \overline{u_i}\right] \left\{ \frac{\chi_c^2}{9} + (\chi_c + 1) - \frac{(\chi_c + 1)^2 f(\chi_s)}{[\chi_s^3 - \chi_s^2 \tanh(\chi_s) - 2f(\chi_s)]\lambda + (\chi_c + 3) f(\chi_s)} \right\}. \tag{1.135}$$

The overbar in the last expression denotes functions in the Laplace domain; χ represents the two dimensionless timescales, also in the Laplace domain,

$$\chi_c = \sqrt{\frac{s\alpha^2}{\nu_f}} \quad \text{and} \quad \chi_s = \sqrt{\frac{s\alpha^2}{\nu_s}} \tag{1.136}$$

and the function $f(\chi)$ is defined as follows:

$$f(\chi) = (\chi^2 + 3)\tanh(\chi) - 3\chi. \tag{1.137}$$

Transient flow with tangential slip at the interface occurs with nanoparticles, submicron-sized drops, and colloidal particles, as well as larger drops and particles in rarefied gases. Michaelides and Feng (1995) performed a study that included the effect of the viscosity ratio, λ, and also allowed for the existence of a finite tangential velocity slip at the interface. The analysis proved that an expression for the complete hydrodynamic force may only be obtained Laplace domain:

$$\begin{aligned} \overline{F^i} = &-6\pi a \mu_c \left[\overline{v_i}(s) - \overline{u_i}(\vec{Y}(t), s)\right] \\ &\times \left\{ \frac{\chi_c^2}{9} + \chi_c + 1 - \frac{(\chi_c + 1)^2 < [\chi_s^3 - \chi_s^2 \tanh(\chi_s) - 2f(\chi_s)]\lambda(\mu/\alpha\beta) + f(\chi_s) >}{[1 + (\mu/\alpha\beta)(\chi_c + 3)][\chi_s^3 - \chi_s^2 \tanh(\chi_s) - 2f(\chi_s)]\lambda + (\chi_c + 3) f(\chi_s)} \right\}, \end{aligned} \tag{1.138}$$

where the variables χ_c and χ_s are the same as in expression (1.134) and β is the same slip parameter that was defined earlier in Equation 1.114 for the steady drag coefficients.

When there is no slip on the surface of the sphere, that is, $\beta \to \infty$, Equation 1.136 reduces to the Galindo and Gerbeth equation (1.133). Remarkably, the case of a sphere with perfect slip, $\beta = 0$, and the case of an inviscid sphere, $\lambda = 0$, are equivalent and result in the same equation of motion. This equation was first derived for an inviscid bubble by Morrison and Stewart (1976) in an implicit integrodifferential form. Therefore, if extremely small particles and drops in the last stages of vaporization/combustion are to be modeled by a continuum approach with finite velocity slip at their interface, then the values of their drag coefficients would be between the theoretical values for the drag coefficients of bubbles and the drag coefficients of rigid particles.

Parmar et al. (2011) examined the effects of fluid compressibility on the transient motion of a solid sphere in a compressible flow. They performed an analytical study at $Re_r \ll 1$ and expressed the effects of the fluid compressibility by a correction function, which depends on Kn and the ratio of the bulk to the dynamic viscosities. In a companion study, Ling et al. (2011a,b) determined the effects of the unsteady terms on the dispersion of small particles in shock waves. The results of the two studies show that the transient term contributions to the hydrodynamic force and heat transfer coefficients of the particles are significant. At the early stages of the blast wave, when particles are traveling in the expansion fan, the gas density surrounding the particles is larger. This makes the transient components of the hydrodynamic force and the rate of heat transfer to be of the same order of magnitude as the steady terms. Consequently, the error from neglecting the transient terms in such applications may become significant.

1.4.3.6.2 Finite but Small Reynolds Numbers Sano (1981) used an asymptotic analysis to derive an expression for the transient hydrodynamic force acting on a rigid sphere at small but finite values of Re_r, when the sphere undergoes a step change in its velocity, from 0 to v_i:

$$F_i(t) = 3\pi d\mu_f v_i \left\{ H(t^\star) + \frac{1}{3}\delta(t^\star) + \frac{1}{2\sqrt{\pi t^\star}} + \frac{3}{16}Re_r \left[\left(1 + \frac{16}{Re_r^4 t^{\star 2}} \right) \operatorname{erf}\left(0.5 Re_r t^{\star 1/2} \right) \right.\right.$$
$$\left.\left. + \frac{2}{(\pi t^\star)^{1/2} Re_r} \left(1 - \frac{2}{Re_r^2 t^\star} \right) \exp\left(-\frac{1}{4} Re_r^2 t^\star \right) - \frac{8}{3(\pi t^\star)^{1/2} Re_r} \right] + \frac{9}{160} Re_r^2 \ln\left(\frac{1}{2} Re_r \right) \right\} + O\left(Re_r^2 \right). \quad (1.139)$$

The time variable in this equation is made dimensionless by dividing with a characteristic time based on the properties of the viscous fluid, $\tau_f = a^2\rho_f/\mu_f$. The expression in the square brackets results from the contribution of the outer velocity field and is a consequence of the advective terms in the Oseen equations. For this reason, it has been referred to as the "Oseen contribution." It appears that the most important effect of the higher Re_r on the hydrodynamic force is on the history term. The last term of the Oseen contribution cancels the third term in the right-hand side, $(\pi t)^{-1/2}$. The remaining transient history terms decay exponentially. This rate of decay is faster than the decay of the transient terms of the creeping flow equation. From the physical point of view, this occurs because the finite velocity difference allows for the faster advection and evolution of the vorticity field around the sphere. While in the creeping flow case the vorticity field around the sphere was transported by viscous diffusion alone, which is a slower molecular process, in the case of advection, the finite velocity "carries" the vorticity field far from the sphere with the characteristic velocity of advection. With the faster decay of the transient terms, a spherical particle does not retain any "memory" of its initial velocity, which is characteristic of the $t^{-1/2}$ rate of decay.

Mei et al. (1991) conducted such a numerical study on the motion of a rigid spherical particle in the range $0 < Re_r < 50$ when the free-stream velocity fluctuates with a small amplitude. The results of this study show that, in the low-frequency limit, the history term of the hydrodynamic force decays faster than the conventional $t^{-1/2}$ rate. Subsequently, Mei and Adrian (1992) obtained an analytical solution for the motion of a solid sphere, which is valid at very low frequencies ($Sl \ll Re_r < 1$). Their results revealed a different history term for the hydrodynamic force acting on the particle, which may be written as follows:

$$\int_0^t \frac{(dv_i/d\tau) - (du_i/d\tau)}{\left[\left(\frac{\pi\nu_c}{a^2}(t-\tau) \right)^{1/4} + \left(\frac{\pi}{2a\nu_c} \left(\frac{|u_i(\tau)|}{f_H} \right)^3 (t-\tau)^2 \right)^{1/2} \right]^2} d\tau, \quad (1.140)$$

where f_H is a function, which has been correlated from the numerical data

$$f_H = 0.75 + 0.105 Re_r. \quad (1.141)$$

It is evident that, at short times, this history term matches the asymptotic behavior of the typical history term at creeping flow, $t^{-1/2}$, while at long times the term decays asymptotically as t^{-2}. With this functional form of long-term decay, the sphere does not retain any memory of its initial velocity. Lovalenti and Brady (1993) confirmed this in a more general study on the transient flow of particles.

1.4.3.6.3 High Reynolds Numbers: The Semiempirical Equations While all the known analytical expressions for the transient hydrodynamic force on particles, bubbles, or drops apply to low Re_r, many engineering applications occur at higher ranges of this parameter: slurry transport and practical pneumatic conveying systems operate in the range $10^1 < Re_r < 10^3$; drops in combustion processes may reach Re_r up to 10^3; bubble columns in chemical processes operate in a range of Re_r from 0 to 10^3, depending on the properties of the

carrier fluid; and particulate flows in the environment may reach relative, Re_r, up to 10^4. Since there is no applicable theory, other than some asymptotic studies that only lead to approximate analytical expressions for the hydrodynamic force at $Re_r > 1$, experimental data and empirical correlations have been used for the calculation of the steady as well as for the transient hydrodynamic force and the corresponding drag coefficient.

The steady flow empirical relations for the drag coefficients of a solid or a viscous sphere have been presented in Section 1.4.3.2 and are summarized in the standard drag curve of Figure 1.8. Following the practice used for the steady term, Odar and Hamilton (1964) proposed modifications and correlation functions that extend to the transient terms of the hydrodynamic force. They essentially treated the three terms of the Boussinesq–Basset expression as separate forces and associated each one of them with a correction factor or function that accounts for the higher Re_r. Their equation is

$$F_i = C_1 6\pi a \mu_f (v_i - u_i) + \Delta_A \frac{1}{2} m_f \frac{d(v_i - u_i)}{dt} + \Delta_H a^2 \sqrt{\pi \rho_f \mu_f} \int_0^t \frac{\dfrac{d(v_i - u_i)}{d\tau}}{\sqrt{t - \tau}} d\tau, \tag{1.142}$$

where the functions C_1, Δ_A, and Δ_H are the empirical functions determined by experiments. Odar and Hamilton used the Schiller and Nauman (1933) correlation for the coefficient C_1 (Equation 1.104) and reduced their experimental data to derive the following expressions for the added mass and history term coefficients:

$$\Delta_A = 1.05 - \frac{0.066}{0.12 + Ac^2} \quad \text{and} \quad \Delta_H = 2.88 + \frac{3.12}{(1 + Ac)^3}, \tag{1.143}$$

where Ac is the dimensionless acceleration number

$$Ac = \frac{|u_i - v_i|^2}{2a\left|\dfrac{dv_i}{dt}\right|}. \tag{1.144}$$

Bataille et al. (1990) measured independently the added mass coefficient for bubbles and concluded that, within the experimental error of the measurements, the added mass coefficient Δ_A is consistently equal to 1 up to $Re_r = 1000$, even when some of the bubbles are not exactly spherical. Also Auton et al. (1988) and Mei et al. (1991) confirmed analytically that the potential flow solution, which yields the value $\Delta_A = 1$ for the added mass coefficient, is correct and that neither the Reynolds number nor the acceleration number has a significant impact on this term. Based on these analytical and experimental observations, Michaelides and Roig (2011) reinterpreted and recorrelated the original data by Odar and Hamilton (1964) and determined that for $\Delta_A = 1$, the correct expression for the history coefficient is

$$\Delta_{HNEW} = 6.00 - 3.16\left[1 - \exp\left(-0.14 Re_r Sl^{0.82}\right)^{2.5}\right]. \tag{1.145}$$

A more thorough discussion on the use of the semiempirical expressions as well as the results of several other analytical, computational, and experimental studies is that by Michaelides (2003, 2006).

1.4.3.7 Deformable and Irregular Particles

Simple experiments based on sedimentation have shown that the drag coefficients for nonspherical particles are significantly different from those of spheres. Shape factors have been proposed for the quantification of the effect of nonsphericity of particles, bubbles, and drops. Wadell (1933) suggested that the volume-equivalent diameter of a sphere, d_V, or the area-equivalent diameter be used as the characteristic length of

the particles for the determination of the drag coefficient. These two diameters may be given in terms of the volume and the projected area of the irregular particle as follows:

$$d_V = \sqrt[3]{6V/\pi} \quad \text{and} \quad d_p = \sqrt{4A_p/\pi} \tag{1.146}$$

where

V is the total volume of the particle

A_p is the projected area of the particle in the direction of the flow

For the determination of d_p, one must have information on the orientation of the particle during the flow. Wadell (1933) suggested that a shape factor, Ψ, may be defined as a dimensionless measure of the irregularity of the particle:

$$\Psi = \frac{d_V^2}{d_p^2} = \frac{\pi^{1/3}(6V)^{2/3}}{A_p}. \tag{1.147}$$

Since the drag coefficient is defined in terms of the projected area of the particle, the shape factor may be used to correct for the irregular shape of particles according to the following expression:

$$\Psi C_D A = (C_D A)_s. \tag{1.148}$$

The quantity in the parenthesis in the last expression pertains to the characteristics of a sphere, defined in terms of the volume-equivalent diameter, d_V.

While Equation 1.148 may be used as a first approximation for a correction to the steady drag coefficient for particles that are nearly spherical, several other researchers (Haider and Levenspiel, 1989, Hartman and Yates, 1993) determined that when particles are very elongated and the correction factors are very large, this equation introduces significant errors in the determination of the drag coefficient. For this reason, another quantity, the circularity, which is also called surface sphericity, c, was introduced:

$$c = \frac{\pi d_A}{P_p}, \tag{1.149}$$

where P_p is the projected perimeter of the particle in its direction of motion, which is an easier parameter to measure in particles than the projected area. The circularity suffers from the drawback that it yields the same value for some 3D and 2D objects. For example, spheres and disks that fall on their flat sides have the same circularity, while their drag coefficients differ significantly.

Expressions for the drag coefficients of irregular particles have been derived by several researchers for different types and shapes of particles, including Pettyjohn and Christiansen (1948), Masliyah and Epstein (1970), Lasso and Weidman (1986), Haider and Levenspiel (1989), and Hartman and Yates (1993). Each one of these correlations applies to a specific type of particles (e.g., disks, pyramids, prisms) or to a group of shapes. Chhabra et al. (1995) conducted an experimental study and determined the drag coefficients of chains of agglomerates of spheres in viscous fluids at relatively low Reynolds numbers ($Re_r < 2.5$). They concluded that in all cases the drag of the irregular agglomerate is higher (up to 50%) than the drag of a sphere with diameter d_V. Madhav and Chhabra (1995) presented experimental data for the terminal velocity and the drag coefficients of spheres, cylinders, needles, and prisms in the range $1 < Re_r < 400$.

More recently, Tran Cong et al. (2003) performed an experimental study that included several types of irregular particles: spheroids; prisms; star-shaped; H-shaped; elongated bars and cylinders; X-shaped; and cross-shaped. They correlated their data using several suitable functional forms and concluded that the following expression not only correlates the data best but also agrees very well with the correlations of the others:

$$C_D = \frac{24}{Re_r}\frac{d_A}{d_V}\left[1 + \frac{0.15}{\sqrt{c}}\left(\frac{d_A}{d_V}Re_r\right)^{0.687}\right] + \frac{0.42}{\sqrt{c}\left[1 + 4.25\times10^4\left(\frac{d_A}{d_V}Re_r\right)^{-1.16}\right]}. \tag{1.150}$$

This is valid in the ranges $0.15 < Re_r < 1500$, $0.80 < d_A/d_V < 1.50$, and $0.4 < c < 1.0$. These ranges cover most of the irregularly shaped particles in engineering applications.

1.4.3.8 Deformable Bubbles and Drops

Oftentimes, bubbles and drops become spheroidal. Lawrence and Weinbaum (1986, 1988) conducted an analytical study on the transient motion of a rigid spheroid of revolution with small eccentricity, under creeping flow conditions. The results of this study are applicable to bubbles and drops if the internal circulation has negligible effect. The study used essentially the method employed by Maxey and Riley (1983) with the added complexity of domain decomposition to account for the eccentricity and extended to the second-order expansion in terms of ε. The resulting expression for the transient hydrodynamic force on the spheroid is

$$F_i = -6\pi\mu_f a\left[\left(v_i-u_i\right)\left(1-\frac{\varepsilon}{5}+\frac{37\varepsilon^2}{175}\right)+\frac{a}{\sqrt{\nu\pi}}\left(1-\frac{2\varepsilon}{5}+\frac{81\varepsilon^2}{175}\right)\int_0^t\frac{d\left(v_i-u_i\right)/d\tau}{\sqrt{t-\tau}}d\tau\right.$$
$$\left.+\frac{a^2}{9\nu}\left(1+\frac{\varepsilon}{5}-\frac{26\varepsilon^2}{175}\right)\frac{d\left(v_i-u_i\right)}{dt}+\frac{8a\varepsilon^2}{175\sqrt{\pi\nu}}\int_0^t\frac{d\left(v_i-u_i\right)}{d\tau}G\left(t-\tau\right)d\tau\right] \tag{1.151}$$

The function G of the last term is a frequency-dependent term:

$$G\left(t\right)=Im\left[\sqrt{\frac{\pi\phi}{3}}e^{\phi t}erfc\sqrt{\phi t}\right],\ \text{with}\ \phi=\frac{3}{2}\left(1+i\sqrt{3}\right). \tag{1.152}$$

The first three terms of (1.149) are similar to the steady drag, the history, and the added mass term of the Boussinesq–Basset equation. Their form is the same as the form of the corresponding terms of Equations 1.132 and 1.133 with the correction terms due to the eccentricity of the spheroid. However, the last term of Equation 1.151 does not have a counterpart in the Boussinesq–Basset expression. The term depends on the eccentricity as well as the frequency of variation of the velocity of the fluid and vanishes asymptotically as ε^2. This is a new history integral term, which emanates from the elongated shape of the immersed object. The presence of such terms in an equation derived under the creeping flow assumption is another indication that the transient Boussinesq–Basset and Maxey–Riley expressions are significantly modified when there are departures from the assumptions these equations were derived from and which were listed in Section 1.4.3.6. Given that the modifications are on the functional form of these expressions, simple empirical corrections of the three terms of the hydrodynamic force would not be sufficient for the development of the correct transient expressions.

The motion of bubbles and drops in viscous fluids at finite Re_r creates surface stresses that deform the spherical symmetry of these objects. This has a very important effect on the transport coefficients, because the shape of an object is one of the primary determinants of the hydrodynamic force, the heat, and the mass transfer coefficient. The physical properties of the bubbles/drops and the carrier fluid, such as surface tension and viscosity, play an important role in the deformation of the bubbles and drops as well as in the determination of their shapes. For bubbles freely rising in a column of water under the action of gravity, Haberman and Morton (1953) concluded that the following variables determine their shape:

1. The terminal velocity, v
2. The characteristic length, defined as the diameter of the volume-equivalent sphere, d_V
3. The density of the carrier fluid, ρ_f
4. The viscosity of the carrier fluid, μ
5. The surface tension, σ
6. The gravitational acceleration, g

Three independent dimensionless groups may be derived from these six variables:

1. The Reynolds number, $Re = \rho_f d_V v/\mu$, or, equivalently, the relative Reynolds number, Re_r
2. The Eötvös number, $Eo = g\rho_f d_V^2/\sigma$
3. The Morton number, $Mo = g\mu_f^4/\rho_f\sigma^{\,3}$

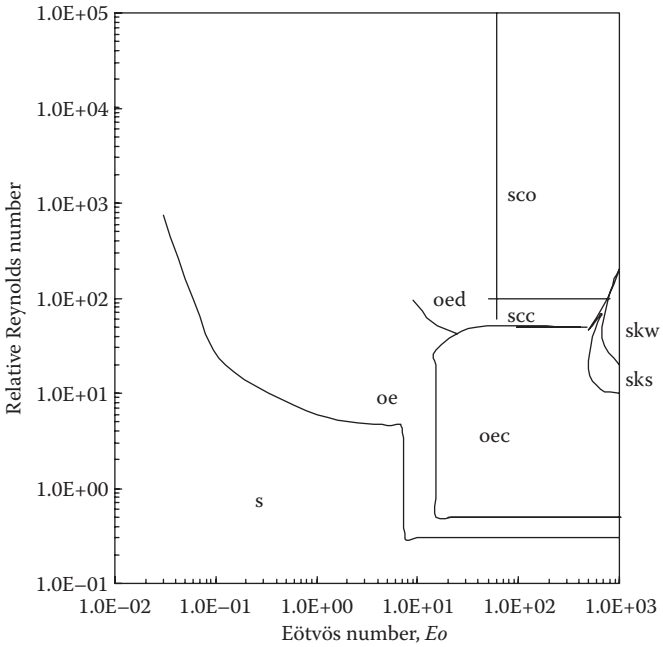

Figure 1.12

The shape map of the deformed bubbles. (Reproduced from the data of Bhaga, D. and Weber, M.E., *J. Fluid Mech.*, 105, 61, 1981.)

Another dimensionless group that appears often in the literature, the Weber number, is defined by the relationship $We = \rho_f v^2 d_V/\sigma$, or $We = Re^2(Mo/Eo)^{-1/2}$.

When experiments are carried in a constant gravitational field, such as laboratories on the Earth's surface, the list of the important variables is reduced to five. This leaves only 2D groups that would determine the shape of bubbles. This pair may be one of the combinations (*Re*, *Eo*), (*Re*, *Mo*), or (*Eo*, *Mo*).

It is standard practice to reduce experimental observations on the shape of bubbles and drops in the so-called shape maps with two of the aforementioned dimensionless groups as coordinates. Such a shape-map has been constructed from the data by Bhaga and Weber (1981) and is reproduced in Figure 1.12. The acronyms on the map are

- s: spherical
- scc: spherical cap with steady, closed wake
- sco: spherical cap with open unsteady wake
- oe: oblate ellipsoidal
- oed: oblate ellipsoidal disk (very elongated and wobbling in motion)
- oec: oblate ellipsoidal with cap in the bottom
- sks: skirted with steady skirt
- skw: skirted with wavy unsteady skirt

It is apparent in this figure that while there is a complexity with the conditions on the shapes of bubbles, in general, bubbles assume the spherical shape at low Reynolds numbers, regardless of the value of the Eötvös number. Also, bubbles are spherical at intermediate values of Re_r, when $Eo < 1$. Bubbles become ellipsoidal at intermediate values of Eötvös numbers and high Re_r. Finally, bubbles assume the shape of a spherical cap at high *Eo* and at relatively high Re_r.

While a shape map, such as that given earlier, which represents static or steady conditions, is useful in determining the shape of flowing bubbles, recent experimental studies on the subject suggest that the method of the creation and release of bubbles also affects their shape, their drag coefficients, and their trajectories. Tomiyama (2001) observed that when bubbles are released with small initial deformation, their shape remains very close to spherical, their drag coefficient is higher than expected, and their motion is rectilinear or zigzag on a plane. However, when the bubbles are released with high initial deformations as ellipsoids,

their shape continues to be ellipsoidal, their drag coefficient is higher, and their motion is helical or rectilinear. In a similar study, Wu and Gharib (2002) also concluded that the initial method of the release of bubbles (whether they are released from a narrow or from a wide tube) plays a role in the eventual shape, the rise velocity, and the drag coefficient. Apparently, the shape oscillations that occur after a bubble is detached from the nozzle are strong enough to disperse the contaminants and to render the bubble surface clean, at least in the initial stage of the bubble trajectory. In most practical cases, the surrounding water contains a sufficient concentration of contaminants for the bubble surface to become immediately contaminated. However, in the case of very pure systems such as the ones used in the study by Wu and Gharib (2002), the recontamination process of the surface was very slow, the bubbles' surface remained clean for the duration of the experiment, and the bubbles remained spherical at significantly higher values of Re_r.

The drag coefficient of inviscid spheres (bubbles) is of importance in practical applications, such as boiling, aeration, and water purification. In this case, the surfactants and contaminants in the water that finally line up on the interface of the bubble and the carrier fluid also play an important role in the determination of the drag coefficient of bubbles. Among the various studies on the drag coefficients, Tomiyama et al. (1998) studied the rise of bubbles in a wide range of Reynolds and Eötvös numbers and derived the following expression for the drag coefficients of clean uncontaminated bubbles:

$$C_D = \max\left\{\min\left(\frac{16}{Re_r}\left(1+0.15Re_r^{0.687}\right),\frac{48}{Re_r}\right),\frac{8Eo}{3Eo+12}\right\}. \tag{1.153}$$

This expression is consistent with the correlations of the numerical data that were given in Section 1.4.3.2, Equations 1.107 through 1.112. It must be noted that when the bubbles become bigger, their shape becomes ellipsoidal. Consequently, the drag coefficient of bubbles depends strongly on the surface tension, which is a determinant of their shape. In the case of elongated bubbles, their drag coefficient is independent of Re_r and is given by the last expression in Equation 1.153, which is a simple function of the Eötvös number. This expression is valid for fairly large hemispherical bubbles, up to 3 cm in diameter.

Because the surfactants in the gas–fluid interface play a major role in the friction part of the drag force and contaminants/surfactants accumulate on this interface, the degree of contamination of the liquid is an important factor in the determination of the drag coefficient of bubbles. The data by Sridhar and Katz (1995) suggest that small bubbles in filtered water, which may be characterized as *contaminated*, behave as solid spheres, and their drag coefficients are very well correlated by the Schiller and Nauman (1933) expression (Equation 1.104) up to $Re_r = 85$. In the case of *grossly contaminated* bubbles, such as those involving tap or industrial water, Loth (2000) recommends the Oseen expression (Equation 1.102) for $Re_r < 1$ and the following expressions, which are based on data from Clift et al. (1978):

$$C_D = \frac{24}{Re_r}\left(1+0.1935Re_r^{0.6305}\right),\quad 1<Re_r<78 \quad \text{and} \quad C_D = \frac{24}{Re_r}\left(1+0.03875Re_r\right),\quad 78<Re_r<300. \tag{1.154}$$

Beyond this range of Re_r, it is very likely that the bubbles are not spherical, and hence, their shape is the major factor that influences the drag coefficient. It must be noted that the drag coefficient expressions for *clean* and *grossly contaminated* conditions may be considered as the lower and the upper limits for the drag coefficients of bubbles. The actual value of the drag coefficient of bubbles is expected to be between these two limits.

1.4.3.9 Lift Effects and Transverse Forces

The drag force is always acting in the direction of the motion of the particle, and its magnitude is monotonically increasing with the relative velocity of the sphere. Particle rotation combined with finite relative velocity or fluid velocity gradients (shear) induces a transverse component in the hydrodynamic force on the sphere, which is often called the "lift force."

When the rigid, spherical particle travels in an inviscid fluid with a relative velocity and also rotates with respect to the far field of the flow, the velocity asymmetry around the particle induces a transverse pressure difference on the surface of the sphere, which generates the *Magnus force* (Magnus, 1861):

$$F_{LMi} = \pi\alpha^3\rho_f[e_{ijk}\Omega_j(u_k - v_k)], \tag{1.155}$$

where Ω_j is the relative rotation of the particle with respect to the inviscid fluid. The term in the square brackets represents the vector product of the relative rotation and the relative velocity vectors. It is apparent that the direction of the Magnus force is perpendicular to the plane of the relative velocity and the axis of rotation.

The functional form of the lift force in a viscous fluid is influenced by the Reynolds number. In this case, the magnitude of the lift force is often expressed as a function of a dimensionless *lift coefficient*, C_{LM}, which is correlated with experimental data. While many expressions have appeared in the past, the investigation by Oesterle and Bui-Dinh (1998) appears to be based on accurate data and is recommended to be used for the lift coefficient of a sphere rotating in an infinite fluid:

$$C_{LM} = \frac{\left|\vec{F}_{LM}\right|}{\pi\alpha^3\rho_c\left|\vec{\Omega}\right|\left|\vec{u}-\vec{v}\right|} = 0.45 + \left(\frac{Re_R}{Re_r} - 0.45\right)\exp\left(-0.05684 Re_R^{0.4} Re_r^{0.3}\right) \quad \text{for } Re_R < 140, \tag{1.156}$$

where Re_R is the Reynolds number based on the relative rotational speed of the sphere

$$Re_R = \frac{\rho_f d^2\left|\vec{\Omega}\right|}{\mu_c}. \tag{1.157}$$

The lift coefficient is, in general, a monotonically decreasing function of Re_R and increases with the dimensionless *rotation parameter*, $(|\vec{\Omega}|d)/(|\vec{u}-\vec{v}|)$. This is a dimensionless measure of the rotational speed of the particle. Experiments at low values of the rotation parameter suggest that C_{LM} may become negative (Tanaka et al., 1990). This is most likely due to a higher relative velocity on one side of the sphere and a premature transition to turbulence of the boundary layer on that side. As a consequence, the wake behind the sphere deflects in a direction that is opposite to what is expected in rotating flow. This reverses the direction of the lift force.

Saffman (1965, 1968) considered the case of a very small sphere in a shear flow at the limit of vanishing Reynolds numbers (creeping flow). He derived an expression for the lift force due to shear, which is

$$\vec{F}_{LS} = \frac{6.46\alpha^2\sqrt{\rho_c\mu_c}}{\sqrt{\left|\vec{\gamma}\right|}}\left(\vec{u}-\vec{v}\right)\times\vec{\gamma}, \tag{1.158}$$

where $\vec{\gamma}$ is the fluid velocity shear evaluated at the center of the sphere. The direction of this force is the perpendicular direction to the plane defined by the relative velocity vector and the shear vector. Sufficient conditions for the validity of the aforementioned expression are very low Re_r as well as:

$$\left|\vec{v}-\vec{u}\right| \ll (\gamma\nu)^{1/2}, \quad \gamma a^2/\nu \gg 1 \quad \text{and} \quad a^2\left|\vec{\Omega}\right|/\nu \ll 1. \tag{1.159}$$

The last three conditions imply one of the following alternatives:

- **a.** Either very low particle velocity, shear, and angular rotation for the particle
- **b.** Extremely high kinematic viscosity for the fluid if the particle has finite velocity, shear, or angular rotation

The first alternative is compatible with the assumptions implied in the derivation of the transient Basset–Boussinesq equation. The second alternative implies very high viscosity in combination with finite shear or rotation and is not strictly compatible with the implied conditions of the transient equation. It must be noted that although Saffman's result (Equation 1.158) is occasionally referred to as the "Saffman force," it is not a separate force from the *Magnus force* but a special case of the latter at the limit $Re_r \to 0$. For this reason, the lift force must be only accounted once in computations of particle dynamics.

The lift force developed on a sphere is very much weaker than the longitudinal drag force. However, the transverse lift plays a dominant role in the lateral migration of bubbles, drops, and particles toward the walls

of cylindrical pipes as well as in dispersion processes. This occurs because in most engineering systems particles, bubbles, and drops have to travel relatively very short distances in order to approach the walls of a pipe or a channel and, hence, a weak force would be sufficient to induce a lateral motion that covers such short distances. These weak transverse forces contribute significantly to radial diffusion and dispersion, wall deposition, mixing, and separation processes.

Tsuji et al. (1985) measured experimentally the shear-induced lift on bubbles and concluded that the expression by Saffman yields satisfactory results for the magnitude of the force. McLaughlin (1991) extended the theoretical analysis by Saffman to higher Re_r and derived a correction to the expression by Saffman, which shows that the magnitude of F_{LS} decreases with the increase of Re_r. McLaughlin's expression for the lift force is as follows:

$$F_{LS} = \frac{9}{\pi}\mu_f a^2 |\vec{v} - \vec{u}| \sqrt{\frac{\gamma \rho_f}{\mu_f}} J(\varepsilon), \tag{1.160}$$

where ε is the dimensionless velocity ratio $\varepsilon = \sqrt{\gamma \mu_f / \rho_f}\,/|\vec{v} - \vec{u}|$ and the function $J(\varepsilon)$ is given in tabular form by McLaughlin (1991). Two approximate asymptotic expressions for this function are $J(\varepsilon) = 2.255 - 0.6463/\varepsilon^2$ for $\varepsilon \gg 1$ and $J(\varepsilon) = 32\pi^2\varepsilon^5 \ln(\varepsilon^{-2})$ for $\varepsilon \ll 1$.

The numerical results for the shear lift force exerted on a sphere obtained by Dandy and Dwyer (1990) were reduced to a useful correlation by Mei (1992):

$$\begin{aligned} C_{LS} &= \frac{F_L}{6.44\rho_f a^2 \gamma^{1/2} \nu^{-1/2}} = \left(1 - 0.3314\sqrt{\beta}\right)\exp\left(-\frac{Re_r}{10}\right) + 0.3314\sqrt{\beta} \quad \text{for } Re_r \le 40 \\ C_{LS} &= 0.0524\sqrt{\beta Re_r} \quad \text{for } Re_r > 40, \\ \text{where} \quad \beta &= \frac{d|\nabla \times \vec{u}|}{2|\vec{u} - \vec{v}|}. \end{aligned} \tag{1.161}$$

The parameter β in the last equation is a dimensionless measure of the shear. The recommended range of this correlation is $0.005 < \beta < 0.4$, and Mei (1992) showed that this empirical equation fits well McLaughlin's results.

There is no widespread agreement on the magnitude of the lift coefficients. The experimental results by Sridhar and Katz (1995) suggest that at least for bubbles, the magnitude of the lift component of the hydrodynamic force is higher than the values predicted by the two aforementioned expressions. Another experimental study by Tomiyama et al. (1999) for bubbles in shear flows concluded that the lift coefficient of larger bubbles depends on the surface tension too and included the Eötvös number in the correlation. Tomiyama et al. (1999) also concluded that rising bubbles tend to accumulate close to the walls if their radii are less than 6 mm, while bigger bubbles with $a > 6$ mm migrate toward the center of the apparatus.

The lift of growing or receding bubbles and drops close to a wall is very important in the boiling, condensation, and evaporation processes, because the global rate of the heat transfer greatly depends on the amount of vapor in contact with the wall or in the immediate vicinity of the wall. In convective boiling systems, such as heated pipes, the lift due to shear facilitates the detachment of small spherical bubbles from the wall and subsequently the nucleation and the commencement of the growth process of other bubbles. Thorncroft et al. (2001) studied the growth and detachment of bubbles from a surface and concluded that the growth of a bubble, whose radius is a function of time, $a(t)$, close to a wall enhances the lift force exerted by the shear. In their analytical and computational study, Thorncroft et al. (2001) derived the following expression for the lift, due to the shear:

$$F_{SLi} = \frac{1}{2}|\vec{u} - \vec{v}|\left(u_i - v_i\right)\pi\rho_f a^2(t)\gamma^{1/2}\left\{\left[\frac{1.46J}{Re_r^{1/2}}\right]^2 + \left[\frac{3}{4}\gamma^{1/2}\right]^2\right\}^{1/2}, \tag{1.162}$$

where J is a scalar function of the dimensionless shear rate and Re_r. The augmented lift force in this case facilitates the detachment of the bubble from the wall, reduces the amount of vapor close to this wall, and thus contributes to the enhancement of the heat transfer from the wall to the bulk fluid.

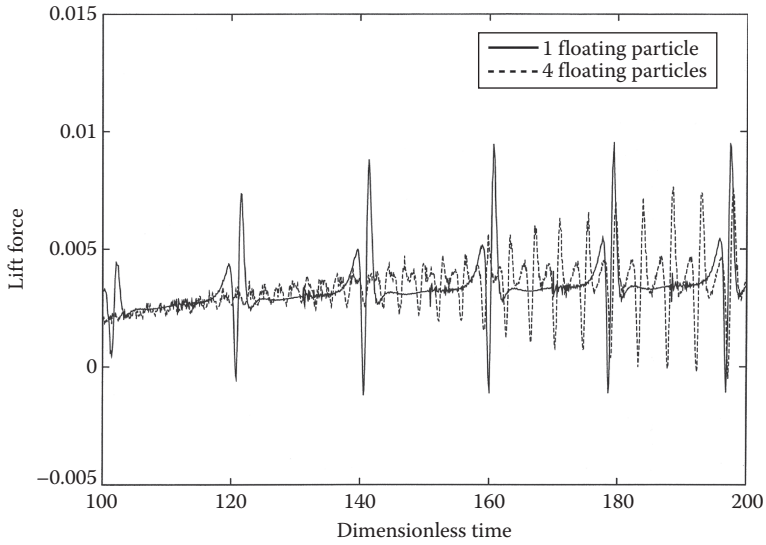

Figure 1.13

The effect of the flow of suspended particles on the lift and drag on a stationary particle.

The transverse force on particles is also influenced by the advection of other particles in the flow. The shear-induced lift on solid spheres attached or deposited on a boundary, in the presence of other spheres in the flow field, known as suspension flow, was studied numerically by Feng and Michaelides (2002a). Their results show that the instantaneous hydrodynamic force exerted by the suspension flow on a solid particle attached to a wall is increased by a factor of 2–4 by the presence of similar particles, which are carried by the fluid. This effect is depicted in Figure 1.13, which shows the instantaneous lift on an embedded sphere, when other spheres in the suspension pass by it. This augmentation includes both the lift and the drag components of the hydrodynamic force and is caused by the interactions of the suspended spherical particles with the stationary particle when they are in the range of 0–5 diameters. As a result of this type of hydrodynamic interaction, a particle that lies on a horizontal plane may be lifted and become part of the suspension flow without any physical collisions with other particles.

Regardless of the method of evaluation of the lift component, the ratio of the transverse component to the longitudinal component of the hydrodynamic force, F_L/F_D, is of the order of $d(\gamma/\nu)^{1/2}$, which is typically a very small number. Despite this, the transverse component of the hydrodynamic force is important in engineering because it causes the lateral migration and dispersion of spheres and plays an important role in several applications, such as bubble detachment from the pipe walls during boiling, particle sedimentation, and resuspension in water as well as particulate and aerosol dispersion in the atmosphere. The accurate knowledge of the transverse component of the transient hydrodynamic force is of importance in calculations that pertain to such processes, even though the method of the determination of the drag component is not fully compatible with the assumptions used for the determination of the lift. It is common practice in such calculations to superpose an expression for the transverse or lift component, such as Equation 1.153 or Equation 1.158 with an expression for the transient hydrodynamic force in the longitudinal direction, such as Equation 1.133, and compute the longitudinal and transverse motion of particles, bubbles, and drops. The result of such a superposition is that the transient hydrodynamic force on a sphere appears to have a lateral, albeit steady, component in addition to the longitudinal component. Although the superposition is not justified on analytical grounds, it is very convenient to use and the results obtained appear to be accurate. When one uses this superposition, it is important to ensure that the necessary conditions for the validity of the expressions used for the several components of the hydrodynamic force are not violated. This implies that there is very low relative velocity and that the local shear is low.

The influence of mass transfer from the sphere (evaporation or sublimation) on the lift has been investigated experimentally and numerically. A numerical study by Kurose et al. (2003) determined that in linear shear flow, the outflow from a sphere acts in a way to push the sphere toward the lower flow velocity side. Thus, a negative lift is developed at high Reynolds numbers. This counteracts the positive lift on the sphere, which is directed toward the higher velocity side. According to Kurose et al. (2003), the diffusion

and reaction rates are strongly affected by the outflow velocity and the fluid shear because of the deformation of the vortices that appear behind the evaporating sphere. This suggests that surface evaporation and/or reaction influences significantly the lateral motion of drops and hence the concentration field of the drops.

1.4.3.10 Effects of the Boundaries

The effect of a wall, in general, is to retard the motion of particles in both the parallel and the perpendicular direction to the wall, thus reducing the rate of mass transport. In addition, the presence of particles and bubbles in boundary layers and mixing layers significantly modifies the stability and transport properties of these layers. The motion of particles, bubbles, and drops in the vicinity of a boundary is important in many practical applications especially those related to boiling of liquids and the transport of particulates and slurries. In particulate transport processes, particle collisions with the walls cause pipeline erosion and particle adhesion to the walls, scale buildup, and oftentimes pipeline clogging.

Faxen (1922) was the first to consider the motion of a particle in rectilinear motion parallel to a wall and to derive an expression for the hydrodynamic force on a spherical particle. He used the method of reflections for the movement of the sphere under creeping flow conditions and obtained an asymptotic solution for the total force acting on a sphere, which settles along the centerline of an orthogonal cylinder. The ratio, Ξ, of the particle diameter, d, to the diameter of the cylinder, D, ($\Xi = d/D$) is the most important parameter that affects the hydrodynamic force. Faxen's expression for the hydrodynamic force is given in terms of a wall drag multiplier, K_{wall}. This is the ratio of the steady hydrodynamic force to the Stokesian force the same sphere experiences in an unbounded flow. By using the same method, Bohlin (1960) obtained a higher-order approximation for the wall drag multiplier, which may be written as follows:

$$K_{wall} = \frac{1}{1 - 2.01443\Xi + 2.088777\Xi^3 - 6.94813\Xi^5 - 1.372\Xi^6 + 3.87\Xi^8 - 4.19\Xi^{10} + \cdots}. \tag{1.163}$$

Haberman and Sayre (1958) developed a theoretical method to compute the wall correction factor, K_{wall}, for spheres settling in cylinders up to very high values of Ξ, and later Paine and Scherr (1975) computed the values for K_{wall}. Their results are tabulated in the range $0 \leq \Xi \leq 0.9$. A comparison between the expression by Bohlin (Equation 1.160) and the exact theory by Haberman and Sayre (1958) shows that the last equation yields accurate results only up to $\Xi = 0.6$. There are also several experimental studies pertaining to the settling of a sphere along the centerlines of orthogonal circular cylinders or plane walls. Among them, the experimental studies by Iwaoka and Ishii (1979) and Miyamura et al. (1981) demonstrate good agreement with the theoretical predictions by Faxen (1922), Bohlin (1960), and Paine and Scherr (1975).

Happel and Brenner (1986) considered creeping as well as inertia flows for the settling of a sphere in a cylinder and stipulated that the total effect on the hydrodynamic force is a simple linear combination of the separate effects of proximity to the outside boundary and inertia:

$$K = K_{wall} + K_{inertia} - 1, \tag{1.164}$$

where

K_{wall} is the effect of the wall at creeping flow conditions as calculated by an expression similar to (1.160)
$K_{inertia}$ is the additional correction factor due to inertia at higher Re_r

The last equation simply implies that the drag on a sphere is composed of two additive terms: one term is due to the effect of the cylindrical boundary and the other to flow inertia. The latter is usually obtained from one of the empirical correlations for the drag coefficient at higher Re_r, such as the one by Schiller and Nauman (1933). Equation 1.164 is a conjecture, partly based on the experimental data by Fayon and Happel (1960). The data set pertains to a diameter ratio, Ξ, in the range of 0.1250–0.3125 and the Reynolds numbers in the range 0.1–40.

Feng and Michaelides (2002b) conducted a more general numerical study in the ranges $0.1 < \Xi < 0.8$ and $0 < Re_r < 35$ for cylindrical as well as for prismatic enclosures. They concluded that the two effects of inertia and of flow confinement are not additive and may not be linearly combined as Equation 1.164 implies. Because of this, in calculating the hydrodynamic force on a sphere, it is more accurate to use computational and experimental results, which are not restricted by the conjecture (1.161). One of the significant results by Feng and

Table 1.2 Wall Correction Factors for Various Orthogonal Rectangular Prisms

$L/W = 1.0$								
$\Xi(=d/W)$	0.2	0.3	0.4	0.5	0.6	0.7	0.8	0.9
K	1.72	2.30	3.18	5.01	8.03	13.98	27.9	61.8
$L/W = 1.5$								
$\Xi(=d/W)$	0.3	0.4	0.5	0.6	0.7	0.8		
K	1.90	2.47	3.32	4.46	6.11	9.24		
$L/W = 2.0$								
$\Xi(=d/W)$	0.3	0.4	0.5	0.6	0.7	0.8		
K	1.73	2.12	2.67	3.33	4.37	5.76		
$L/W = 5.0$								
$\Xi(=d/W)$	0.3	0.4	0.5	0.6	0.7	0.8		
K	1.53	1.75	2.11	2.48	3.06	3.78		

Michaelides (2002b) is that at the higher values of the parameter, $\Xi > 0.5$, the effect of inertia is less than 10% of the total correction factor, K. Table 1.2, which is reproduced from this study, shows the total correction factor, K, for a sphere of diameter, d, when it falls in a rectangular prismatic enclosure whose cross section has length, L, and width, W. The results shown are for $Re_r \ll 1$.

It must be noted that the effect of boundaries on settling spheres is different in the case of prismatic enclosures than in circular cylinders, because secondary flows are induced in the corners of the prisms. Even though the secondary flows are relatively weak, they affect considerably the hydrodynamic force on the spheres.

The asymmetrical velocity and pressure fields due to walls cause the radial migration of particles in pressure-driven flows in pipes and small capillaries away from the wall. Cox and Brenner (1967) expressed the effect of a vertical wall on a particle using the concept of a *migration velocity* of a sphere that is falling freely close to a wall. An analytical expression for the migration velocity is as follows:

$$V_r = \frac{6\pi V_t^2}{\nu} I_h, \tag{1.165}$$

where

V_t is the terminal velocity of the sphere in a stagnant, unbounded fluid

I_h is an integral of Green's function for the point force representing the sphere

The last expression is valid under the conditions $Re_r \ll a/l_w \ll 1$, where l_w is the distance of the center of the sphere from the wall. The implications of this condition are that the sphere is relatively far from the wall and the flow field is Stokesian (creeping flow). Later, Cox and Hsu (1977) calculated analytically the integral, I_h, for spheres and derived the following expression for the migration velocity:

$$V_r = \frac{3}{64} Re_r V_t, \tag{1.166}$$

which is also valid under the condition $Re_r \ll a/l_w \ll 1$. A close look at the last expression reveals that the migration velocity of the sphere is independent from its distance from the wall. This does not constitute a paradox, because the expression is valid only at distances sufficiently far from the wall as required by the condition $a/l_w \ll 1$.

Vasseur and Cox (1976) derived analytically another expression for the lateral migration velocity of a sphere:

$$V_r = \frac{3}{8}\frac{\alpha v_s^2}{\nu}\left[\left(\frac{\nu}{l_w V_t}\right)^2 + 2.219\left(\frac{\nu}{l_w V_t}\right)^{5/2}\right]. \tag{1.167}$$

The terms in the two parentheses are obviously the inverse of a Reynolds number, which is based on the distance of the center of the sphere from the wall. The last expression was later confirmed by the experimental data of Cherukat and McLaughlin (1990) to be valid up to $Re_r = 3.0$.

The repulsive effect of the wall on particles is very important in the distribution of phases in dispersed flows in pipes as well as in sedimentation–resuspension processes with particles. The effect has been demonstrated in a number of experimental and numerical studies, such as the one by Segre and Silberberg (1962) with neutrally buoyant spheres. They concluded that neutrally buoyant particles in a pressure-driven Poiseuille flow (pipe flow) experience a radial force and tend to align at 0.6 pipe radii away from the centerline. This shows that there exists an equilibrium position, where the radial force is zero and where particles tend to accumulate. Two-dimensional numerical studies have also concluded that there is an equilibrium position for cylinders at a distance of 0.4234 half-channel width away from the centerline. Inamuro et al. (2000) concluded that this distance is the same for both a single cylinder and a group of naturally buoyant cylinders in pressure-driven channel flows. Mortazavi and Tryggvason (2000) also studied the lateral migration of 2D drops in Poiseuille flows and determined that drops either move halfway between the pipe centerline and the wall, as Segre and Silberberg (1962) also observed, or they oscillate around an off-center equilibrium position. In a study involving the resuspension of particles in simple shear flow over a flat plate, Feng and Michaelides (2003) concluded that particles, which are slightly heavier than the fluid, do not settle down on a flat surface, but reach an equilibrium position at a certain height from the plane and then drift with the main flow at this vertical position without settling. Their numerical results are shown in Figure 1.14, where the lower facing triangles denote particles that settled under gravity and the upper facing triangles denote particles that drifted at a vertical equilibrium distance. The dividing line separates the settled particles from the particle that reach the equilibrium position, which is usually at a height less than a single diameter from the flat surface. Feng and Michaelides (2003) derived the following expression for the line that separates the settled from the suspended particles:

$$Re_\gamma = \frac{\rho_f \gamma d^2}{\mu_f} = 58\left[\frac{\rho_s}{\rho_f} - 1\right]^{0.59}. \tag{1.168}$$

At a given shear Reynolds number heavier particles settle, while lighter particles move to an equilibrium position and stay suspended in the flow, even though they may be heavier than the fluid. Patankar et al. (2001) also examined the behavior of particles close to the wall in a Poiseuille flow and observed a similar

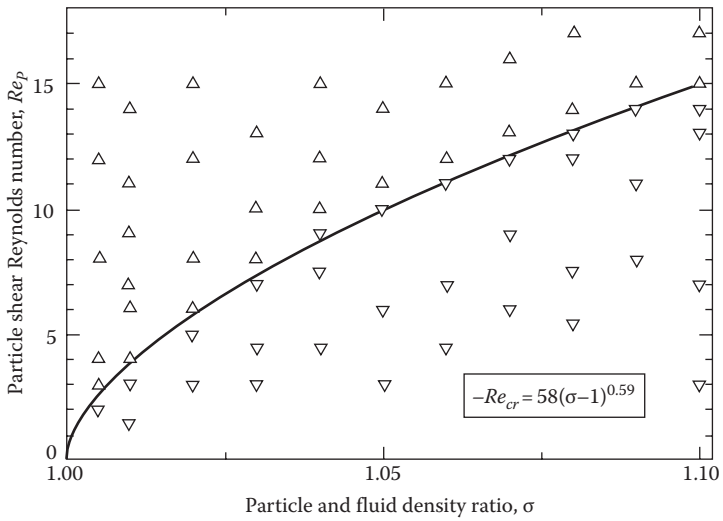

Figure 1.14

Settling or suspended particles with the density ratio and Reynolds number as parameters. The symbol Δ is for suspended and ∇ is for settled particles.

behavior for the particles. They developed a corresponding expression for Re_γ and the density ratio, which may be written as follows:

$$\frac{\rho_s}{\rho_f} - 1 = 2.3648 \frac{\mu_f^2}{d^3 \rho_f^2 g} Re_\gamma^{1.3904}. \tag{1.169}$$

Equation 1.168 applies to shear flows over flat plates, while (1.167) applies to pipes and channels, where Poiseuille flows are more likely to occur. It must be noted that neither of the last two equations takes into account turbulence in the flow nor turbulent bursts that result in the advection of particles and the resuspension of groups of particles.

Walls also retard the movement of spheres that travel perpendicular to them. Regarding these flows, Brenner (1961) obtained asymptotically a first-order correction for the drag coefficient of a small rigid sphere moving toward the wall and concluded that the Stokes drag coefficient, f, increased by a factor:

$$f = \frac{C_D}{24/Re_r} = 0.625 \left(\frac{d}{l_w} \right)^{-1}, \tag{1.170}$$

where l_w is the distance from the center of the sphere to the wall. Brenner's results indicate that the hydrodynamic force on the particle increases dramatically when the particle approaches very closely the wall. This is related to the thin fluid layer that develops between the particle and the wall. Draining such thin layers, where viscous effects dominate, is a very slow process. In this case, the hydrodynamic force opposing the motion of the sphere becomes very large and the particle velocity drops significantly. The study by Kalio (1993) indicates that the influence of the wall on the drag of the particles is important when the particle is within 20 diameters from the wall. The experimental and computational study by ten Cate et al. (2002) confirmed this rapid and significant increase in the drag coefficient of settling spheres, which are within one diameter from a horizontal wall.

It must be pointed out that the analytical expressions of all transverse components of the hydrodynamic force and of the effect of the walls on the motion of a sphere are not based on a rigorous derivation of the transient equation of motion, but on specific analytical, experimental, and numerical studies, most of which were performed at steady flow conditions. One has to be aware that the rectilinear transient equations of motion mentioned in Section 1.4.3.6 implicitly assume that there is no rotation of the sphere, no significant shear in the flow, and the sphere is in an unbounded fluid, which essentially means far from any wall or other boundary. The addition of the lift or of any wall effect on a rigorously derived transient equation for the rectilinear motion of a particle must be viewed as an *ad hoc* assumption. Such assumptions are frequently used, because practice has shown that they produce reliable results on the average movement of particles. It must be remembered, however, that such assumptions, even though justified by validation with experiments or other means, have practical limitations.

1.4.3.11 Thermophoresis and Turbophoresis

When particles, bubbles, or drops are present in a fluid where a temperature gradient is applied, they experience molecular impulses that are stronger on the side of higher temperatures. This induces stronger Brownian motion in the hotter regions of the flow domain than in the colder ones. As a result, the particles, on the average, migrate to the colder regions of the flow domain, as was first observed by Tyndal (1870). A constant temperature gradient creates the steady average movement of an ensemble of particles, bubbles, and drops to the colder regions of the flow domain, a phenomenon called "thermophoresis." The latter is expressed quantitatively in terms of a thermophoretic velocity, v_{tp}, or of a thermophoretic force, F_{tp} (Epstein, 1929, Brock, 1962, Talbot et al., 1980). The directions of the thermophoretic force and thermophoretic velocity are opposite to the temperature gradient, and their magnitudes are

$$v_{tp} = -K_{tp} \frac{\mu_f}{\rho_f} \frac{\nabla T}{T_\infty} \quad \text{and} \quad F_{tp} = -6\pi\mu_f^2 \alpha K_{tp} \frac{\nabla T}{\rho_f T_\infty}. \tag{1.171}$$

The function K_{tp} depends on the Knudsen number, $K_{tp}(Kn)$, and on the properties of the fluid and the solid particles. By considering the velocity slip as well as a temperature slip of particles in gases, the

following expression for K_{tp}, in terms of the thermal conductivities, and the Knudsen number, Kn, was derived by Brock (1962):

$$K_{tp} = \frac{2C_s\left(k_f + 2k_s Kn\right)}{(1+6C_m Kn)(2k_f + k_s + 4k_s C_t Kn)}. \tag{1.172}$$

The parameters C_s, C_m, and C_t are determined empirically from the flow field around the particles and the discontinuities on the fluid–particle interface. Talbot et al. (1980) used the velocity slip expression that was recommended by Millikan (1923) and derived empirical correlations for these parameters. Experimental data and engineering practice have shown that reasonable results may be obtained by treating these parameters as constants with the numerical values for gases $C_s = 1.17$, $C_m = 1.14$, and $C_t = 2.18$ in the range $Kn < 0.1$. For liquids, McNabb and Meisen (1973) showed that the magnitude of the thermophoretic force is much lower, approximately 17% of the values predicted by Equations 1.171 and 1.172.

However, a disadvantage of the last two equations becomes obvious: when the equations are used for liquids with highly conducting particles (nanofluids), the thermophoretic velocity becomes vanishingly small, because $K_n \ll 1$ and $k_f \ll k_s$ for typical nanofluids. Since thermophoresis is a consequence of the Brownian movement, its effects are significant in very small particles, bubbles, and drops in the submicron range and becomes insignificant for larger particles of mm sizes. Michaelides (2015) used a stochastic Lagrangian method to derive the functional relationship for the dimensionless thermophoretic coefficient of spherical particles K_{tp} that appears in the last two equations:

$$K_{tp} = A\left(\frac{\alpha}{\alpha_0}\right)^{-B} \Rightarrow v_{tp} = -A\left(\frac{\alpha}{\alpha_0}\right)^{-B} \frac{\mu_f}{\rho_f T_\infty}\nabla T, \tag{1.173}$$

where $\alpha_0 = 1$ nm appears to correlate well all the combinations of particle types and base fluids. One of the advantages of the last expression is that it has been derived specifically for liquids, where typically $K_n \ll 1$ and applies to all types of spheres including the highly conducting spheres of nanofluids. The pairs of coefficients (A, B) for 20 common combinations of particles and fluids used in nanofluids are given in Table 1.3.

It must be noted that an implicit assumption of Equation 1.171 and all similar expressions of thermophoresis is that the effect of a temperature gradient on the motion of the particle is decoupled from all the other forces that act on the particle, such as lift forces and effects of boundaries. Also, although the thermophoretic force is a weak force and has a vanishing effect on larger particles, it may become the dominant force for very small nanoparticles, where gravity—as well as all other volume/body forces—is very weak. A glance at Equation 1.171 proves that the ratio of the thermophoretic to the force of gravity varies as α^{-2} and that the thermophoretic force would be dominant on nanoparticles in a gravitational field with a strong temperature gradient. Because of this, thermophoresis has often been used for the collection of nanoparticles on collection surfaces (Leung and Crowe, 1993). Nevertheless, the thermophoretic force is weak and this collection method takes very long time. It also requires precise equipment and suppression of any flow instabilities. Artificial centrifuging is a more effective method to concentrate and collect nanoparticles (Michaelides, 2014).

It must be emphasized that the thermophoretic force is a consequence of the molecular collisions, which also cause the Brownian motion. The thermophoretic and Brownian forces are not independent forces to be accounted separately in the Lagrangian simulations of particle motion. The simple inclusion of the Brownian

Table 1.3 Pairs of Coefficients (A,B) for the Correlation of Equation 1.173 for Several Spherical Particles in Common Fluids

	Water	Engine Oil	Ethyl Glycol	R-134a
Aluminum	(1264, 1.417)	(3.0920, 1.242)	(14.615, 1.869)	(4401, 1.774)
Aluminum oxide	(1227, 1.434)	(7.1026, 1.579)	(5.1095, 1.621)	(6270, 1.819)
CNT	(945.5, 1.263)	(5.8044, 1.445)	(3.6765,1.406)	(8580, 1.894)
Copper	(2039, 1.870)	(7.1391, 1.724)	(2.3558, 1.587)	(4191, 1.659)
Gold	(3155, 1.799)	(6.6483, 1.917)	(4.2431, 1.672)	(2721, 1.603)

force in the Lagrangian simulations of particle motion in fluids with temperature gradients will reproduce the thermophoretic velocity as the steady *drift velocity* of the particles toward the colder regions of the system.

Turbophoresis is a phenomenon similar to thermophoresis and results from the gradients of turbulence intensity, which develop in boundary and shear layers. In this case, the particle is subjected to a higher force on the side where turbulence is higher. Thus, the net turbophoretic force acts in the direction opposite to $\nabla\overline{u'^2}$. Analysis and experiments have shown that in a wall boundary layer, the process of turbophoresis tends to bring the particles closer to the wall, where the turbulent fluctuations are weaker. However, when the particle concentration at the wall becomes high, the accumulation of particles and the more frequent interparticle collisions cause a *drift velocity* away from the high particle concentrations. The balance of the two driving forces, turbulence and concentration, leads to an equilibrium condition. Portela et al. (2002) concluded that the local equilibrium predict well the particulate concentration, except when very close to the wall ($y^+ < 20$) where the turbulent fluctuations are very weak and turbophoresis cannot even be defined in a physically meaningful way.

1.4.4 Heat Transfer

While the development of the equation of motion for a sphere was based predominantly on analytical work followed by corrections derived from experiments, most of the analyses on the subject of heat transfer are based on Fourier's work (Fourier, 1822). His treatise, which was preceded by his seven shorter articles on heat conduction, has been subsequently supplemented by numerous experimental studies that have provided semiempirical correlations for the rate of heat transfer or, equivalently, for the Nusselt number. For this reason, the subject of heat transfer from spheres is based primarily on correlations that stem from experiments or, in the recent past, from numerical studies.

The governing equations for the heat transfer and for the mass transfer are strictly similar. For this reason, the solution of one equation also yields the solution of the other equation by simple substitution of the corresponding dimensionless numbers. Therefore, all the results, analytical, experimental, or computational, for the heat transfer coefficients are also applicable to the pertinent mass transfer coefficients.

An important parameter in the study of convective heat and mass transfer from spheres is the Peclet number (for heat or mass transfer), which accounts for the heat or mass advected by the fluid. The Peclet number is analogous to the Reynolds number in the equation of motion and is defined as follows for the cases of heat transfer and mass transfer, respectively:

$$Pe = d\rho_f c_{pf} U/k_f \left(\text{or } Pe = Re^* Pr\right) \quad \text{and} \quad Pe_M = \frac{dU}{D}, \tag{1.174}$$

where

U is the characteristic velocity of the fluid
c_{pf} is the specific heat capacity of the fluid
k_f is the conductivity of the fluid
D is the diffusivity of the fluid

The Prandtl number, Pr, is the dimensionless group of the fluid properties, $Pr = \mu_f c_{pf}/k_f$. When there is relative motion between the sphere and the fluid, which is characteristic of most advection processes, the magnitude of the relative velocity is used as the characteristic velocity U in the expressions for the Peclet number as in Equation 1.22. The Nusselt number, the Sherwood number, and the Biot number, which are also given in Equation 1.22, are other dimensionless groups frequently used in heat transfer from particles, bubbles, and drops.

1.4.4.1 Creeping or Stokes Flow

As in the case of momentum transfer, creeping flow or Stokes flow implies $Re_r \ll 1$. Since $Pe_r = Re_r * Pr$, unless Pr for the sphere is very large, as is the case of some organic oils, this condition also implies that $Pe_r \ll 1$, or at least that $Pe_r < 1$. Heat convection comprises two parts, conduction and advection. Since in creeping flows the advection is negligible, the conduction part dominates in the convection process. Therefore, studies that implicitly or explicitly assume that $Pe_r \ll 1$ or $Re_r \ll 1$ essentially neglect the effects of the advection part of the process and are treating the conduction part of the process alone.

The solution of the conduction equation (or $Pe_r \ll 1$) yields the following expression for the steady flow Nusselt number:

$$Nu = 2. \tag{1.175}$$

Acrivos and Taylor (1962) conducted a study on the heat transfer from a solid sphere, analogous to the study by Proudman and Pierson (1956) for the equation of motion. They implicitly assumed a Stokesian flow around a sphere and derived an asymptotic heat transfer solution, which is valid at higher order of Pe_r. With the corrections in the coefficients (Acrivos, 1980), their expression for the steady Nu, which is applicable in the ranges $Re_r \ll 1$ and $Pe_r < 1$, is

$$Nu = 2 + \frac{Pe_r}{2} + \frac{1}{4} Pe_r^2 \ln \frac{Pe_r}{2} + 0.2073 Pe_r^2 + \frac{1}{16} Pe_r^3 \ln \frac{Pe_r}{2}. \tag{1.176}$$

Acrivos and Taylor (1962) also proved that the functional relationship $Nu(Pe_r)$ obtained for creeping flow is less sensitive to an increase of Re_r than the corresponding functional relation for the drag coefficient, $C_D(Re_r)$, of solid spheres. Therefore, it is generally accepted that the last equation is valid not only under creeping flow conditions but also when Re_r is finite but small.

Acrivos and Goddard (1965) also derived an asymptotic solution for high Pe_r assuming a Stokesian velocity distribution. Their expression, which is valid for $Pe_r > 5$, is

$$Nu = 1.249 \left(\frac{Pe_r}{2} \right)^{1/3} + 0.922 \tag{1.177}$$

In the case of viscous spheres, with viscosity ratio, λ, Levich (1962) derived an asymptotic first-order solution for a liquid sphere at very large Pe_r and $Re_r \ll 1$:

$$Nu = \sqrt{\frac{4 Pe_r}{3\pi(1+\lambda)}}. \tag{1.178}$$

Feng and Michaelides (2000b) under the assumption of a Stokesian velocity profile around a viscous sphere (drop or bubble) solved numerically the energy equation and derived the following correlation for the heat transfer coefficients:

$$Nu = 1.49 Pe_r^{0.322 + \frac{0.113}{0.361\lambda + 1}}. \tag{1.179}$$

It must also be pointed out that the implicit conditions for the use of the last three expressions are as follows: $Re_r < 1$ and $Pe_r \gg 1$. These conditions are satisfied for spheres with $Pr \gg 1$. Several organic liquids, including gasoline and engine oil, satisfy these conditions.

More recently, Feng (2014) used a combined regular and singular perturbation method to solve the heat and mass transfer from a slightly deformed sphere at low but finite Peclet numbers in Stokes flow. The deformed sphere was assumed to be axisymmetric, and its shape is described in the spherical coordinates (r, θ, ϕ) by a power series of a small parameter ε ($|\varepsilon| \ll 1$) as follows:

$$r = 1 + \varepsilon \sum_{n=0}^{\infty} b_n P_n(\cos\theta) + O(\varepsilon^2). \tag{1.180}$$

Here, the origin of the spherical coordinate system is at the center of the undeformed sphere, $P_n(\cos\theta)$ is the Legendre polynomial of nth order, and b_n are constants of order $O(1)$. The correction to the Nusselt number due to the deformation of the sphere was obtained through a regular perturbation method, while the correction to Nu number due to the small Peclet number was obtained through a singular perturbation method.

The analytical solution for the averaged Nusselt number in terms of the Peclet number and the deformation parameter is

$$Nu = 2 + \frac{1}{2}Pe_r + \frac{1}{4}Pe_r^2 \ln Pe_r + 0.03404Pe_r^2 + \frac{1}{16}Pe_r^3 \ln Pe_r + \varepsilon\Delta(Pe_r) + O(\varepsilon^2) + O(Pe_r^3), \tag{1.181}$$

where

$$\Delta(Pe_r) = 2b_0 + b_0 Pe_r + \left(\frac{3}{4}b_0 - \frac{1}{20}b_2\right)Pe_r^2 \ln Pe_r + \left[\left(\frac{1721}{2400}b_0 + \frac{1}{16}b_1 + \frac{611}{8400}b_2\right) - \left(\frac{3}{16}b_0 - \frac{1}{80}b_2\right)\ln 2\right]Pe_r^2$$
$$+ \left(\frac{3}{16}b_0 - \frac{1}{80}b_2\right)Pe_r^3 \ln Pe_r. \tag{1.182}$$

In the case of a spheroid with its surface described in Cartesian coordinates by,

$$\frac{x^2 + y^2}{[(1+\varepsilon)c]^2} + \frac{z^2}{c^2} = 1. \tag{1.183}$$

If we choose the semiaxis c as the reference length ($c = 1$), the surface points of the spheroid are described by the equation

$$r = 1 + \varepsilon\left[\frac{2}{3}P_0(\cos\theta) - \frac{2}{3}P_2(\cos\theta)\right] + O(\varepsilon^2). \tag{1.184}$$

If $\varepsilon > 0$, the spheroid is an oblate; if $\varepsilon < 0$, it is a prolate; if $\varepsilon = 0$, it reduces to a sphere. By letting $b_0 = 2/3$ and $b_2 = -2/3$, the Nusselt number becomes

$$Nu = 2 + \frac{1}{2}Pe + \frac{1}{4}Pe^2 \ln Pe + 0.03404Pe^2 + \frac{1}{16}Pe^3 \ln Pe$$
$$+ \varepsilon\left[\frac{4}{3} + \frac{2}{3}Pe + \frac{8}{15}Pe^2 \ln Pe + 0.33714Pe^2 + \frac{3}{15}Pe^3 \ln Pe\right] + O(\varepsilon^2) + O(Pe^3). \tag{1.185}$$

1.4.4.2 Reynolds Number Effects

1.4.4.2.1 Solid Spheres Among the correlations of experimental data that have been used for the steady heat transfer from a solid sphere due to forced convection without mass transfer on the surface, for example, in the absence of evaporation, sublimation, or chemical reactions, are the expressions derived by Ranz and Marshal (1952) and Whitacker (1972), which may be written, respectively, as follows:

$$Nu = 2 + 0.6Re_r^{0.5}Pr^{0.33} \tag{1.186}$$

and

$$Nu = 2 + (0.4Re_r^{1/2} + 0.06Re_r^{2/3})Pr^{0.4}. \tag{1.187}$$

These correlations are valid for solid spheres only and may be used up to $Re_r = 10^4$.

In many heating and cooling applications involving dispersed flows, the convective heat transfer is of a mixed type, with the free convection part induced by the different temperature of particles. Since the free convection takes place in the direction of gravity and the forced convection is arbitrary, the directions of the free and forced convection are not necessarily the same. The overall heat transfer of a sphere resulting from the mixed flow is significantly influenced by the direction of the forced flow. Musong and Feng (2014) examined numerically the mixed convection from a heated sphere at an arbitrary incident flow angle in laminar

flows at moderate Reynolds numbers ($1 \le Re_r \le 100$) and Richardson numbers ($1 \le Ri \le 5$). Based on the simulation results, they developed a correlation for the mixed convection with incident angles in the range $0 \le \theta < \pi/2$:

$$Nu = aRe^{b}Ri^{0.5b}\theta^2 + cRe^{d}Ri^{0.5d}\theta + nRe^{f}Ri^{0.5f} - gRe^{1+h}Ri^{0.5} - kRe^{m}, \tag{1.188}$$

where $a = -0.0208$, $b = 0.4851$, $c = 0.0250$, $d = 0.05$, $n = 1.436$, $f = 0.3642$, $g = 0.2534$, $h = -0.722$, $k = -0.2602$, and $m = 0.2412$. The units of the incident angle θ are radians.

1.4.4.2.2 Viscous Spheres Feng and Michaelides (2000a, 2001b) conducted two numerical studies on the subject of heat transfer from viscous spheres without mass transfer at the interface and derived useful and accurate correlations, with Re_r and Pe_r as independent variables. The first study pertains to high Re_r and any Pe_r and the second to any values of Re_r and Pe_r. Their results in correlation form are summarized in the following equations:

1. At small but finite values of Re_r ($0 < Re_r < 1$) and $Pe_r > 10$, the expression for the Nusselt number is

$$Nu(\lambda, Pe_r, Re_r) = \left(\frac{0.651}{1+0.95\lambda}Pe_r^{1/2} + \frac{0.991\lambda}{1+\lambda}Pe_r^{1/3}\right)\left(1+\alpha(Re_r)\right) + \left(\frac{1.65\left(1-f(Re_r)\right)}{1+0.95\lambda} + \frac{\lambda}{1+\lambda}\right), \tag{1.189}$$

where the function $f(Re_r)$ is defined as

$$f(Re_r) = \frac{0.61Re_r}{Re_r+21} + 0.032. \tag{1.190}$$

2. As with the drag coefficient in Section 1.4.3.2, for higher Re_r and Pe_r, the analysis of numerical data revealed that the most accurate correlations of the numerical data are obtained when the general expression for Nu is given in terms of the following three functions, which pertain to specific values of the viscosity ratio λ:

a. The correlation for an inviscid sphere ($\lambda = 0$), which is given by the following expression:

$$Nu(0, Pe_r, Re_r) = 0.651Pe_r^{1/2}\left(1.032 + \frac{0.61Re_r}{Re_r+21}\right) + \left(1.60 - \frac{0.61Re_r}{Re_r+21}\right). \tag{1.191}$$

b. The Nusselt number expression for a solid sphere ($\lambda = \infty$):

$$Nu(\infty, Pe_r, Re_r) = 0.852Pe_r^{1/3}\left(1+0.233Re_r^{0.287}\right) + 1.3 - 0.182Re_r^{0.355}. \tag{1.192}$$

c. The corresponding function for a sphere with $\lambda = 2$, which was derived from the numerical results:

$$Nu(2, Pe_r, Re_r) = 0.64Pe_r^{0.43}\left(1+0.233Re_r^{0.287}\right) + 1.41 - 0.15Re_r^{0.287}. \tag{1.193}$$

Accordingly, the final correlations for the heat transfer coefficients are given by the following expressions in the two ranges of the viscosity ratio, $0 \le \lambda < 2$ and $2 < \lambda \le \infty$:

$$Nu(Pe_r, Re_r, \lambda) = \frac{2-\lambda}{2}Nu(Pe_r, Re_r, 0) + \frac{4\lambda}{6+\lambda}Nu(Pe_r, Re_r, 2)$$
$$\text{for } 0 \le \lambda \le 2 \quad \text{and} \quad 10 \le Pe_r \le 1000 \tag{1.194}$$

and

$$Nu\left(Pe_r,Re_r,\lambda\right)=\frac{4}{\lambda+2}Nu\left(Pe_r,Re_r,2\right)+\frac{\lambda-2}{\lambda+2}Nu\left(Pe_r,Re_r,\infty\right)$$
$$\text{for } 2\le\lambda\le\infty \quad \text{and} \quad 10\le Pe_r\le 1000. \tag{1.195}$$

For smaller values of $Pe_r < 10$, it was not possible to obtain a simple correlation of the numerical results, $Nu(Pe_r, Re_r, \lambda)$, with any satisfactory degree of accuracy. For this reason, for applications in the range $0 < Pe_r < 10$, it is recommended that one uses the numerical results in the original publication (Feng and Michaelides, 2001b), which are given in tabular form and their accuracy is only limited by the numerical accuracy of the method.

As in the case of the hydrodynamic force on a viscous sphere, it was determined that for a fixed value of Re_r and viscosity ratio, λ, the variations of the density ratio, ρ_s/ρ_f, have only a minimal effect on the external flow field. When one considers the governing equation for the heat or mass transfer processes and the pertinent boundary conditions, one will conclude that the density ratio (as well as the internal Reynolds number, Re_i) does not affect appreciably the corresponding transport coefficients, h and h_M, and, consequently, the Nusselt and Sherwood numbers. This was verified numerically by Feng and Michaelides (2001a,b) for both the hydrodynamic force and the rate of heat transfer: the influence of the density ratio on the heat transfer coefficient is less than 0.1%. This is of the same order of magnitude as the numerical uncertainty of the computations and much lower than the required accuracy for engineering calculations.

1.4.4.2.3 Interfacial Velocity Slip and Temperature Difference All the aforementioned expressions for Nu are based on the no-slip velocity condition at the interface as well as on the assumption that the temperatures of the sphere and the fluid at their interface are equal. It has been experimentally observed that when the size of particles is comparable to the mean free path of the base fluid, there is a significant discontinuity of both the velocity and the temperature at the solid–fluid interface. The effect of the two discontinuities is to decrease the magnitude of the convective heat transfer. The velocity discontinuity at the interface is modeled as in Equations 1.114 and 1.115. The discontinuity at the solid–liquid interface is usually modeled in terms of an *accommodation coefficient*, $\zeta = f(T)$, defined in terms of the molecular collisions on the surface of the sphere. Accordingly, the temperature discontinuity at the solid–liquid interface is expressed by the following boundary condition:

$$T_f-T_s\big|_{r=\alpha}=\left(\frac{c_p}{c_v}\right)\frac{2\left(2-\zeta\right)L_{mol}}{\left(\frac{c_p}{c_v}+1\right)\zeta Pr}\frac{\partial T_f}{\partial r}. \tag{1.196}$$

In most cases with liquids, the ratio of the specific heats of the fluid, c_p/c_v, is approximately equal to 1. When the mean free path is expressed in terms of the Knudsen number, the last equation becomes

$$T_f-T_s\big|_{r=\alpha}=\frac{2\left(2-\zeta\right)aKn}{\zeta Pr}\frac{\partial T_f}{\partial r}. \tag{1.197}$$

Brun (1982) also derived an expression for the heat transfer from a sphere using this thermal boundary condition and verified his solution with experimental data and other analytical results. Feng and Michaelides (2012) used an asymptotic method and derived a solution to the more general problem of heat transfer from solid spheres with velocity and thermal slip at the interface. Their expression agrees with the expression by Brun (1982) for a solid sphere with thermal slip only and with the experimental data by Mikami et al. (1966) in the range $0.01 < Kn < 2$. This general expression for the viscous spheres is

$$Nu=\frac{2}{1+\lambda_t}+\frac{1}{2\left(1+\lambda_t\right)^2}Pe_r+\frac{f_s}{4\left(1+\lambda_t\right)^2}Pe_r^2\ln\left(Pe_r\right)+\frac{1}{2\left(1+\lambda_t\right)^2}$$
$$\times\left[\frac{-156+148f_s-152\lambda+341\lambda f_s+129f_s^2+528\lambda f_s^2}{960\left(1+2\lambda_t\right)}-0.06+0.58\lambda_t\right]Pe_r^2+\frac{1}{16\left(1+\lambda_t\right)^3}Pe_r^3\ln\left(Pe_r\right)+O\left(Pe_r^3\right), \tag{1.198}$$

where f_s is a dimensionless parameter related to the dimensionless velocity slip, $S = 2\mu_c/\beta\alpha$:

$$f_s = \frac{\beta\alpha + 2\mu_c}{\beta\alpha + 3\mu_c} = \frac{1+2S}{1+3S}. \tag{1.199}$$

This parameter is evident in the expression for the drag force on a solid sphere with slip, Equation 1.114. λ_t is another dimensionless parameter that characterizes the thermal slip as modeled by Equation 1.197:

$$\lambda_t = \frac{2(2-\zeta)}{\zeta}\frac{Kn}{Pr}. \tag{1.200}$$

Because λ_t is always positive, the effect of the thermal slip is to reduce *Nu* and by extent the convective heat transfer coefficient of the solid sphere. Equation 1.198 reveals that the velocity slip affects the heat transfer process only at the higher values of Pe_r. Since velocity and temperature discontinuities are observed only with very small spheres of submicron dimensions, where the internal circulation effects are restricted, Equation 1.200 is also a good approximation to the heat (and mass) transfer from viscous spheres as well.

1.4.4.3 Effects of Rotational Motion

The problem of convection heat (or mass) transfer over a heated rotating sphere in a fluid is a classical problem that has been studied extensively in the past. There are several studies found in the literature focusing on the development of experimental techniques to measure the mean heat transfer rate or the average Nusselt number. Kreith et al. (1965) studied the cooling and heating of a solid sphere in several fluids including oil, water, and air. They correlated their measurements for the forced convection heat transfer with the following equation:

$$Nu = 0.43 Pr^{0.4} Re_{rot}^{0.5}. \tag{1.201}$$

Tieng and Yan (1993) studied the mixed convection of a rotating sphere in air. They considered the mixed convection as a resultant effect composed of both free and forced convections. Their results for forced convection at large Reynolds numbers also supported this correlation. However, for smaller Re they suggested a new correlation:

$$Nu = 2 + 0.175 Re_{rot}^{0.583}, \quad Re_{rot} < 33{,}320, \quad Pr = 0.71. \tag{1.202}$$

This is a similar expression as the one initially proposed by Farouk (1985) for the Nusselt number of forced convective heat transfer of a rotating sphere in air. Dorfman and Serazetdinov (1973) used boundary layer theory and derived analytically a similar relation to Equation 1.201, but with a smaller coefficient of 0.33.

The correlations in Equations 1.201 and 1.202 were obtained for flows of Reynolds number above 1000, where a boundary layer is formed at the surface of the sphere. These correlations show that the Nusselt number is proportional to $Re_{rot}^{1/2}$, a characteristic arising from laminar boundary layer theory. For flows of small to moderate Reynolds numbers where the boundary layer theory may not be valid, these correlations are not applicable.

Feng (2014) employed a direct numerical simulation approach combined with immersed boundary method (IBM) to study the convective heat transfer of a heated rotating sphere in otherwise stationary air at low to moderate Reynolds numbers. The sphere is assumed to have a constant temperature; the Prandtl number of air is chosen to be 0.72; the flow Reynolds numbers in study range from 0 to 1000. Figure 1.15 shows the relationship between the mean Nusselt numbers and Reynolds numbers. The correlations by Kreith et al. (1965), by Tieng and Yan (1993), and by Dorfman and Serazetdinov (1973) are also plotted in the figure. It can be seen that these correlations fail to predict the mean Nusselt numbers correctly at $Re < 500$. At Reynolds number between $0 \le Re \le 500$, the simulation data are best fit by the following correlation, as seen in Figure 1.15:

$$Nu = 2 + 0.00051 Re_{rot}^{1.5}, \quad Pr = 0.72, \quad 0 \le Re_{rot} \le 500. \tag{1.203}$$

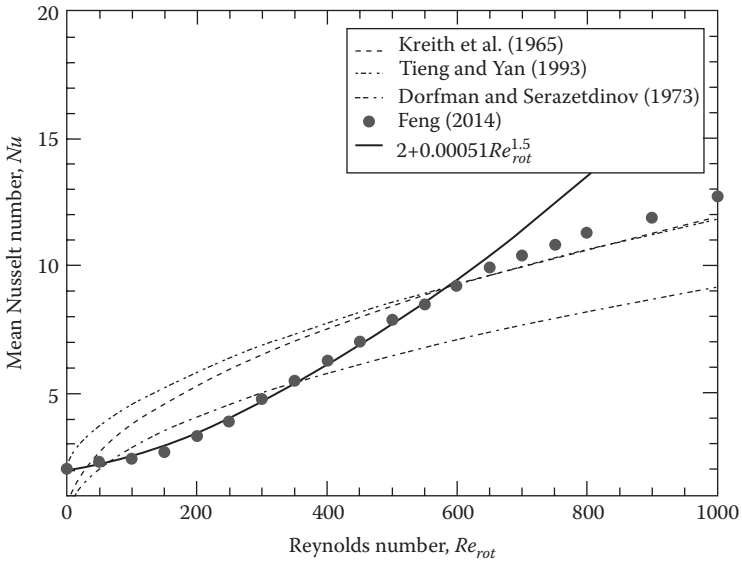

Figure 1.15

Mean Nusselt number versus Reynolds number of rotation for $0 \le Re_{rot} \le 1000$.

1.4.4.4 Effects of Flow Turbulence

As in the case the drag coefficient of particles, free-stream turbulence causes an increase in the heat transfer coefficients. Early experimental studies by Raithby and Eckert (1968) in grid-generated turbulence show that Nu increases rapidly with the turbulence intensity up to $I_r = 1\%$ when Re_r is of the order of 10^3. The Nusselt number subsequently increases, but only linearly with I_r. When Re_r is of the order of 10^4, Nu is proportional to I_r in the whole range of the investigations. Based on several sets of available experimental data, Clift et al. (1978) suggest the following correlation for the increase in the heat transfer coefficient:

$$\frac{Nu}{Nu_0} = 1.0 + 4.8 * 10^{-4} \frac{I_r}{I_{rc}} Re_r^{0.57}, \tag{1.204}$$

where

Nu_0 is the Nusselt number in the absence of free-stream turbulence
I_r is the turbulence intensity
I_{rc} is the critical turbulence intensity

The latter is defined in a way that it makes the Reynolds number of the particle, Re_r, equal to the critical Reynolds number, which was defined in Equation 1.118. From that expression, one may derive the following expression for the critical turbulence intensity, I_{rc}:

$$\begin{aligned} I_{rc} &= \left[5.477 - \log_{10}\left(Re_r\right)\right]/15.8 \quad \text{for } I_r \le 0.15 \\ \text{and} \quad I_{rc} &= \left[3.71 - \log_{10}\left(Re_r\right)\right]/1.75 \quad \text{for } I_r > 0.15. \end{aligned} \tag{1.205}$$

A more recent study on the effect of free-stream turbulence by Yearling and Gould (1995) conducted with evaporating droplets of water, ethanol, and methanol yields the following dependence of Nu on the intensity of turbulence:

$$\frac{Nu}{Nu_0} = 1 + 3.4 I_r^{0.843}. \tag{1.206}$$

Since Yearling and Gould (1995) considered evaporating droplets, Nu_0 is the Nusselt number with the blowing effects, which is given by Equation 1.210. The film properties must be used for all the properties of the materials in the last equation.

1.4.4.5 Blowing Effects

Blowing effects are important for burning droplets when the timescale of burning (mass transfer from the droplet) is of equal or lesser order of magnitude than the timescale for energy transfer. As in the case of momentum transfer, corrections to the heat transfer coefficient have been developed. These corrections take into account the change of the properties of the gaseous boundary layer and the phase change on the surface of the sphere. The two dimensionless numbers, *blowing factors or transfer numbers*, B_H and B_M, which were defined in Equations 1.121 and 1.123, account for the heat and mass transfer effects on the surface of the sphere. These factors are used in corrections for the empirical and analytical correlations on heat and mass transfer from the surface of a constant volume sphere.

Since the origin of the two blowing factors is the radial mass transfer from the surface of the sphere to the carrier fluid, it is evident that the two are not independent. Abramzon and Sirignano (1989) conducted an analytical study on the evaporation of drops and derived expressions for these blowing factors to be used in engineering calculations. In the case of a fuel droplet that burns in air, they derived the following relationship between the two blowing factors:

$$B_H = (1 + B_M)^n - 1. \tag{1.207}$$

The exponent n represents the ratio

$$n = \frac{c_{pF}}{c_{pf}} \frac{1}{Le} \frac{1 + \frac{k}{2}\frac{\sqrt{Re_r/2}}{F(B_M)}}{1 + \frac{k}{2}\frac{\sqrt{Re_r/2}}{F(B_H)}}. \tag{1.208}$$

In the last equation

c_{pF} is the specific heat of the fuel vapor
c_{pf} is the specific heat of the carrier gas
Le is the dimensionless Lewis number
k is an empirical coefficient equal to 0.848
F is a function of the corresponding blowing factor

$$F(B) = (1 + B)^{0.7} \frac{\log(1 + B)}{B}. \tag{1.209}$$

When there is thermodynamic equilibrium and the properties of the material satisfy the conditions $Pr = Sc = 1$, the two transfer coefficients are equal: $B_H = B_M$ (Sirignano, 1999).

Abramzon and Sirignano (1989) obtained semianalytical expressions for the Nusselt and Sherwood numbers for a drop with mass transfer on its surface. Chiang et al. (1992) improved on that study by relaxing some of the most restrictive assumptions and conducting numerical computations on the vaporization of drops. They derived a more general and, very likely, more accurate correlations for the heat and mass transfer coefficients:

$$Nu = 1.275\left(1 + B_H\right)^{-0.678} Re_m^{0.438} Pr_m^{0.619} \tag{1.210}$$

and

$$Sh = 1.224\left(1 + B_M\right)^{-0.568} Re_m^{0.385} Sc_m^{0.492}. \tag{1.211}$$

Both the Reynolds and Schmidt numbers, Re_m and Sc_m, must be calculated using the film transport coefficients, defined by Equation 1.119 and, in the case of Re_m, the free-stream gas density, $\rho_{f\infty}$, far from the droplet. One may use the aforementioned correlations with the heat and mass transport equations to derive the following expressions for the rate of heat and mass transfer of vapor from the surface of a spherical drop:

$$\begin{aligned} \dot{Q} &= 1.275\pi k_f d\left(T_s - T_\infty\right)\left(1 + B_H\right)^{-0.678} Re_m^{0.438} Pr_m^{0.619} \\ \dot{m} &= 1.224\pi d\rho_f D\left(Y_s - Y_\infty\right) B_M \left(1 + B_M\right)^{-0.568} Re_m^{0.385} Sc_m^{0.492}. \end{aligned} \tag{1.212}$$

An alternative method to calculate the heat and mass transfer from a drop is to use another empirical relationship, which is derived from the experimental results by Renksizbulut and Yuen (1983). They correlated their experimental data on the heat transfer from a sphere with mass transfer at its surface by the expression

$$Nu = \frac{2 + 0.584 Re_m^{0.5} Pr^{0.33}}{\left(1 + B_M\right)^{0.7}}. \tag{1.213}$$

This yields the following expressions for the rates of heat and mass transfer from the surface of the spherical drop:

$$\dot{Q} = \pi k_f d\left(T_s - T_\infty\right) \frac{2 + 0.584 Re_m^{0.5} Pr^{0.33}}{\left(1 + B_M\right)^{0.7}} \tag{1.214}$$

and

$$\dot{m} = \pi d \rho_f D (Y_s - Y_\infty) \frac{2 + 0.584 Pe_m^{0.5} Sc^{0.33}}{(1 + B_M)^{0.7}}. \tag{1.215}$$

All the fluid properties in the last four equations that define the Nusselt, Prandtl, and Schmidt numbers are the film properties defined by Equation 1.119. In addition, the relative Reynolds and Peclet numbers Re_m and Pe_m are defined in terms of the gas-film viscosity as in Equation 1.119 and the free-stream gas density, $\rho_{f\infty}$, which is far from the droplet. It is evident from an inspection of these equations that their functional form and coefficients are very similar. It has been confirmed (Sirignano, 1999) that the results of the two expressions do not differ substantially.

1.4.4.6 Transient Effects

Michaelides and Feng (1994) conducted a study on the transient energy equation for spheres, which is analogous to the one by Maxey and Riley (1983) for the equation of motion. The implicit and explicit assumptions for this study are similar to the assumptions for the derivation of the equation of motion and may be summarized as follows:

a. Spherical shape
b. Infinite fluid domain
c. No rotation
d. Highly conducting ($Bi \ll 1$ or $k_f/k_s \ll 1$)
e. Zero initial relative temperature
f. Negligible advection ($Pe_r \ll 1$)

For a rigid, isothermal sphere in a time-variable, nonuniform fluid temperature field $T_f(x_i, t)$, the final form of the transient Lagrangian energy equation is

$$m_s c_{ps} \frac{dT_s}{dt} = -m_f c_{pf} \frac{DT_f}{Dt} - 4\pi a k_f \left[T_s - T_f - \frac{1}{6} a^2 T_{f,jj} \right] - 4\pi a^2 k_f \int_0^t \frac{d/d\tau \left[T_s - T_f - \frac{1}{6} \alpha^2 T_{f,jj} \right]}{\left[\pi \alpha_f (t - \tau) \right]^{1/2}} d\tau, \tag{1.216}$$

where

c_{pf} and c_{ps} are the specific heat capacities of the fluid and the sphere, respectively
α_f in the denominator of the last term is the thermal diffusivity of the fluid, which is equal to $k_f/\rho_f c_{pf}$
The differential operator D/Dt represents the Lagrangian derivative with a reference system of coordinates at the center of the sphere
The temperature T_f is the temperature function of the fluid far from the sphere
The left-hand side of the aforementioned equation denotes the change in the temperature of the sphere due to the heat transfer

The first term in the right-hand side is analogous to the inertia term in the momentum equation and accounts for the (Lagrangian) change in temperature of the mass of displaced fluid. The second term is the usual conduction term from the sphere to the fluid and is analogous to the steady drag term of the equation of motion. This term represents the rate of heat transfer due to the bulk temperature difference between the fluid and the sphere. It is similar to the well-known conduction term that appears in texts, with the inclusion of the Laplacian derivative, which accounts for any nonuniformities of the temperature field. The Laplacian terms are analogous to the Faxen terms of the equation of motion and scale as a^2/L^2. In most of the practical applications where the particle radius is significantly smaller than the characteristic dimension of the fluid and $a^2/L^2 \ll 1$, these corrections are insignificant and may be neglected. The last term in the energy equation is a history integral, which results from the diffusion of the temperature gradients in the fluid temperature field and is also corrected for the nonuniformity (curvature) of the temperature field. It is apparent that this history term depends on the temporal as well as the spatial variation of the temperature field and is exactly analogous to the history term of the equation of motion. This history term may account for a significant part of the transient heat transfer to a sphere, as it may be seen in Figure 1.16.

It must be pointed out that the added mass term in the equation of motion derives from the pressure gradient term in the momentum equation. Since the governing equation for the energy transfer does not have a term equivalent to ∇p, there is no term corresponding to the added mass term in the transient energy equation. The absence of the added mass term is the main difference in the functional forms of the equations of motion and temperature variation under creeping flow conditions as well as at finite Reynolds numbers. It is apparent that there is not a mathematical similarity between the transient equations of motion and energy for particles, drops, or bubbles. However, there are several analogous results in the momentum and heat exchange processes for viscous and solid spheres.

As with the equation of motion, the assumption of equal temperatures at the interface may be relaxed. In this case, the history term is substituted by the expression

$$4\pi a^2 k_f \int_0^t \frac{d/d\tau\left[T_s - T_f - \frac{1}{6}a^2 T_{f,jj}\right]}{\left[\pi\alpha_f(t-\tau)\right]^{1/2}} d\tau + 4\pi a^2 k_f \frac{T_s(0) - T_f(0)}{\sqrt{\pi a_f t}}. \tag{1.217}$$

Gay and Michaelides (2003) conducted a numerical study to compute the effect of the history term on the heat transferred to a sphere at creeping flow conditions by considering three types of variation of the carrier fluid temperature: (1) a step change, (2) a ramp change, and (3) a sinusoidal variation. The main parameters for this

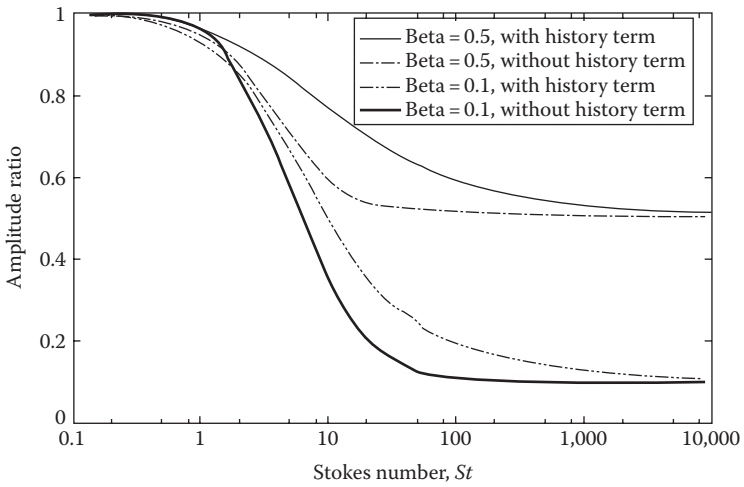

Figure 1.16

The effect of the thermal Stokes number on the heat transfer from rigid particles with and without the history term.

study are the volumetric heat capacity ratio $\beta = \rho_f c_{pf}/\rho_s c_{ps}$ and a thermal Stokes number, St_t, which is defined as the ratio of the thermal timescale of the particle $\tau_s = a^2\rho_f c_f/k_f$ to the characteristic timescale of the fluid:

$$St_t = \frac{a^2 \rho_f c_f \omega}{k_f}. \tag{1.218}$$

The history term is of importance in the computations of the heat flux when the ratio of the volumetric heat capacities, β, is between 0.002 and 0.5. This is the range of liquid–solid flows and droplet flows in heavier gases. The study found almost no effect of the history term on the heat transfer for bubbles, which are in the range $\beta > 10$. Typical result of these computations for a sinusoidal oscillation of the fluid temperature field with frequency ω is depicted in Figure 1.16 (from Gay and Michaelides, 2003). This figure demonstrates that neglecting the history term in the energy equation may lead to an underestimation of the instantaneous rate of heat transfer by as much as 35%, a significant fraction for most engineering computations.

Feng and Michaelides (1997) performed a study on the transient energy equation for a spheroid of eccentricity ε, which is analogous to the study by Lawrence and Weinbaum (1986) for the drag on a spheroid. They derived the following equation for the heat transfer from a spheroid:

$$Q(t^\star) = -4\pi\left\{\left(1+\frac{2}{3}\varepsilon-\frac{1}{45}\varepsilon^2\right)(T_s^\star - T_\infty^\star)+\left(1+\frac{4}{3}\varepsilon-\frac{2}{3}\varepsilon^2\right)\int_0^t \frac{d/d\tau^\star (T_s^\star - T_\infty^\star)}{\sqrt{\pi(t^\star-\tau^\star)}}d\tau^\star + \right.$$
$$\left. +\frac{1}{3}\left(1+\frac{2}{9}\varepsilon+\varepsilon^2\right)\frac{DT_\infty^\star}{Dt^\star}+\varepsilon^2\frac{4}{45}\sqrt{\frac{\pi}{3}}\int_0^t\left[\frac{d}{dt^\star}(T_s^\star - T_\infty^\star)\right]G'(t^\star-\tau^\star)d\tau^\star\right\}, \tag{1.219}$$

where all the variables are in dimensionless form and the function $G'(t)$ depends on the frequency of variation of the fluid temperature field

$$G'(t) = Im\left[\sqrt{\pi\Phi}e^{\Phi t^\star}erfc\left(\sqrt{\Phi t^\star}\right)\right] \quad \text{and} \quad \Phi = 3e^{i\frac{\pi}{3}}. \tag{1.220}$$

The last term in Equation 1.219 depends entirely on the eccentricity and the frequency of variation of the external temperature field. The kernel of this term does not necessarily follow the $t^{-1/2}$ decay of the typical history term in creeping flows and depends on the frequency of the variation of the velocity of temperature fields. Feng and Michaelides (1997) showed that when the frequency of variation of the velocity and temperature fields is not high, the contribution of this new history term to the total heat flux is much smaller than the contributions of the other transient terms.

Feng and Michaelides (1998a) also performed a study on the energy equation of a particle with arbitrary motion and in an arbitrary temperature field with finite but small inertia. This study is analogous to the one performed by Lovalenti and Brady (1993) for the equation of motion, and its results are expressed in terms of Pe_r and *Sl*. Details of the transient hydrodynamic force and heat transfer of particles, bubbles, and drops at finite Re_r and Pe_r may be found in Michaelides (2006).

1.4.4.7 Radiation Effects

Thermal radiation is the mode of heat transfer through which electromagnetic energy is continuously emitted and absorbed by a system. This energy exchange applies to the system under observation as well as all the other systems in its surroundings. For a sphere whose surface temperature is T_s, the emitted radiation energy is equal to

$$\dot{Q}_{rad}^{em} = \sigma\varepsilon\pi d^2 T_s^4, \tag{1.221}$$

where

σ is the Stefan–Boltzmann constant, $5.669 * 10^{-8}$ W/m^2 K^4

ε is the emissivity of the sphere

The emissivity of a blackbody is equal to one. Similarly, the sphere absorbs heat from all the objects in its surroundings. In the simple case where the sphere is enclosed by a single medium of temperature T_∞, the sphere absorbs thermal radiation equal to

$$\dot{Q}_{rad}^{ab} = \sigma\alpha\pi d^2 T_\infty^4, \tag{1.222}$$

where α is the absorptivity of the sphere. In general, the absorptivity and the emissivity of a material are functions of its temperature and are equal in magnitude: $\alpha(T_s) = \varepsilon(T_s)$.

The net rate of energy that enters the sphere as a result of thermal radiation is equal to the difference of the two aforementioned equations and, in analogy with the convection mode of heat transfer, may be given in terms of a radiation coefficient, h_{rad}:

$$\dot{Q}_{rad}^{ab} - \dot{Q}_{rad}^{em} = \sigma\varepsilon\pi d^2 (T_\infty^4 - T_s^4) = \pi d^2 h_{rad} (T_\infty - T_s). \tag{1.223}$$

The radiation coefficient is a strong function of temperature. It is obvious that when the temperature difference of the sphere and its surroundings is sufficiently high, the net energy exchanged by radiation is significant and may actually surpass the energy exchange due to the other two modes of heat transfer, conduction and convection. The total rate of heat entering the sphere is the sum of the convection and radiation:

$$\dot{Q}_T = \pi d^2 (h_{rad} + h)(T_\infty - T_s). \tag{1.224}$$

It must be pointed out that in the case of radiation one has to account not only for the carrier gas but also for all the boundaries and other objects in the vicinity of the sphere. The sphere exchanges radiation with any other object or surface that it "sees." In the general case, when this body is surrounded by many objects, including other similar bodies in the same carrier fluid, the determination of the net thermal radiation or the thermal radiation coefficient must be carried out by carefully evaluating the effects of all the surfaces in the surroundings and the shape factors of these surfaces. This may become a challenging task. A more extensive description of the processes and the methods used for the determination of radiative heat transfer may be found in a specialized treatise on the subject, such as the one by Siegel and Howel (1981).

An interesting consequence of radiation heat transfer with particles is that radiation may cause a significant deviation of the temperature of the particle from that of the surrounding fluid and in extreme cases natural convection from a particle. Let us consider a spherical particle in a fluid stream of temperature T_f and velocity u, inside a long channel whose walls are at a different temperature T_w. The particle reaches an equilibrium temperature, which is defined by a zero net heat gain at its surface and is characterized by equal and opposite magnitudes of the convection and radiation. In the simplest case of blackbody radiation and a nonabsorbing gas, this equilibrium yields the following expression for the temperature of the particle:

$$h_c (T_f - T_s) = h_{rad} (T_{th} - T_w) \Rightarrow T_s = \frac{h_c T_f + h_{rad} T_w}{h_c + h_{rad}}. \tag{1.225}$$

This analysis implies that the particle temperature will be close to the temperature of the gas, T_f, only when $h_c \gg h_{rad}$. On the contrary, the particle temperature will be close to that of the surrounding boundaries, T_w, when $h_c \ll h_{rad}$. In all cases, the particle will reach an intermediate temperature, which is not equal to the temperature of the fluid, T_f, that surrounds it. Several interesting effects may occur if the temperature difference between fluid and particles, $T_s - T_f$, becomes significant: natural convection and buoyancy effects will develop around the particles and the particles will experience an upward draft. The draft affects both the particle motion and the heat transfer from it. If this natural convection is strong enough, the particles may even be carried upward with the locally buoyant fluid (Feng and Michaelides, 2008, 2009).

1.4.5 Effects of Concentration

Most of the analytical, experimental, and numerical results presented in the previous sections were derived for single particles, bubbles, and drops. However, the majority of practical applications involve the flow of groups of interacting particles, bubbles, or drops. Interactions of these objects and the formation of clusters

and aggregates with correlated motions play an important role on the value of the hydrodynamic force and heat transfer. It is accepted, in general, that one may use the results and apply the theory of single particles, bubbles, and drops in a flowing mixture if the mixture is *dilute*, that is, if the concentration of the mixture is less than 6.5%. In dispersed mixtures like this, spheres are separated on the average by one diameter. Intermediate concentrations are in the range $6.5\% < C < 30\%$. In this range, particle-to-particle interactions are as important in the determination of all the transport coefficients as particle-to-fluid interactions. In applications with very dense concentrations, $C > 30\%$, particle interactions are the main mechanism for the transport processes and particle–fluid interactions are of lesser importance. Therefore, the effect of concentration on the transport coefficients is of paramount importance in engineering processes.

Regarding the steady hydrodynamic force, Richardson and Zaki (1954) carried one of the earlier series of experiments on the sedimentation of particles in a quiescent fluid, which is bounded by a channel of diameter D. By correlating the settling velocity of the particles to the concentration of the mixture, they concluded that the drag coefficient of a single sphere must be multiplied by a correction factor equal to

$$(1 - C)^{-K}, \tag{1.226}$$

where

C is the concentration of solids

exponent K is a weak function of the Reynolds number

K was correlated as follows:

$$\begin{array}{ll} Re_r \le 0.2 & K = 4.65 + 19.5 d/D \\ 0.2 < Re_r \le 1 & K = (4.35 + 17.5 d/D) Re_r^{-0.03} \\ 1 < Re_r \le 200 & K = (4.45 + 18 d/D) Re_r^{-0.1} \\ 200 < Re_r \le 500 & K = 4.45 Re_r^{-0.1} \\ Re_r > 500 & K = 2.39. \end{array} \tag{1.227}$$

It is apparent that the exponent K may attain any value in the range 2.4–5.7. Later experimental data by Rowe (1961) with arrays of solid spheres in water and air determined that the drag coefficients are better correlated with the single constant $K = 3$.

Another correlation, which is widely used in fluidization systems, is the one by Wen and Wu (1966). They included the effects of Re_r on the terminal velocity of a single particle and derived a correlation for the effect of concentration that is independent of the Reynolds number:

$$C_D = C_{D0}(1-C)^{-K} \quad \text{with } K = 3.7\,. \tag{1.228}$$

Wen and Wu (1966) recommend the Schiller and Nauman expression for the drag coefficient at zero concentration, $C_{D0} = 24(1 + 0.15 Re_r^{0.687})/Re_r$.

Di Felice (1994) used several sets of data available in the literature, including those by Richardson and Zaki (1954) and Wen and Wu (1966), to develop a more general and probably more accurate expression for the drag coefficient. He derived the following correlation, which is applicable in the range $10^{-2} < Re_r < 10^4$:

$$C_D = C_{D0}\left(1-C\right)^{-K} \quad \text{with } K = 3.7 - 0.65 \exp\left[-\frac{\left(1.5 - \log Re_r\right)^2}{2}\right]. \tag{1.229}$$

The subject of interacting particles, bubbles, and drops is rather difficult to investigate experimentally, but ideally suited for computational simulations, where different initial conditions may be examined and statistical results are relatively easy to derive. Modern computational techniques and more powerful computers have allowed the accurate modeling of groups of spheres with the flow properties of solid particles, bubbles, or drops to be studied in numerical experiments. Finite element methods and the lattice

Boltzmann method (LBM) have enabled scientists and engineers to perform *thought experiments* of groups of interacting spheres and, thus, to obtain the effect of interactions on the hydrodynamic force exerted on individual spheres under specific and well-defined conditions. In particular, the LBM and its derivative, the IBM (Feng and Michaelides, 2004b, 2005), are ideally suited methods for the determination of the interaction of groups of particles, drops, and bubbles of any shape and material properties. These recently developed methods have enabled the simulation of processes involving very large groups of particles, of the order of tens of thousands.

Kaneda (1986) used an asymptotic method to derive the steady component of the hydrodynamic force on an array of solid spheres at small but not vanishing Re_r and very low concentrations. He developed the following relationship for the average drag coefficient, C_D:

$$C_D = 1 + (\sqrt{2}/3)C^{1/2} + (\sqrt{2}/40)C^{-1/2}Re_r^2, \tag{1.230}$$

which is valid at distances where the inertia of the sphere is important. In the case of flows with several interacting objects, inertia becomes important at distances far from the *Brinkman screening length*. In the case of an array of spheres, the Brinkman screening length is equal to $C^{1/2}$, and hence, the range of applicability of this expression is $C^{1/2} \gg Re_r$. Kaneda (1986) also concluded that in the opposite limit, ($C^{1/2} \ll Re_r$), the Oseen correction to the Stokes drag ($1 + 3/16Re_r$) should be used for the average drag coefficient of the spheres. Working with arrays of two-dimensional particles in flows at small but finite Re_r and using the LBM, Koch and Ladd (1997) and Rojas and Koplik (1998) also confirmed that the Oseen relationship for the steady component of the hydrodynamic force applies to particles at small but finite Re_r.

Koch and Sangani (1999) used the LBM for a packed bed of particles and performed calculations on the rectilinear drag coefficients with fixed arrays of spheres. Their system is essentially a well-organized porous medium. They found out that the steady drag component may be scaled as Re_r^2 in high-concentration suspensions and depends on the concentration. Koch and Sangani (1999) obtained the following relationship for the steady hydrodynamic force in dense concentrations, $C > 40\%$, applicable to finite but small values of Re_r:

$$C_D = C_{D0}(C) + C_{D1}(C)Re_r^2. \tag{1.231}$$

The first function of this expression, which is the equivalent of the dimensionless Stokes drag force, is

$$C_{D0}(C) = \frac{1 + 3(C/2)^{1/2} + 2.11C\ln C + 16.14C}{1 + 0.681C - 8.48C^2 + 8.16C^3}. \tag{1.232}$$

The ratio of the functions C_{D1}/C_{D0} in this study diminishes with the increasing concentration of the solid particles. Hence, the second term in Equation 1.231 is very small in comparison to the first term at sufficiently high values of C. Because of this, Koch and Sangani (1999) claimed that the nonlinear behavior of the steady part of the average hydrodynamic force for close-packed arrays is difficult to be observed with the currently available experimental means.

Koch and Hill (2001) also performed computational studies using the LBM at higher Reynolds numbers and concluded that the steady component of the hydrodynamic force increases linearly with Re_r according to the following correlation:

$$C_D = C_{D0}(C) + \left[0.0673 + 0.212C + 0.0232(1 - C)^{-5}\right]Re_r, \tag{1.233}$$

where the function $C_{D0}(C)$ is the same as in Equation 1.231. Koch and Hill (2001) concluded that this expression agrees very well with experimental results and empirical relations derived in the past for packed beds of particles.

Bubbles are modeled as inviscid and weightless spheres moving in a medium, which is often idealized as an inviscid fluid. Because in the case of bubbles the added mass term is by far greater than the other components of the hydrodynamic force, such spheres accelerate as if their masses were equal to the mass of the

fluid occupying half of their volume, that is, fluid of mass $m_s = 2/3\pi\rho_f a^3$. For swarms of bubbles moving in a fluid with concentration C, the added mass coefficient, Δ_A, is a function of the concentration of the bubbles. Zuber (1964) used the simple theory of a bubble in a cell model for the flow of groups of bubbles to obtain analytically the following correction to the added mass coefficient:

$$\Delta_A = \frac{1+2C}{1-C}. \tag{1.234}$$

This expression is very simple to use in repetitive computations, and according to Sangani et al. (1991), it is sufficiently accurate and applies to a wide variety of conditions. Van Wijngaarten (1976) performed an asymptotic analytical study in the case of a swarm of bubbles that are impulsively accelerated and concluded that, with accuracy of the order of C^2, the added mass coefficient of a group with concentration C is equal to

$$\Delta_A = 1 + 2.76C + O(C^2). \tag{1.235}$$

A great deal of knowledge on the behavior of interacting bubbles has been recently developed as a result of computer simulations. Spelt and Sangani (1998) performed such a simulation to determine the influence of the fluid pseudo-turbulence—the velocity fluctuations in the carrier fluid, due to the motion of particles and bubbles—on the hydrodynamic force and the drag coefficient of a swarm of bubbles. They concluded that there is a weak dependence of the added mass coefficient on the fluid velocity fluctuations, but a significant dependence of the added mass on the bubble concentration. Their final expression, valid for $C < 0.3$, is

$$\Delta_A = \frac{1+2C+0.225CJ_A}{1-C}, \tag{1.236}$$

where J_A is a dimensionless measure of the temporal velocity fluctuations of the fluid. With a similar analysis, Spelt and Sangani (1998) obtained the following expression for the steady viscous drag coefficient for a swarm of bubbles in a viscous fluid:

$$C_D = \frac{1+0.15CJ_A}{(1-C)^2}. \tag{1.237}$$

1.4.5.1 Porous Particles

Large groups of interacting particles, clusters, and aggregates in dense flows may be approximated and treated as porous media. The permeability and porosity of such a porous media depend on the concentration. Similarly, clouds or large groups of smaller spheres may be approximated as larger porous spheres that are transported in a fluid medium. Jones (1973) obtained an expression for the steady hydrodynamic force on a porous sphere at creeping flow conditions:

$$F_i = 6\pi a\mu_f (u_i - v_i)\frac{2\zeta^2(1+2\eta\zeta^{-1})}{2\zeta^2+3+6\eta\zeta+6\eta\zeta^{-1}}, \tag{1.238}$$

where

ζ is the inverse of the dimensionless permeability of the sphere ($\zeta = a/\kappa^{1/2}$, with κ being the permeability of the sphere)

η is a dimensionless constant that depends on the properties of the porous medium

The permeability, κ, of a group of particles that form a porous medium is related to the porosity and, by extent, to the concentration, C, by the so-called Carman–Kozeny equation:

$$\kappa = \frac{(1-C)^3}{180C^2}d^2. \tag{1.239}$$

Feng and Michaelides (1998b) used an asymptotic expansion and extended this result to finite Reynolds numbers, Re_r, by developing corrections for Re_r up to the order Re_r^2. Their final expression for the drag force of such porous spheres is

$$F_i = 6\pi a\mu_f\left(u_i - v_i\right)\frac{2\left(1+\frac{\eta}{\zeta}\right)\zeta^2}{4\eta\zeta+2\zeta^2+3\frac{\eta}{\zeta}+1}\left[1+Re_r\frac{3\left(1+\frac{\eta}{\zeta}\right)\zeta^2}{4\left(4\eta\zeta+2\zeta^2+3\frac{\eta}{\zeta}+1\right)}+Re_r^2\ln\left(Re_r\right)\frac{9\left(1+\frac{\eta}{\zeta}\right)^2\zeta^4}{10\left(4\eta\zeta+2\zeta^2+3\frac{\eta}{\zeta}+1\right)^2}\right]. \tag{1.240}$$

$$C_D = \frac{24}{Re_r}\frac{2\left(1+\frac{\eta}{\zeta}\right)\zeta^2}{4\eta\zeta+2\zeta^2+3\frac{\eta}{\zeta}+1}\left[1+Re_r\frac{3\left(1+\frac{\eta}{\zeta}\right)\zeta^2}{4\left(4\eta\zeta+2\zeta^2+3\frac{\eta}{\zeta}+1\right)}+Re_r^2\ln\left(Re_r\right)\frac{9\left(1+\frac{\eta}{\zeta}\right)^2\zeta^4}{10\left(4\eta\zeta+2\zeta^2+3\frac{\eta}{\zeta}+1\right)^2}+O\left(Re_r^2\right)\right]$$

Re_r is based on the diameter of the whole cloud of small spheres and on the average relative velocity of the cloud. The last equation yields the correct behavior in the extreme cases of zero and infinite permeability: for a solid sphere ($\kappa \to 0$), this expression yields the hydrodynamic force expression obtained by Proudman and Pearson (1956) (Equation 1.103), while at low permeability ($\kappa \to 0$), it yields the result by Joseph and Tao (1964). At creeping flow, it yields the expression for the drag force that was first predicted by the study of Saffman (1971).

Looker and Carnie (2004) studied the transient hydrodynamic force of an oscillating porous sphere with velocity slip at its interface (a condition that was also studied by Saffman, 1971). They derived an asymptotic expression for the transient hydrodynamic force on the porous sphere with slip, valid up to the order of $\kappa^{1/2}$. Most of the results of this study may also be derived from the fundamental equation of a sphere with slip at its interface, Equation 1.138.

Nomenclature

Latin

a	Particle, droplet radius (m)
A	Area (m^2)
B_H	Blowing factor
B_M	Blowing parameter
c	Specific heat
c_p	Specific heat at constant pressure (J/kg·K)
c_v	Specific heat at constant volume (J/kg·K)
C	Concentration
C_D	Drag coefficient
C_L	Lift coefficient
d	Particle, droplet diameter (m)
d_A	Area-equivalent diameter (m)
d_V	Volume-equivalent diameter (m)
D	Diffusion coefficient (m^2/s)
D	Pipe/channel diameter (m)
f	Frequency distribution (continuous)
$f,$	Frequency distribution (discrete)
$F,$	Cumulative distribution
F	Force (N)
F_D,$F_{D,i}$	Drag force vector (N)
F_L,$F_{L,i}$	Lift force vector (N)
g,g_i	Gravity vector (m/s^2)
h	Specific enthalpy (J/kg), heat transfer coefficient (J/m^2-K)
h_{fg}	Latent heat of evaporation (J/kg)

h_M	Mass transfer coefficient
ΔH	Heat of combustion
I	Turbulence intensity
k	Thermal conductivity (J/m-K)
k	Ratio specific heats
l_m	Molecular mean free path
l_w	Distance to wall
L	Characteristic length (m)
m	Mass (kg)
$\dot{m}$	Mass flow rate (kg/s)
M	Molecular weight (kmol/kg)
n	Number density ($1/m^3$)
p	Pressure (Pa)
$\dot{Q}$	Heat transfer rate (W)
r, r_i	Radius vector
R	Gas constant (kJ/kg·K)
R_u	Universal gas constant (kJ/kmol K)
S	Dimensionless slip
T	Temperature (K)
t	Time (s)
u	Phase velocity of fluid (m/s)
U_a	Superficial velocity of phase "a" (m/s)
u	Velocity component in x-direction (m/s)
u_i,u	Velocity vector, continuous phase (m/s)
U	Characteristic velocity (m/s)
v_i,v	Velocity vector, dispersed phase (m/s)
V	Volume (m^3)
V_r	Migration velocity (m/s)
V_s	Settling velocity (m/s)
V_t	Terminal velocity (m/s)
w	Relative velocity (m/s)
w_i	Relative velocity vector (m/s)
x_i	Coordinate vector (m)
x	Quality, coordinate direction (m)
X	Mole fraction
y	Coordinate direction (m)
Y	Mass fraction
z	Vertical coordinate direction (m)
Z	Loading

Greek

α	Absorptivity
α_a	Volume fraction of phase "a"
β	Density ratio
β	Slip parameter
γ	Shear, rate of strain
Δ	Additional term of the Nusselt number
Δ_A	Added mass coefficient
Δ_H	History term coefficient
ε	Emissivity
ζ	Inverse of the dimensionless permeability
η	Dimensionless constant
θ	Angle, azimuthal angle (°)
κ	Permeability
λ	Viscosity ratio
μ	Dynamic viscosity (N/m-s), mean value

ν	Kinematic viscosity (m^2/s)
Ξ	Particle–cylinder diameter ratio
ρ	Density (kg/m^3)
ρ_m	Mixture density (kg/m^3)
σ	Surface tension (N/m)
σ	Standard deviation
σ	Stefan–Boltzmann constant
τ_V	Velocity response time (s)
τ_T	Thermal response time (s)
τ_c	Collision time (s)
ϕ	Velocity ratio
ψ	Stream function
Ψ	Shape factor for particles
Ω	Angular velocity (1/s)

Subscripts

c	Continuous phase, cluster
cr	Critical
d	Dispersed phase
f	Fluid
GM	Geometric mean
HM	Harmonic mean
m	Maximum, mass
M	Magnus, median
n	Number
p	Particle
r	Relative
s	Solid
S	Dimensionless slip ratio
*S*M	Surface mean
T, t	Thermal
VM	Volumetric mean
w	Wall
θ	Circumferential, tangential direction
∞	Free stream

Dimensionless Numbers

Ac	Acceleration number
Bo	Bond number
Eo	Eötvös number
Kn	Knudsen number
Le	Lewis number
Ma	Mach number
Mo	Morton number
Nu	Nusselt number
Pe	Peclet number
Pr	Prandtl number
Re	Reynolds number
Re_γ	Shear Reynolds number
Re_r	Relative Reynolds number
Re_R	Rotation Reynolds number
Sc	Schmidt number
Sh	Sherwood number
Sl	Strouhal number
St	Stokes number
We	Weber number

References

Abramzon, B. and Sirignano, W.A., Droplet vaporization for spray combustion calculations, *Int. J. Heat Mass Transfer*, 32, 1605–1618, 1989.

Achenbach, E., Vortex shedding from spheres, *J. Fluid Mech.*, 62, 209–221, 1974.

Acrivos, A., A note on the rate of heat or mass transfer from a small particle freely suspended in linear shear field, *J. Fluid Mech.*, 98, 299–304, 1980.

Acrivos, A. and Goddard, J.D., Asymptotic expansions for laminar convection heat and mass transfer, *J. Fluid Mech.*, 23, 273–291, 1965.

Acrivos, A. and Taylor, T.E., Heat and mass transfer from single spheres in stokes flow, *Phys. Fluids*, 5, 387–394, 1962.

Auton, T.R., Hunt, J.R.C., and Prud'homme, M., The force exerted on a body in inviscid unsteady non-uniform rotational flow, *J. Fluid Mech.*, 197, 241–257, 1988.

Barndorff-Nielsen, O., Exponentially decreasing distributions of the logarithm of particle size, *Proc. Res. Soc. Lond. A*, 353, 401, 1977.

Basset, A.B., *Treatise on Hydrodynamics*, Bell, London, U.K., 1888a.

Basset, A.B., On the motion of a sphere in a viscous liquid, *Philos. Trans. R. Soc. Lond.*, 179, 43–63, 1888b.

Bataille, J., Lance, M., and Marie, J.L., Bubbly turbulent shear flows, in J. Kim, U. Rohatgi, and M. Hashemi (Eds.), *ASME-FED*, *99*, New York, 1990, pp. 1–7.

Bhaga, D. and Weber, M.E., Bubbles in viscous liquids: Shapes, wakes and velocities, *J. Fluid Mech.*, 105, 61–85, 1981.

Bohlin, T., *Terminal Velocities of Solid Spheres in Cylindrical Enclosures*, Report # 155, Transactions of the Royal Institute of Technology, Stockholm, Sweden, 1960.

Bond, W.N. and Newton, D.A., Bubbles, drops and Stokes law, *Philos. Mag.*, 5, 794–800, 1928.

Boussinesq, V.J., Sur la Resistance qu' Oppose un Liquide Indéfini en Repos…, *Comptes Rendu*, *Acad. Sci. Paris*, 100, 935–937, 1885.

Brenner, H., The slow motion of a sphere through a viscous fluid toward a plane surface, *Chem. Eng. Sci.*, 16, 242–251, 1961.

Brock, J.R., On the theory of thermal forces acting on aerosol particles, *J. Colloid Interface Sci.*, 17, 768–780, 1962.

Brun, P.O., Heat or mass transfer from single spheres in a low Reynolds number flow, *Int. J. Eng. Sci.*, 20, 817–822, 1982.

Bushell, G.C., Yan, Y.D., Woodfield, D., Raper, J., and Amal, R., On techniques for the measurement of the mass fractal dimension of aggregates, *Adv. Colloid Interface Sci.*, 95(1), 1–50, 2002.

Carlson, D.J. and Hoglund, R.F., Particle drag and heat transfer in rocket nozzles, *AIAA J.*, 2, 1980–1984, 1964.

Cherukat, P. and McLaughlin, J.B., Wall-induced lift on a sphere, *Int. J. Multiphase Flow*, 16, 899–907, 1990.

Chhabra, R.P., Singh, T., and Nandrajog, S., Drag on chains and agglomerates of spheres in viscous Newtonian and power law fluids, *Can. J. Chem. Eng.*, 73, 566–571, 1995.

Chiang, C.H., Raju, M.S., and Sirignano, W.A., Numerical analysis of a convecting, vaporizing fuel droplet with variable properties, *Int. J. Heat Mass Transfer*, 35, 1307–1327, 1992.

Clamen, A. and Gauvin, W.H., Effects of turbulence on the drag coefficients of spheres in a supercritical flow regime, *AIChE J.*, 15, 184–189, 1969.

Clift, K.A. and Lever, D.A., Isothermal flow past a blowing sphere, *Int. J. Numer. Methods Fluids*, 5, 709–715, 1985.

Clift, R. and Gauvin, W.H., The motion of particles in turbulent gas streams, *Proc. Chem. ECA*, 1, 14–24, 1970.

Clift, R., Grace, J.R., and Weber, M.E., *Bubbles*, *Drops and Particles*, Academic Press, New York, 1978.

Cox, R.G. and Brenner, H., The slow motion of a sphere through a viscous fluid towards a plane surface, *Chem. Eng. Sci.*, 22, 1753–1777, 1967.

Cox, R.G. and Hsu, S.K., The lateral migration of solid spheres in a laminar flow near a plane, *Int. J. Multiphase Flow*, 3, 201–222, 1977.

Crowe, C.T., Babcock, W.R., and Willoughby, P.G., Drag coefficient for particles in rarefied low Mach number flows, *Prog. Heat Mass Transfer*, 6, 419–428, 1973.

Crowe, C.T., Babcock, W.R., Willoughby, P.G., and Carlson, R.L., Measurement of particle drag coefficients in flow regimes encountered by particles in a rocket nozzle, United Technology Centre Report, 2296-FR, Sunnyvale, CA, 1969.

Crowe, C.T., Sommerfeld, M., and Tsuji, Y., *Multiphase Flows with Droplets and Particles*, CRC Press, Boca Raton, FL, 1998.
Dandy, D.S. and Dwyer, H.A., A sphere in shear flow at finite Reynolds number: Effect of particle lift, drag and heat transfer, *J. Fluid Mech.*, 226, 381–398, 1990.
Di Felice, R., The voidage function for fluid–particle interaction systems, *Int. J. Multiphase Flow*, 20, 153–162, 1994.
Dorfman, L.A. and Serazetdinov, A.Z., Laminar flow and heat transfer near rotating axisymmetric surface, *Int. J. Heat Mass Transfer*, 8, 317–327, 1973.
Eisenklam, P., Arunachalam, S.A., and Weston, J.A., Evaporation rates and drag resistance of burning drops, in *Proceedings of the 11th International Symposium on Combustion*, Pittsburgh, PA, 1967, pp. 715–721.
Epstein, P., Zur theorie des radiometers, *Z. Physik*, 54, 537–563, 1929.
Farouk, B., Mixed convective flow around a slowly rotating isothermal sphere, *Trans. ASME, J. Heat Transfer*, 107, 431–438, 1985.
Faxen, H., Der Widerstand gegen die Bewegung einer starren Kugel in einer zum den Flussigkeit, die zwischen zwei parallelen Ebenen Winden eingeschlossen ist, *Ann. Phys.*, 68, 89–119, 1922.
Fayon, A.M. and Happel, J., Effect of a cylindrical boundary on a fixed rigid sphere in a moving viscous fluid, *AIChE J.*, 6, 55–58, 1960.
Feng, Z.G., A correlation of the drag force coefficient on a sphere with interface slip at low and intermediate Reynolds numbers, *J. Dispersion Sci. Technol.*, 31, 968–974, 2010.
Feng, Z.G., Forced heat and mass transfer from a slightly deformed sphere at small but finite Peclet numbers in Stokes flow, *J. Heat Transfer*, 135, 081702, 2013.
Feng, Z.G., Direct numerical simulation of forced convective heat transfer from a heated rotating sphere in laminar flows, *J. Heat Transfer*, 136, 041707, 2014.
Feng, Z.-G. and Michaelides, E.E., Transient heat and mass transfer from a spheroid, *AIChE J.*, 43, 609–616, 1997.
Feng, Z.-G. and Michaelides, E.E., Transient heat transfer from a particle with arbitrary shape and motion, *J. Heat Transfer*, 120, 674–681, 1998a.
Feng, Z.-G. and Michaelides, E.E., Motion of a permeable sphere at finite but small Reynolds numbers, *Phys. Fluids*, 10, 1375–1383, 1998b.
Feng, Z.-G. and Michaelides, E.E., A numerical study on the transient heat transfer from a sphere at high Reynolds and Peclet numbers, *Int. J. Heat Mass Transfer*, 43, 219–229, 2000a.
Feng, Z.-G. and Michaelides, E.E., Mass and heat transfer from fluid spheres at low Reynolds numbers, *Powder Technol.*, 112, 63–69, 2000b.
Feng, Z.-G. and Michaelides, E.E., Drag coefficients of viscous spheres at intermediate and high Reynolds numbers, *J. Fluids Eng.*, 123, 841–849, 2001a.
Feng, Z.-G. and Michaelides, E.E., Heat and mass transfer coefficients of viscous spheres, *Int. J. Heat Mass Transfer*, 44, 4445–4454, 2001b.
Feng, Z.-G. and Michaelides, E.E., Inter-particle forces and lift on a particle attached to a solid boundary in suspension flow, *Phys. Fluids*, 14, 49–60, 2002a.
Feng, Z.-G. and Michaelides, E.E., Hydrodynamic force on spheres in cylindrical and prismatic enclosures, *Int. J. Multiphase Flow*, 28, 479–496, 2002b.
Feng, Z.-G. and Michaelides, E.E., Equilibrium position for a particle in a horizontal shear flow, *Int. J. Multiphase Flow*, 29, 943–957, 2003.
Feng, Z.-G. and Michaelides, E.E., An immersed boundary method combined with lattice Boltzmann method for solving fluid and particles interaction problems, *J. Comput. Phys.*, 195, 457–472, 2004b.
Feng, Z.-G. and Michaelides, E.E., Proteus: A direct forcing method in the simulations of particulate flow, *J. Comput. Phys.*, 202, 20–51, 2005.
Feng, Z.G. and Michaelides, E.E., Inclusion of heat transfer computations for particle laden flows, *Phys. Fluids*, 20, 1–10, 2008.
Feng, Z.G. and Michaelides, E.E., Heat transfer in particulate flows with Direct Numerical Simulation (DNS), *Int. J. Heat Mass Transfer*, 52, 777–786, 2009.
Feng, Z.G. and Michaelides, E.E., Heat transfer from a nano-sphere with temperature and velocity discontinuities at the interface, *Int. J. Heat Mass Transfer*, 55, 6491–6498, 2012.
Feng, Z.G., Michaelides, E.E., and Mao, S.L., On the drag force of a viscous sphere with interfacial slip at small but finite Reynolds numbers, *Fluid Dyn. Res.*, 44, 025502, 1–16, 2012.
Fourier, J., *Theorie Analytique de la Chaleur*, Acad. de Paris, Paris, France, 1822.
Galindo, V. and Gerbeth, G., A note on the force on an accelerating spherical drop at low Reynolds numbers, *Phys. Fluids*, 5, 3290–3292, 1993.
Gay, M. and Michaelides, E.E., Effect of the history term on the transient energy equation of a sphere, *Int. J. Heat Mass Transfer*, 46, 1575–1586, 2003.

Haberman, W.L. and Morton, R.K., *An Experimental Investigation of the Drag and Shape of Air Bubbles Rising in Various Liquids*, D.W. Taylor Model Basin Report, Vol. 802, Department of the Navy, Washington, DC, 1953.
Haberman, W.L. and Sayre, R.M., *Motion of Rigid and Fluid Spheres in Stationary and Moving Liquids Inside Cylindrical Tubes*, Report No. 1143, David Taylor Model Basin, U.S. Navy, Washington, DC, 1958.
Hadamard, J.S., *Mouvement Permanent Lent d' une Sphere Liquide et Visqueuse dans un Liquide Visqueux*, Compte-Rendus de' l' Acad. des Sci., Paris, France, Vol. 152, 1911, pp. 1735–1738.
Haider, A.M. and Levenspiel, O., Drag coefficient and terminal velocity of spherical and nonspherical particles, *Powder Technol.*, 58, 63–70, 1989.
Happel, J. and Brenner, H., *Low Reynolds Number Hydrodynamics*, Martinus Nijhoff, Washington, DC (reprint, orig. publ. 1963), 1986.
Hartman, M. and Yates, J.G., Free-fall of solid particles through fluids, *Collect. Czech. Chem. Commun.*, 58, 961–974, 1993.
Hermsen, R.W., Review of particle drag models, *JANAF Performance Standardization Subcommittee 12th Meeting*, Vol. CPIA 113, Washington, DC, 1979.
Inamuro, T., Maeba, K., and Ogino, F., Flow between parallel walls containing the lines of neutrally buoyant circular cylinders, *Int. J. Multiphase Flow*, 26, 1981–2004, 2000.
Iwaoka, M. and Ishii, T., Experimental wall correction factors of single solid spheres in circular cylinders, *J. Chem. Eng. Jpn.*, 12, 239–242, 1979.
Jones, I.P., Low Reynolds number flow past a porous spherical shell, *Proc. Camb. Philos. Soc.*, 73, 231–238, 1973.
Joseph, D.D. and Tao, L.N., The effect of permeability on the slow motion of a porous sphere in a viscous liquid, *Z. Angew. Math. Mech.*, 44, 361–367, 1964.
Kalio, G.A., Random walk modeling of particle deposition, in D.E. Stock et al. (Eds.), *Gas–Solid Flows—1993*, ASME FED, New York, 166, 1993, pp. 161–167.
Kaneda, Y., The drag on a sparse random array of fixed spheres in flow at small but finite Reynolds number, *J. Fluid Mech.*, 167, 455–463, 1986.
Kim, J.H., Mulholland, G.W., Pui, D.Y.H., and Kukuck, S.R., Slip correction measurements of certified psl nanoparticles using a nanometer Differential Mobility Analyzer (nano-DMA) for Knudsen number from 0.5 to 83, *J. Res. Natl. Inst. Stand. Technol.*, 110, 31–54, 2005.
Kim, S. and Karila, S.J., *Microhydrodynamics: Principles and Selected Applications*, Butterworth-Heineman, Boston, MA, 1991.
Koch, D.L. and Hill, R.J., Inertial effects in suspension and porous media flows, *Annu. Rev. Fluid Mech.*, 33, 619–647, 2001.
Koch, D.L. and Ladd, A.J.C., Moderate Reynolds number flows through periodic and random arrays of aligned cylinders, *J. Fluid Mech.*, 349, 31–66, 1997.
Koch, D.L. and Sangani, A.S., Particle pressure and marginal stability limits for a homogeneous monodisperse gas fluidized bed: Kinetic theory and numerical calculations, *J. Fluid Mech.*, 400, 229–263, 1999.
Kreith, F., Roberts, L.G., Sullivan, J.A., and Sinha, S.N., Convection heat transfer flow phenomena of rotating sphere, *Int. J. Heat Mass Transfer*, 6, 881–895, 1965.
Kurose, R., Makino, H., Komori, S., Nakamura, M., Akamatsu, F., and Katsuki, M., Effects of outflow from surface of sphere on drag, shear lift and scalar diffusion, *Phys. Fluids*, 15, 2338–2351, 2003.
Lasso, I.A. and Weidman, P.D., Stokes drag on hollow cylinders and conglomerates, *Phys. Fluids*, 29, 3921–3934, 1986.
Lawrence, C.J. and Weinbaum, S., The force on an axisymmetric body in linearized time-dependent motion: A new memory term, *J. Fluid Mech.*, 171, 209–218, 1986.
Lawrence, C.J. and Weinbaum, S., The unsteady force on a body at low Reynolds number: The axisymmetric motion of a spheroid, *J. Fluid Mech.*, 189, 463–498, 1988.
Le Clair, B.P. and Hamielec, A.E., A theoretical and experimental study of the internal circulation in water drops falling at terminal velocity in air, *J. Atmos. Sci.*, 29, 728–740, 1972.
Leal, L.G., *Laminar Flow and Convective Transport Processes*, Butterworth-Heinemann, Boston, MA, 1992.
Lee, C. and Kramer, T.A., Prediction of three-dimensional fractal dimensions using the two-dimensional properties of fractal aggregates, *Adv. Colloid Interface Sci.*, 112(1–3), 49–57, 2004.
Leeder, M.R., *Sedimentology, Process and Product*, Allen and Unwin, London, U.K., 1982.
Lerner, S.L., Homan, H.S., and Sirignano, W.A., Multicomponent droplet vaporization at high Reynolds numbers-size, composition and trajectory histories, *AIChE Annual Meeting*, Chicago, IL, 1980.
Leung, A.L. and Crowe, C.T., Collection of nanoclusters by thermophoresis, in D.E. Stock et al. (Eds.), *Gas–Solid Flows—1993*, ASME, New York, 1993.
Levich, V.G., *Physicochemical Hydrodynamics*, Prentice-Hall, Englewood Cliffs, NJ, 1962.
Li, X.-Y. and Logan, B.E., Permeability of fractal aggregates, *Water Res.*, 35(14), 3373–3380, 2001.

Lien, F.S., Chen, C.K., and Cleaver, J.W., Mixed and free convection over a rotating sphere with blowing and suction, *ASME J. Heat Transfer*, 108, 398–404, 1986.
Ling, Y., Haselbacher, A., and Balachandar, S., Importance of unsteady contributions to force and heating for particles in compressible flows: Part 1: Modeling and analysis for shock–particle interaction, *Int. J. Multiphase Flow*, 37, 1026–1044, 2011a.
Ling, Y., Haselbacher, A., and Balachandar, S., Importance of unsteady contributions to force and heating for particles in compressible flows: Part 2: Application to particle dispersal by blast waves, *Int. J. Multiphase Flow*, 37, 1013–1025, 2011b.
Looker, J.R. and Carnie S.L., The hydrodynamics of an oscillating porous sphere, *Phys. Fluids*, 16, 62–72, 2004.
Loth, E., Numerical approaches for the motion of dispersed particles, droplets, or bubbles, *Prog. Energy Combust. Sci.*, 26, 161–223, 2000.
Lovalenti, P.M. and Brady, J.F., The hydrodynamic force on a rigid particle undergoing arbitrary time-dependent motion at small Reynolds numbers, *J. Fluid Mech.*, 256, 561–601, 1993.
Madhav, G.V. and Chhabra, R.P., Drag on non-spherical particles in viscous fluids, *Int. J. Miner. Process.*, 43, 15–29, 1995.
Magnus, G., A note on the rotary motion of the liquid jet, *Ann. Phys. Chem.*, 63, 363–365, 1861.
Mandelbrot, B.B., How long is the coast of Britain? *Science*, 156, 636–638, 1967.
Marshall, W.R., Atomization and spray drying, *Chem. Eng. Prog. Monogr. Ser.*, 50(2), AIChE, New York, 1954.
Masliyah, J.H. and Epstein, N., Numerical study of steady flow past spheroids, *J. Fluid Mech.*, 44, 493–512, 1970.
Maxey, M.R. and Riley, J.J., Equation of motion of a small rigid sphere in a non-uniform flow, *Phys. Fluids*, 26, 883–889, 1983.
Maxworthy, T., Experiments on the flow around a sphere at high Reynolds numbers, *J. Appl. Mech.*, 91, 598–607, 1969.
Maxworthy, T., Accurate measurements of a sphere drag at low Reynolds numbers, *J. Fluid Mech.*, 23, 369–372, 1975.
McLaughlin, J.B., Inertial migration of a small sphere in linear shear flows, *J. Fluid Mech.*, 224, 261–274, 1991.
McNabb, G.S. and Meisen, A., Thermophoresis in liquids, *J. Colloidal Interface Sci.*, 44, 339–346, 1973.
Mei, R., An approximate expression of the shear lift on a spherical particle at finite Reynolds numbers, *Int. J. Multiphase Flow*, 18, 145–160, 1992.
Mei, R. and Adrian, R.J., Flow past a sphere with an oscillation in the free-stream and unsteady drag at finite Reynolds number, *J. Fluid Mech.*, 237, 323–341, 1992.
Mei, R., Lawrence, C.J., and Adrian, R.J., Unsteady drag on a sphere at finite Reynolds number with small fluctuations in the free-stream velocity, *J. Fluid Mech.*, 233, 613–631, 1991.
Michaelides, E.E., A novel way of computing the Basset term in unsteady multiphase flow comput., *Phys. Fluids A*, 4, 1579–1582, 1992.
Michaelides, E.E., Hydrodynamic force and heat/mass transfer from particles, bubbles and drops—The Freeman Scholar Lecture, *J. Fluids Eng.*, 125, 209–238, 2003.
Michaelides, E.E., *Particles*, *Bubbles and Drops—Their Motion*, *Heat and Mass Transfer*, World Scientific Publishers, Singapore, in print, 2006.
Michaelides, E.E., Transport properties of nanofluids—A critical review, *J. Non-Equilib. Thermodyn.*, 38, 1–79, 2013a.
Michaelides, E.E., *Heat and Mass Transfer in Particulate Suspensions*, Springer, New York, 2013b.
Michaelides, E.E., *Nanofluidics—Thermodynamic and Transport Properties*, Springer, New York, 2014.
Michaelides, E.E., Brownian movement and thermophoresis of nanoparticles in liquids, *Int. J. Heat Mass Transfer*, 81, 179–187, 2015.
Michaelides, E.E. and Feng, Z.-G., Heat transfer from a rigid sphere in a non-uniform flow and temperature field, *Int. J. Heat Mass Transfer*, 37, 2069–2076, 1994.
Michaelides, E.E. and Feng, Z.-G., The equation of motion of a small viscous sphere in an unsteady flow with interface slip, *Int. J. Multiphase Flow*, 21, 315–321, 1995.
Michaelides, E.E. and Roig, A., A reinterpretation of the Odar and Hamilton data on the unsteady equation of motion of particles, *AIChE J.*, 57(11), 2997–3002, 2011.
Mikami, H., Endo, Y., and Takashima, Y., Heat transfer from a sphere to rarefied gas mixtures, *Int. J. Heat Mass Transfer*, 9, 1435–1448, 1966.
Millikan, R.A., The general law of fall of a small spherical body through a gas and its bearing upon the nature of molecular reflection from surfaces, *Phys. Rev.*, 22, 1–23, 1923.

Miyamura, A., Iwasaki, S., and Ishii, T., Experimental wall correction factors of single solid spheres in triangular and square cylinders, and parallel plates, *Int. J. Multiphase Flow*, 7, 41–46, 1981.
Morrison, F.A. and Stewart, M.B., Small bubble motion in an accelerating fluid, *J. Appl. Mech.*, 97, 399–402, 1976.
Mortazavi, S. and Tryggvason, G., A numerical study of the motion of drops in Poiseuille flow. Part 1: Lateral migration of one drop, *J. Fluid Mech.*, 411, 325–350, 2000.
Mugele, R.A. and Evans, H.D., Droplet size distribution in sprays, *Ind. Eng. Chem.*, 43, 1317–1324, 1951.
Musong, S. and Feng, Z.G., Mixed convective heat transfer from a heated sphere at an arbitrary incident flow angle in laminar flows, *Int. J. Heat Mass Transfer*, 78, 34–44, 2014.
Odar, F. and Hamilton, W.S., Forces on a sphere accelerating in a viscous fluid, *J. Fluid Mech.*, 18, 302–303, 1964.
Oesterle, B. and Bui-Dihn, T., Experiments on the lift of a spinning sphere in the range of intermediate Reynolds numbers, *Exp. Fluids*, 25, 16–22, 1998.
Oliver, D.L. and Chung, J.N., Flow about a fluid sphere at low to moderate Reynolds numbers, *J. Fluid Mech.*, 177, 1–18, 1987.
Oseen, C.W., Uber den Goltigkeitsbereich der Stokesschen Widerstandsformel, *Ark. Mat. Astron. Fysik*, 9(19), 1–15, 1913.
Paine, P.L. and Scherr, P., Drag coefficients for the movement of rigid spheres through liquid-filled cylindrical pores, *Biophys. J.*, 15, 1087–1091, 1975.
Parmar, M., Haselbacher, A., and Balachandar, S., Generalized Basset-Boussinesq-Oseen equation for unsteady forces on a sphere in a compressible flow, *Phys. Rev. Lett.*, 106, 084501, 2011.
Patankar, N., Ko, T., Choi, H.G., and Joseph, D.D., A correlation for the lift-off of many particles in plane Poiseuille flows of Newtonian fluids, *J. Fluid Mech.*, 445, 55–76, 2001.
Pettyjohn, E.S. and Christiansen, E.R., Effect of particle shape on free-settling rates of isometric particles, *Chem. Eng. Prog.*, 44, 157–172, 1948.
Portela, L.M., Cota, P., and Oliemans, R.V.A., Numerical study of the near-wall behaviour of particles in turbulent pipe flows, *Powder Technol.*, 125, 149–157, 2002.
Proudman, I. and Pearson, J.R.A., Expansions at small Reynolds numbers for the flow past a sphere and a circular cylinder, *J. Fluid Mech.*, 2, 237–262, 1956.
Raithby, G.D. and Eckert, E.R.G., The effect of turbulence parameters and support position on the heat transfer from spheres, *Int. J. Heat Mass Transfer*, 11, 1233–1246, 1968.
Ranz, W.E. and Marshall, W.R., Evaporation from drops, *Chem. Eng. Prog.*, 48, 141–146, 1952.
Renksizbulut, M. and Yuen, M.C., Experimental study of droplet evaporation in high temperature air stream, *J. Heat Transfer*, 105, 364–388, 1983.
Richardson, J.F. and Zaki, W.N., The fall velocities of spheres in viscous fluids, *Trans. Inst. Chem. Eng.*, 32, 35–41, 1954.
Rivkind, V.Y., Ryskin, G.M., and Fishbein, G.A., Flow around a spherical drop in a fluid medium at intermediate Reynolds numbers, *Appl. Math. Mech.*, 40, 687–691, 1976.
Rojas, S. and Koplik, J., Non-linear flow in porous media, *Phys. Rev.*, E58, 4776–4782, 1998.
Rowe, P.N., The drag coefficient of a sphere, *Trans. Inst. Chem. Eng.*, 39, 175–181, 1961.
Rybczynski, W., On the translatory motion of a fluid sphere in a viscous medium, *Bull. Acad. Sci., Krakow, Ser. A*, 40, 40–46, 1911.
Saffman, P.G., The lift on a small sphere in a slow shear flow, *J. Fluid Mech.*, 22, 385–398, 1965.
Saffman, P.G., The lift on a small sphere in a slow shear flow-corrigendum, *J. Fluid Mech.*, 31, 624–625, 1968.
Saffman, P.G., On the boundary condition at the surface of a porous medium, *Stud. Appl. Math.*, 50, 93–101, 1971.
Sangani, A.S., Zhang, D.Z., and Prosperetti, A., The added mass, Basset and viscous drag coefficients in nondilute bubbly liquids undergoing small-amplitude oscillatory motion, *Phys. Fluids*, A3, 2955–2970, 1991.
Sano, T., Unsteady flow past a sphere at low Reynolds number, *J. Fluid Mech.*, 112, 433–441, 1981.
Schaaf, S.A. and Chambre, P.L., Fundamentals of gas dynamics, in H.W. Emmons (Ed.), *High Speed Aerodynamics and Jet Propulsion*, Vol. 3, Princeton University Press, Princeton, NJ, 1958, pp. 689–793.
Schiller, L. and Nauman, A., Uber die grundlegende Berechnung bei der Schwekraftaufbereitung, *Ver. Deutch Ing.*, 44, 318–320, 1933.

Seeley, L.E., Hummel, R.L., and Smith, J.W., Experimental velocity profiles in laminar flow around spheres at intermediate Reynolds numbers, *J. Fluid Mech.*, 68, 591–608, 1975.
Segre, G. and Silberberg, A., Behavior of macroscopic rigid spheres in Poiseuille flow, *J. Fluid Mech.*, 14, 115–157, 1962.
Siegel, R. and Howel, J.R., *Thermal Radiation Heat Transfer*, McGraw-Hill, New York, 1981.
Sirignano, W.A., Fluid dynamics of sprays, *ASME J. Fluids Eng.*, 115, 345–378, 1993.
Sirignano, W.A., *Fluid Dynamics and Transport of Droplets and Sprays*, Cambridge University Press, Cambridge, U.K., 1999.
Spelt, P.D.M. and Sangani, A.S., Properties and averaged equations for flows of bubbly liquids, in A. Biesheuvel and G.F. van Heijst (Eds.), *Fascination of Fluid Dynamics*, Kluwer Academic, Dordrecht, the Netherlands, 1998, pp. 337–386.
Sridhar, G. and Katz, J., Drag and lift forces on microscopic bubbles entrained by a vortex, *Phys. Fluids*, 7, 389–399, 1995.
Stokes, G.G., On the effect of the internal friction of fluids on the motion of a pendulum, *Trans. Camb. Philos. Soc.*, 9, 8–106, 1851.
Talbot, L., Cheng, R.K., Schefer, R.W., and Willis, D.R., Thermophoresis of particles in a heated boundary layer, *J. Fluid Mech.*, 101, 737–758, 1980.
Tanaka, T., Yamagata, K., and Tsuji, Y., Experiment on fluid forces on a rotating sphere and a spheroid, in *Proceedings of the Second KSME-JSME Fluids Engineering Conference*, Seoul, Korea, Vol. 1, 1990, pp. 266–378.
Taneda, S., Experimental investigation of the wake behind a sphere at low Reynolds numbers, *J. Phys. Soc. Jpn.*, 11, 1104–1108, 1956.
Tate, R.W. and Marshall, Jr., W.R., Atomization by centrifugal pressure nozzles (Part II), *Ind. Eng. Prog.*, 49, 226–234, 1953.
ten Cate, A., Nieuwstad, C.H., Derksen, J.J., and Van den Akker, H.E.A., Particle imaging velocimetry experiments and lattice-Boltzmann simulations on a single sphere settling under gravity, *Phys. Fluids*, 14, 4012–4025, 2002.
Tieng, S.M. and Yan, A.C., Experimental investigation on convective heat transfer of heated rotating sphere, *Int. J. Heat Mass Transfer*, 36, 599–610, 1993.
Thorncroft, G.E., Klausner, J.F., and Mei, R., Bubble forces and detachment models, *Multiphase Sci. Technol.*, 13, 35–76, 2001.
Tomiyama, A., Reconsideration of three fundamental problems in modeling bubbly flows, in *39th European Two-Phase Flow Group Meeting*, Aveiro, Portugal, 2001.
Tomiyama, A., Kataoka, I., Zun, I., and Sakaguchi, T., Drag coefficients of single bubbles under normal and micro gravity conditions, *JSME Int. J., Ser. B*, 41, 472–479, 1998.
Tomiyama, A., Tamai, H., Zun, I., and Hosokawa, S., Transverse migration of single bubbles in simple shear flows, in *Proceedings of Second International Symposium on Two-Phase Flow Modeling and Experimentation*, Pisa, Italy, Vol. 2, 1999, pp. 941–948.
Tran Cong, S., Gay, M., and Michaelides, E.E., Drag coefficients of irregularly shaped particles, *Powder Technol.*, 139, 21–32, 2004.
Tsuji, Y., Morikawa, Y., and Mizuno, O., Experimental measurements of the magnus force on a rotating sphere at low Reynolds numbers bubble in an axisymmetric shear flow, *J. Fluids Eng.*, 107, 484–498, 1985.
Tyndall, J., On haze and dust, *Proc. R. Inst.*, 6, 1–6, 1870.
van Wijngaarden, L., Hydrodynamic interaction between bubbles in a liquid, *J. Fluid Mech.*, 77, 27–44, 1976.
Vasseur, P. and Cox, R.G., The lateral migration of spherical particles in two-dimensional shear flow, *J. Fluid Mech.*, 78, 385–413, 1976.
Vicsek, T., *Fractal Growth Phenomena*, 2nd edn., World Scientific, Singapore, 1999.
Vojir, D.J. and Michaelides, E.E., The effect of the history term on the motion of rigid spheres in a viscous fluid, *Int. J. Multiphase Flow*, 20, 547–556, 1994.
Wadell, H., Sphericity and roundness of rock particles, *J. Geol.*, 41, 310–331, 1933.
Wang, W. and Chau, Y., Self-assembled peptide nanorods as building blocks of fractal patterns, *Soft Matter*, 5(24), 4893–4898, 2009.
Wen, C.Y. and Wu, Y.H., Mechanics of fluidization, *Chem. Eng. Prog. Symp. Ser.*, 62, 100–125, 1966.

Whitaker, S., Forced convection heat transfer correlations for flow in pipes past flat plates, single cylinders, single spheres, and for flow in packed beds and tubes bundles, *AIChE J.*, 18, 361–371, 1972.
Winnikow, S. and Chao, B.T., Droplet motion in purified systems, *Phys. Fluids*, 9, 50–61, 1966.
Wu, M. and Gharib, M., Experimental studies on the shape and path of small air bubbles rising in clean water, *Phys. Fluids*, 14, L49–L52, 2002.
Yearling, P.R. and Gould, R.D., Convective heat and mass transfer from a single evaporating water, ethanol and methanol droplet, *Proc. ASME-FED*, 233, 33–39, 1995.
Yuen, M.C. and Chen, L.W., On drag of evaporating droplets, *Combust. Sci. Technol.*, 14, 147–154, 1976.
Zuber, N., On the dispersed two-phase flow in the laminar flow regime, *Chem. Eng. Sci.*, 19, 897–917, 1964.

2

Computational Methods

2.1 Overview of Numerical Approaches

Eric Loth

2.1.1 Classification by Particle Reference Frame

While continuous-flow computational fluid dynamics (CFD) formulations are generally considered in an Eulerian reference, the dispersed-phase characteristics (velocity, concentration, diameter, etc.) can be treated with either Lagrangian or Eulerian representations. This difference of the reference frame for dispersed phase is the key division between the different multiphase numerical methods. The Lagrangian representation for particles is a natural approach since the particle positions are declared and updated along the particle paths. These paths are defined by the center of mass of the particle (or center of mass for a cloud of particles) as shown in Figure 2.1a. This approach can include wall collisions and other trajectory information in a straightforward manner. In contrast, the Eulerian approach for the particles considers cell-averaged particle characteristics based on the continuous-phase grid nodes (Figure 2.1b). This approach is efficient in terms of predicting particle concentration.

The two different approaches (Lagrangian and Eulerian) lead to significantly different formulations and numerical constraints. The Lagrangian approach leads to ordinary differential equations (ODEs) along the particle path but requires interpolation of the continuous-phase properties to the particle centroids. In contrast, the Eulerian approach leads to partial differential equations (PDEs) for the particle characteristics on an Eulerian grid but requires a continuum assumption for the particle characteristics. These two approaches are, respectively, discussed in the following two sections.

2.1.1.1 Lagrangian Approach for the Dispersed Phase

2.1.1.1.1 Lagrangian Particle Equation of Motion Since the dispersed phase is treated in terms of individual particle paths (or a group of particles), the Lagrangian method is also sometimes referred to as the "discrete" approach. When coupled with an Eulerian representation of the continuous phase, this combined treatment is termed the "Eulerian–Lagrangian" approach.

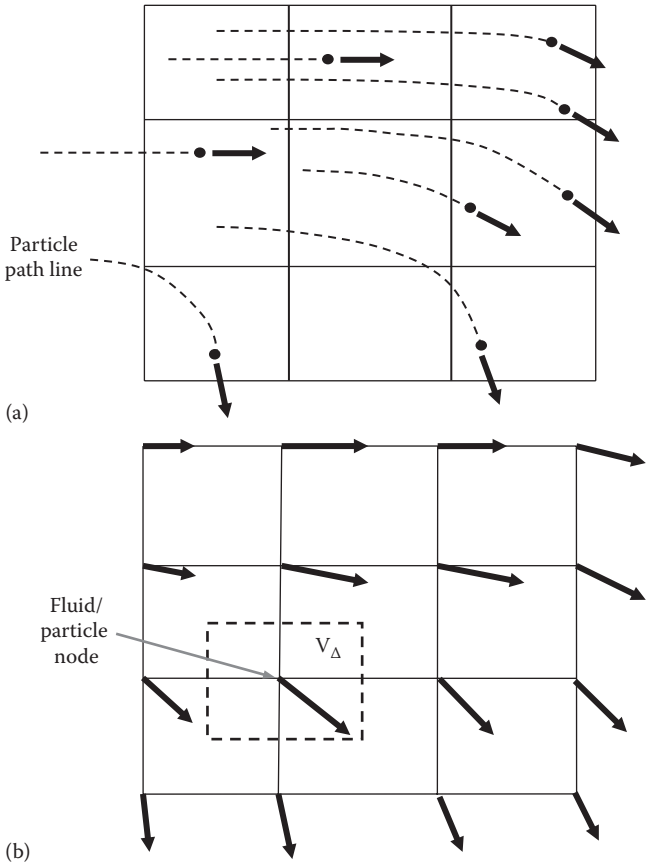

Figure 2.1

Particle velocity vectors in different reference frames in the context of an Eulerian continuous-phase grid: (a) Lagrangian vectors based on particle positions and (b) Eulerian particle velocity vectors based on average over a control volume centered at a discrete grid node used to store fluid properties and particle properties.

In the Lagrangian methodology, ODEs for the particle properties are based on particle path derivatives. The differential equations for particle position ($\mathbf{x}_p$), velocity ($\mathbf{v}$), mass (m_p), and internal energy (e_p) are summarized as follows:

$$\frac{d\mathbf{x}_p}{dt} \equiv \mathbf{v} \tag{2.1}$$

$$m_p \frac{d\mathbf{v}}{dt} = \mathbf{F}_{body} + \mathbf{F}_{sur} + \mathbf{F}_{coll} \tag{2.2}$$

$$\frac{dm_p}{dt} \equiv \dot{m}_p \tag{2.3}$$

$$m_p \frac{de_p}{dt} = \dot{Q}_p + \dot{m}_p h_{phase} \tag{2.4}$$

The RHS of Equation 2.2 contains the body force ($\mathbf{F}_{body}$), the fluid dynamic surface force ($\mathbf{F}_{sur}$), and the collision force with other particles or walls ($\mathbf{F}_{coll}$). The RHS of Equation 2.3 contains the mass transfer rate to the particle ($\dot{m}_p$, which is positive when the particle mass is increasing). The RHS of Equation 2.4 contains the heat transfer to the particle ($\dot{Q}_p$, which is positive when the particle temperature is increasing) and enthalpy for phase change (h_{phase}). The particle specific energy is equal to the product of the particle specific heat at constant pressure and particle temperature ($e_p = c_{p,p}T_p$). If there is negligible mass

or heat transfer (e.g., if temperature variations are small), the last two ODEs are not needed. The models for these RHS terms are listed as follows.

For a steady uniform continuum surrounding fluid moving past a single solid spherical particle at finite Reynolds numbers, the momentum RHS term (of Equation 2.2) neglecting collision effects can be modeled as

$$\mathbf{F}_{\text{body}} + \mathbf{F}_{\text{sur}} = -3\pi d\mu_f f \mathbf{w} + \rho_f \forall_p \left[\left(\frac{\rho_p}{\rho_f} - 1 \right) \mathbf{g} + \frac{3}{2} \frac{\mathcal{D}\mathbf{u}_{@p}}{\mathcal{D}t} - \frac{1}{2} \frac{d\mathbf{v}}{dt} \right] \tag{2.5}$$

$$\mathbf{w}(t) \equiv \mathbf{v}(t) - \mathbf{u}_{@p}(t) \tag{2.6}$$

$$f = 1 + \frac{Re_p/4}{1 + \sqrt{Re_p}} + \frac{Re_p}{60} \tag{2.7}$$

$$Re_p = \frac{\rho_f w d}{\mu_f} \tag{2.8}$$

In these expressions,

- d is the particle diameter
- μ_f is the fluid viscosity
- $\mathbf{w}$ is the particle relative velocity
- ρ_f is the fluid density
- $\forall_p$ is the particle volume
- ρ_p is the particle density
- $\mathbf{g}$ is the gravitational acceleration
- $\mathbf{u}_{@p}$ is the undisturbed fluid velocity (seen by the particle and interpolated to the particle centroid)
- Re_p is the particle Reynolds number

The RHS terms for mass and energy transfer (of Equations 2.3 and 2.4) can be modeled as

$$\dot{m}_p = -\pi d \rho_f Sp \Theta_{p@f} Sh \tag{2.9}$$

$$Sh = \left(2 + 0.6 \cdot Re_p^{1/2} \cdot Sc_f^{1/3}\right) \frac{\ln(1+Sp)}{Sp} \tag{2.10}$$

$$\dot{Q}_p = \pi d \kappa_f \left(T_{f@p} - T_p\right) Nu \tag{2.11}$$

$$Nu = \left(2 + 0.6 \cdot Re_p^{1/2} \cdot Pr_f^{1/3}\right) \frac{\ln(1+Sp)}{Sp} \tag{2.12}$$

In these expressions,

- Sp is the Spalding number
- $\Theta_{p@f}$ is the mass diffusivity of the particle matter into the surrounding fluid
- Sh is the Sherwood number
- Sc_f is the Schmidt number
- κ_f is the fluid thermal diffusivity
- $T_{f@p}$ is the fluid temperature extrapolated to the particle centroid
- Nu is the Nusselt number

These RHS terms neglect effects of lift, history force, collisions, internal recirculation, turbulence, and three-way coupling. Additions and corrections for these effects are described by Crowe et al. (1998, 2012), Loth (2000), and Michaelidis (2006, 2014).

2.1.1.1.2 Numerical Interpolation from Eulerian Grid To numerically integrate the particle ODEs, one must obtain the fluid properties interpolated to the particle centroid, for example, $\mathbf{u}_{@p}$ and $T_{f@p}$. These properties can be interpolated numerically from the Eulerian nodes of the continuous phase. For example, if the continuous-phase discretization is based on grid shape functions Φ, then the "unhindered" fluid velocity extrapolated to the particle centroid is given by

$$\mathbf{u}_{@p}(\mathbf{x}_p,t)=\sum_{j=1}^{N_\Phi}\mathbf{u}_j(t)\Phi_j(\mathbf{x}_p) \tag{2.13}$$

In this equation, N_Φ is all the number of computational cells associated with a particle location. The use of the shape function allows the velocity of all surrounding nodes to be included in the evaluation of $\mathbf{u}_{@p}$. This is shown schematically in Figure 2.2a for a 2D grid.

To predict particle concentration with a Lagrangian particle approach, the distribution of discrete particle positions must be translated into discrete volume averages. This can be accomplished by averaging all the respective particle volumes ($V_{p,j}$) whose centroids are within a discrete cell volume (V_Δ). Denoting this sum of particles in a cell as $N_{p\Delta}$, the particle number density (n_p) and particle volumetric fraction (ϕ_d) can be given as

$$n_p=\frac{N_{p\Delta}}{V_\Delta} \tag{2.14}$$

$$\phi_d=\frac{1}{V_\Delta}\sum_{j=1}^{N_{pD}}\forall_{p,j}=\frac{N_{p\Delta}\langle V_p\rangle}{V_\Delta} \tag{2.15}$$

The RHS of Equation 2.15 uses angled brackets, that is, <..>, to indicate a cell-based ensemble average. This cell-based ensemble averaging is illustrated in Figure 2.2b, and similar equations can convert Lagrangian particle velocities and temperatures to cell-averaged Eulerian particle velocities and temperatures. To ensure that ϕ_d can vary spatially as a continuum, the mixed-fluid volume should encompass many particles so that the concentration is continuously differentiable in space, that is,

$$N_{p,\Delta}\gg 1 \quad \text{for a well-posed continuum particle concentration} \tag{2.16}$$

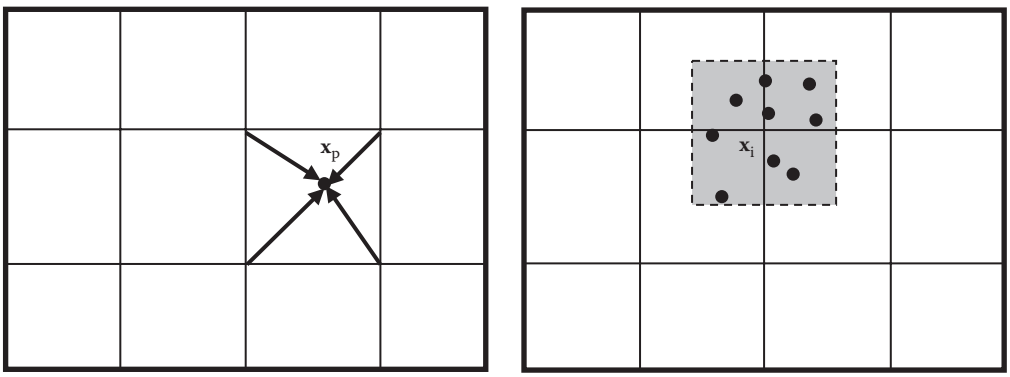

(a) Interpolate $\mathbf{u}_{@p}$ at particle location (b) Collect ϕ_d for cell volume associated with a node

Figure 2.2

Schematic of Lagrangian point-force particles in a 2D Eulerian continuous-phase grid showing (a) interpolation of fluid velocity of the surrounding nodes to the particle position at $\mathbf{x}_p$ and (b) summation of particle volumes in a computational volume to compute volume fraction associated with a node $\mathbf{x}_i$.

If a continuum of particle concentration is not required, a more relaxed discrete concentration requirement can be imposed specifying that $\phi_d < 1$. Using the particle diameter (d) and assuming an isotropic grid ($\Delta x = \Delta y = \Delta z$), this inequality can be roughly expressed as

$$d < \Delta x \quad \text{for a well-posed discrete particle concentration} \tag{2.17}$$

If the grid is anisotropic, the RHS of this inequality can be replaced with grid length scale, for example, $(\Delta x \Delta y \Delta z)^{1/3}$ or the minimum of the three grid scales. This criterion ensures that the interpolation used in Equation 2.13 is reasonable assuming that the flow gradients within a given computational cell are small. Thus, the particle size is limited for a given discretization of the continuous phase. Approaches not bound by this constraint will be discussed in Section 2.1.3.

If the number of physical particles is very high (e.g., hundreds of particles per computation cell), it may be impossible or inconvenient to track all of the particles with individual Lagrangian ODEs. An alternative approach is to use representative Lagrangian particles called "parcels." These representative particle groups are essentially a small cloud of particles that are all modeled with the same Lagrangian trajectory and are also sometimes called "computational particles" or "superparticles." If we denote N_{pP} as the number of physical particles in a parcel and $N_{P\Delta}$ as the number of parcels in a cell, the particle concentration can be evaluated as

$$\phi_d = \frac{1}{V_\Delta} \sum_{j=1}^{N_{P\Delta}} N_{pP,j} V_{P,j} = \frac{N_{P\Delta} \left\langle N_{pP} V_P \right\rangle}{V_\Delta} \tag{2.18}$$

Further denoting $\mathbf{v}_P$ as the velocity of the parcel, the corresponding ODEs for the trajectory and momentum are given as

$$N_{pP} \left(\frac{d\mathbf{x}_P}{dt} \right) = N_{pP} \mathbf{v}_P \tag{2.19}$$

$$N_{pP} m_P \left(\frac{d\mathbf{v}_P}{dt} \right) = N_{pP} \left(\mathbf{F}_{body} + \mathbf{F}_{sur} + \mathbf{F}_{coll} \right) \tag{2.20}$$

$$\frac{N_{pP} dm_P}{dt} = N_{pP} \dot{m}_P \tag{2.21}$$

In this expression, all the particles in a parcel are assumed to have the same properties (i.e., diameter, temperature, and mass). If there is no mass transfer, breakup, or coalescence, the number of particles per parcel will be constant along its trajectory. In this case, the aforementioned trajectory and momentum equations for a single parcel are the same as those for a single particle (i.e., Equations 2.19 through 2.21 normalized by N_{pP} is the same as Equations 2.1 through 2.4). Thus, the parcel approach is much more computationally efficient as the number of equations reduces as the number of particles per parcel increases, for example, $N_{pP} = 100$ allows the number of computed trajectories to be reduced 100-fold. This is the key benefit of the parcel approach. However, there is an upper limit to how many particles per parcel can be used. In particular, if the parcel cloud is too large, there can be a substantial variation of continuous-phase flow variables across its length so that Equations 2.13 and 2.18 are not reasonable.

The parcel cloud volume (V_P) is the mixed-fluid volume occupied by the particles and the surrounding fluid. If the particle and surrounding fluid are both incompressible and there is no loss of particles (N_{pP} remains constant), the parcel "cloud" volume will stay fixed along its trajectory and be initialized based on the initial particle concentration prescription ($\phi_{d,inj}$)

$$V_P \equiv \text{volume occupied by particles and fluid for a parcel} = \frac{V_P N_{pP}}{\phi_{d,inj}} \tag{2.22}$$

To ensure that particles associated with a parcel will, on average, be physically within the computational cell (to be consistent with Equation 2.18), the parcel cloud volume should be smaller than the host computational cell volume, that is,

$$V_P < V_\Delta \quad \text{for a well-posed continuum particle concentration} \tag{2.23}$$

If particle concentration is needed, this criterion (combined Equation 2.22) places an upper bound on the number of particles per parcel (N_{pP}) at the point of injection as well as anywhere the parcel will travel.

2.1.1.2 Eulerian Approach for the Dispersed Phase

2.1.1.2.1 Eulerian Dispersed-Phase Equations of Motion In the Eulerian approach, the particle concentration and momentum are solved with transport equations in a manner similar to the density and momentum for the continuous phase. To allow this, we assume that the particle concentration (n_p or ϕ_d) can be described as a continuum (the requirements for this will be discussed later). Based on this assumption, the conservation equations for the Eulerian dispersed-phase mass, momentum, and energy can be derived. For continuity, the rate of mass change in a control volume is equal to the mass flux through its boundaries and any mass source term within the control volume. Written in PDE form and ignoring particle collisions, the governing equations for particle mass, momentum, and energy (per unit volume of the mixed-volume fluid) can be obtained in conservative form (Crowe et al., 1998) as

$$\frac{\partial\left(m_p n_p\right)}{\partial t} + \nabla\left(m_p n_p \mathbf{v}\right) = n_p \dot{m}_p \tag{2.24}$$

$$\frac{\partial\left(m_p n_p \mathbf{v}\right)}{\partial t} + \nabla\cdot\left(m_p n_p \mathbf{v}\mathbf{v}\right) = n_p\left(\mathbf{F}_{body} + \mathbf{F}_{sur} + \dot{m}_p \mathbf{v}\right) \tag{2.25}$$

$$\frac{\partial\left(m_p n_p e_p\right)}{\partial t} + \nabla\left(m_p n_p e_p \mathbf{v}\right) = n_p\left[\dot{Q}_p + \dot{m}_p h_{phase} + \dot{m}_p e_p\right] \tag{2.26}$$

Note the conservative form results in a RHS mass transfer term for the momentum and energy equations. These Eulerian equations can be rewritten in terms of particle volume fraction as

$$\frac{\partial\left(\phi_d \rho_p\right)}{\partial t} + \nabla\left(\phi_d \rho_p \mathbf{v}\right) = \frac{\phi_d}{V_p}\dot{m}_p \tag{2.27}$$

$$\frac{\partial\left(\phi_d \rho_p \mathbf{v}\right)}{\partial t} + \nabla\cdot\left(\phi_d \rho_p \mathbf{v}\mathbf{v}\right) = \frac{\phi_d}{V_p}\left(\mathbf{F}_{body} + \mathbf{F}_{sur} + \dot{m}_p \mathbf{v}\right) \tag{2.28}$$

$$\frac{\partial\left(\phi_d \rho_p e_p\right)}{\partial t} + \nabla\left(\phi_d \rho_p e_p \mathbf{v}\right) = \frac{\phi_d}{V_p}\left[\dot{Q}_p + \dot{m}_p\left(h_{phase} + e_p\right)\right] \tag{2.29}$$

The RHS values for these equations are given by Equations 2.5 through 2.8.

Once the Eulerian conservation equations are discretized, each (cell-averaged) node in the computational domain will include cell-averaged particle-phase variables. When coupled with an Eulerian representation of the continuous phase, this overall multiphase treatment is termed the "Eulerian–Eulerian" or "two-fluid" approach. Importantly, this approach allows the dispersed-phase PDEs to be treated with the same discretization techniques as used for the continuous-phase PDEs. It also conveniently allows the same grid for both phases so that the grid resolution is equivalent ($\Delta x_f = \Delta x_p$). Because of this, the average interphase coupling terms are treated in the same manner for both phases so that Eulerian–Eulerian approaches are especially efficient and accurate when two-way coupling effects are present (to be discussed in Section 2.1.1.2.2).

2.1.1.2.2 Dispersed-Phase Continuum Approximation A formal derivation of the Eulerian dispersed-phase equations requires careful consideration of the spatial and temporal averaging limits and the assumption of small but finite particle size. As such, the reader is particularly referred to details given by Drew (1983), Zhang and Prosperetti (1994), Crowe et al. (1998), and Prosperetti (2007). There are subtle differences among these derivations in these sources that are particular to different assumptions. However, a key tenant for the Eulerian description of the dispersed phase is that the particle properties (such as concentration, velocity, or temperature) can be approximated as a continuum at the grid scale. This is generally known as the "particle-phase continuum" assumption (Drew and Passman, 1999) and requires that changes in grid cell position or further refinements in grid cell do not fundamentally alter the predicted particle concentration distribution.

The particle-phase continuum assumption is related to the number of physical particles per computational cell ($N_{p\Delta}$). To demonstrate this, consider two neighboring control volumes with a particle concentration defined as $n_{p,i}$ and $n_{p,i+1}$ as shown in Figure 2.3a. In this case, one may apply a Taylor series expansion to express the number concentration at node i + 1 in terms of the value and gradients at node i + 1/2 using a forward shift (Δx/2) as

$$n_{p,i+1} = n_{p,i+1/2} + \frac{\Delta x}{2}\left(\frac{\partial n_p}{\partial x}\right)_{i+1/2} + \frac{1}{2!}\left(\frac{\Delta x}{2}\right)^2\left(\frac{\partial^2 n_p}{\partial x^2}\right)_{i+1/2} + O(\Delta x)^3 \ldots \tag{2.30}$$

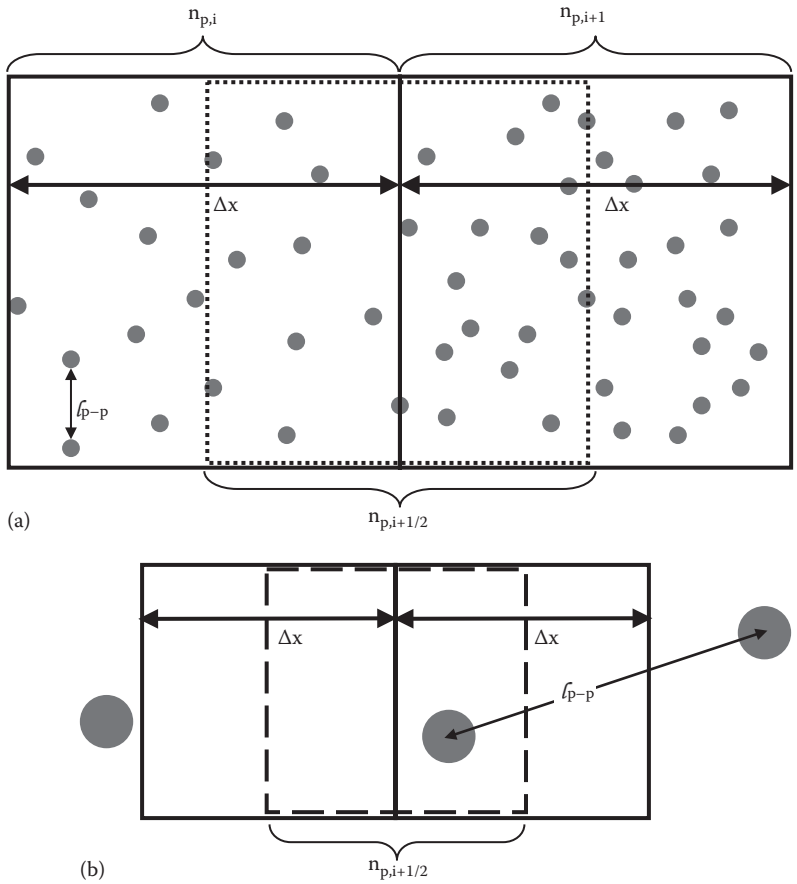

Figure 2.3

Two-dimensional Eulerian grid that contains discrete particles in adjoining computational control volumes: (a) $N_{p,\Delta} \gg 1$ allowing a continuum approximation and (b) $N_{p,\Delta} \sim 1$ so that a continuum approximation is *not* appropriate.

The last term on the RHS term corresponds to all terms of Δx^2 or higher. Comparing this result to a similar expansion for $n_{p,i}$ but with a backward shift ($-\Delta x/2$) yields

$$\left(\frac{\partial n_p}{\partial x}\right)_{i+1/2} = \frac{n_{p,i+1} - n_{p,i}}{\Delta x} + O(\Delta x)^2 \tag{2.31}$$

By dropping the second RHS term (which corresponds to terms of order Δx^2 or higher), we obtain a second-order finite difference expression. Such expressions can be used to discretize the spatial gradients for the Eulerian approach, for example, Equations 2.24 through 2.26. If the computational cell volume contains many particles as shown in Figure 2.3a, the number density will vary smoothly between cells and will not depend significantly on the exact volume position, that is, it will be continuously differentiable. A much different result arises if $N_{p\Delta}$ is no longer large. In this case, the grid resolution is on the order of the local interparticle spacing ($\Delta x \sim \ell_{p-p}$), which leads to discontinuities in particle concentration depending on where the grid cell is taken. For example, $n_{pi+1} = 1$ while $n_{p,i} = 0$ as in Figure 2.3b. This leads to uncertainty with respect to the spatial gradient of particle concentration. This uncertainty can be quantified for uniformly or randomly space particle positions. If the particles are uniformly spaced, the error of number density ($\mathcal{U}n_p$) is proportional to the number of particles

$$\frac{\mathcal{U}n_p}{n_p} \sim \frac{1}{N_{p\Delta}} \tag{2.32}$$

Thus, 10 particles are needed to achieve 10% accuracy. For a random Gaussian distribution of particle positions, the error is proportional to the square root of the sample size

$$\frac{\mathcal{U}n_p}{n_p} \sim \frac{1}{\sqrt{N_{p\Delta}}} \tag{2.33}$$

Thus, 100 particles per cell are needed for an uncertainty of 10%. In either case, if $N_{p\Delta}$ is order unity, the error in n_p will be on the order of 100% as shown in Figure 2.3b.

Therefore, a large number of particles per cell are needed for an accurate instantaneous Eulerian representation of n_p or ϕ_d, that is,

$$N_{p\Delta} \gg 1 \quad \text{for approximate Eulerian particle concentration "continuum"} \tag{2.34}$$

Thus, 10 or more particles in a cell are a practical lower bound for this approximation. Concentration continuum can be more rigorously specified by stating that the grid spacing should be much larger than the particle–particle spacing, that is,

$$\Delta x \gg \ell_{p-p} \quad \text{for an Eulerian particle concentration "continuum"} \tag{2.35}$$

This requirement reflects a lower bound for the computational grid size for which the concentration and its gradients are well defined.

In a sense, the requirement of Equation 2.35 is similar to the continuum assumption for a single-phase flow that requires a large number of molecules within a fluid control volume, that is,

$$\Delta x \gg \ell_{f-f} \quad \text{for a fluid "continuum" on an Eulerian grid} \tag{2.36}$$

Since the mean free path for most fluids is extremely small (e.g., on the order of nanometers), the requirement of Equation 2.36 is readily met for most CFD grids while that of Equation 2.35 is more conservative and more likely to be constraining.

It should be noted that the continuum approximation constraint for instantaneous concentration (Equation 2.35) may be relaxed if just the *mean* or properties are of interest. For example, consider the time-averaged number density obtained from an unsteady simulation over a number of time steps ($N_{\Delta t}$) as

$$\bar{n}_p = \frac{\bar{N}_{p\Delta}}{V_\Delta} = \frac{1}{V_\Delta N_{\Delta t}} \sum_{k=0}^{N_{\Delta t}} N_{p\Delta}(t_o + k\Delta t) \tag{2.37}$$

If the total number of particles considered all times (the summation on the RHS) is large, then $\bar{n}_p$ can be considered as a continuum in the mean sense, even if $N_{p\Delta}$ at a given instant is small or even zero. For example, a mean can be based on 0.1 particles in a cell (equivalent to a 10% probability that one particle is in the cell at any given time). Similar reasoning can be used if a time-averaged Reynolds-averaged Navier–Stokes approach is employed. As such, the uncertainty of Equation 2.33 only arises if one wishes to convert this probability into an instantaneous realization. Using a time average such as this allows the constraints of Equations 2.18 and 2.34 to be relaxed, but the continuum approximation still requires that the cell volume be well posed (Equation 2.17) so that

$$d < \Delta x \quad \text{for a mean particle concentration "continuum"} \tag{2.38}$$

This more relaxed criterion allows a smaller computational grid size as compared to Equation 2.35.

2.1.1.3 Eulerian Approach for the Continuous Phase

For two-way and three-way coupling, the continuous-phase mass, momentum, and energy must incorporate interphase transfer of mass, momentum, and energy interphase to the particles as sinks into the single-phase equations. In particular, these conservation equations must also take into account that the continuous-phase mass only occupies part of the mixed-fluid volume, for example, the continuous-phase fluid mass per mixed-fluid volume is $(1 - \phi_d)\rho_f$. Application of the Reynolds transport theorem to this quantity yields the continuous-phase continuity equation, where the interphase mass transfer is included as a sink term

$$\frac{\partial\left[(1-\phi_d)\rho_f\right]}{\partial t} + \nabla\left[(1-\phi_d)\rho_f \mathbf{u}\right] = -\frac{\phi_d}{V_p}\dot{m}_p \tag{2.39}$$

The RHS is thus equal and opposite to the source term used for the particle-phase Eulerian transport of Equations 2.27 through 2.29.

2.1.1.3.1 Continuous-Phase Momentum Conservation with Two-Way Coupling The same principle applied to mass conservation for Equation 2.39 can be applied to the continuous-phase momentum by defining the interphase force ($\mathbf{F}_{int}$) as the interphase momentum transfer from the continuous fluid to a single particle. This force is equal but opposite to the force that a particle exerts on the fluid ($-\mathbf{F}_{int}$), which is the sink term for continuous-phase equation. However, the fluid stress acts on a volume regardless of whether the volume is occupied by a particle or by fluid element. As such, it is not part of the interphase force, which can then be written as

$$\mathbf{F}_{int} = \mathbf{F}_{surf} - V_p\left(-\nabla p + \nabla \cdot \tau_{ij}\right) \tag{2.40}$$

$$\tau_{ij} = \mu_f\left(\frac{\partial u_i}{\partial x_j} + \frac{\partial u_j}{\partial x_i} - \frac{2}{3}\delta_{ij}\nabla \cdot \mathbf{u}\right) \tag{2.41}$$

The fluid stress term on the RHS of Equation 2.30 is the sum of the pressure gradient and that of the viscous stress. A rigorous derivation and discussion of the term is given by Prosperetti (2007).

Applying the Reynolds transport theorem to describe the change in continuous-phase momentum per unit volume yields

$$\frac{\partial\left[(1-\phi_d)\rho_f \mathbf{u}\right]}{\partial t} + \nabla \cdot \left[(1-\phi_d)\rho_f \mathbf{u}\mathbf{u}\right] = (1-\phi_d)\rho_f \mathbf{g} + (1-\phi_d)\left[\nabla \cdot \tau_{ij} - \nabla p\right] - \frac{\phi_d}{V_p}\left(\mathbf{F}_{int} + \dot{m}_p \mathbf{v}\right) \tag{2.42}$$

The first and second terms on the RHS are the body and fluid stress forces applied to the continuous-phase mass per unit volume, while the third term stems from Equations 2.40 and 2.41.

A coupled continuous-phase energy equation can be similarly obtained by employing the same assumptions used for particle energy transport (Equations 2.9 through 2.12) and by neglecting effects associated with particle volume or shape changes

$$\begin{aligned}&\frac{\partial\left[(1-\phi_d)\rho_f e_{tot}\right]}{\partial t}+\nabla\left[(1-\phi_d)\rho_f e_{tot}\mathbf{u}\right]=(1-\phi_d)\rho_f\mathbf{u}\cdot\mathbf{g}-\frac{\phi_d}{V_p}\left(\mathbf{F}_{int}\cdot\mathbf{v}\right)\\&+\frac{\partial\left[(1-\phi_d)\tau_{ij}u_i\right]}{\partial x_j}-\nabla\cdot\left[(1-\phi_d)p\mathbf{u}\right]+\tau_{ij}\frac{\partial\left(\phi_d v_i\right)}{\partial x_j}-p\nabla\cdot\left(\phi_d\mathbf{v}\right)\\&-\frac{\phi_d}{V_p}\left[\dot{Q}_p+\dot{m}_p\left(h_{phase}+e_p\right)+\left(\dot{m}_p\mathbf{v}\cdot\mathbf{v}\right)\right]+\nabla\cdot\left[k_{eff}\nabla T\right]\end{aligned}\tag{2.43}$$

The LHS terms on the first line include the Eulerian and convective changes in the total fluid energy, while the RHS terms on this first line include the work associated with moving the fluid against the body force and against the particle interphase force. The RHS terms on the second line include work against the fluid stress forces, while those on the third line arise from heat and mass transfer as well as the thermal diffusion within the continuous-phase volume. The thermal diffusion is based on an effective conductivity (k_{eff}), typically taken to be the mixed-fluid conductivity (k_m). This mixed-fluid conductivity is based on the volume fraction weighted values from the particles and from the continuous phase:

$$k_{eff}\approx k_m\equiv\phi_d k_p+(1-\phi_d)k_f\tag{2.44}$$

This approximation is appropriate if the particles have a small thermal response time compared to the timescale of temperature changes in the fluid. On the other hand, a very long particle thermal response time will limit the thermal diffusivity to only that conducted through the continuous phase, that is, $k_{eff}\rightarrow(1-\phi_d)k_f$. Since the differences in thermal conductivities for most substances do not vary widely, the difference between these two limits is small for most dispersed flows ($\phi_d < 10\%$). As such, Equation 2.44 is both common and generally reasonable (Crowe et al., 1998, Elghobashi, 2006).

Finally, the terms in the third line include interphase energy coupling due to heat and mass transfer, the kinetic energy losses due to generation of particle mass, and the work required to move the particles based on interphase force and fluid stress force. A more detailed derivation and accounting of these terms is given by Crowe et al. (1998).

2.1.1.3.2 Influence of Dispersed-Phase Reference Frame The Eulerian transport equation given earlier for the continuous phase can be paired with dispersed-phase equations in the form of either the Lagrangian ODEs or Eulerian PDEs. In both cases, the key is determining the cell-averaged volume fraction at the continuous-phase nodes. If the particles are treated with an Eulerian approach, the interphase coupling terms can be obtained directly via the particle concentration predicted from Equations 2.27 through 2.29. For example, the interphase force per unit volume evaluated at the fluid node i is simply

$$\left(\frac{\phi_d}{V_p}\mathbf{F}_{int}\right)_i=\frac{\phi_d\left(\mathbf{x}_i,t\right)\mathbf{F}_{int}\left(\mathbf{x}_i,t\right)}{V_{p,i}}\tag{2.45}$$

This Eulerian–Eulerian formulation is numerically convenient since communication of data between the phases occurs at coincident node locations so that there is no interpolation error.

For Lagrangian particles, the coupling to a continuous-phase node can be computed based on the computational volumes associated with the nodes as shown in Figure 2.2b. For example, the interphase force coupling term for particle and parcel approaches can be given as

$$\left(\frac{\phi_d}{V_p}\mathbf{F}_{int}\right)_i=\frac{1}{V_{\Delta,i}}\sum_{j=1}^{N_{p\Delta}}\mathbf{F}_{int,j}=\frac{1}{V_{\Delta,i}}\sum_{j=1}^{N_{p\Delta}}N_{pP,j}\mathbf{F}_{int,j}\tag{2.46}$$

In this expression, $V_{\Delta,i}$ is the volume associated with node $\mathbf{x}_i$ that contains $N_{p\Delta}$ number of particles per cell if individual trajectories are followed or (as given by the RHS) contains $N_{P\Delta}$ parcels per cell with N_{pP} particles per parcel. To ensure that the coupling to the continuous phase can be described as a continuum, the constraint of Equation 5.14 must be placed on the number of Lagrangian particles or a similar constraint based on the number of parcels as

$$N_{P\Delta} \gg 1 \quad \text{for Lagrangian parcels with two-way or three-way coupling} \tag{2.47}$$

For example, four or more particles or parcels per element are typically needed for accurate two-way coupling. As a result, the Eulerian–Lagrangian approach can be an order of magnitude less efficient for two-way coupling as compared to the Eulerian–Eulerian approach (Druzhinin and Elghobashi, 1998, 1999).

2.1.2 Classification by Relative Velocity Magnitude

There is a second type of classification that is based on increasing particle relative velocity and includes mixed-fluid, weakly separated, and separated-fluid treatments. The separated-fluid treatment generally assumes that the continuous phase and dispersed phase have distinct transport equations and is described earlier for the Eulerian–Lagrangian approach and the Eulerian–Eulerian approach. The separated-fluid approach places no restriction on the magnitude of the relative velocity but can require significant computation to compute the associated surface forces. In contrast, the mixed-fluid approach assumes that the relative velocity be negligible compared to the fluid velocity ($w/u \to 0$). Finally, the weakly separated approach is intermediate to the other two approaches as it assumes a small but finite relative velocity ($w/u \ll 1$). These mixed-fluid and weakly separated approaches are discussed later and are advantageous to use when the test conditions are appropriate because they generally only require one momentum PDE for both phases.

2.1.2.1 Mixed-Fluid Approach

The mixed-fluid approximation assumes that the dispersed phase and the continuous phase are in local kinetic and thermal equilibrium, that is, the relative velocities and temperatures between the two phases are negligible in comparison to variations of the overall flow field

$$\frac{w}{u} \to 0 \tag{2.48}$$

for kinetic and thermal equilibrium assumption

$$\frac{(T_p - T)}{T_p} \to 0 \tag{2.49}$$

Using these assumptions, the mixed-fluid values are set equal to the respective continuous phase and particle values at the centroid locations for the mixed-fluid approach, that is,

$$\mathbf{u}_m(\mathbf{x},t) \equiv \left[\mathbf{u}_{@p}(\mathbf{x},t) = \mathbf{v}(\mathbf{x},t)\right] \tag{2.50}$$

mixed-fluid treatment

$$T_m(\mathbf{x},t) \equiv \left[T(\mathbf{x},t) = T_p(\mathbf{x},t)\right] \tag{2.51}$$

This is equivalent to assuming negligible momentum and thermal inertias (zero response times), which is consistent with particles for which all the relevant Stokes numbers are much less than unity, for example, $St_D \ll 1$ for the macroscopic flow or $St_\lambda \ll 1$ for turbulent flow. Therefore, the mixed-fluid approach is only reasonable for very small particles (equivalent to an *immiscible* mixture distributed throughout a domain). Since the velocities and temperatures of both phases are now assumed to be represented by single values, this mixed-fluid approach has also been termed the *locally homogeneous flow* approach (Faeth, 1987), the *single-fluid scalar transport* approach, and the *modified-density* approach.

Since both phases move at the same velocity, the overall mixture can be described to have a mixed-fluid density that is simply the mass of all phases per unit volume and can be related to the volume fraction as

$$\rho_m \equiv \rho_p \phi_d + \rho_f (1 - \phi_d) \tag{2.52}$$

As a result, the mixed-fluid approximation results in a single set of conservation equations for the flow mixture (as opposed to one set for the continuous phase and one set of the dispersed phase). In particular, the transport of mass, momentum, and energy can be obtained by applying Equations 2.50 and 2.51 to both the Eulerian dispersed-phase and continuous-phase equations and then summing the two sets of equations together

$$\frac{\partial \rho_m}{\partial t} + \nabla\left(\rho_m \mathbf{u}_m\right) = 0 \tag{2.53}$$

$$\frac{\partial\left(\rho_m \mathbf{u}_m\right)}{\partial t} + \nabla \cdot \left(\rho_m \mathbf{u}\mathbf{u}\right) = \rho_m \mathbf{g} - \nabla p + \nabla \cdot \tau_{m,ij} \tag{2.54}$$

$$\frac{\partial\left(\rho_m e_m\right)}{\partial t} + \nabla\left(\rho_m e_m \mathbf{u}\right) = \left(\tau_{m,ij} - p\delta_{ij}\right)\frac{\partial u_{m,i}}{\partial x_j} + \nabla \cdot \left(k_m \nabla T_m\right) \tag{2.55}$$

The second and third equations include a mixed-fluid viscous stress tensor ($\tau_{m,ij}$) that can be written in terms of a mixed-fluid viscosity

$$\tau_{m,ij} = \mu_m\left(\frac{\partial u_{m,i}}{\partial x_j} + \frac{\partial u_{m,j}}{\partial x_i} - \frac{2}{3}\delta_{ij}\nabla \cdot \mathbf{u}_m\right) \tag{2.56}$$

A key benefit for this approach is that the relative velocity and momentum ODE need not be employed (the same is true for the relative particle temperature and energy transfer ODE). Thus, the presence of the particle is only realized through the modification of the mixture density (ρ_m).

These aspect differences between the mixed-fluid and separated-fluid approaches are illustrated in Figure 2.4. Some key aspects of the mixed-fluid approach are especially relevant. First, the mixed-fluid set of equations is inherently a two-way coupled system since all phases act in concert and collision effects are ignored since $\mathbf{u} = \mathbf{v}$. Second, a single set of equations (without interphase momentum and energy transfer formulations) allows significant numerical simplicity, which should be used whenever appropriate (Equations 2.48 and 2.49). Third, the mixed-fluid approach generally uses the Eulerian reference frame for both phases, that is, an Eulerian–Eulerian approach. Figure 2.4 shows that the mixed-fluid method and the separated-fluid method are quite different. However, there is an intermediate method, as described later, which retains some of the features of each of these two distinct approaches.

2.1.2.2 Weakly Separated Approach

A hybrid approach between that of separated flow and mixed-fluid flow is the weakly separated approach or also called the "partially mixed" method. This approach is useful to describe motion of small particles whose dynamics are primarily controlled by the surrounding flow but which have a small but significant settling velocity. The simplest and most common version of the weakly separated method assumes that the particle relative acceleration is negligible in comparison to the fluid acceleration. This assumption allows a finite relative velocity that can be approximated by the terminal velocity

$$\mathbf{v}(\mathbf{x},t) = \mathbf{u}_{@p}(\mathbf{x},t) + \mathbf{w}_{term} \tag{2.57}$$

This is also called the "terminal velocity" approach and can be used for flows with slow sedimentation or rise. If the particle is considered to be in thermal equilibrium $T_p = T$, the dispersed phase only requires a mass transport equation given by either the Eulerian particle concentration PDE or a Lagrangian position ODE

$$\frac{\partial\left(\phi_d \rho_p\right)}{\partial t} + \nabla\left[\phi_d \rho_p\left(\mathbf{u}_{@p} + \mathbf{w}_{term}\right)\right] = \frac{\phi_d}{V_p}\dot{m}_p \tag{2.58}$$

$$\frac{d\left(\mathbf{x}_p\right)}{dt} = \mathbf{u}_{@p} + \mathbf{w}_{term} \tag{2.59}$$

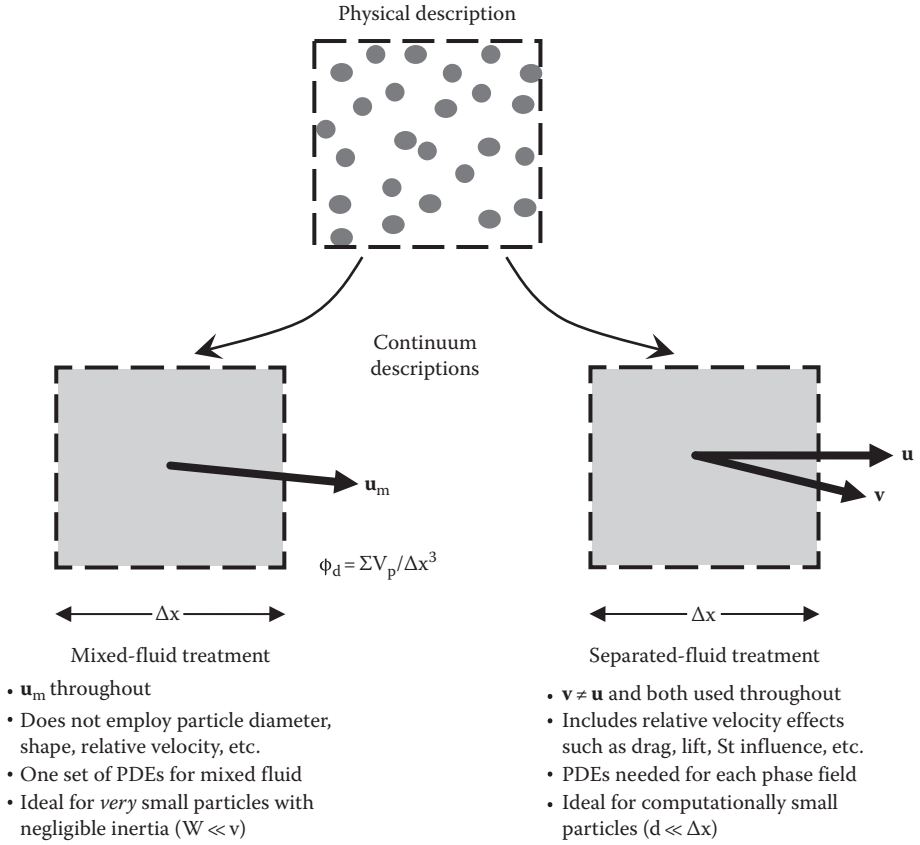

Figure 2.4

Comparison of mixed-fluid and separated-fluid treatments for a computational cell based on an Eulerian–Eulerian approach.

Thus, Equation 2.57 effectively serves as the momentum equation for the particles. This method is thus nearly as efficient as the mixed-fluid method but captures mean relative velocity effects. However, this approach cannot capture any effects associated with an initial particle velocity or due to a collision with a wall or another particle.

2.1.3 Classification by Particle Size Relative to Grid Size

As discussed earlier, there are three main approaches for multiphase numerical treatments based on particle size: point force, distributed force, and resolved surface. The choice is related to the capability in predicting the surface forces acting on the particle ($\mathbf{F}_{surf}$), which is needed for the separated-fluid treatment as discussed earlier. These forces are also needed if two-way and three-way coupling effects are to be included for the continuous-phase fluid solution. In determining $\mathbf{F}_{surf}$, there are three primary approaches: the "point-force" representation for particles smaller than the grid scale ($d < \Delta x$), the "distributed-force" representation for particles on the order of the grid scale ($d \sim \Delta x$), and the "resolved-surface" representation for particles much larger than the grid scale ($d \gg \Delta x$). These are discussed in the following three subsections.

2.1.3.1 Point-Force Approach

The point force (also referred to as the "point mass" or "point volume") has the advantage of eliminating the need to simulate the detailed flow around the particle. For an Eulerian treatment of the dispersed phase, the relative velocity is defined at the grid nodes

$$\mathbf{w}(\mathbf{x}_i, t) = \mathbf{v}(\mathbf{x}_i, t) - \mathbf{u}(\mathbf{x}_i, t) \tag{2.60}$$

Once the unhindered flow characteristics are known, a point-force equation can be used to describe the surface forces based on a linear combination of drag, lift, added mass, history, fluid stress, and so on. The fluid dynamic forces on the particle can be obtained with empirical or theoretical treatments.

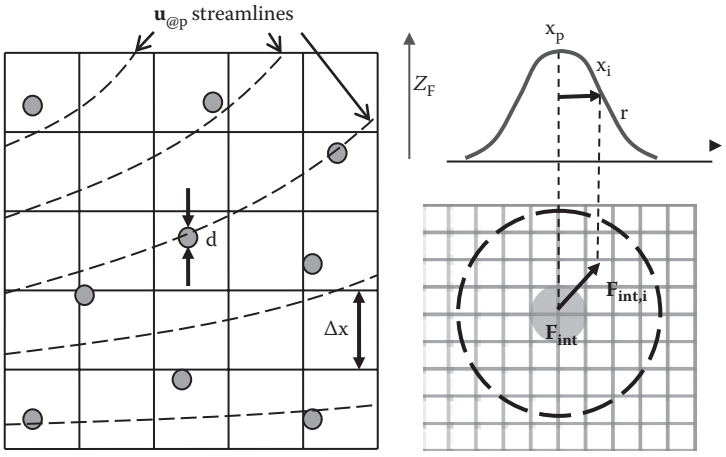

Figure 2.5

Different representations for particle treatment based on particle size in relation to continuous-fluid grid resolution for (a) a point-force representation and (b) a distributed-force representation.

The continuous-phase characteristics in either case do not include the fluid disturbances associated with individual particles. This indicates that the particle should be smaller than the length scales associated with continuous-phase gradients. Since this is also true for the discretization of the continuous phase, it yields a size criterion based on computational resolution

$$d < \Delta x \quad \text{for point force with one-way coupling} \tag{2.61}$$

A more rigorous criterion would be d « Δx (Figure 2.5a) such that the particle will see only very weak continuous-fluid gradients over the length scale associated with its diameter. Since the continuous-phase computational resolution must be small enough to provide grid-independent results, the point-force technique is limited to particles that are smaller than any spatial features to be resolved in the computational domain. For example, a direct numerical simaultion (DNS) description of turbulent flow requires that the particle diameter be smaller than the friction length scale if in the laminar sublayer ($d^+ < 1$) or less than the Kolmogorov turbulent microscale (d < λ) if in the outer portion or above the boundary layer.

2.1.3.2 Distributed-Force Approach

The distributed-force technique is employed when the particle diameter is on the order of the spatial resolution of the continuous phase, that is,

$$d \sim \Delta x \quad \text{for distributed-force treatment} \tag{2.62}$$

In this case, the variations in the flow properties in the region of the particle should be considered since the fluid interactions between the two phases occur over distances extending several particle diameters. As such, the coupling should extend over a region larger than a single grid cell (Figure 2.5b). To include the surface force on the particle, there are two distributed-force methods: "spatially averaged" and "semiresolved." The spatially averaged approach approximates the unhindered conditions (e.g., $\mathbf{u}_{@p}$) by surface and volume averages in the vicinity of the particle as opposed to using a single interpolated point at the centroid. This approach is generally limited to d < 3Δx without two-way coupling but d < Δx with two-way coupling.

In contrast, the semiresolved approach directly integrates two-way coupling effects and thus allows for larger particles (or finer resolutions) based on $3\Delta x < d < 10\Delta x$. Note that both techniques share a similar approach for distributing the interphase force on the fluid.

For two-way coupling, there are many variants of the distributed-force technique. To impart $\mathbf{F}_{int}$ over a region (instead of at a point), a force distribution function ($\mathcal{Z}_F$) can be used about the vicinity of the particle as illustrated in Figure 2.5b. Similar distributions can be applied for mass and heat transfer. The distributed-force technique is thus a hybrid between the point-force approach and the resolved-surface approach, the latter of which is discussed later.

2.1.3.3 Resolved-Surface Approach

For very large particles, the resolved-surface approach can be used if the detailed local flow over the particle surface is numerically discretized and computed. This approach resolves the fluid surface stresses so that they may be computationally integrated to compute the resulting fluid dynamic forces on the particle. This method is also called the "full DNS" approach and requires the computational resolution to sufficiently describe the detailed stress distribution over the particle surface, for example,

$$d \gg \Delta x \quad \text{for resolved-surface treatment} \tag{2.63}$$

This criterion requires many fluid nodes per individual particle, for example, hundreds or thousands depending on the particle geometry, Reynolds number, and so on. As such, this technique is only reasonable when there are few particles in the computational domain. However, this technique has the advantage of allowing complex particle geometries and incorporating detailed nonlinear flow fields around the particles (Figure 2.6).

Since the surface force is obtained from the surrounding flow, it does not require any force decomposition in terms of lift, drag, added mass, history, fluid stress, and so on since all these effects are directly incorporated by the discrete surface integration. In particular, no assumptions of particle shape, particle Reynolds number, particle or flow acceleration, surface conditions, flow gradients, and so on are required for the use of this formulation. Thus, there is no need to determine $\mathbf{u}_{@p}$, and no empirical or analytical force expressions for $\mathbf{F}_{sur}$ are required. Furthermore, in the case of a fluid particle (e.g., drop or bubble), the internal fluid dynamics may also be directly simulated using internal discretization (this can be important since the recirculation can affect the surface stresses). Also note that two-way coupling, three-way coupling, and four-way coupling are automatically included in the resolved-surface approach since the interstitial fluid and contact dynamics can be fully resolved as well. As such, the resolved-surface technique is the most desirable in terms of accuracy as it allows the most physically realistic surface force method but is also the most computationally intensive approach.

There are two primary treatments for the resolved-surface method that depend on how the interface between the particle and the continuous phase is treated: the "gridded interface method" (GIM) and the "immersed interface method" (IIM). These two approaches are illustrated in Figure 2.6 (where the outward normal of the interface is $\mathbf{n}$) and are overviewed in the following sections.

2.1.3.3.1 Gridded Interface Method The GIM approach is typically used when the particle shape is simple (e.g., a sphere or an ellipsoid) so that the grid resolution over the surface is straightforward. In this case, the interface between the particle and the surrounding fluid is discontinuous, that is, infinitely thin (Figure 2.6b). The boundary condition on a solid particle surface is typically specified as *a no slip for continuum conditions*. For an uncontaminated fluid particle with significant recirculation, the particle interior should also be discretized.

Once the flow field around the particle surface is known and described by the resolved velocity and pressure ($\mathbf{U}$ and P), the surface force can be determined by numerically integrating the pressure and the continuous-phase shear stress over the discretized surface elements

$$\mathbf{F}_{sur} = \sum_{k=1}^{N_k} \left(-P\mathbf{n} + \tau_{resolved,ij} n_j \right)_k \Delta A_{p,k} \tag{2.64}$$

$$\tau_{resolved,ij} = \mu_f \left(\frac{\partial U_i}{\partial x_j} + \frac{\partial U_j}{\partial x_i} - \frac{2}{3}\delta_{ij} \nabla \cdot \mathbf{U} \right) \tag{2.65}$$

In this equation, ΔA_p is a discrete particle surface area element, while $\mathbf{U}$ and P are the resolved velocity and pressure, that is, the values on the particle surface that take into account the particle's volume and impact

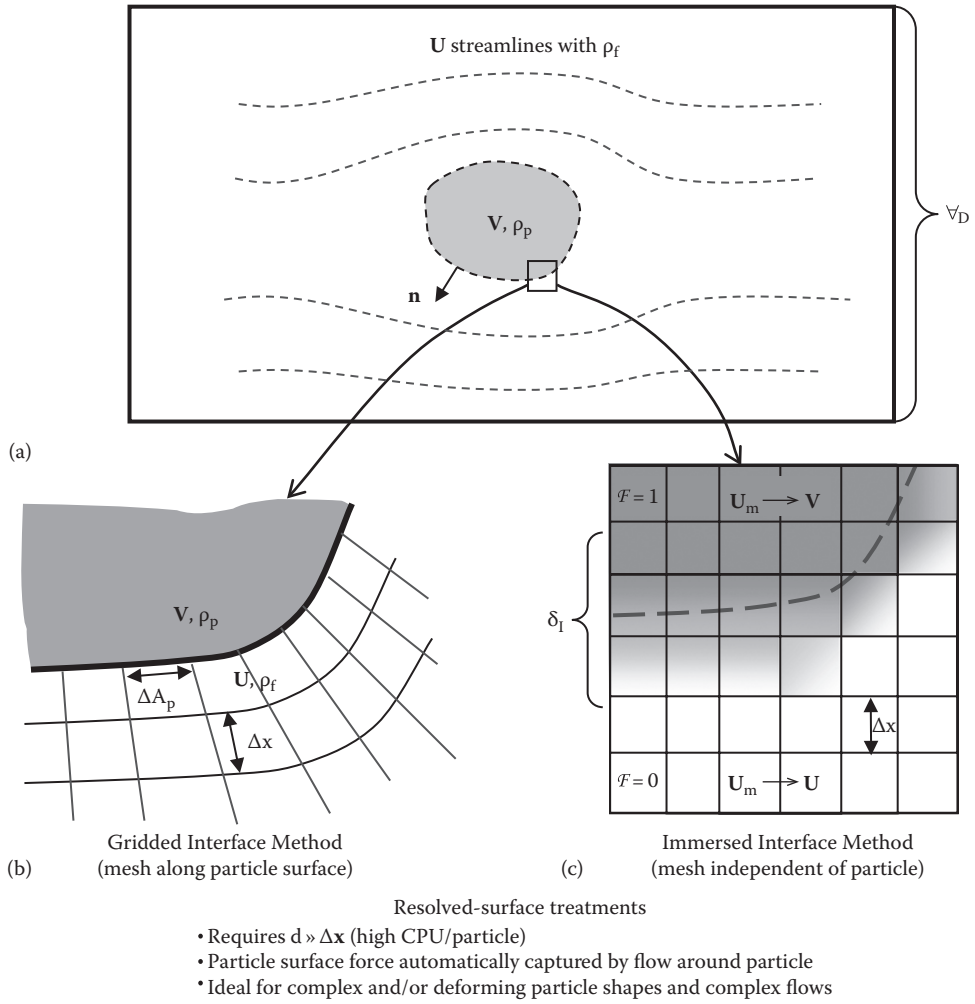

Figure 2.6

Resolved-surface approaches showing (a) schematic of particle in a computational domain along with (b) near-surface close-ups of a GIM mesh, and (c) that of an IIM mesh superimposed on the marker function distribution.

on the flow. This resolved-surface force can be combined with Equation 2.1 to move the particle to the next position with a new velocity and acceleration.

2.1.3.3.2 Immersed Interface Method The IIM is fundamentally based on a structured Eulerian grid for the computational domain that does not need to coincide with the particle surface. This allows the flow PDEs to be solved efficiently on simple Cartesian grids. A popular IIM category is the continuous interface methods that can be applied if the particle is a fluid. The approach introduces a nonphysical interface thickness (δ_I) as shown in Figure 2.6c. Instead of letting the flow properties between the particle and the surrounding fluid jump discontinuously (as is physically appropriate) across the molecularly thin interface, the CIM smoothly distribute these flow properties of velocity, density, and viscosity across a finite thickness interface that is several grid cell thick. This smooth distribution is accomplished with a "marker function" ($\mathcal{F}$) that is defined as the fraction of the computational cell occupied by particle matter. This function $\mathcal{F}$ equals 0 outside of the particle, varies smoothly from 0 to 1 across this interface, and equals 1 inside the particle. This function assumes that a computational cell volume is much smaller than the particle diameter. This function is distinct from the continuum-based volume fraction that assumes a computational volume much larger than the particle diameter. This marker function can then be used to define the "one-fluid" density that tends to the physical values outside the interface as

$$\rho = (1-\mathcal{F})\rho_f + \mathcal{F}\rho_p \tag{2.66}$$

Similarly, the velocity fields of both phases are represented by a one-fluid velocity ($\mathbf{U}_m$) that reverts to the correct physical limits outside of the interface but takes on a nonphysical (numerically convenient) value within the interface

$$\mathcal{F} = 0 \quad \mathbf{U}_m \rightarrow \mathbf{U} \text{ (outside of the particle)} \tag{2.67}$$

$$0 < \mathcal{F} < 1 \quad \mathbf{U}_m \rightarrow \mathbf{V}_I \text{ (within particle interface)} \tag{2.68}$$

$$\mathcal{F} = 1 \quad \mathbf{U}_m \rightarrow \mathbf{V} \text{ (inside of the particle)} \tag{2.69}$$

This formulation provides a single set of continuum PDEs for the entire domain based on $\mathbf{U}_m$ using the one-fluid density and viscosity. This allows for solutions on a simple Cartesian grid (which generally allows the fastest computation for a given number of grid points). Note that the finite interface thickness is nonphysical but is constructed to be as thin as possible while still allowing a stable continuum variation of velocity, density, and viscosity across the grid. This typically results in a prescribed thickness of 2–4 computational cells depending on the magnitude of the density ratio (although specialized sharp interface methods can reduce this thickness to one computational cell). A distinct advantage of the one-fluid approach is that the surface force of Equations 2.64 and 2.65 is satisfied (in contrast to the GIM). As such, this one-fluid approach avoids the ODEs needed to update particle velocity and rotation and complexities associated with gridding along the particle surface.

References

Crowe, C.T., Sommerfeld, M., and Tsuji, Y., *Multiphase Flows with Droplets and Particles*, CRC Press, Boca Raton, FL, 1998.

Crowe, C.T., Schwarzkopf, J.D., Sommerfeld, M., and Tsujii, T., *Multiphase Flow with Droplets and Particles,* CRC Press, 2nd edition, Taylor and Francis group, 2012.

Drew, D.A., Mathematical modeling of two-phase flow, *Ann. Rev. Fluid Mech.*, 15, 261–291, 1983.

Drew, D.A. and Passman, S.L., *Theory of Multicomponents Fluids*, Springer, New York, 1999.

Druzhinin, O.A. and Elghobashi, S., Direct numerical simulations of bubble-laden turbulent flows using the two-fluid formulation, *Phys. Fluids*, 10(3), 685–697, 1998.

Druzhinin, O.A. and Elghobashi, S., On the decay rate of isotropic turbulence laden with micro-particles, *Phys. Fluids*, 11(3), 602–610, 1999.

Elghobashi, S., in C. Crowe (Ed.), Direct simulation of turbulent flows laden with dispersed particles, *Multiphase Flow Handbook*, CRC Press, Boca Raton, FL, 2006.

Faeth, G.M., Mixing, transport and combustion in sprays, *Prog. Energy Combust. Sci.*, 13, 293–345, 1987.

Loth, E., Numerical approaches for motion of dispersed particles, bubbles, and droplets, *Prog. Energy Combust. Sci.,* 26, 161–223, 2000.

Michaelides, E., *Particles, Bubbles, and Droplets: Their Motion, Heat and Mass Transfer*, World Scientific Publishing, Hackensack, NJ, 2006.

Michaelides, E., *Nanofluidics – Thermodynamic and Transport Properties*, Springer, New York, 2014.

Prosperetti, A., Averaged equations for multiphase flow, in A. Prosperetti and G. Tryggvason (Eds.), *Computational Methods for Multiphase Flow*, Cambridge University Press, Cambridge, U.K., 2007.

Zhang, D.Z. and Prosperetti, A., Averaged equations for inviscid dispersed two-phase flow, *J. Fluid Mech.*, 267, 185–219, 1994.

2.2 Direct Numerical Simulations of Gas–Liquid Flows

Gretar Tryggvason

An analytical solution of the equations governing multiphase flows is the ultimate reference to which experimental results and approximate models can be compared to. Unfortunately, analytical solutions for multiphase flows are few and limited to very simple systems. Solutions of the equations using numerical methods have, since the latter part of the last century, come to the rescue, and it is now possible to obtain accurate solution for a wide range of parameters, where analytical solutions, even approximate ones, cannot be found. Numerical solutions have, however, done much more than simply provide solutions where analytical

techniques do not work. It is now possible to solve the governing equations for the unsteady motion of systems that approach the complexity that was only addressable by experiments earlier. The emergence of direct numerical simulations (DNS) has changed multiphase flow research in fundamental ways, and yet, it is clear that so far we have only started to explore the full potentials of this approach. It is useful for the purpose of the present discussion to define DNS as simulations of unsteady complex flow with a large range of scales where every continuum spatial and temporal scale is fully resolved. The early computations of the Rayleigh–Taylor instability, gravity currents, and droplet splatting by the marker-and-cell (MAC) method—impressive as those were—are therefore not DNS by the present definition, since the range of length and timescales was so limited. For single-phase flows, DNS generally require the flow to be turbulent, but for multiphase flows the unsteady motion of different phases can lead to the expected range of scales.

In many industrial and natural processes, multiphase gas–liquid flows consist of one phase in the form of well-defined bubbles or drops dispersed in another continuous phase. Bubbly flows occur in boiling heat transfer, cloud cavitation, aeration and stirring of reactors in water purification and wastewater treatment plants, bubble columns and centrifuges in the chemical industry, cooling circuits of nuclear reactors, the exchange of gases and heat between the oceans and the atmosphere, and explosive volcanic eruptions, just to name a few examples. Similarly, drops are found in sprays used in atomization of liquid fuels, painting and coating, emulsions, and rain. Understanding the evolution and properties of *dispersed* flows is therefore of major technological as well as scientific interest.

For engineering applications involving a large number of bubbles and drops, computational modeling usually relies on equations that describe the average flow field. The two-fluid model, where separate equations are solved for the dispersed and the continuous phase, is the most common approach. Since no attempt is made to resolve the unsteady motion of individual particle, closure relations are necessary for the unresolved motion and the forces between the particle and the continuous phase. Closure relations are usually determined through a combination of dimensional arguments and correlation of experimental data. The situation is analogous to computations of turbulent flows using the Reynolds-averaged Navier–Stokes equations where momentum transfer due to unsteady small-scale motion must be modeled. For details of two-fluid modeling, see Drew (1983), Ishii (1975), Drew and Lahey (1993), and Zhang and Prosperetti (1994). For the turbulent motion of single-phase flows, DNS, where the unsteady Navier–Stokes equations are solved on fine enough grids to fully resolve all flow scales, have had a major impact on closure modeling. The goal of DNS of multiphase flows is similar. In addition to information about how the drift Reynolds number, velocity fluctuations, and bubble dispersion change with the properties of the system, the computations should yield insight into how bubbles and drops interact, both with each other and with the continuous phase. The simulations should show whether there is a predominant microstructure and/or interaction mode, and if the flow forms structures that are much larger than the size of the dispersed particles. Information about the microstructure is essential for the construction of models of multiphase flows and can also help to identify what approximations can be made.

In this section, we first review briefly the various numerical techniques developed for the DNS of multiphase flows and then discuss a few results, focusing mostly on disperse flows of gas bubbles in liquids. Although the focus is on simulations of complex systems with a broad range of scales, most of the methods used are applicable to much simpler systems and, indeed, the methods have been developed and tested for such problems. Thus, some references to computations of simple problems—even if they are not DNS by the definition used here—are unavoidable.

2.2.1 Simple Flows (Re = 0 and Re = ∞)

In the limit of high and low Reynolds numbers, it is sometimes possible to simplify the flow description considerably either by ignoring inertia completely (Stokes flow) or by ignoring viscous effects completely (inviscid, potential flow). Early attempts to understand the collective motion of bubbles, drops, and solid particles therefore focused on these limits. For undeformable spheres, it is, in both these limits, possible to reduce the governing equations to a system of coupled ordinary differential equations for the particle positions. For Stokes flows, several authors have examined the properties of suspensions of solid particles in shear flows (see Brady and Bossis, 1988, for a review of early work), but studies of inviscid systems are more limited. Sangani and Didwania (1993) and Smereka (1993) examined the behavior of many bubbles in periodic domains, specifying the rise velocity to prevent continuing acceleration. They observed that the bubbles tended to form horizontal "rafts," particularly when the variance of the bubble velocities was small. As this "rafting" is generally not observed experimentally, the results cast considerable doubt on the utility of the potential flow approximation for the interactions of many bubbles. This is somewhat unexpected since for single bubble this approximation is rather good (see, however, Harper, 1997) for a discussion of bubbles

rising in-line). Deformable bubbles and drops can be simulated using boundary integral techniques in both the Stokes and the inviscid limits. Several authors have examined suspensions of very viscous drops, including Li and Pozrikidis (2000) and Zhou and Pozrikidis (1993), who followed the dynamics of 2D drops in a channel, and Loewenberg and Hinch (1996) and Zinchenko and Davis (2000) have examined fully 3D drops. The boundary integral method for Stokes flow has been described in detail in the book by Pozrikidis (1992), and Pozrikidis (2001) gives a detailed summary of various applications. Unlike Stokes flow, inviscid models are generally only suitable for a transient short-time evolution since eventually viscous dissipation becomes important (see Chahine and Duraiswami, 1992, for early work). Although studies of flows in the limits of zero and infinite Reynolds number played an important role in early work on multiphase flows, their role is now much diminished, although there are situations where they constitute important limiting cases.

2.2.2 Methods for Finite Reynolds Number Flows

For intermediate Reynolds numbers, it is necessary to solve the full Navier–Stokes equations. The first method to allow computations of multifluid flows was the MAC method developed at Los Alamos by Harlow and collaborators. In Harlow and Welch (1965), the method was introduced and two sample computations of the so-called dam breaking problem shown. Several papers quickly followed: Harlow and Welch (1966) examined the Rayleigh–Taylor problem and Harlow and Shannon (1967) studied the splash when a drop hits a liquid surface. As originally implemented, the MAC method assumed a free surface, so there was only one fluid involved. This required boundary conditions to be applied at this surface and the fluid in the rest of the domain to be completely passive. The Los Alamos group quickly realized, however, that the same methodology could be applied to two-fluid problems. Daly (1969b) computed the evolution of the Rayleigh–Taylor instability for finite density ratios, and Daly and Pracht (1968) examined the initial motion of density currents. Surface tension was then added by Daly (1969a), and the method was again used to examine the Rayleigh–Taylor instability. The MAC method quickly attracted a small group of followers that used it to study several problems: Chan and Street (1970) applied it to free surface waves, Foote (1973) and Foote (1975) simulated the oscillations of an axisymmetric drop and the collision of a drop with a rigid wall, and Chapman and Plesset (1972) and Mitchell and Hammitt (1973) simulated the collapse of a cavitation bubble. Although the MAC method was designed specifically for multifluid problems (hence the M for Markers!), it was also the first method to successfully solve the Navier–Stokes equation using the primitive variables (velocity and pressure). The staggered grid used was a novelty, and today, it is common practice to refer to any method using a projection-based time integration on a staggered grid as a MAC method.

The next generation of methods for multifluid flow evolved gradually from the MAC method. It was already clear in the Harlow and Welch (1965) paper that the marker particles could cause inaccuracies, and among the number of algorithmic ideas explored by the Los Alamos group, the replacement of the particles by a marker function soon became the most popular alternative. Thus, the volume-of-fluid (VOF) method was born. VOF was first discussed in a refereed journal article by Hirt and Nichols (1981), but the method apparently originated a few years earlier. While the results were generally superior to those of the MAC method, early VOF results showed considerable irregularities at the interface between the different fluids. In the 1980s and early 1990s, better advection methods (Youngs, 1982) and new ways to find surface tension (Brackbill et al., 1992) improved the results significantly. Fairly advanced VOF methods are now available, and many commercial CFD codes include the option of simulating free surface or multiphase flows using the VOF method. For a review of VOF methods, see Scardovelli and Zaleski (1999) and Tryggvason et al. (2011). Other methods, based on similar ideas but advecting the marker function in a different way, include the level set method (reviewed by Osher and Fedkiw, 2001, and Sethian, 2001) and the CIP method of Yabe and collaborators (see Yabe et al., 2001).

While the MAC methodology and its successors were being developed, other techniques were also being explored to capture fluid interfaces. Hirt et al. (1970) describe one of the earliest use of structured boundary-fitted Lagrangian grids. This approach is particularly well suited when the interface topology is relatively simple and no unexpected interface configurations develop. In a related approach, a grid line is aligned with the fluid interface, but the grid away from the interface is generated using standard grid generation techniques such as conformal mapping or other more advanced elliptic grid generation schemes. Such a method was used by Ryskin and Leal (1984) to compute the steady rise of buoyant, deformable, axisymmetric bubbles. Ryskin and Leal assumed that the fluid inside the bubble could be neglected, but Dandy and Leal (1989) and Kang and Leal (1987) extended the method to two-fluid problems and unsteady flows. Several authors have used this approach to examine relatively simple problems such as the steady-state motion of single particles or moderate deformation of free surfaces. Fully 3D simulations are relatively rare, and it is probably fair to say that it is unlikely that this approach will be the method of choice for very complex problems such

as the 3D unsteady motion of several particles. Similar comments apply to methods based on resolving the fluid by unstructured grid that are updated to ensure that the interface coincides with a grid line.

Several hybrid methods combine the ideas discussed earlier in a variety of ways. Front tracking, where the interface is marked by connected marker points but a fixed grid is used for the fluid within each phase has been particularly successful. In the method of Tryggvason and collaborators (Unverdi and Tryggvason, 1992, Tryggvason et al., 2001), the tracked front is used to advect a smoothed marker function and to compute the surface tension. The method is therefore very similar to methods that work directly with a grid-marker function, but the advection of the interface is greatly improved. For other implementation of similar ideas, see van Sint Annaland et al. (2006), Hao and Prosperetti (2004), Hua and Lou (2007), and Muradoglu and Kayaalp (2006). Other methods have been designed to capture the interface more accurately. These include the method of Glimm and collaborators (Glimm and McBryan, 1985) where the fixed grid is modified near the front to make a grid line follow the interface, as well as more recent "sharp-interface methods" (such as Fedkiw et al., 1999, Ye et al., 1999, Lee and LeVeque, 2003). The increased accuracy does, however, come at the cost of a considerably increased complexity, and it is not clear at the time of this writing what the impact of these new methods will be on the DNS of finite Reynolds numbers flows.

The most recent addition to the collection of methods capable of simulating finite Reynolds number multiphase flows is the lattice Boltzmann method (LBM). Although there have been some doubts about the accuracy and correctness of the LBM, it seems now clear that they can be used to produce results of accuracy comparable to more conventional methods. It is still not clear whether the LBM is significantly faster or simpler than other methods (as sometimes claimed), but most likely these methods are here to stay. For a discussion see, for example, Shan and Chen (1993).

Although there are many possible ways to solve the Navier–Stokes equations for multiphase flows, the most successful approaches have been based on the so-called one-fluid formulation, where one set of equations are solved for the whole flow field and the phase boundary is treated as an embedded interface by adding the appropriate source terms. These source terms are in the form of delta functions localized at the interface and are selected to provide the correct matching conditions at the phase boundary. Although the integral form is often used as a starting point, here we write the "one-fluid" Navier–Stokes equations for incompressible flows in the following differential form:

$$\frac{\partial \rho \mathbf{u}}{\partial t} + \nabla \rho \mathbf{u}\mathbf{u} = -\nabla p \cdot \rho \mathbf{g} + \nabla \cdot \mu(\nabla \mathbf{u} + \nabla \mathbf{u}^T) + \int_f \sigma \kappa \mathbf{n} \delta(\mathbf{x} - \mathbf{x}_f) ds. \tag{2.70}$$

Here,

u is the velocity
p is the pressure
ρ and μ are the discontinuous density and viscosity fields, respectively
σ is a 3D delta function constructed by repeated multiplication of 1D delta functions
κ is twice the mean curvature
n is a unit vector normal to the front

Formally, the integral is over the entire front, thereby adding the delta functions together to create a force that is concentrated at the interface, but smooth along the front. **x** is the point at which the equation is evaluated and $\mathbf{x}_f$ is the position of the front. In most cases, the flow is assumed to be incompressible, so Equation 2.70 is supplemented by

$$\nabla \cdot \mathbf{u} = 0. \tag{2.71}$$

When combined with the momentum equation, this leads to an elliptic equation for the pressure. The single field formulation naturally incorporates the correct mass, momentum, and energy balances across the interface and integration of the conservation equations across the interface directly yields the standard jump conditions.

Equations 2.70 and 2.71 are usually solved on a regular staggered grid using a projection method for the time integration. The spatial and temporal accuracy are usually of second order, although sometimes higher-order time integration is used and the advection terms are treated by methods that are more robust than centered differences such as QUICK, ENO, or WENO. The elliptic pressure equation is generally solved by a multigrid iteration or Krylov subspace methods.

This solution strategy is, in particular, used in most implementations of VOF, level set, and front-tracking methods. What distinguishes between the various methods is how the marker function identifying the different fluids is updated. For flows where the material properties are constant in each fluid, a marker function is usually used to identify the different fluids. The marker moves with the fluid velocity:

$$\frac{DH}{Dt} = \frac{\partial H}{\partial t} + \mathbf{u} \cdot \nabla H = 0, \tag{2.72}$$

where

$$H(\mathbf{x}) = \begin{cases} 1 \text{ in fluid } 1 \\ 0 \text{ in fluid } 2 \end{cases}. \tag{2.73}$$

The density and viscosity are then set as functions of H, usually by

$$\rho = \rho_2 + (\rho_1 - \rho_2)H(\mathbf{x}) \quad \text{and} \quad \mu = \mu_2 + (\mu_1 - \mu_2)H(\mathbf{x}) \tag{2.74}$$

Other material properties are set similarly, when needed. Sometimes, the density is used as a marker function and other variables set as functions of the density.

In the VOF method, the marker function is advected directly, using specialized techniques to ensure that the interface stays sharp and well defined. In level set methods, a smooth function is advected and the interface identified by the zero contour line. The marker function is then constructed by mapping the smooth function into a function that transitions relatively sharply from one value to the other. To keep the mapping well behaved, the smooth function is readjusted periodically to keep it close to a distance function in the vicinity of the interface. In both VOF and level set methods, surface tension must be computed from the marker function on the fixed grid. In front-tracking methods, the phase boundary is tracked by connected marker points (the "front") that are advected by the flow velocity, interpolated from the fixed grid. The gradient of the marker function becomes a delta function when the change is abrupt across the boundary. To transfer the front singularities to the fixed grid, the delta functions are approximated by smoother functions with a compact support on the fixed grid. At each time step, after the front has been advected, the marker function is reconstructed by integration of the smooth grid-delta function. The surface tension is computed on the front, distributed to the grid, and then added to the nodal values of the discrete Navier–Stokes equations.

Many reviews are available that discuss computational methods for multiphase flows. Early reviews that discuss the many possible approaches include Hyman (1984) and Floryan and Rasmussen (1989), and more specialized treatment can be found in Scardovelli and Zaleski (1999) for VOF methods, Anderson et al. (1998) for phase field methods, and Osher and Fedkiw (2002) who discuss level set methods. The book by Shyy et al. (1996) also covers several aspects of computations of multiphase flows. Several articles about various aspects of computations of multiphase systems and related problems can be found in a special issue of the *Journal of Computational Physics* (volume 169, 2001). More recent coverage, focusing on VOF and front-tracking method, can be found in Tryggvason et al. (2011).

2.2.3 Bubbly Flows

One of the major applications of DNS of multiphase flows has been of bubbly flows. Studies of many interacting bubbles in periodic domains can be found in Esmaeeli and Tryggvason (1998, 1999) who simulated the unsteady motion of several 2D and 3D bubbles and Bunner and Tryggvason (1999, 2002a,b) who examined 3D systems with a much larger number of bubbles. The results of these simulations have helped clarify various aspects of the bubble interactions. One of the fundamental questions was, in particular, if relatively modest number of bubbles in fully periodic domains could be used to model homogeneous bubbly flows. The simulations showed that relatively low-order statistics, such as the average rise velocity of the bubbles and the pair probability distribution, converge rapidly with increasing size of the simulated domain, but other quantities, like the self-diffusion coefficient, converge much more slowly. The results also showed that for nearly spherical buoyant bubbles at modest Reynolds numbers that the dominant interaction mode is the "drafting, kissing, and tumbling" mechanism described by

Fortes et al. (1987). Thus, a bubble behind another bubble is drawn into the wake of the bubble in front, once in the wake it catches up and collides with the one in front and the two bubbles then "tumble" and move apart. This collision mode is inherently a finite Reynolds number effect, since two buoyant bubbles in Stokes flow do not change their orientation unless acted on by the third bubble and bubbles in potential flow repel each other if they are rising in an in-line configuration. The results also helped clarify the very different dynamics of nearly spherical bubbles that tender to line up side by side and more deformable ones that often rose one behind the other.

A number of recent studies have also focused on bubbles in laminar and turbulent flows in channels (Lu et al., 2005, 2006, Lu and Tryggvason, 2006, 2008, 2013). The results show that for clean bubbles in vertical channels, the flow structure is determined by the lift force on the bubbles. Nearly spherical bubbles in upflow are pushed to the walls, resulting in a bubble-rich wall layer and a lower void fraction in the middle, while in downflow the bubbles move away from the wall and the void fraction in the middle increases. For steady-state flow, this results in a very simple model for the void fraction. The removal of bubbles from the core region in upflow decreases the mixture density, and eventually, the weight of the mixture balances the imposed pressure gradient and the transfer stops. For downflow, the addition of bubbles to the core decreases the mixture density and again, the transfer continues until the buoyancy of the mixture matches the weight of the mixture. Thus, in both cases, the void fraction at steady state in the channel core is easily found, and if the average void fraction is known, then the void fraction in the wall layer for upflow and the thickness of the bubble free wall layer for downflow can be computed. The lift on deformable bubbles is generally either small or in a direction opposite to nearly spherical bubbles, so bubble-rich wall layers are not seen, in agreement with experimental studies. Simulations of the transient evolution toward the steady state have shown that while the lateral migration of bubbles occurs relatively fast, the velocity takes longer to adjust to the changes in the void fraction distribution.

As computer power increases, it is possible to examine both larger and more complex systems. In Figure 2.7, one example of a relatively large-scale simulation of bubbles in a turbulent channel flow is shown. The domain size is $2\pi \times 4 \times \pi$ computational units in the streamwise, wall-normal, and spanwise direction, respectively, resolved by about 0.4 billion grid points. The physical parameters are selected such that the Morton number is equal to 5.75×10^{-10} and the void fraction is about 3%. The bubbles come in four sizes, with the smallest bubbles having a diameter of 0.16 in computational units, and the largest one with a diameter of 0.44. The majority of the bubbles are small, and we expect the smallest bubbles to accumulate at the wall. The flow is driven upward by an imposed pressure gradient, giving a friction Reynolds number of $Re^+ = 500$. The bubbles are initially distributed nearly uniformly across the domain but as they start to rise, the smaller bubbles start to migrate toward the walls and form a dense wall layer. In the figure, the bubbles are shown at a relatively early time, where many of the small bubbles have moved to the wall, but there are still several small bubbles in the middle, along with most of the larger bubbles. The bubbles are shown along with the vorticity, visualized using the λ_2 method (Jeong and Hussain, 1995), where dark and light color indicates rotation in the opposite direction. Near the wall, most of the vortices are aligned with the flow and usually come in pairs, where nearby vortices have opposite rotation. Although bubbles moving toward the walls disrupt the vortices there, some have survived, at least at the time plotted here. The figure also shows that the vorticity shed by the large bubbles is responsible for the majority of the vorticity in the interior of the channel. Figure 2.8 shows a close-up of the bubbles and the vortices near the right wall, where we have selected a different value for the isocontour of λ_2.

For other simulations of various aspects of bubbly flows, see, for example, the LBM studies by Takada et al. (2000, 2001) and Sankaranarayanan et al. (2002); VOF simulations by Rabha and Buwa (2010); and computations using a front-tracking method similar to the one used for the results in Figure 2.7 by Dijkhuizen et al. (2010a,b). Large-scale simulations using a finite element flow solver coupled with a level set method to advect the phase boundary can be found in Bolotnov et al. (2011) and Bolotnov (2013).

Although bubbly flows have received considerable attention, the interface topology is often much more complex, particularly if the void fraction is high. Not only can the interface topology be very complex, but the interfaces may undergo repeated coalescence and breakup. Modeling such flows is still very primitive, but DNS should be able to provide considerable light on the various processes governing the flow. Topology changes in multiphase flows occur through two primary mechanisms: films that rupture and threads that break. Methods that track the indicator function identifying the different fluids directly on an Eulerian grid (such as VOF or level set methods) lead to coalescence or breakup whenever the film or the thread is underresolved, but front-tracking methods will generally not allow a change in topology. If the interface is tracked, it is possible to either prevent or allow topology changes. Generally, threads that

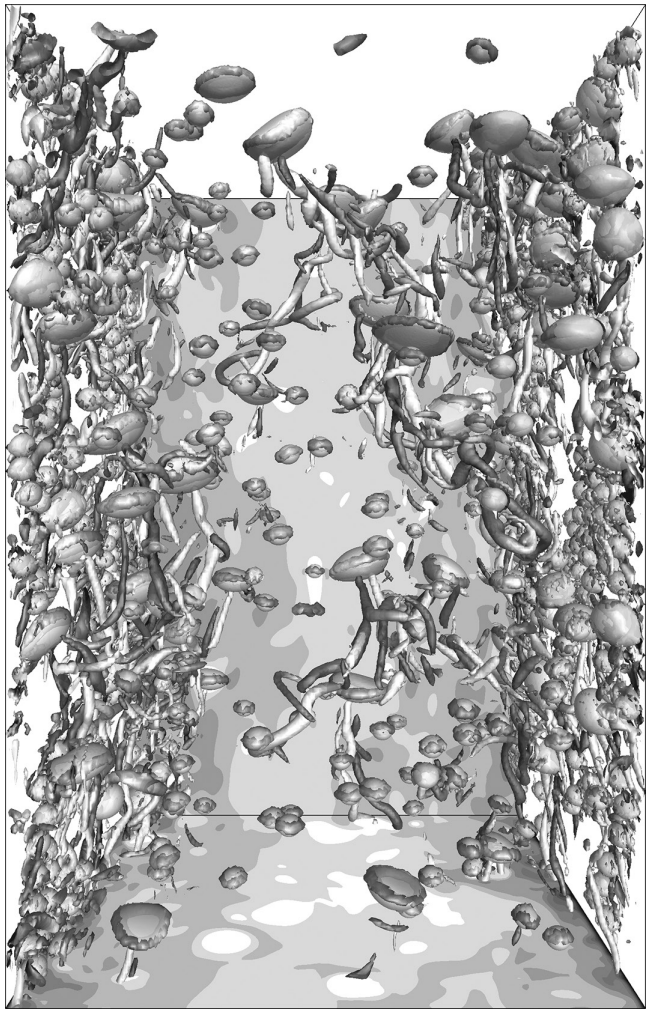

Figure 2.7

One frame from a simulation of many bubbles of different sizes in a turbulent channel flow. The bubbles and the vortical structures, visualized by $\lambda_2 = -2$, along with contours of the vertical velocity in the bottom horizontal plane and the back vertical plane. (Courtesy of Dr. Jiacai Lu, University of Notre Dame, Notre Dame, IN.)

break are by far the easier to deal with than the rupture of thin films. The diameter of threads goes to zero in a finite time, and the evolution is governed by the Navier–Stokes equations so that no additional physical modeling needs to be included. In addition, the breakup is very fast, so even if the final stage is not well resolved, that often does not have a significant effect on the overall flow dynamics. Thus, thread breakup is generally handled easily by most methods. Film draining and rupture are more complex, since the topology change takes place due to short-range attractive forces that are usually not included in the simulations. The attractive forces lead to an instability that results in holes that are then enlarged either by the formation of other holes that merge with the first one or by the enlargement of the original hole by rim breakup involving the formation of very small drops that are difficult to resolve. While methods that track the indicator function directly often produce ruptures that look plausible, the rupture is an artifact of the finite resolution, and in some cases, it is found that refining the grid postpones the rupture and prevents the solution from converging. It is possible that in some cases it does not make a big difference whether the rupture is physical or due to the resolution, but, in general, the importance of capturing the rupture accurately is not well understood. When the interface is tracked by connected marker points, it is necessary to explicitly add a strategy to rupture the interfaces when they are close enough, but at least it is possible to control when rupture takes place and when it does not. Thus, it should be possible to examine how sensitive the overall evolution of the flow is to how the rupture takes place, even if a complete rupture model is not included.

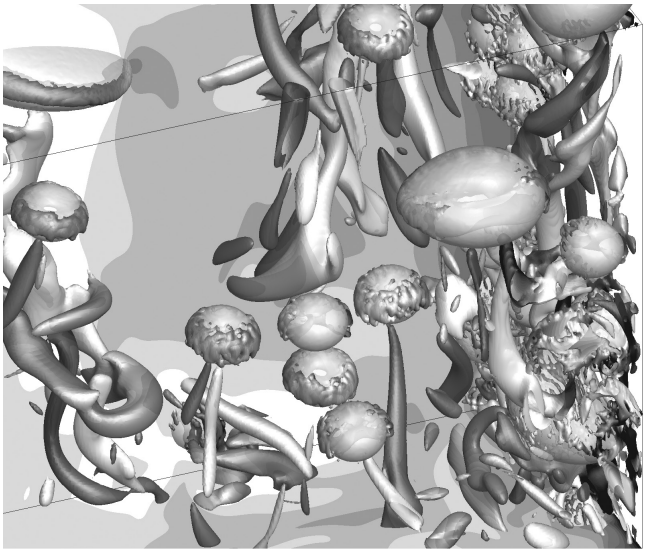

Figure 2.8

A close-up for the results shown in Figure 2.7, showing bubbles and vortical structures near the right wall. Here, $\lambda_2 = -1$. (Courtesy of Dr. Jiacai Lu, University of Notre Dame, Notre Dame, IN.)

Figure 2.9 shows results from two simulations of 40 bubbles in a channel flow. The bubbles are initially placed in a rectangular channel of size $\pi \times 2 \times \pi/2$ computational units in the streamwise, wall-normal, and spanwise direction, respectively, resolved by a $192 \times 128 \times 96$ grid. The bubble diameter is selected such that the void fraction is 13.6%. The flow is initially turbulent, with a friction Reynolds number of 128. All parameters except the surface tension are the same for both runs, giving a Morton number of 2.41×10^{-12} for the high surface tension case and 1.54×10^{-7} for the low surface tension case. The initial Eötvös

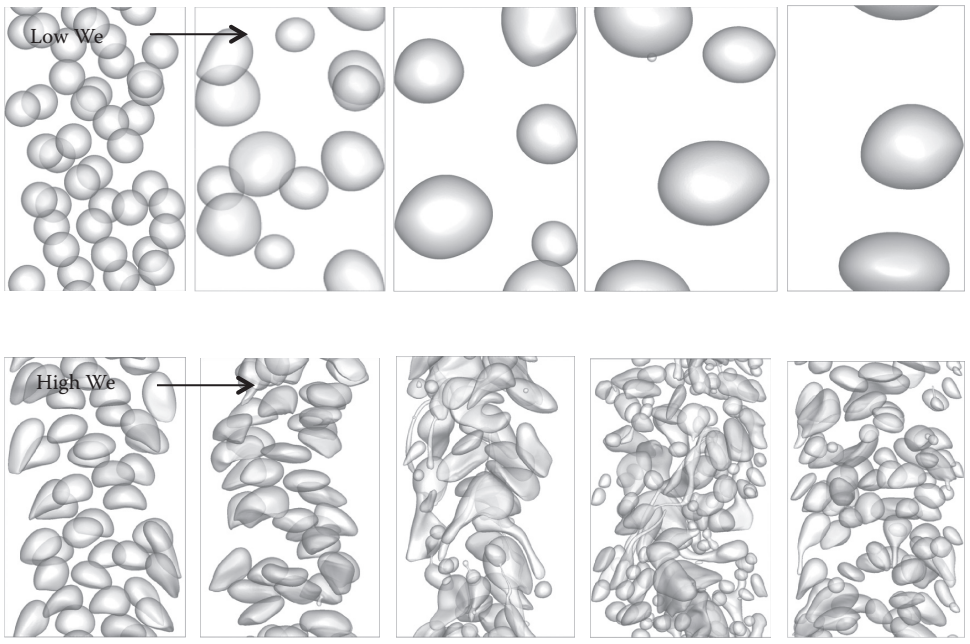

Figure 2.9

A few frames from two simulations of the evolution of several bubbles placed in an initially turbulent channel flow, when the bubbles are allowed to coalesce. In the top frames the surface tension is high and in the bottom frames the surface tension is low, so the bubbles break up after the initial coalescence. (Courtesy of Dr. Jiacai Lu, University of Notre Dame, Notre Dame, IN.)

number is 0.2 for the first case and 8.0 for the second case. As the bubbles rise, they collide and coalesce if the liquid film between them becomes sufficiently thin. For the high surface tension case, the bubbles keep coalescing until there is only one large bubble left (the two bubbles in the last frame will eventually become one), but for the high Weber number the bubbles first coalesce and then breakup again, eventually leading to a mixture of bubble sizes. Here, the thin films are ruptured if they become thinner than a third of a grid spacing, thus making the results similar to what we would expect from a VOF or level set computation.

While simulations of bubbles undergoing topology changes are just starting, many authors have examined the atomization of liquid jets, where the topology changes are critical for the formation of drops. Such studies include air-assisted breakup due to the coinjection of air as well as the breakup due to cross flow (Ménard et al., 2007, Desjardins et al., 2008, Gorokhovski and Herrmann, 2008, Lebas et al., 2009, Desjardins and Pitsch, 2010, Herrmann, 2011). The breakup remains the main challenge in these simulations and in spite of very large grids (Shinjo and Umemura, 2010, 2011) or the use of locally refined grids (Fuster et al., 2009), the breakup is generally dependent on the grid resolution and the smallest drops are underresolved. Thus, several authors have proposed hybrid approaches, where very small drops are modeled as point particles whose motion is modeled by empirical correlations for the drag force and ordinary differential equations are solved for the velocity and location (Herrmann, 2010, Tomara et al., 2010). The challenge is when to convert a fluid blob resolved on a grid to a point particle, and sometimes back again, in such a way that all conservation principles are satisfied.

2.2.4 Outlook

DNSs of multiphase flows have come a long way during the last decade. It is now possible to follow the motion of hundreds of bubbles, drops, and particles at finite Reynolds numbers in simple geometries for sufficiently long time so that meaningful averages can be computed. Much remains to be done, however. At higher Reynolds numbers, the number of grid points required to resolve each bubble and the flow around them increases and the cost of doing simulations with many bubbles increases. With larger computers, such simulations will become increasingly more feasible. The formation of bubbles and drops, as well as coalescence, must also be addressed and except for a few simulations of the breakup of drops in well-defined flows, little has been done. These problems are, nevertheless, well within reach.

As DNS of multiphase flows become more common, the need for advances in the development of the theoretical framework for modeling such flows is also becoming more urgent. Current models have mostly been developed in an environment where relatively little has been known about the details of the flow, and for the most part, these models are far behind what is available for single-phase turbulent flows. While our abilities to simulate directly more and more complex multiphase systems will certainly increase dramatically in the next few years, it is important to realize that our desire to compute will always be ahead of what we can do by DNS. Thus, the condensation of knowledge obtained by DNSs into reduced or averaged models that allow faster predictions will remain at the core of multiphase flow research for a long time to come. Given the experience from modeling turbulent single-phase flows, it is likely that many such models will involve resolving the large-scale motion but modeling the smallest scales. Efforts to develop such large eddy simulation–like model have just started (Labourasse et al., 2007, Toutant et al., 2008, 2009, Vincent et al., 2008).

Although much more can be done for two-fluid disperse systems, it is the longer-term development of the ability to compute the coupled motion of complex systems that will bring about the full impact of DNS. Most engineering fluid systems include a large number of physical phenomena such as fluid flow, evaporation, solidification, and chemical reactions, and simulations of the full systems will allow unprecedented insight. Real bubbles are, for example, rarely clean, and it is well known that surfactants change the behavior of a single bubble significantly. Extensions of various of methods to include surfactants can be found in James and Lowengrub (2004), Muradoglu and Tryggvason (2008), Booty and Siegel (2010), and Muradoglu and Tryggvason (2014), and results for a single bubble show significant effects, including changes in the lift force. However, DNS studies of the collective dynamics of many contaminated bubbles remain to be done. Heat transfer has been examined by Deen and Kuipers (2013), who showed that the passage of a small group of bubbles generally increases the local heat transfer, and by Tanaka (2011) and Dabiri and Tryggvason (2015) examined the motion of many bubbles in turbulent channel flows and showed that the bubbles enhance the overall heat transfer, both for nearly spherical bubbles that form wall layers and for more deformable ones that stay away from the walls. Mass transfer and reactions require us to solve additional advection/diffusion equations that include source terms when there are reactions, but the large range of scales, due to low mass diffusivities and fast reactions, introduce significant challenges. Similarly, several authors have simulating

boiling flows (for early work for relatively simple systems, see Juric and Tryggvason, 1998, Son and Dhir, 1998, Shin and Juric, 2002, and Esmaeeli and Tryggvason, 2003). The main challenge for most of these systems is that the different physical processes take place on very different temporal and spatial scales. While adaptive grid refinement can, in principle, be used for most of those cases, the reality is that that approach will quickly consume all the available grid points. In some cases, the small-scale motion is relatively simple, because surface tension and viscosity are significant, and the dynamics is well described by analytical models. When applicable, it is tempting to couple an analytical model of the small-scale motion with a full simulation of the larger-scale motion. The point particle approximation for small bubbles and drops is perhaps the best example, but a similar approach has also been used for nucleate boiling (Son and Dhir, 1998) and mass transfer (Aboulhasanzadeh et al., 2012). Although we defined DNS as simulations where all continuum length and timescales are fully resolved, and one can argue that we do not really have a DNS if some scales are treated differently, it is likely that as our problems become more complex, our numerical strategies must allow for more flexible approaches. As additional physical processes are incorporated into our mathematical models, we are also likely to be faced with increased uncertainty in the mathematical models used to describe the new physics, rendering traditional DNS less applicable.

References

Aboulhasanzadeh, B., Thomas, S., Taeibi-Rahni, M., and Tryggvason, G., Multiscale computations of mass transfer from buoyant bubbles, *Chem. Eng. Sci.*, 75, 456–467, 2012.

Anderson, D.M., McFadden, G.B., and Wheeler, A.A., Diffuse-interface methods in fluid mechanics, *Ann. Rev. Fluid Mech.*, 30, 139–165, 1998.

Bolotnov, I.A., Influence of bubbles on the turbulence anisotropy, *J. Fluids Eng.*, 135, 051301, 2013.

Bolotnov, I.A., Jansen, K.E., Drew, D.A., Oberai, A.A., Lahey, R.T. Jr., and Podowski, M.Z., Detached direct numerical simulations of turbulent two-phase bubbly channel flow, *Int. J. Multiphase Flow*, 37, 647–659, 2011.

Booty, M.R. and Siegel, M., A hybrid numerical method for interfacial fluid flow with soluble surfactant, *J. Comput. Phys.*, 229, 38643883, 2010.

Brackbill, J.U., Kothe, D.B., and Zemach, C., A continuum method for modeling surface tension, *J. Comput. Phys.*, 100, 335–354, 1992.

Brady, J.F. and Bossis, G., Stokesian dynamics, *Ann. Rev. Fluid Mech.*, 20, 111–157, 1988.

Bunner, B. and Tryggvason, G., Direct numerical simulations of three-dimensional bubbly flows, *Phys. Fluids*, 11, 1967–1969, 1999.

Bunner, B. and Tryggvason, G., Dynamics of homogeneous bubbly flows. Part 1. Rise velocity and microstructure of the bubbles, *J. Fluid Mech.*, 466, 17–52, 2002a.

Bunner, B. and Tryggvason, G., Dynamics of homogeneous bubbly flows. Part 2. Velocity fluctuations, *J. Fluid Mech.*, 466, 53–84, 2002b.

Chahine, G.L. and Duraiswami, R., Dynamic interactions in a multibubble cloud, *ASME J. Fluids Eng.*, 114(4), 680–686, 1992.

Chan, R.K.-C. and Street, R.L., A computer study of finite-amplitude water waves, *J. Comput. Phys.*, 6, 68–94, 1970.

Chapman, R.B. and Plesset, M.S., Nonlinear effects in the collapse of a nearly spherical cavity in a liquid, *Trans. ASME, J. Basic Eng.*, 94, 142, 1972.

Dabiri, S. and Tryggvason, G., Heat transfer in turbulent bubbly flow in vertical channels, *Chem. Eng. Sci.*, 122, 106–113, 2015.

Daly, B.J., A technique for including surface tension effects in hydrodynamic calculations, *J. Comput. Phys.*, 4, 97–117, 1969a.

Daly, B.J., Numerical study of the effect of surface tension on interface instability, *Phys. Fluids*, 12, 1340–1354, 1969b.

Daly, B.J. and Pracht,W.E., Numerical study of density-current surges, *Phys. Fluids*, 11, 15–30, 1968.

Dandy, D.S. and Leal, G.L., Buoyancy-driven motion of a deformable drop through a quiescent liquid at intermediate Reynolds numbers, *J. Fluid Mech.*, 208, 161–192, 1989.

Deen, N.G. and Kuipers, J.A.M., Direct numerical simulation of wall-to liquid heat transfer in dispersed gas–liquid two-phase flow using a volume of fluid approach, *Chem. Eng. Sci.*, 102, 268282, 2013.

Desjardins, O., Moureau, V., and Pitsch, H., An accurate conservative level set/ghost fluid method for simulating turbulent atomization, *J. Comput. Phy.*, 227, 83958416, 2008.
Desjardins, O. and Pitsch, H., Detailed numerical investigation of turbulent atomization of liquid jets, *Atomization Sprays*, 20, 311336, 2010.
Dijkhuizen, W., Roghair, I., Annaland, M.V.S., and Kuipers, J., DNS of gas bubbles behaviour using an improved 3d front tracking model–drag force on isolated bubbles and comparison with experiments, *Chem. Eng. Sci.*, 65, 1415–1426, 2010a.
Dijkhuizen, W., Roghair, I., Annaland, M.V.S., and Kuipers, J., DNS of gas bubbles behaviour using an improved 3d front tracking model–model development, *Chem. Eng. Sci.*, 65, 1427–1437, 2010b.
Drew, D.A., Mathematical modeling of two-phase flow, *Ann. Rev. Fluid Mech.*, 15, 261–291, 1983.
Drew, D.A. and Lahey, R.T. Jr. Analytical modeling of multiphase flow, in *Particulate Two-Phase Flow*, Editor M. C. Roco, Butterworth-Heinemann Series in Chemical Engineering 1993, pp. 509–566.
Esmaeeli, A. and Tryggvason, G., Direct numerical simulations of bubbly flows. Part I. Low Reynolds number arrays, *J. Fluid Mech.*, 377, 313–345, 1998.
Esmaeeli, A. and Tryggvason, G., Direct numerical simulations of bubbly flows. Part II. Moderate Reynolds number arrays, *J. Fluid Mech.*, 385, 325–358, 1999.
Esmaeeli, A. and Tryggvason, G., Computations of explosive boiling in microgravity, *J. Sci. Comput.*, 19, 163–182, 2003.
Fedkiw, R., Aslam, T., Merriman, B., and Osher, S., A non-oscillatory Eulerian approach to interfaces in multimaterial flows (the ghost fluid method), *J. Comput. Phys.*, 152, 457–492, 1999.
Floryan, J.M. and Rasmussen, H., Numerical analysis of viscous flows with free surfaces, *Appl. Mech. Rev.*, 42, 323–341, 1989.
Foote, G.B., A numerical method for studying liquid drop behavior: Simple oscillations, *J. Comput. Phys.*, 11, 507–530, 1973.
Foote, G.B., The water drop rebound problem: Dynamics of collision, *J. Atmos. Sci.*, 32, 390–402, 1975.
Fortes, A., Joseph, D.D., and Lundgren, T., Nonlinear mechanics of fluidization of beds of spherical particles, *J. Fluid Mech.*, 177, 467–483, 1987.
Fuster, D., Bague, A., Boeck, T., Moyne, L., Leboissetier, A., Popinet, S., Ray, P., Scardovelli, R., and Zaleski, S., Simulation of primary atomization with an octree adaptative mesh refinement and vof method, *Int. J. Multiphase Flow*, 35, 550565, 2009.
Glimm, J. and McBryan, O., A computational model for interfaces, *Adv. Appl. Math.*, 6, 422–435, 1985.
Gorokhovski, M. and Herrmann, M., Modeling primary atomization, *Ann. Rev. Fluid Mech.*, 40, 343–366, 2008.
Hao, Y. and Prosperetti, A., A numerical method for three-dimensional gas–liquid flow computations, *J. Comput. Phys.*, 196, 126–144, 2004.
Harlow, F.H. and Shannon, J.P., The splash of a liquid drop, *J. Appl. Phys.*, 38, 3855–3866, 1967.
Harlow, F.H. and Welch, J.E., Numerical calculation of time-dependent viscous incompressible flow of fluid with a free surface, *Phys. Fluid*, 8, 2182–2189, 1965.
Harlow, F.H. and Welch, J.E., Numerical study of large-amplitude free-surface motions, *Phys. Fluid*, 9, 842–851, 1966.
Harper, J.F., Bubbles rising in line: Why is the first approximation so bad? *J. Fluid Mech.*, 351, 289–300, 1997.
Herrmann, M., A parallel eulerian interface tracking/lagrangian point particle multi-scale coupling procedure, *J. Comput. Phys.*, 229, 745759, 2010.
Herrmann, M., On simulating primary atomization using the refined level set grid method, *Atomization Sprays*, 21, 283301, 2011.
Hirt, C.W., Cook, J.L., and Butler, T.D., A Lagrangian method for calculating the dynamics of an incompressible fluid with a free surface, *J. Comput. Phys.*, 5, 103–124, 1970.
Hirt, C.W. and Nichols, B.D., Volume of Fluid (VOF) method for the dynamics of free boundaries, *J. Comput. Phys.*, 39, 201–226, 1981.
Hua, J. and Lou, J., Numerical simulation of bubble rising in viscous liquid, *J. Comput. Phys.*, 222, 769–795, 2007.
Hyman, J.M., Numerical methods for tracking interfaces, *Phys. D*, 12, 396–407, 1984.
Ishii, M., *Thermo-Fluid Dynamic Theory of Two-phase Flows*, Eyrolles, Paris, 1975.
James, A.J. and Lowengrub, J., A surfactant-conserving volume-of-fluid method for interfacial flows with insoluble surfactants, *J. Comput. Phys.*, 201, 685722, 2004.
Jeong, J. and Hussain, F., On the identification of a vortex, *J. Fluid Mech.*, 285, 69–94, 1995.

Juric, D. and Tryggvason, G., Computations of boiling flows, *Int. J. Multiphase Flow*, 24, 387–410, 1998.
Kang, I.S. and Leal, L.G., Numerical solution of axisymmetric, unsteady free-boundary problems at finite Reynolds number. I. Finite-difference scheme and its applications to the deformation of a bubble in a uniaxial straining flow, *Phys. Fluids*, 30, 1929–1940, 1987.
Labourasse, E., Lacanette, D., Toutant, A., Lubin, P., Vincent, S., Lebaigue, O., Caltagirone, J.-P., and Sagaut, P., Towards large eddy simulation of isothermal two-phase flows: Governing equations and a priori tests, *Int. J. Multiphase Flow*, 33, 1–39, 2007.
Lebas, R., Menard, T., Beau, P.A., Berlemont, A., and Demoulin, F.X., Numerical simulation of primary break-up and atomization: Dns and modelling study, *Int. J. Multiphase Flow*, 35, 247260, 2009.
Lee, L. and LeVeque, R.J., An immersed interface method for incompressible Navier–Stokes equations, *SIAM J. Sci. Comput.*, 25, 832–856, 2003.
Li, X. and Pozrikidis, C., Wall-bounded shear flow and channel flow of suspensions of liquid drops, *Int. J. Multiphase Flow*, 26, 1247–1279, 2000.
Loewenberg, M. and Hinch, E.J., Numerical simulation of a concentrated emulsion in shear flow, *J. Fluid Mech.*, 321, 395–419, 1996.
Lu, J., Biswas, S., and Tryggvason, G., A DNS study of laminar bubbly flows in a vertical channel, *Int. J. Multiphase Flow*, 32, 643–660, 2006.
Lu, J., Fernandez, A., and Tryggvason, G., The effect of bubbles on the wall shear in a turbulent channel flow, *Phys. Fluids*, 17, 095102, 2005.
Lu, J. and Tryggvason, G., Numerical study of turbulent bubbly downflows in a vertical channel, *Phys. Fluids*, 18, 103302, 2006.
Lu, J. and Tryggvason, G., Effect of bubble deformability in turbulent bubbly upflow in a vertical channel, *Phys. Fluids*, 20, 040701, 2008.
Lu, J. and Tryggvason, G., Dynamics of nearly spherical bubbles in a turbulent channel upflow, *J. Fluid Mech.*, 732, 166–189, 2013.
Ménard, T., Tanguy, S., and Berlemont, A., Coupling level set/vof/ghost fluid methods: Validation and application to 3d simulation of the primary break-up of a liquid jet, *Int. J. Multiphase Flow*, 33, 510–524, 2007.
Mitchell, T.M. and Hammitt, F.H., Asymmetric cavitation bubble collapse, *Trans. ASME, J. Fluids Eng.*, 95, 29–37, 1973.
Muradoglu, M. and Kayaalp, A.D., An auxiliary grid method for computations of multiphase flows in complex geometries, *J. Comput. Phys.*, 214, 858–877, 2006.
Muradoglu, M. and Tryggvason, G., A front-tracking method for computation of interfacial flows with soluble surfactants, *J. Comput. Phys.*, 227, 2238–2262, 2008.
Muradoglu, M. and Tryggvason, G., Simulations of soluble surfactants in 3d multiphase flow, *J. Comput. Phys.*, 274, 737–757, 2014.
Osher, S. and Fedkiw, R.P., Level set methods: An overview and some recent results, *J. Comput. Phys.*, 169, 463–502, 2001.
Osher, S. and Fedkiw, R.P., *Level Set Methods and Dynamic Implicit Surfaces*, Springer, 2002.
Pozrikidis, C., *Integral and Singularity Methods for Linearized Viscous Flow*, Cambridge University Press, Cambridge, U.K., 1992.
Pozrikidis, C., Interfacial dynamics for Stokes flow, *J. Comput. Phys.*, 169, 250–301, 2001.
Rabha, S.S., and Buwa, V.V., Volume-of-fluid (VOF) simulations of rise of single/multiple bubbles in sheared liquids, *Chem. Eng. Sci.*, 65, 527–537, 2010.
Ryskin, G. and Leal, L.G., Numerical solution of free-boundary problems in fluid mechanics. Part 2. Buoyancy-driven motion of a gas bubble through a quiescent liquid, *J. Fluid Mech.*, 148, 19–35, 1984.
Sangani, A. and Didwania, A.K., Dynamic simulations of flows of bubbly liquids at large Reynolds numbers, *J. Fluid Mech.*, 250, 307–337, 1993.
Sankaranarayanan, K., Shan, X., Kevrekidis, I.G., and Sundaresan, S., Analysis of drag and virtual mass forces in bubbly suspensions using an implicit formulation of the lattice Boltzmann method, *J. Fluid Mech.*, 452, 61–96, 2002.
Scardovelli, R. and Zaleski, S., Direct numerical simulation of free-surface and interfacial flow, *Ann. Rev. Fluid Mech.*, 31, 567–603, 1999.

Sethian, J.A., Evolution, implementation, and application of level set and fast marching methods for advancing fronts, *J. Comput. Phys.*, 169, 503–555, 2001.
Shan, X.W. and Chen, H.D., Lattice Boltzmann model for simulating flows with multiple phases and components, *Phys. Rev. E*, 47, 1815–1819, 1993.
Shin, S. and Juric, D., Modeling three-dimensional multiphase flow using a level contour reconstruction method for front tracking without connectivity, *J. Comput. Phys.*, 180, 427–470, 2002.
Shinjo, J. and Umemura, A., Simulation of liquid jet primary breakup: Dynamics of ligament and droplet formation, *Int. J. Multiphase Flow*, 36, 513532, 2010.
Shinjo, J. and Umemura, A., Detailed simulation of primary atomization mechanisms in diesel jet sprays (isolated identification of liquid jet tip effects), *Proc. Combust. Inst.*, 33, 20892097, 2011.
Shyy, W., Udaykumar, H., Rao, M., and Smith, R., *Computational Fluid Dynamics with Moving Boundaries*, Taylor & Francis, 1996.
Smereka, P., On the motion of bubbles in a periodic box, *J. Fluid Mech.*, 254, 79–112, 1993.
Son, G. and Dhir, V.K., Numerical simulation of film boiling near critical pressures with a level set method, *J. Heat Transfer*, 120, 183–192, 1998.
Tanaka, M., Numerical study on flow structures and heat transfer characteristics of turbulent bubbly upflow in a vertical channel. In: Zhu, J. (Ed.), *Computational Simulations and Applications*. InTech, Rijeka, Croatia, 119–142, 2011.
Takada, N., Misawa, M., Tomiyama, A., and Fujiwara, S., Numerical simulation of two- and three-dimensional. two-phase fluid motion by lattice Boltzmann method, *Comput. Phys. Commun.*, 129, 233–246, 2000.
Takada, N., Misawa, M., Tomiyama, A., and Hosokawai, S., Simulation of bubble motion under gravity by lattice Boltzmann method, *J. Nucl. Sci. Technol.*, 38, 330–341, 2001.
Tomara, G., Fustera, D., Zaleskia, S., and Popine, S., Multiscale simulations of primary atomization, *Comput. Fluids*, 39, 18641874, 2010.
Toutant, A., Chandesris, M., Jamet, D., and Lebaigue, O., Jump conditions for filtered quantities at an under-resolved interface. part 2: A priori tests, *Int. J. Multiphase Flow*, 35, 11191129, 2009.
Toutant, A., Labourasse, E., Lebaigue, O., and Simonin, O., DNS of the interaction between a deformable buoyant bubble and spatially decaying turbulence: A priori tests for LES two-phase flow modelling, *Comput. Fluids*, 37, 877–886, 2008.
Tryggvason, G., Bunner, B., Esmaeeli, A., Juric, D., Al-Rawahi, N., Tauber, W., Han, J., Nas, S., and Jan, Y.-J., A front tracking method for the computations of multiphase flow, *J. Comput. Phys.*, 169, 708–759, 2001.
Tryggvason, G., Scardovelli, R., and Zaleski, S., *Direct Numerical Simulations of Gas-Liquid Multiphase Flows*, Cambridge University Press, Cambridge, U.K., 2011.
Unverdi, S.O. and Tryggvason, G., A front-tracking method for viscous, incompressible, multi-fluid flows, *J. Comput. Phys.*, 100, 25–37, 1992.
van Sint Annaland, M., Dijkhuizen, W., Deen, N., and Kuipers, J., Numerical simulation of gas bubbles behaviour using a 3D front tracking method, *AIChE J.*, 52, 99–110, 2006.
Vincent, S., Larocque, J., Lacanette, D., Toutant, A., Lubin, P., and Sagaut, P., Numerical simulations of phase separation and a priori two-phase les filtering, *Comp. Fluids*, 37, 898–906, 2008.
Yabe, T., Xiao, F., and Utsumi, T., The constrained interpolation profile (CIP) method for multi-phase analysis, *J. Comput. Phys.*, 169, 556–593, 2001.
Ye, T., Mittal, R., Udaykumar, H.S., and Shyy, W., An accurate cartesian grid method for viscous incompressible flows with complex immersed boundaries, *J. Comput. Phys.*, 156, 209–240, 1999.
Youngs, D.L., Time dependent multimaterial flow with large fluid distortion, in K. M. Morton and M.J. Baines (Eds.), *Numerical Methods for Fluid Dynamics*, Academic Press, New York, 1982, pp. 27–39.
Zhang, D.Z. and Prosperetti, A., Ensemble phase-averaged equations for bubbly flows, *Phys. Fluids*, 6, 2956–2970, 1994.
Zhou, H. and Pozrikidis, C., The flow of ordered and random suspensions of two-dimensional drops in a channel, *J. Fluid Mech.*, 255, 103–127, 1993.
Zinchenko, A.Z. and Davis, R.H., An efficient algorithm for hydrodynamical interaction of many deformable drops, *J. Comput. Phys*, 157, 539–587, 2000.

2.3 The Lattice Boltzmann Method

Cyrus K. Aidun, Dennis E. Oztekin, Yuanzheng Zhu, Tomas Rosén, and Fredrik Lundell

2.3.1 Introduction and Basics of Lattice Boltzmann Method

The lattice Boltzmann method (LBM) is a computational tool that has been growing in popularity since its development due to the simplicity with which it is implemented and the ease with which it can be scaled to parallel processing systems. The method was introduced in the late 1980s (Higuera and Jimenez, 1989) and addressed a number of problems with its predecessor, the lattice gas automation method (Frisch et al., 1987). New variations of the method are being developed constantly, extending range of applicable problems for LBM. This constant development creates opportunities for new investigations on a variety of fronts.

This chapter will focus primarily on four areas that have been under intense study recently as fields of research that lend themselves well to newer lattice Boltzmann variants. The first section will focus on fluid–solid interaction. Here, the bounce-back boundary condition will be discussed, along with the newer external boundary force (EBF) method for treating solid interfaces. Following this, there will be a section about the suspension of deformable capsules and then a section about the suspension of deformable fibers. Finally, there will be a section on the methods by which lattice Boltzmann deals with liquid–gas problems.

2.3.1.1 Brief Background

All of lattice Boltzmann research is based on the Boltzmann equation, which states

$$\frac{\partial f}{\partial t} + \boldsymbol{\zeta} \cdot \nabla f + \frac{\boldsymbol{F}}{m_p} \cdot \frac{\partial f}{\partial \boldsymbol{\zeta}} = \left\{ \frac{\partial f}{\partial t} \right\}_{collision} \tag{2.75}$$

In this equation,

$\boldsymbol{F}$ is the term of body forces

m_p is the particle mass

$\boldsymbol{\zeta}$ is the velocity of the particle

f is the density distribution function, that is, for some position and some time, the number of particles per volume, or density ρ, with a velocity between $\boldsymbol{\zeta}$ and $\boldsymbol{\zeta} + d\boldsymbol{\zeta}$. From this definition, we can write

$$\rho = \int f d\boldsymbol{\zeta} \tag{2.76}$$

The moment of this equation can be taken to get a very important relationship in recovering the conservation of momentum:

$$\rho \boldsymbol{u} = \int \boldsymbol{\zeta} f d\boldsymbol{\zeta} \tag{2.77}$$

Here, it is very important to distinguish $\boldsymbol{u}$, the macroscopic fluid velocity, from $\boldsymbol{\zeta}$, the particle velocity. The macroscopic fluid velocity is the property that is commonly utilized in fluid mechanics; as such, this is the property that is typically solved for in the following sections. The particle velocity is only the velocity of a single particle; if it is assumed that the individual particles only move along a discretized grid, this will be reduced to the aptly named lattice velocity, $\boldsymbol{e}_k$. This will be presented later. Before any discretization can occur, the Boltzmann equation needs to be reduced to a usable form. First, the forcing term is dropped. Later in the chapter, more numerically friendly methods of including the force will be discussed. The next term that needs to be addressed is the rate of change of the density distribution due to the collision of particles. This is the right-hand side of the Boltzmann equation displayed earlier. To address this term, the Lattice Bhatnagar-Gross-Krook, LBGK, approximation (Bhatnagar et al., 1954) is applied. This approximation

introduced an equilibrium density distribution function f^{eq}, which is a function of velocity and density, and a relaxation time τ, which is a function of viscosity. The approximation becomes

$$\left\{\frac{\partial f}{\partial t}\right\}_{collision} = \frac{f^{eq} - f}{\tau} \tag{2.78}$$

With this, the Boltzmann equation is put into a usable form and is ready for discretization.

2.3.1.2 Discretization

The most immediate effect of the discretization is allowing the expansion of the derivative term remaining on the left-hand side of the Boltzmann equation. With these simplifications, the Boltzmann equation is reduced to

$$f_k(\boldsymbol{x}+\boldsymbol{e}_k, t+1) - f_k(\boldsymbol{x},t) = -\frac{1}{\tau}\left[f_k(\boldsymbol{x},t) - f_k^{eq}(\boldsymbol{x},t)\right] = \boldsymbol{C}\left(f_k\left(\boldsymbol{x},t\right)\right) \tag{2.79}$$

where the subscript k denotes the lattice direction and $\boldsymbol{C}$ is the collision operator. The lattice direction represents which path from the lattice node a given particle might be taking. For reference, the lattice arrangements used in this study are D2Q9 and D3Q19. Where the notation DxQy means there are x dimensions and y lattice arrangements. D2Q9 is commonly used two dimensional arrangement which includes the node itself, the four cardinal direction, and its four diagonals. D3Q19 is a common three dimensional arrangement which includes the node itself, its six cardinal directions, and the twelve diagonals that lie on the three planes normal to the cardinal directions. From this equation, commonly called the evolution equation, the equilibrium density distribution function can be determined in a number of ways; however, the most general way is demonstrated by He and Luo (1997). This derivation starts with a Maxwell–Boltzmann distribution and takes a Taylor expansion about the macroscopic velocity. The result is

$$f_k^{eq}(x,t) = \frac{3\rho}{(2\pi c^2)^{D/2}}\left\{1 + \frac{6\boldsymbol{e}_k\boldsymbol{u}}{c^2} - \frac{3\boldsymbol{e}_k^2}{c^2} + \frac{9\boldsymbol{e}_k\boldsymbol{u}^2}{c^4}\right\} \tag{2.80}$$

Here,

D is the number of dimensions being modeled

c is called the lattice speed, which is the distance between two adjacent nodes divided by the time of a single time step.

2.3.2 Fluid–Solid Interaction

In this section, we will discuss how fluid–solid interaction can be modeled in Lattice Boltzmann, LB, simulations. As an example, we will consider a single solid particle suspended in the fluid domain and describe two methods for coupling the solid and fluid motion.

2.3.2.1 Standard Bounce-Back Method

The standard bounce-back (SBB) method for simulating particles in flows was described by Aidun et al. (1998) and will be summarized in this section.

Consider a particle at a position $\boldsymbol{X}(t)$ with a certain velocity $\boldsymbol{U}(t)$ and angular velocity $\Omega(t)$ at time instance t. The particle has mass m and inertial tensor $\boldsymbol{I}$. The position, orientation, and geometry of the particle determine the location of the particle boundary $\Gamma(t)$. Using the SBB method, the following steps are performed:

1. Each link k is classified according to the boundary $\Gamma(t)$ (see Figure 2.10). The link in the opposite direction of k is denoted k'. The link is
   - **a.** A boundary link (*BL*) if it is crossing the particle boundary
   - **b.** A regular link (*RL*) otherwise

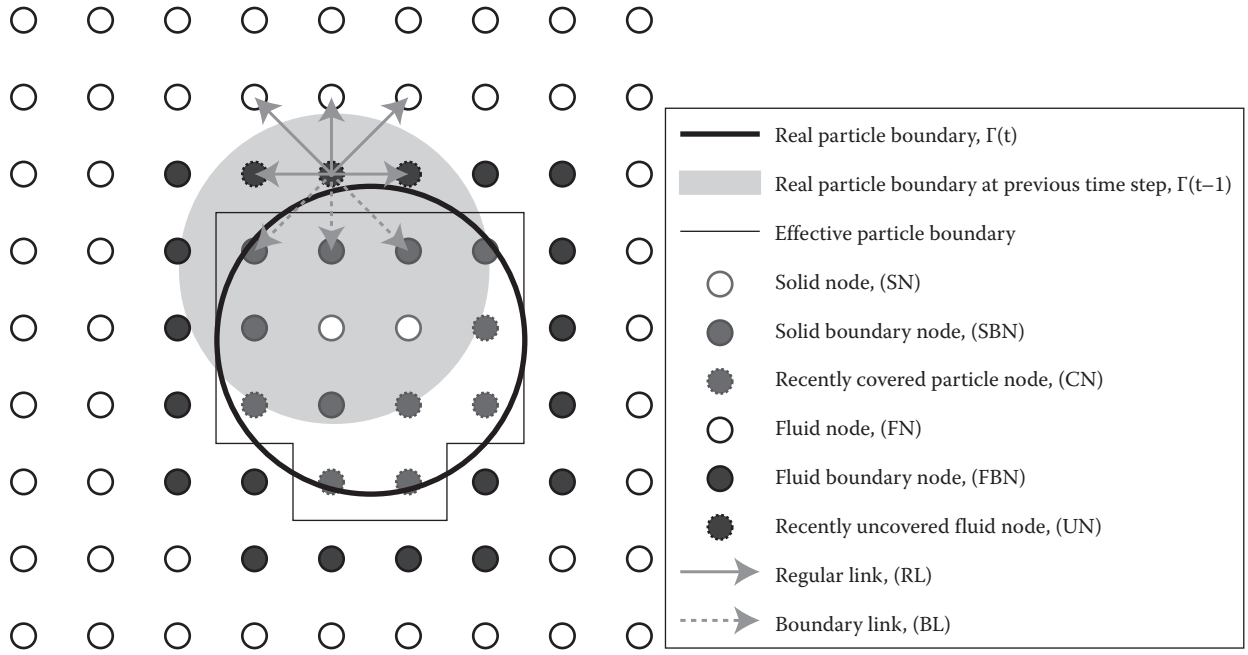

Figure 2.10

Definitions and classifications of the standard bounce-back method for a D2Q9 arrangement.

Note that the effective boundary of the particle is defined by the halfway point of the BLs and thus gets a staircase shape.

2. The lattice nodes are classified according to the boundary $\Gamma(t)$ (see Figure 2.10). The node is
   - **a.** A fluid node (*FN*) if the node is outside $\Gamma(t)$ and all links are RLs
   - **b.** A fluid boundary node (*FBN*) if the node is outside $\Gamma(t)$ and has one or more BLs
   - **c.** A recently uncovered node (*UN*) if the node is outside $\Gamma(t)$ but was inside $\Gamma(t-1)$
   - **d.** A solid node (*SN*) if the node is inside $\Gamma(t)$ and all links are RLs
   - **e.** A solid boundary node (*SBN*) if the node is inside $\Gamma(t)$ and has one or more BLs
   - **f.** A recently covered node (*CN*) if the node is inside $\Gamma(t)$ but was outside $\Gamma(t-1)$.
3. Density and velocity are corrected for UNs:

$$\rho(\boldsymbol{x},t)=\frac{1}{N_b}\sum_{k\in RL}\rho(\boldsymbol{x}+\boldsymbol{e}_k,t) \tag{2.81}$$

$$\boldsymbol{u}(\boldsymbol{x},t)=\boldsymbol{U}(t)+\boldsymbol{\Omega}(t)\times[\boldsymbol{x}-\boldsymbol{X}(t)] \tag{2.82}$$

where N_b is the amount of RLs for the UN and $\boldsymbol{x}\in UN$.

4. Collision step:

$$f_k(\boldsymbol{x},t_+)=\boldsymbol{C}f_k(\boldsymbol{x},t) \tag{2.83}$$

where $\boldsymbol{C}$ is the collision operator described in the previous section.

5. Propagation step:

$$\tilde{f}_k(\boldsymbol{x},t+1)=\begin{cases} f_{k'}(\boldsymbol{x},t_+) & \text{if } k'\in BL \\ f_k(\boldsymbol{x}+\boldsymbol{e}_{k'},t_+) & \text{otherwise} \end{cases} \tag{2.84}$$

6. The correct fluid density is obtained at each node through

$$\rho(\boldsymbol{x},t+1)=\frac{\sum_k \tilde{f}_k(\boldsymbol{x},t+1)}{1-2\sum_{k'\in BL} B_k \boldsymbol{u}_{k'}(t)\cdot\boldsymbol{e}_k} \tag{2.85}$$

where $B_0 = 1/3$, $B_{1-6} = 1/6$, and $B_{7-18} = 1/12$ in the D3Q19 lattice arrangement. The velocity of the wall $\boldsymbol{u}_k$, crossing the BL $k' \in BL$, is obtained through

$$\mathbf{u}_{k'}(t)=\mathbf{U}(t)+\boldsymbol{\Omega}(t)\times\left[\boldsymbol{x}+\frac{1}{2}\boldsymbol{e}_{k'}-\boldsymbol{X}(t)\right] \tag{2.86}$$

7. The modification of the distribution function components is obtained through

$$f_k(\boldsymbol{x},t+1)=\begin{cases}\tilde{f}_k(\boldsymbol{x},t+1)+2\rho(\boldsymbol{x},t+1)B_k\boldsymbol{u}_{k'}(t)\cdot\boldsymbol{e}_k & \text{if } k'\in BL\\ \tilde{f}_k(\boldsymbol{x},t+1) & \text{otherwise}\end{cases} \tag{2.87}$$

8. The force and torque contributions on the particle from the BLs are obtained through

$$\boldsymbol{F}_k^{BL}\left(\boldsymbol{x}+\frac{1}{2}\boldsymbol{e}_{k'},t+\frac{1}{2}\right)=2\boldsymbol{e}_{k'}[f_k(\boldsymbol{x},t+1)+\rho(\boldsymbol{x},t+1)B_k\boldsymbol{u}_{k'}(t)\cdot\boldsymbol{e}_{k'}] \tag{2.88}$$

$$\boldsymbol{T}_k^{BL}\left(\boldsymbol{x}+\frac{1}{2}\boldsymbol{e}_{k'},t+\frac{1}{2}\right)=\left[\boldsymbol{x}+\frac{1}{2}\boldsymbol{e}_{k'}-\boldsymbol{X}(t)\right]\times\boldsymbol{F}_k^{BL}\left(\boldsymbol{x}+\frac{1}{2}\boldsymbol{e}_{k'},t+\frac{1}{2}\right) \tag{2.89}$$

where $k' \in BL$.

9. The force and torque contributions on the particle from the recent CNs are obtained through

$$\boldsymbol{F}^{CN}\left(\boldsymbol{x},t+\frac{1}{2}\right)=\sum_k f_k(\boldsymbol{x},t)\boldsymbol{e}_k \tag{2.90}$$

$$\boldsymbol{T}^{CN}\left(\boldsymbol{x},t+\frac{1}{2}\right)=[\boldsymbol{x}-\boldsymbol{X}(t)]\times\boldsymbol{F}^{CN}\left(\boldsymbol{x},t+\frac{1}{2}\right) \tag{2.91}$$

where $\boldsymbol{x} \in CN$.

10. The force and torque contributions on the particle from the recent UNs are obtained through

$$\boldsymbol{F}^{UN}\left(\boldsymbol{x},t+\frac{1}{2}\right)=-\rho(\boldsymbol{x},t)\boldsymbol{u}(\boldsymbol{x},t) \tag{2.92}$$

$$\boldsymbol{T}^{UN}\left(\boldsymbol{x},t+\frac{1}{2}\right)=[\boldsymbol{x}-\boldsymbol{X}(t)]\times\boldsymbol{F}^{UN}\left(\boldsymbol{x},t+\frac{1}{2}\right) \tag{2.93}$$

where $\boldsymbol{x} \in UN$.

11. The force and torque contributions are summed together according to

$$\boldsymbol{F}\left(t+\frac{1}{2}\right)=\sum_{\boldsymbol{x}\in FBN}\sum_{k'\in BL}\boldsymbol{F}_k^{BL}\left(\boldsymbol{x}+\frac{1}{2}\boldsymbol{e}_{k'},t+\frac{1}{2}\right)+ \\ +\sum_{\boldsymbol{x}\in CN}\boldsymbol{F}^{CN}\left(\boldsymbol{x},t+\frac{1}{2}\right)+\sum_{\boldsymbol{x}\in UN}\boldsymbol{F}^{UN}\left(\boldsymbol{x},t+\frac{1}{2}\right) \tag{2.94}$$

$$\boldsymbol{T}\left(t+\frac{1}{2}\right)=\sum_{\boldsymbol{x}\in FBN}\sum_{k'\in BL}\boldsymbol{T}_k^{BL}\left(\boldsymbol{x}+\frac{1}{2}\boldsymbol{e}_{k'},t+\frac{1}{2}\right)+ \\ +\sum_{\boldsymbol{x}\in CN}\boldsymbol{T}^{CN}\left(\boldsymbol{x},t+\frac{1}{2}\right)+\sum_{\boldsymbol{x}\in UN}\boldsymbol{T}^{UN}\left(\boldsymbol{x},t+\frac{1}{2}\right) \tag{2.95}$$

12. Force $\boldsymbol{F}(t)$ and torque $\boldsymbol{T}(t)$ on the particle are found through averaging with the previous time step:

$$\boldsymbol{F}(t)=\frac{1}{2}\left[\boldsymbol{F}\left(t+\frac{1}{2}\right)+\boldsymbol{F}\left(t-\frac{1}{2}\right)\right] \tag{2.96}$$

$$\boldsymbol{T}(t)=\frac{1}{2}\left[\boldsymbol{T}\left(t+\frac{1}{2}\right)+\boldsymbol{T}\left(t-\frac{1}{2}\right)\right] \tag{2.97}$$

13. The new particle position $\boldsymbol{X}(t+1)$, velocity $\boldsymbol{U}(t+1)$, angular velocity $\boldsymbol{\Omega}(t+1)$, and orientation are found through numerical integration of the particle equations of motion:

$$m\frac{d\boldsymbol{U}(t)}{dt}=\boldsymbol{F}(t) \tag{2.98}$$

$$\boldsymbol{I}\cdot\frac{d\boldsymbol{\Omega}(t)}{dt}+\boldsymbol{\Omega}(t)\times[\boldsymbol{I}\cdot\boldsymbol{\Omega}(t)]=\boldsymbol{T}(t) \tag{2.99}$$

14. The particle boundary $\Gamma(t+1)$ is updated according to the new particle position and orientation.

2.3.2.2 External Boundary Force Method

The EBF method is an improved way of simulating particles in flows using LBM and was described by Wu and Aidun (2010a). Instead of having the particle defined on the fixed Eulerian fluid grid, the particle is defined by an overlapping Lagrangian grid that can move freely in the domain. The nodes in the fluid domain are denoted as $\boldsymbol{x}^e \in \Pi_f$ and the nodes in the particle grid are denoted (for the jth node) $\boldsymbol{x}_j^l \in \Gamma_s$. Each node in the particle grid is associated with an area element of size ΔA_j and gets a characteristic volume $\Delta v_j = \Delta A_j^{3/2}$. The best results are obtained by keeping $\Delta A_j \approx (\Delta x)^2$, with Δx as the node spacing in the fluid grid.

Fluid quantities are mapped onto the particle grid by using a discrete delta function as defined by Peskin (2002):

$$D(\boldsymbol{x})=\begin{cases}\dfrac{1}{64\Delta x^3}\left(\left(1+\cos\left(\dfrac{\pi x}{2\Delta x}\right)\right)\left(1+\cos\left(\dfrac{\pi y}{2\Delta x}\right)\right)\left(1+\cos\left(\dfrac{\pi z}{2\Delta x}\right)\right)\right), & |\boldsymbol{x}|\le 2\Delta x \\ 0, & |\boldsymbol{x}|>2\Delta x.\end{cases} \tag{2.100}$$

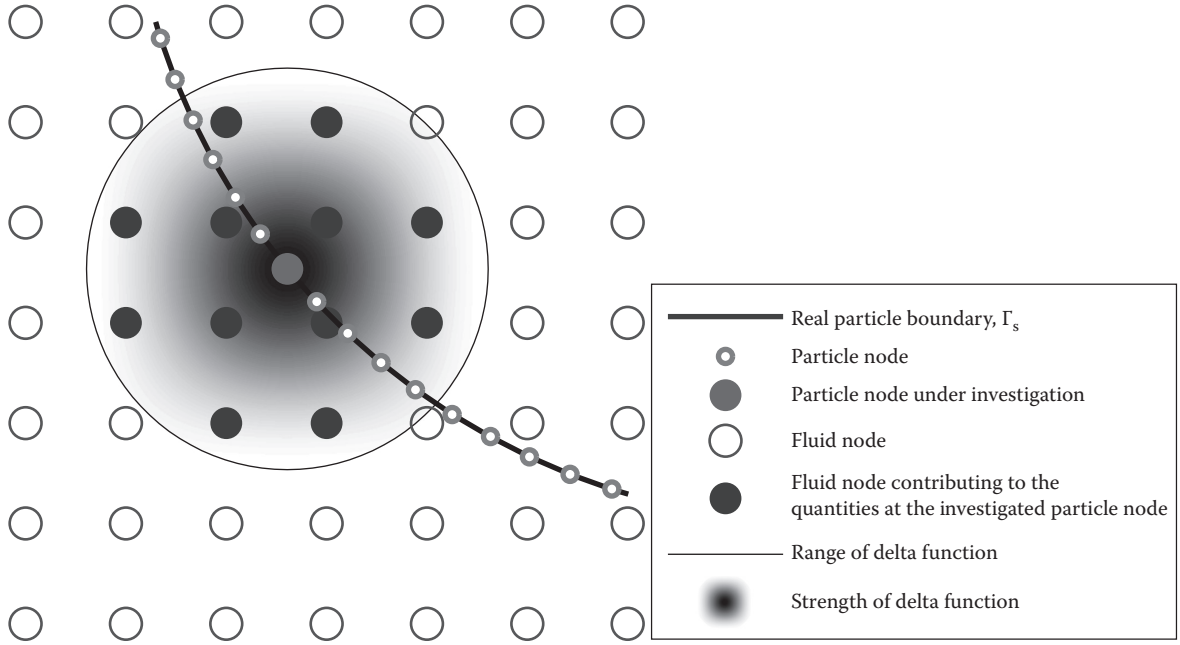

Figure 2.11

Illustration of the principle of the external boundary force method; the mapping of fluid quantities onto a particle node of investigation is done through a discrete delta function.

Again, we consider a particle with mass m, inertial tensor $\boldsymbol{I}$, position $\boldsymbol{X}(t)$, velocity $\boldsymbol{U}(t)$, and angular velocity $\boldsymbol{\Omega}(t)$ at time instance t. The following steps are performed when using the EBF method:

1. Propagation step:

$$\tilde{f}_k(\boldsymbol{x}^e,t) = f_k(\boldsymbol{x}^e + \boldsymbol{e}_{k'}, t-1) \tag{2.101}$$

2. The precollisional distributions $\tilde{f}_k(\boldsymbol{x}^e,t)$ are used to calculate the fluid velocity $\boldsymbol{u}(\boldsymbol{x}^e,t)$, which is then mapped to the particle grid through (see Figure 2.11):

$$\boldsymbol{u}(\boldsymbol{x}_j^l,t) = \sum_{\boldsymbol{x}^e \in \Pi_f} \boldsymbol{u}(\boldsymbol{x}^e,t) D(\boldsymbol{x}^e - \boldsymbol{x}_j^l)(\Delta x)^3. \tag{2.102}$$

3. The force acting on the particle node is calculated through

$$\boldsymbol{F}^{fsi}(\boldsymbol{x}_j^l,t) = \boldsymbol{f}^{fsi}(\boldsymbol{x}_j^l,t)\cdot\Delta v_j = \rho_0[\boldsymbol{u}(\boldsymbol{x}_j^l,t) - \boldsymbol{U}_p(\boldsymbol{x}_j^l,t-1)]\cdot\Delta v_j \tag{2.103}$$

with $\boldsymbol{f}^{fsi}(\boldsymbol{x}_j^l,t)$ as the force density at the jth particle node, ρ_0 as the reference fluid density, and $\boldsymbol{U}_p(\boldsymbol{x}_j^l,t-1)$ as the jth particle node velocity at time $t-1$.

4. The particle force $\boldsymbol{F}(t)$ and torque $\boldsymbol{T}(t)$ are determined by summing the contributions from the nodes:

$$\boldsymbol{F}(t) = \sum_{\boldsymbol{x}_j^l \in \Gamma_s} \boldsymbol{F}^{fsi}(\boldsymbol{x}_j^l,t) \tag{2.104}$$

$$\boldsymbol{T}(t) = \sum_{x_j^l \in \Gamma_s} (\boldsymbol{x}_j^l - \boldsymbol{x}^{lc}) \times \boldsymbol{F}^{fsi}(\boldsymbol{x}_j^l,t) \tag{2.105}$$

where $\boldsymbol{x}^{lc}$ is the center of gravity of the particle.

5. The new particle position $\boldsymbol{X}(t+1)$, velocity $\boldsymbol{U}(t+1)$, angular velocity $\boldsymbol{\Omega}(t+1)$, and orientation are found through numerical integration of the particle equations of motion:

$$m\frac{d\boldsymbol{U}(t)}{dt} = \boldsymbol{F}(t) \tag{2.106}$$

$$\boldsymbol{I}\cdot\frac{d\boldsymbol{\Omega}(t)}{dt} + \boldsymbol{\Omega}(t)\times[\boldsymbol{I}\cdot\boldsymbol{\Omega}(t)] = \boldsymbol{T}(t) \tag{2.107}$$

6. The force acting on the FNs from the particle is determined by

$$\boldsymbol{g}(\boldsymbol{x}^e,t) = -\sum_{\boldsymbol{x}_j^l\in\Gamma_s} \boldsymbol{f}^{fsi}(\boldsymbol{x}_j^l,t)D(\boldsymbol{x}^e-\boldsymbol{x}_j^l)\Delta v_j \tag{2.108}$$

7. Collision step:

$$f_k(\boldsymbol{x},t) = \boldsymbol{C}\tilde{f}_k(\boldsymbol{x},t) + 3w_k\boldsymbol{g}(\boldsymbol{x}^e,t)\cdot\boldsymbol{e}_k \tag{2.109}$$

where $\boldsymbol{C}$ is the collision operator, $w_0 = 1/3$, $w_{1-6} = 1/18$, and $w_{7-18} = 1/36$.

Even though the EBF method has many advantages over the SBB method, one drawback of EBF is that the code gets unstable as the particle density becomes significantly lighter than the density of the surrounding fluid. For simulating a particle with $\rho_p < \rho_f$, the SBB method is a better choice.

2.3.2.3 Example: Single Prolate Spheroid in Linear Shear Flow

One of the several advantages of the SBB and EBF methods is the ability to efficiently study nonspherical particles in flows with inertia. In many industrial applications, for example, in papermaking, the particles of interest are elongated and thus highly nonspherical fibers. The quality of the final product is dependent not only on the spatial distribution but also on the orientation distribution of fibers. This, in turn, is dependent on the orientational dynamics of the fibers due to local velocity gradients in the flow of paper pulp. Consequently, it is important to understand how a single fiber behaves in a linear shear flow. The easiest way of going from a spherical particle to a fiber is to consider a prolate spheroid, which can be seen as a sphere that is elongated along a line. This line is thus an axis of rotational symmetry $\boldsymbol{s} = (s_x, s_y, s_z)$ and also determines the particle orientation. The aspect ratio of the particle is given by $r_p = l/w$, where l is the particle length and w is the equatorial diameter.

Considering a single prolate spheroid in a linear shear flow (illustrated in Figure 2.12a), there are two dimensionless quantities governing the orientational dynamics. The fluid inertia is quantified by the particle Reynolds number $Re_p = \dot{\gamma}l/\nu$ ($\dot{\gamma}$ is the shear rate and ν is the kinematic viscosity), and the particle inertia is quantified by the Stokes number $St = (\rho_s/\rho_f)\,Re_p$ (ρ_s and ρ_f are the solid and fluid densities, respectively).

Without any inertia ($Re_p = St = 0$), Jeffery (1922) found that the prolate spheroid is rotating in one of an infinite amount of periodic orbits determined by the initial orientation (see trajectories of (s_x, s_y) in Figure 2.12b). Using the EBF method, the flow problem was investigated by Rosén et al. (2014, 2015). It was found that there are several dynamical transitions that occur when increasing Re_p, which leads to different stable rotational states as described in Table 2.1 and illustrated in Figure 2.12c. Depending on the choice of Re_p and St, certain rotational states are stable, and it is found that there are 13 distinct regimes in the Re_p/St parameter space according to Figure 2.13. This parameter space furthermore looks qualitatively the same (i.e., the same sequence of transitions with increasing Re_p and/or St, but quantitative values are different) for any prolate spheroid with $r_p = 2$–6 but is believed to be even qualitatively valid for a wider range of r_p.

In regimes II–IV, the planar states (rotating or tumbling) coexist with a nonplanar state (Log-rolling, inclined rolling, inclined kayaking, or kayaking). In these regimes, there is an unstable limit cycle that separates the initial orientations leading to the planar and nonplanar rotation, respectively (see Figure 2.12), for example, a particle initialized at rest with an orientation inside the unstable limit cycle will enter a nonplanar rotation.

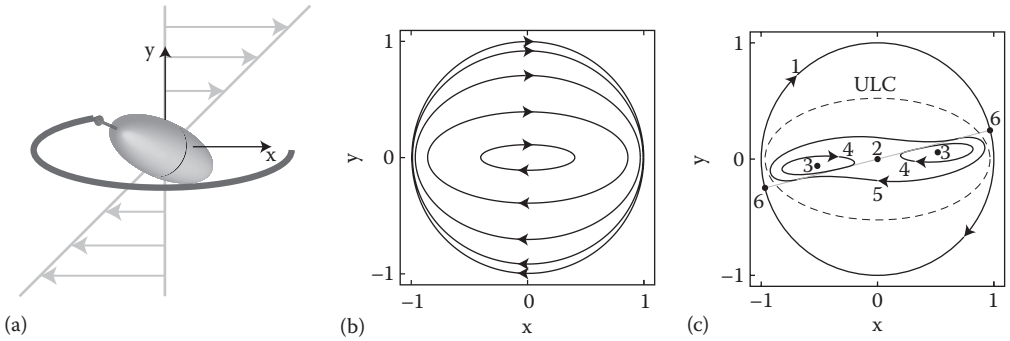

Figure 2.12

(a) A prolate spheroid is placed in a linear shear flow. The particle orientation is given by the direction of its symmetry axis, $\boldsymbol{s}$. (b) Trajectories of (s_x, s_y) at $Re_p = St = 0$ for a particle with $r_p = 4$ given by Jeffery (1922). (c) Schematic trajectories of (s_x, s_y) of stable rotational states at $Re_p > 0$. (1) Tumbling or rotating. (2) Log-rolling. (3) Inclined rolling. (4) Inclined kayaking. (5) Kayaking. (6) Steady state; An unstable limit cycle separates the nonplanar states (2–5) with the coexisting planar state (1).

Table 2.1 Description of the Rotational States of the Prolate Spheroid in Shear Flow

Rotational State	Rotational State (Abbr.)	Definition
Tumbling	T	$s_z = 0, \boldsymbol{s} = \boldsymbol{s}(t), \tau_p > \tau_c$
Rotating	R	$s_z = 0, \boldsymbol{s} = \boldsymbol{s}(t), \tau_p < \tau_c$
Steady state	S	$s_z = 0, \boldsymbol{s} = const.$
Log-rolling	LR	$s_z = 1, \boldsymbol{s} = const.$
Inclined rolling	IR	$0 < s_z < 1, \boldsymbol{s} = const.$
Inclined kayaking	IK	$0 < s_z < 1, \boldsymbol{s} = \boldsymbol{s}(t), \langle s_x \rangle \neq 0$
Kayaking	K	$0 < s_z < 1, \boldsymbol{s} = \boldsymbol{s}(t), \langle s_x \rangle = 0$

τ_p is the period of the rotation and $\tau_c = (\pi/\dot{\gamma}) \cdot (r_p + r_p^{-1} + 2)$.

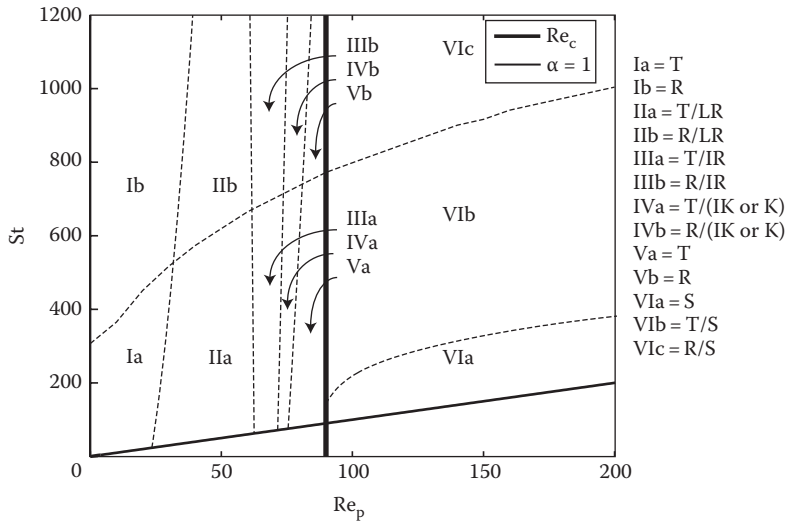

Figure 2.13

Stable rotational states of a prolate spheroid of $r_p = 4$ in a linear shear flow as found by Rosén et al. (2014, 2015); in regions with two stable states, the final state depends on initial conditions; and the steady state is created in a saddle-node bifurcation at $Re_p = Re_c$. The abbreviations of rotational states are found in Table 2.1.

At $Re_p = Re_c$, a steady state is created through a saddle-node bifurcation. This state will exist at all $Re_p > Re_c$. However, if St is high enough, the particle can gain enough angular momentum for a planar rotation to coexist with the steady state.

One of the main difficulties with the presented methods in this section (SBB and EBF) is the fact that there is no local grid refinement close to the particle surface. At higher Re_p, boundary layers need to be resolved around the particle to get quantitative results of critical Reynolds numbers (e.g., Re_c) that are independent of grid resolution. On the other hand, increasing resolution to fulfill the desired accuracy might be computationally unfeasible due to the uniform grid. Fortunately, the qualitative dynamics and the sequence of bifurcations are independent of resolution using the EBF method as long as $w \geq 6\Delta x$ (Rosén et al., 2015). The conclusion is that these methods are excellent tools for exploring unknown qualitative features of non-spherical particles in flows, but methods with local grid refinement are desirable for obtaining quantitative results at higher Re_p.

2.3.3 Suspension of Deformable Particles and Capsules

The dynamics of deformable capsules, vesicles, and soft particles have been of continued interest to the scientific community. Deformable particles exhibit much more complex dynamic behavior than rigid particles. Also, treating them as rigid solids will not properly capture the micro and macroscopic properties.

In suspensions, these complex dynamics affect the rheology of the bulk flow, creating non-Newtonian flow characteristics. For example, one of the most intensely studied deformable capsules, the red blood cell (RBC), is the major constituent of blood. As the local shear increases, so does the deformation of RBC, which results in a decreased suspension viscosity. This effect causes the shear-thinning behavior of blood.

2.3.3.1 Coupling Lattice Boltzmann with Finite Element Method

MacMeccan et al. (2009) introduced a method to simulate both deformable solid particles and deformable fluid-filled membranes, namely, capsules. This method couples the LBM for the fluid phase to a linear-elastic finite element analysis (FEA) describing particle deformation.

For deformable solid particles, the shear elastic number (Goddard Miller, 1967, Pal, 2003), $N_s e = \mu\gamma \cdot /G_S$, governs particle deformation, where μ is the fluid dynamic viscosity, γ is the fluid shear rate, and G_S is the particle shear modulus. For fluid-filled elastic capsules, the capillary number, $Ca_G = \mu\gamma \cdot R/G_M$, governs particle deformation, where R is the particle radius and G_M is the effective membrane shear modulus ($G_M = G_S \cdot t_M$ for membranes with thickness, t_M).

In both cases, deformable solid particle and fluid-filled elastic capsules, the trajectory and deformation of an elastic deformable particle are governed by Cauchy's equation,

$$\frac{D\rho_s \boldsymbol{u}_s}{Dt} = \nabla \cdot \boldsymbol{T} \tag{2.110}$$

in which the left-hand side is the material derivative of solid momentum and $\boldsymbol{T}$ is the elastic stress tensor. A transient FEA is chosen to calculate the time evolution of deformable particles in suspension, which integrates virtual work over the volume of the element:

$$\int tr(\bar{\boldsymbol{\varepsilon}} \otimes \boldsymbol{T}) dV = \int \bar{\boldsymbol{X}} \cdot \boldsymbol{F}^{tr} dA + \int \bar{\boldsymbol{X}} \cdot \boldsymbol{F}^{b} dV \tag{2.111}$$

where

$\bar{\boldsymbol{X}}$ is the elemental virtual displacements
$\bar{\boldsymbol{\varepsilon}}$ is an elemental virtual strain due to virtual displacements
$\boldsymbol{F}^{tr}$ are the traction stresses on the surface
$\boldsymbol{F}^{b}$ is the body stresses
A is the surface area
V is the volume

In this method, linear-elastic solid elements are used to model solid deformable particles such as platelets, and linear-elastic shell elements are used to model deformable fluid-filled membranes such as RBCs. The linear-elastic solid element is shown in Figure 2.14a with four nodes, and the linear-elastic shell element is shown in Figure 2.14b with three nodes.